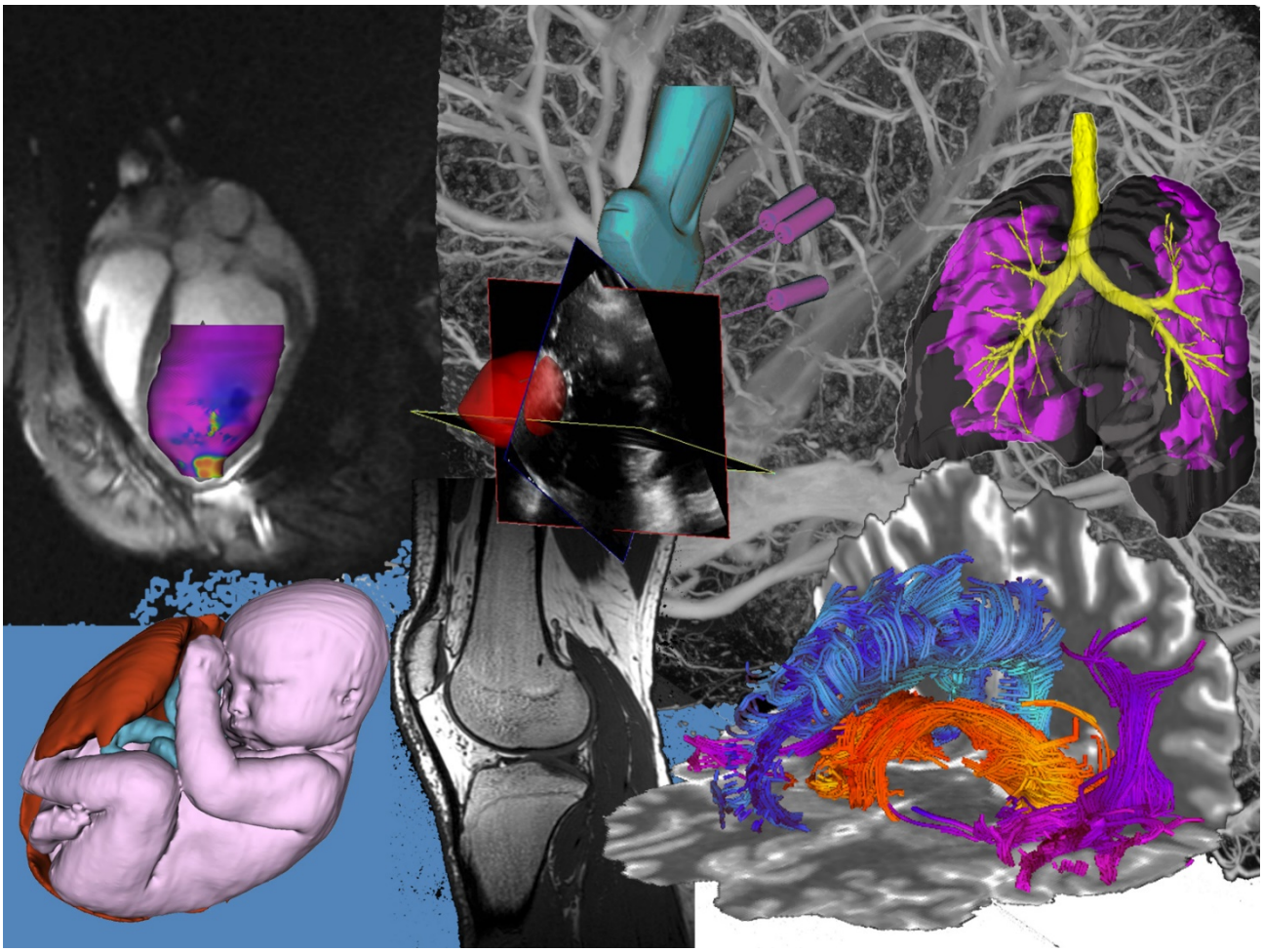

VIRTUAL

Proceedings of the 20th Annual Symposium Imaging Network Ontario

March 22 – 24, 2022

Table of Contents

ImNO 2022 Co-Chairs 4

Welcome Letter 5

Imaging Network Ontario (ImNO) Code of Conduct 6

Supporting Consortia 7

Machine Learning in Medical Imaging Consortium (MaLMIC) 7

Ontario Institute for Cancer Research Imaging Program 7

Image-Guided Device Interventions for Cardiovascular Disease 7

Corporate Sponsor 8

Scintica 8

Keynote Speakers 9

David Jaffray, MD Anderson Cancer 9

Center Alison Noble, University of Oxford 10

Introduction to Patient Partnerships Speakers 11

Medical Imaging in Global Health Speakers 12

Organizing Committees 13

Scientific Committee 13

Student Committee 13

Planning Committee 13

Abstract Reviewers 13

Oral and Pitch Judges 14

Program 15

Oral and Pitch Abstracts 21

Oral Session 1: Cancer Imaging – Therapy Response 22

Oral Session 2: Neuro Imaging 27

Pitch Session 1: Machine Learning I 32

Pitch Session 2: Neuro Imaging I 41

Oral Session 3: MR Imaging I 50

Oral Session 4: Device, Hardware and System Development 55

Pitch Session 3: MR Imaging 60

Pitch Session 4: Hardware, Software and System Development 69
Oral Session 5: Machine Learning 78
Oral Session 6: Cellular and Molecular 83
Pitch Session 5: Machine Learning II 88
Pitch Session 6: Cardiac, Cellular and Molecular 97
Oral Session 7: Cancer Imaging 106
Oral Session 8: Cardiac and Vascular Imaging 111
Pitch Session 7: Cancer Imaging 116
Pitch Session 8: Ultrasound and Optical Imaging 125
Oral Session 9: Imaging for Musculoskeletal Analysis 134
Oral Session 10: MR Imaging II 139
Pitch Session 9: Imaging for Musculoskeletal Analysis 144
Pitch Session 10: Neuro Imaging II 152
Oral Session 11: Lung Imaging 161
Oral Session 12: Image-Guided Intervention and Surgery 166
Pitch Session 11: Lung Imaging 171
Pitch Session 12: Image-Guided Intervention and Surgery 180
Author Index **189**

ImNO 2022 Co-Chairs

Gabor Fichtinger

Queen's University

Tina Khazaee

Western University

Welcome Letter

March 07, 2022

Dear ImNO 2022 Attendees:

On behalf of the Imaging Network Ontario (ImNO) 2022 scientific and organizing committee, we are honored and delighted to welcome you to the 20th annual ImNO symposium. This meeting will be the third virtual meeting.

ImNO is an initiative created in response to a request by the Ontario Research Development Challenge Fund – now the Ontario Research Fund – for assistance in harmonizing its investments in imaging research. The establishment of ImNO provides a means of harnessing and focusing the intellectual and innovative capabilities at Ontario universities in partnerships with the emerging and established medical imaging industry to create a strong and sustainable internationally competitive imaging industry based on scientific excellence in Ontario.

Since its inception in 2003, the annual ImNO meeting has welcomed invited presentations from world-class scientists and proffered presentations from Ontario and across the county. This year, we are pleased to thank the following four groups for supporting our symposium:

- Image-Guided Device Interventions for Cardiovascular Disease
- Machine Learning in Medical Imaging Consortium (MaLMIC)
- Ontario Institute for Cancer Research Imaging Program
- Scintica Instrumentation Inc.

Our program is rich and varied with 3 keynote sessions featuring 8 leading speakers, and 143 accepted abstracts split between 48 oral presentations and 95 pitch-and-poster presentations. In addition, there will be a lunch-and-learn session on patient partnerships, an educational challenge and social events. There will be numerous opportunities for you to network with your imaging colleagues.

In closing, we would like to acknowledge the significant contributions made by the members of the Scientific, Student and Planning Committees. Together they have worked very hard to bring us this year's meeting. We hope you enjoy the program and world-renowned keynote speakers.

Sincerely,

Gabor Fichtinger and Tina Khazaee
Chairs, Scientific Committee, 2022 ImNO Symposium

Imaging Network Ontario Code of Conduct

All attendees, speakers, sponsors and volunteers at the ImNO symposium are required to agree with the following code of conduct. Organisers will enforce this code throughout the event. We expect cooperation from all participants to help ensure a safe environment for everybody.

Need Help?

If you are being harassed, notice that someone else is being harassed, or have any other concerns, contact the Symposium Manager at imno@imno.ca or send an email to **ombudsperson@ImNO.ca** or **chairs@ImNO.ca**.

Overview

Imaging Network Ontario is committed to providing a harassment-free symposium experience for everyone, regardless of gender, gender identity and expression, age, sexual orientation, disability, physical appearance, body size, race, ethnicity, religion (or lack thereof), or technology choices. We do not tolerate harassment of symposium participants in any form. Use of sexualised language and imagery that does not convey a scientific message is not appropriate. We expect participants and sponsors to follow these rules for the duration of the symposium in any symposium venue or platform, including talks, social events, Twitter and other online media. Symposium participants violating these rules may be sanctioned or expelled from the symposium without a refund at the discretion of the symposium organisers.

Details

All attendees, speakers, sponsors and volunteers at ImNO are subject to the anti-harassment policy.

Harassment includes offensive verbal comments related to gender, gender identity and expression, age, sexual orientation, disability, physical appearance, body size, race, ethnicity, religion, technology choices, sexual images in public spaces, deliberate intimidation, stalking, following, harassing photography or recording, sustained disruption of talks or other events, inappropriate contact, and unwelcome sexual attention. Use of images, activities, uniforms/costumes or other materials that create a sexualised environment will not be tolerated.

Anyone asked to stop any harassing behavior is expected to comply immediately.

If anyone engages in harassing behavior, the symposium organisers may take any action they deem appropriate, including warning the offender or expulsion from the symposium with no refund.

If you are being harassed, notice that someone else is being harassed, or have any other concerns, please contact the Symposium Manager at **imno@imno.ca** immediately. A symposium staff member hosts and actively monitors the Zoom sessions and you may contact them in Zoom through a private chat. You can also send an email to the ImNO ombudsperson, Dr. Maria Drangova, at **ombudsperson@ImNO.ca** or the ImNO 2022 Chairs, Drs. Gabor Fichtinger and Tina Khazaee, at **chairs@ImNO.ca**.

We expect everyone to follow these rules for the duration of the symposium within and outside symposium venues and platforms, including but not limited to symposium-related talks, workshops, and social events involving ImNO attendees, and in all symposium related communications, including social media.

Supporting Consortia

The Annual Meeting of Imaging Network Ontario (ImNO) promotes Canada's role as a leader in medical imaging innovation by cultivating synergy among consortia and partnerships between Ontario and other Canadian imaging entities.

The following consortia and programs supported the 2022 ImNO Symposium financially.

Machine Learning in Medical Imaging Consortium (MaLMIC)

Machine Learning for Medical Imaging Working Group: Aaron Fenster, Anne Martel, Julia Publicover, Amber L. Simpson, Aaron Ward, Martin Yaffe

The Consortium was launched to accelerate research and development of machine learning solutions for unmet needs in medical imaging through collaborations between academic and clinical researchers, and with Canadian industry. It hosts monthly forums on machine learning in medical imaging and promotes collaboration through its website at https://malmic.ca/.

Ontario Institute for Cancer Research Imaging Program

Directors: Dr. Aaron Fenster and Dr. Martin Yaffe **Ontario Institute for Cancer Research**

The OICR Imaging Program accelerates the translation of research into the development of new imaging innovations for earlier cancer detection, diagnosis and treatment through four major projects: probe development and commercialization, medical imaging instrumentation and software, pathology validation, and imaging for clinical trials. The Imaging Program facilitates improved screening and treatment options for cancer patients by streamlining advances in medical imaging through the complex pipeline from discovery to clinical translation and ultimately to clinical use.

Image-Guided Device Interventions for Cardiovascular Disease

Lead Researcher: Dr. Graham Wright **Ontario Research Fund**

With advances in early identification and management of risk factors, combined with effective response to acute events, cardiovascular diseases have evolved from an acute killer to a chronic disease challenge. In recent years, there have been major advances in less invasive treatments. For minimally invasive device therapeutics, imaging and tracking technologies, along with the development of image-modality compatible tools, have unique roles in planning and guiding interventions, as well as monitoring functional results. In electropathophysiology, imaging will guide positioning of pacing devices, identify ablation targets, and direct therapy through fusion of device representations with maps of myocardial structure and function. Similar advances facilitate planning and guidance of both percutaneous and minimally invasive valve repair/replacement and catheter-based revascularization

of chronic total occlusions. Researchers at Sunnybrook and Robarts Research Institutes, working with local, national, and multinational diagnostic imaging and interventional device companies, are advancing the state-of-the-art in image acquisition and analysis with ultrasound, MRI, x-ray, and CT methods, including the design of visualization platforms and associated communication and control interfaces for interventional guidance, facilitating fusion and manipulation of prior and real-time imaging and device information. The ultimate goal is more effective utilization of imaging to improve outcomes for those suffering from chronic ischemia, complex arrhythmias, and heart failure related to structural heart diseases.

Corporate Sponsor

Scintica

Scintica

Scintica's mission is to link scientists with the right precision tools to further research by providing high-value instrumentation and research solutions to scientists and the preclinical research community. We are a leading supplier of medical research solutions and provide elite applications, technical support, and a platform for today's scientists to share their scientific findings.

We carry a diverse portfolio of products, ranging from imaging systems (PET, CT, MRI, optical, DEXA, intravital microscopy, photoacoustic and high-frequency ultrasound systems), lab equipment, instruments, workstations, incubators, tissue culture analysis, and much more.

scintica.com

Keynote Speakers

Tuesday, March 22 at 10:15

Re-wiring Academic Medicine for Integrated Computation and Prediction

David Jaffray, MD Anderson Cancer Center

David Jaffray, Ph.D., is a senior vice president and chief technology and digital officer at The University of Texas MD Anderson Cancer Center. He also is professor of Radiation Physics and professor of Imaging Physics.

David was recruited to MD Anderson in May 2019 as chief technology and digital officer. In this role, he directs the strategic design, acquisition, management and implementation of an enterprise-wide technology infrastructure. David also leads efforts to advance data integration, data governance and data security across MD Anderson's Houston campuses and its national network. Additionally, he is part of the team at MD Anderson striving to advance meaningful partnerships with industry.

Before joining MD Anderson, David served as executive vice president for Technology and Innovation at the University Health Network (UHN)/Princess Margaret Cancer Centre in Toronto, Ontario. He led UHN's information technology transformation, designing the road map for digital transformation. He also served as founding director of the STTARR Innovation Centre and founding director of the Techna Institute for the Advancement of Technology for Health. David was a full professor in the Departments of Radiation Oncology, Medical Biophysics and IBBME at the University of Toronto.

David holds 26 patents and has authored more than 300 peer-reviewed publications in topics related to cancer, including the development of new radiation treatment machines, the exploration of the fundamental limits of imaging system performance, the development of novel nanoparticle formulations for improved detection of cancer, and challenges in global health.

He has received many honors, including the Sylvia Sorkin Greenfield Award, the Farrington Daniels Award and the Sylvia Fedoruk Prize. In 2018, he received the Gold Medal from the American Society for Radiation Oncology. David's interest in commercialization has led to the development of commercial products including software and hardware for high-quality cancer care, and development of radiation therapy technologies, including the development of cone-beam CT guided radiation therapy.

Wednesday, March 23 at 10:05

Ultrasound Video Analysis

Alison Noble, University of Oxford

Professor Alison Noble OBE FRS FREng is the Technikos Professor of Biomedical Engineering at the Institute of Biomedical Engineering (IBME), University of Oxford.

Alison's academic research interests are in ultrasound imaging, and computational (machine-learning based) analysis of images and motivated by clinical unmet needs in western and low-and-middle-income countries healthcare settings. She received the Royal Society Gabor Medal for her inter-disciplinary research contributions in 2019, and the same year received the Medical Image Computing and Computer-Assisted Interventions (MICCAI) Society Enduring Impact award. Alison co-founded Intelligent Ultrasound Ltd to commercial research from her laboratory which was acquired by MedaPhor Group Plc in 2017 (now called Intelligent Ultrasound Group).

Alison is a former president of the MICCAI Society, and her recent UK national roles include Chair of the EPSRC Healthcare Technologies Strategic Advisory Team, and a member of the UK REF 2021 Subpanel 12 (Engineering). She is an active Fellow of the Royal Academy of Engineering and of the Royal Society, an ELLIS Fellow, a Fellow of the MICCAI Society, a former Trustee of the Institute of Engineering Technology (IET) and received an OBE for services to science and engineering in the Queen's Birthday Honours list in June 2013.

Alison has recently been working with MICCAI colleagues to raise the profile of ultrasound in the medical image computing (MIC) and computer assisted interventions (CAI) fields through the establishment of the ASMUS workshop and newly formed Special Interest Group in Medical Ultrasound (SIG-MUS).

Introduction to Patient Partnerships Speakers

Patients can play a variety of roles in research and its translation ranging from being involved in organizations that increase awareness about the importance of research and fundraising to being involved in research planning and execution. In the Patient Partnership session, Justin Noble will start the session with an introduction to patient partnerships. Next Justin and Diana Lemaire will talk about OICR's Patient and Family Advisory Committee. This will be followed by Raymond Kim and Melissa Cable-Cibula talking about how they are working together on the establishment of the Ontario Hereditary Cancer Research Network. The final presentation will be by Glykeria Martou and Sherri McCullough showcasing the collaboration and knowledge translation impact of the partnership the Rose of Hope has with breast reconstruction in Kingston. The presentations will be followed by questions and open discussion with symposium participants.

Wednesday, March 23 at 11:55

Justin Noble

Ontario Institute for Cancer Research

Diana Lemaire

Member, OICR Patient and Family Advisory Committee

Raymond Kim

Princess Margaret Cancer Centre

Melissa Cable-Cibula

M.Corporate Communications

Glykeria Martou

Queen's University

Sherri McCullough

Kingston General Hospital

Medical Imaging in Global Health Speakers

Thursday, March 24 at 15:35

Udunna Anazodo, McGill University

Dr Udunna Anazodo completed her doctoral training in Medical Biophysics at Western University and was a MITACS Accelerate Fellow at The Lawson Health Research Institute. She leads the Multimodal Imaging of Neurodegenerative Disease (MiND) Lab at The Montreal Neurological Institute where her group develops PET and MRI techniques for early detection of neurodegenerative disease. Udunna is very passionate about improving access to diagnostic imaging. She is the founder and Chair of the Consortium for Advancement of MRI Education and Research in Africa (CAMERA), a global network of MRI experts working to establish sustainable access to high-value MRI in Africa. She is also involved in several efforts to provide medical imaging training opportunities to researchers in Africa.

Carlos Torres, University of Ottawa

Dr. Carlos Torres is a Professor of Radiology at the University of Ottawa Faculty of Medicine and a neuroradiologist at The Ottawa Hospital.. He is a member of the Board of Directors of the Canadian Association of Radiologists (CAR) and is President-elect of the Ibero Latin American Society of Neuroradiology (SILAN).

Carlos has given more than 400 national and international invited lectures in 25 different countries and is regularly invited to speak at the major Radiology and Neuroradiology Meetings. He is an International Visiting Professor for RSNA, ASNR and ARRS and has been a National and International Visiting Professor to academic centres in the US, Canada,Brazil, Colombia, El Salvador, Chile, Bhutan, China, Myanmar and Mongolia.

Carlos is actively involved in medical education and research; his main areas of interest include vascular pathologies, demyelinating disease, brachial plexus imaging, spine and tumor imaging. He has multiple peer-reviewed publications and has written 21 book chapters. He is an Associate Editor of the Canadian Association of Radiologists journal, an Editor of the journal 3D Printing in Medicine and a reviewer for multiple journals including AJNR and European Radiology.

He has received numerous departmental, national and international awards for his teaching and research including the 2021 uOttawa Faculty of Medicine Educator of the Year Award, the Undergrad Teacher of the Year Award in 2017 and 2021, the Radiology Staff Teacher of the Year Award in 2020 and 2021, the prestigious RSNA Honored Educator Award and the National Order of Merit Award in the Rank of Officer from the Republic of Colombia (equivalent to The Order of Canada) for his scientific contributions in the field of Diagnostic Neuroradiology.

Organizing Committees

Chairs: Gabor Fichtinger and Tina Khazaee

Scientific Committee

Corey Baron
Maria Drangova
Pascal Fallavollita
Nancy Ford
Richard Frayne
Wenchao Han
David Holdsworth
Miranda Kirby
Sarah Mattonen
Tamie Poepping
Raoul Pereira
Tales Santini
Timothy Scholl
Adam Shuhendler
Sarah Svenningsen
Jesse Tanguay
Rebecca Thornhill
Eran Ukwatta
Jill Weyers
Dan Xiao
Alfred Yu

Student Committee

Faranak Akbarifar
Sarah Aubert
Dana Broberg
Rohini Gaikar
Kesavi Kanagasabai
Liam Lawrence
Nicholas Simard

Planning Committee

Carol Richardson
Kitty Wong

Abstract Reviewers

Coordinators: Miranda Kirby, Sarah Mattonen and Tales Santini

Corey Baron
Timothy Burkhart
Robert DeKemp
Mamadou Diop
Maria Drangova
Pascal Fallavollita
Aaron Fenster
Gabor Fichtinger
Nancy Ford
Richard Frayne
Donna Goldhawk
Leah Groves
Wenchao Han
Michael Hardisty
Matthew Holden
Eno Hysi
Amin Jafarisojahrood
Amoon Jamzad
Ali R. Khan
Miranda Kirby
Emily Lalone
Daniel Lorusso
Chris Macgowan
Anne Martel
Sarah Mattonen
Chris McKenzie
Charles McKenzie
Michael Noseworthy
Terry Peters
Tamie Poepping
Tom Purdie
Jessica Rodgers
Hojjat Salehinejad
Tales Santini
Tim Scholl
Adam Shuhendler
Navneet Singh
John Sled
Chetan Srinidhi
Dafna Sussman
Sarah Svenningsen
Jesse Tanguay
Ali Tavallaei
Matthew Teeter
Jonathan Thiessen
Rebecca Thornhill
Eranga Ukwatta
Tamas Ungi
Justin Wan
Jill Weyers
Cari Whyne
Yiming Xiao
Dan Xiao
Billy Yiu

Oral and Pitch Judges

Coordinator: **Corey Baron, Kitty Wong and Dan Xiao**

Yara Alawneh
Nader Allam
Natasha Alves-Kotzev
Ryan Au
Corey Baron
Rudy Baronette
Layale Bazzi
Amanda Boyle
Dana Broberg
Jordan Broberg
Sofia Chavez
Tricia Chinnery
Jaryd Christie
William Chu Kwan
Kevin Chung
Catherine Coolens
Alicia Cronin
Baraa Daher
Michael Daly
David DeVries
Aaron Fenster
Gabor Fichtinger
Nancy Ford
Kelly Fullerton
Maged Goubran
Leah Groves
Wenchao Han
Helma Heidari
Miriam Hewlett
Rebecca Hisey
Eno Hysi
Amin Jafarisojahrood
Amoon Jamzad
Miranda Kirby
Natasha Knier
Meghan Koo
Philippa Krahn
Emily Lalone
Angus Lau
Daniel Lorusso
Sarah Mattonen
Alexander Mihaescu
Mia Mojica
Amir Moslemi
Maryam Mozaffari
Samal Munidasa
Hareem Nisar
Alison Noble
Julie Ottoy
Claire Park
Jaykumar Patel
Carly Pellow
Jennifer Polus
Mihaela Pop
Tom Purdie
Naila Rahman
Jessica Rodgers
John Ronald
Siddharth Sadanand
Shailaja Sajja
Alice Sant
Simran Sethi
Nidhi Singh
Min Su Kang
Dafna Sussman
Sarah Svenningsen
Mahnaz Tajik
Josephine Tan
Ali Tavallaei
Eran Ukwatta
Joseph Umoh
Tamas Ungi
Tian Duo Wang
Jill Weyers
Dan Xiao
Shuwei Xing
Yiwen Xu
Martin Yaffe
Fatemeh Zabihollahy
Brandon Zanette
Lauren Zelko

ImNO 2022 Program

Tuesday, March 22, 2022

10:00 - 10:15 **Opening Remarks** — Zoom Meeting Room 1

Gabor Fichtinger and Tina Khazaee, ImNO 2022 Chairs

10:15 - 11:00 **Keynote Session I** — Zoom Meeting Room 1

Chairs: Yara Alawneh and Catherine Coolens

Re-wiring Academic Medicine for Integrated Computation and Prediction

David Jaffray, MD Anderson Cancer Center

11:00 - 11:05 **Break**

11:05 - 12:05

Oral 1
Cancer Imaging - Therapy Response
Zoom Meeting Room 1

Chairs: Alice Santilli and Josephine Tan

O1-1: Predicting Recurrence Risk in Lung Cancer Using Multi-Modal Radiomics and Random Survival Forest

Jaryd Christie, Western University

O1-2: Glioma Regions with Low Apparent Diffusion Coefficient: Correlation Between Volumetric Changes During Chemoradiation and Progression-Free and Overall Survival

Liam Lawrence, University of Toronto

O1-3: The Effects of Stereotactic Body Radiotherapy on Tumour Microvasculature: Insights from Optical Coherence Angiography Towards Adaptive Radiation Medicine

Nader Allam, University Health Network

O1-4: Tumour Cell Clusters Surviving After Radiotherapy Can Be Detected Via Texture Analysis of Optical Coherence Tomography Images to Predict Treatment Outcome

Natalia Demidova, University of Toronto

Oral 2
Neuro Imaging
Zoom Meeting Room 2

Chairs: Maged Goubran and Min Su Kang

O2-1: Lower Amyloid-PET Signal in White Matter Lesions Is Associated with Increased Free Water: A Multi-Center Mixed Cohort of Small Vessel Disease and Alzheimer's Pathology

Julie Ottoy, Sunnybrook Research Institute

O2-2: Greater Monoamine Oxidase B Distribution Volume in the Prefrontal Cortex in Traumatic Brain Injury with Persistent Symptoms: An [11C]SL25.1188 PET Study

Yuko Koshimori, Centre for Addiction and Mental Health

O2-3: A Digital Brain Perfusion Phantom to Test the Performance of CT Perfusion Software

Kevin Chung, Robarts Research Institute

O2-4: Physiological and Functional Brain Changes in Adults Recovering from COVID-19

William Kim, Sunnybrook Research Institute

12:05 - 13:05 **Lunch Break** — Gathertown

Gathertown Tutorial (first 10 minutes) and Educational Challenge Kick Off

13:05 - 13:35

Pitch 1
Machine Learning I
Zoom Meeting Room 1

Chairs: Jennifer Polus and Martin Yaffe

P1-1: Domain Transfer Through Image-To-Image Translation in Prostate Cancer Detection

Meng Zhou, Queen's University

P1-2: Computer-Aided Methods to Predict Prostate MRI Quality Via Rectal Content Estimation

Abdullah Al-Hayali, University of Guelph

P1-3: Effects of Feature Type and Multiple Scanners on Brain Metastasis Treatment Outcome Prediction

David DeVries, Western University

P1-4: Unsupervised Learning for Classification of Prostate Cancer Severity

Andrea Perera-Ortega, Queen's University

P1-5: Comparison of Radiomic Features for Bounding Box and Traditional Segmentation Methods of Axillary Lymph Node Metastases from Breast Cancer on CT

Matthew Van Oirschot, University of Toronto

P1-6: Using Deep Learning to Predict Tumour Mutational Burden in Lung Squamous Cell Carcinoma from 20 Centres

Salma Dammak, Western University

P1-7: Prostate Segmentation and Reconstruction for Integration in An Ultrasound-Guided Prostate Biopsy System for Nationwide Implementation in Senegal

Colton Barr, Queen's University

P1-8: Machine Learning Determination of the Relationship Between the uCT-Derived Visceral Adipose Tissue and Whole-Body Adipose Tissue in Rats

Joseph Umoh, Robarts Research Institute

Pitch 2
Neuro Imaging I
Zoom Meeting Room 2

Chairs: Kevin Chung and Julie Ottoy

P2-1: Updated Radiosynthesis of Three High Demand Positron-Emitting Radiotracers for Neuroimaging

Olujide Oyeniran, Western University

P2-2: Beta Amyloid Deposition and Cognitive Decline in Parkinson's Disease: A Study of the PPMI Cohort

Alexander Mihaescu, Centre for Addiction and Mental Health

P2-3: Evaluation of Spinal Cord Registration for Diffusion Tensor Imaging with Pathological Spine Data

Vignesh Sivan, University of Waterloo

P2-4: Chemical Exchange Saturation Transfer (CEST) pH-Weighted MRI Optimization in the Spinal Cord

Alicia Cronin, Western University

P2-5: Piloting a Methodology to Assess Functional Connectivity in Healthy Brain Aging

Abhijot Singh Sidhu, University of Calgary

P2-6: Investigating the Effect of Thrombotic Thrombocytopenic Purpura on Neurocognitive Function

Fahad Hannan, Western University

P2-7: First-in-Human PET Imaging of [18F]SDM-4MP3: A Detour on the Synaptic Imaging Journey, and Cautionary Note

Kim Desmond, Centre for Addiction and Mental Health

P2-8: Investigating the Effect of Tissue Heterogeneity on NIRS Monitoring of Cerebral Oxidative Metabolism

Natalie Li, Western University

13:35 - 14:15 **Meet-and-Greet** — Gathertown
Poster Viewing — Pitch Sessions 1 & 2 Presenting

14:15 - 14:20 **Break**

14:20 - 15:20

Oral 3
MR Imaging I
Zoom Meeting Room 1

Chairs: Jaykumar Patel and Fatemeh Zabihollahy

O3-1: Correcting for Gradient Non-Linearity in Concurrent Field Monitored MRI Data
Paul Dubovan, Western University

O3-2: Tissue Equivalent Agarose/MnCl2 MRI Relaxation Phantom for MR Studies
Daniel Sare, Ryerson University

O3-3: Real-Time Rigid Motion Detection for Brain MRI Using Spherical Navigators
Miriam Hewlett, Western University

O3-4: MRSI Processing and Simulation Using the Fid Appliance (FID-A) Toolkit
Brenden Kadota, Sunnybrook Research Institute

Oral 4
Device, Hardware and System Development
Zoom Meeting Room 2

Chairs: Amoon Jamzad and Nidhi Singh

O4-1: Cautery State Classification for Navigated iKnife Surgery
Josh Ehrlich, Queen's University

O4-2: Continuing Design and Developments of a Forward-Looking Ultrasound Catheter
Alykhan Sewani, Ryerson University

O4-3: Design of a Radio-Ultrasound-Guided System for Breast Cancer Surgery
Sydney Wilson, Western University

O4-4: Development of Photoacoustic Tomography to Monitor Photothermal Therapy of Localized Prostate Cancer
Ivan Kosik, University Health Network

15:20 - 15:25 **Break**

15:25 - 15:55

Pitch 3
MR Imaging
Zoom Meeting Room 1

Chairs: Helma Heidari and Dafna Sussman

P3-1: Monitoring the Effect of Cariporide on Intracellular Acidification By CEST-MRI
Maryam Mozaffari, Robarts Research Institute

P3-2: ExTE-HERMES: An MR Spectroscopy Acquisition for Detection of GABA and GSH in the Human Brain
Peter Truong, Sunnybrook Research Institute

P3-3: MR Image Resolution Enhancement Using Real-ESRGAN
Shawkh Ibne Rashid, Ontario Tech University

P3-4: Retrospective Frequency and Phase Drift Correction in Rosette MRSI Data Using Spectral Registration
Sneha Senthil, Sunnybrook Research Institute

P3-5: A Numerical Bloch Solver with Dynamic Relaxation Calculations for Low-Field MRI Modeling
John Adams, Western University

P3-6: Improving Volumetric Magnetic Resonance Arrythmia Substrate Characterization in Cardiac Sequences with Non-Cartesian Gradients
Saqeeb Hassan, University of Toronto

P3-7: Quantitative Susceptibility Mapping of Brain Regions to Assess Metal Deposition Following Total Hip Arthroplasty and Hip Resurfacing Arthroplasty
Shahnaz Taleb, Western University

P3-8: Multi-Metabolite-Selective Single-Voxel Spectroscopy Sequence Using Ultra-High Field Proton Magnetic Resonance Spectroscopy
Kesavi Kanagasabai, Robarts Research Institute

Pitch 4
Hardware, Software and System Development
Zoom Meeting Room 2

Chairs: Natasha Alves-Kotzev and Rebecca Hisey

P4-1: Feasibility of a Spatially Tracked Three-Dimensional Ultrasound (3DUS) System for Point-of-Care Whole-Breast Imaging
Claire Park, Robarts Research Institute

P4-2: An Open-Source Testbed for Developing Image-Guided Robotic Tumor Bed Inspection
Laura Connolly, Queen's University

P4-3: The CathPilot: Performance Characterization and Comparison to Conventional Catheters
James Zhou, Ryerson University

P4-4: Design of a Novel Side-Looking Catheter for Fenestrated Endovascular Aneurysm Repair Procedures
Yara Alawneh, Ryerson University

P4-5: Open-Source Software for Analysis of Mass Spectrometry Imaging
Mackenzie Sharp, Queen's University

P4-6: Building a Platform for Medical Imaging Federated Analysis
Jenny Lee, TECHNA Institute

P4-7: Open Health Imaging Foundation (OHIF) V3: Workflow-Centric Web-Based Medical Imaging Platform
Alireza Sedghi, Open Health Imaging Foundation

P4-8: Review of Research Tools for Computer-Assisted Interventions
Zaiba Amla, Ryerson University

15:55 - 16:35 **Meet-and-Greet** — Gathertown
Poster Viewing — Pitch Sessions 3 & 4 Presenting

16:35 - 18:35 **Social Event - ImKNOW: Connect with Industry Panelists** — Gathertown

Wednesday, March 23, 2022

10:00 - 10:05 **Opening Remarks** — Zoom Meeting Room 1
Gabor Fichtinger and Tina Khazaee, ImNO 2022 Chairs

10:05 - 10:50 **Keynote Session II** — Zoom Meeting Room 1
Chairs: Anne Martel and Hareem Nisar
Ultrasound Video Analysis
Alison Noble, University of Oxford

10:50 - 10:55 **Break**

10:55 - 11:55

Oral 5
Machine Learning
Zoom Meeting Room 1

Chairs: Ryan Au and Alison Noble

O5-1: Fully Automated Multi-Organ Segmentation of Female Pelvic MRI Using Transfer and Active Learning
Fatemeh Zabihollahy, Johns Hopkins University

O5-2: Automated Fatty Liver Disease Detection in Point-of-Care Ultrasound B-Mode Images
Miriam Naim Ibrahim, University of Guelph

O5-3: Evaluating Faster R-CNN for Cataract Surgery Tool Detection Using Microscopy Video
Hung-Yu Lee, Queen's University

O5-4: Magnetic Resonance T1 Spectrum Analysis Using Neural Networks
Tristhal Parasram, University of Windsor

Oral 6
Cellular and Molecular
Zoom Meeting Room 2

Chairs: Wenchao Han and Mahnaz Tajik

O6-1: In Vitro Testing of Novel Manganese-Derived Paramagnetic Contrast Agents for MRI Reporter Gene Imaging
Sean McRae, Western University

O6-2: Imaging of Neuroinflammation in Chronic Traumatic Encephalopathy
Cassis Varlow, University of Toronto

O6-3: Analysis of Magnetic Resonance Relaxation Rates in Mammalian Cells Expressing Essential Magnetosome Genes
Qin (Daisy) Sun, Lawson Health Research Institute

O6-4: CRISPR Editing of Chimeric Antigen Receptor T (CAR-T) Cells Expressing Human-Derived MRI and PET Reporter Genes
John Kelly, Robarts Research Institute

11:55 - 12:55 **Lunch and Learn — Patient Partnerships Session** — Zoom Meeting Room 1
Chairs: Glenn Bauman and Baraa Daher

Justin Noble, Ontario Institute for Cancer Research
Raymond Kim, Princess Margaret Cancer Centre
Glykeria Martou, Queen's University
Diana Lemaire, OICR Patient and Family Advisory
Melissa Cable-Cibula, M.Corporate Communications
Sherri McCullough, Kingston General Hospital

12:55 - 13:25

Pitch 5
Machine Learning II
Zoom Meeting Room 1

Chairs: Aaron Fenster and Amir Moslemi

P5-1: A CT-Based Radiomics Model for Predicting Feeding Tube Insertion in Oropharyngeal Cancer
Tricia Chinnery, Western University

P5-2: Deep Learning-Based MR Image Re-Parameterization
Abhijeet Narang, Indian Institute of Technology (ISM), Dhanbad

P5-3: Deep Learning Based Differentiation of Solid and Cystic Renal Masses Using T2-Weighted MRI Images
Rohini Gaikar, University of Guelph

P5-4: Automatic Thyroid Nodule Detection and Segmentation Method Based on Mask R-CNN
Ningtao Liu, Robarts Research Institute

P5-5: Deep Image Clustering for Standardization of Radiological Workflows
Dhruv Patel, Queen's University

P5-6: Automated Tumour Reconstruction for Real-Time Visualization in Breast-Conserving Surgical Navigation
Chris Yeung, Queen's University

P5-7: Semi-Supervised Segmentation of 3D Ultrasound Images
Zachary Szentimrey, University of Guelph

P5-8: An Advanced Acquisition/Reconstruction Method for 1H and 129Xe MRI with Deep Learning
Samuel Perron, Western University

Pitch 6
Cardiac and Cellular and Molecular
Zoom Meeting Room 2

Chairs: Layale Bazzi and John Ronald

P6-1: A Highly Modular Activatable Synthetic Biology System to Visualize In Vivo Cell-Cell Communication
TianDuo Wang, Western University

P6-2: Trimodal Tracking of Mesenchymal Stem Cells (MSCs) with Magnetic Particle Imaging (MPI), Bioluminescence Imaging (BLI) and Positron Emission Tomography (PET)
Nourhan Shalaby, Western University

P6-3: Fluorine-19 MRI of Stem Cell-Derived Alveolar-Like Macrophages Tagged with Perfluoropolyether
Janny Kim, The Hospital for Sick Children

P6-4: VivoTrax+TM Improves the Sensitivity and Detection of Cancer Cells with Magnetic Particle Imaging
Kyle Van Beek, Robarts Research Institute

P6-5: PET Imaging of GLUT5 in Rodent Models of Neuroinflammation
Amanda Boyle, Centre for Addiction and Mental Health

P6-6: The Environment Surrounding Iron Oxide Nanoparticles Influences Sensitivity and Resolution for Magnetic Particle Imaging
Maryam Berih, Western University

P6-7: Multi-View 3D Echocardiography Volume Compounding for Mitral Valve Procedure Planning
Patrick Carnahan, Robarts Research Institute

P6-8: The Resurrection of Multi-Energy Subtraction Angiography
Lisa Garland, Robarts Research Institute

13:25 - 14:05 **Meet-and-Greet** — Gathertown
Poster Viewing — Pitch Sessions 5 & 6 Presenting

14:05 - 14:10 **Break**

14:10 - 15:10

Oral 7
Cancer Imaging
Zoom Meeting Room 1

Chairs: Amanda Boyle and Maryam Mozaffari

O7-1: Quantification of the Tumor Microvascular Response to Stereotactic Body Radiation Therapy Using Optical Coherence Tomography Angiography and Dynamic Contrast Enhanced MRI
William Zabel, University Health Network

O7-2: Contrast Enhanced Endobronchial Ultrasound for Malignant Lymph Node Detection and Staging
Sean McGrath, University of Toronto

O7-3: Ventilation Heterogeneity Assessed By V-SPECT and 129Xe MRI in Lung Cancer Patients Prior to Lung Resection: An Interim Analysis of Prevalence and Clinical Relevance
Nisarg Radadia, McMaster University

O7-4: Optical Identification of Biomarkers for Liquid Biopsies
Matthew Chen, University of Toronto

Oral 8
Cardiac and Vascular Imaging
Zoom Meeting Room 2

Chairs: Mia Mojica and Jill Weyers

O8-1: Assessing Acute Cardiac Inflammation After Left-Sided Breast Cancer Radiotherapy with Hybrid PET/MRI
Oi Wai Chau, London Regional Cancer Program

O8-2: Imaging and Electrophysiological Biomarkers in a Novel Preclinical Pig Model of Doxorubicin-Induced Cardiotoxicity
Peter Lin, University of Toronto

O8-3: Imaging Endothelial Cell Mechanosensory Response to Wall Shear Stress at Varying O2 Tensions
Kevin Moore, Western University

O8-4: Characterization of Myocardial Metabolism Using a Novel Dual-Condition PET/MRI Protocol
Fayez Habach, University of Toronto

15:10 - 15:15 **Break**

15:15 - 15:45

Pitch 7
Cancer Imaging
Zoom Meeting Room 1

Chairs: Tricia Chinnery and Tom Purdie

P7-1: Vision Transformers for Prostate Cancer Detection from Ultrasound
Paul Wilson, Queen's University

P7-2: p53 Immunohistochemistry Interpretation Based on Digital Image Analysis for Better Prediction of Mutation Status in Acute Myeloid Leukemia
Ting Xiao, University of Toronto

P7-3: Visualization of Cancer Probability Maps in Micro-Ultrasound Guided Prostate Biopsy
Hung-Yu Lee, Queen's University

P7-4: Discriminating Optically Turbid Media by Scatterer Size and Scattering Coefficient Using Backscattered Linearly and Circularly Polarized Light
Michael Singh, University of Toronto

P7-5: Modelling the Radiation Distribution of Stereotactic Radiotherapy in the Treatment of Patients with Multiple Lung Lesions
Edward Wang, Western University

P7-6: Visualization of the Zonal Anatomy for Transrectal Ultrasound Guided Prostate Biopsy
Catherine Wu, Queen's University

P7-7: Cell Phenotyping Using Unsupervised Clustering on Multiplexed Fluorescence Images of Breast Cancer Tissue Specimens
Wenchao Han, Sunnybrook Research Institute

P7-8: Impact of the Location of Tumor in Prostate Cancer Detection on 3-T Multiparametric MRI Based on the Prostate Sector Map
Fatemeh Zabihollahy, University of California, Los Angeles

Pitch 8
Ultrasound and Optical Imaging
Zoom Meeting Room 2

Chairs: Miranda Kirby and Amin Jafarisojahrood

P8-1: Development of a Simulation Training Curriculum for Ultrasound-Guided Vascular Access for Sustainable Translation to West Africa
Sarah Ryan, Queen's University

P8-2: In Vitro and in Vivo Assessment of Focused Ultrasound-Triggered Docetaxel-Loaded Nanobubbles for Locally Advanced Breast Cancer Therapy
Patrick Dong Min Chang, University of Toronto

P8-3: Label Noise Compensation in Prostate Cancer Classification
Mahdi Gilany, Queen's University

P8-4: Automated Catheter Segmentation in 3D Ultrasound Images from High-Dose-Rate Prostate Brachytherapy
Nicole Kitner, Queen's University

P8-5: 3D Spatial-Frequency Domain Imaging for Oral Cancer Surgery: Initial Simulations Using Deep Learning
Arjun Jagota, University Health Network

P8-6: Development & Evaluation of a Bone-Targeted Photoacoustic Imaging Agent
Rowan Swann, McMaster University

P8-7: Methotrexate-Loaded Microbubbles for Imaging and Treatment of Inflammatory Bowel Disease
Yara Ensminger, University of Toronto

P8-8: Ideal Chromophore for Intralipid-Based Tissue-Mimicking Phantom
Rasa Eskandari, Western University

15:45 - 16:25 **Meet-and-Greet** — Gathertown
Poster Viewing — Pitch Sessions 7 & 8 Presenting

16:25 - 18:25 **Social Event - ImNO Trivia** — Gathertown

Thursday, March 24, 2022

10:00 - 10:05 **Opening Remarks** — Zoom Meeting Room 1

Gabor Fichtinger and Tina Khazaee, ImNO 2022 Chairs

10:05 - 11:05

Oral 9
Imaging for Musculoskeletal Analysis
Zoom Meeting Room 1

Chairs: Nader Allam and Gabor Fichtinger

O9-1: In-Vitro Characteristics of Embolic Agents for Osteoarthritis
Kierdra Dowling, University of Toronto

O9-2: Four-Dimensional Computed Tomography Scanning Allows for the Visualization and Measurement of Glenohumeral Joint Arthrokinematics
Baraa Daher, Western University

O9-3: Estimating Muscle Fiber Composition Via Resting-State Muscle BOLD Signal Complexity
Joshua McGillivray, McMaster University

O9-4: 3D Ultrasound to Characterize Synovial Volume in First Carpometacarpal Osteoarthritis Patients
Carla Du Toit, Robarts Research Institute

Oral 10
MR Imaging II
Zoom Meeting Room 2

Chairs: Sofia Chavez and Miriam Hewlett

O10-1: Advanced Diffusion MRI Metrics Reveal Acute Sensitivity to Mild Traumatic Brain Injury in a Mouse Model
Naila Rahman, Western University

O10-2: Human Brain Multi-Slice Imaging Using Hyperpolarized 129Xe
Vira Grynko, Lakehead University

O10-3: Tracking Disease Progression in Parkinson's Disease Using Striato-Cortical Gradients
Dimuthu Hemachandra, Robarts Research Institute

O10-4: The Impact of Western Diet Consumption Upon Guinea Pig Placental Metabolism At Two Time Points in Pregnancy Using [1-13C]Pyruvate MRI
Lindsay Morris, Western University

11:05 - 11:10 **Break**

11:10 - 11:40

Pitch 9
Imaging for Musculoskeletal Analysis
Zoom Meeting Room 1

Chairs: Jordan Broberg and Jessica Rodgers

P9-1: The Exploration of the Relationship Between Kinematic Joint Contact and Subchondral Volumetric Bone Mineral Density in People with and Without Wrist Trauma
Lauren Straatman, Western University

P9-2: Optical Imaging for Rheumatoid Arthritis Disease Activity Monitoring: An In Silico and Disease-Mimicking Phantom Study
Seva Ioussoufovitch, Western University

P9-3: Provocative Scapholunate Instability Wrist Positioning
Elizabeth Norman, Western University

P9-4: A Deep Learning Algorithm for Automatic Cartilage Segmentation in Knee 3D Ultrasound Images
Nathan Orlando, Robarts Research Institute

P9-5: A Comparative Study of Bone Plug Movement in Rectangular Versus Cylindrical Bone Tunnel Using Bone-Patellar Tendon-Bone Grafts
Michele Matsubara, University of Toronto

P9-6: A Convolutional Neural Network for Detection of Corrosion on Retrieved Hip Arthroplasty Systems
Anastasia Codirenzi, Western University

P9-7: [18F]FEPPA Autoradiography As a Measure of Macrophage Content in Knee Synovial Tissue
Zachary Koudys, Western University

Pitch 10
Neuro Imaging II
Zoom Meeting Room 2

Chairs: Alexander Mihaescu and Dan Xiao

P10-1: Neuroimaging VMAT2 in Parkinson's Disease with Rapid Eye Movement Sleep Behaviour Disorder
Mikaeel Valli, Centre for Addiction and Mental Health

P10-2: Quantifying Lasting Regional Microstructural and Functional Abnormalities in Aging Retired Professional Football Players
Ethan Danielli, McMaster University

P10-3: Quantifying Myelin Water Fraction in the Fetal Guinea Pig Brain
Simran Sethi, Western University

P10-4: Resting-State Brain Activity in Pediatric Concussion: A Sex-Based Analysis
Bhanu Sharma, McMaster University

P10-5: Neural Correlates of Connected Speech in Cerebrovascular Disease
Dana Broberg, Western University

P10-6: Hyperpolarized 129Xe Time-of-Flight Pulse Sequence for Substantial Brain Signal Stability Improvement
Yurii Shepelytskyi, Lakehead University

P10-7: 7 Tesla Diffusion MRI in Subcortical Structures Following COVID-19 Infection
Helma Heidari, Robarts Research Institute

P10-8: Evaluating Regional Correlations Between Glutamate+Glutamine and GABA+ in the Resting Human Brain
Claire Shyu, Centre for Addiction and Mental Health

11:40 - 12:20 **Meet-and-Greet** — Gathertown

Poster Viewing — Pitch Sessions 9 & 10 Presenting

12:20 - 13:20 **Lunch Break** — Zoom Meeting Room 1

Educational Challenge Presentations
Chairs: Corey Barron and Sarah Mattonen

13:20 - 14:20

Oral 11
Lung Imaging
Zoom Meeting Room 1

Chairs: Nancy Ford and Meghan Koo

O11-1: Investigating the Relationship Between Quantitative Ute MRI Measurements and Pulmonary Function of Healthy Pediatric Subjects
Daniel Genkin, Ryerson University

O11-2: Abnormal 129Xe Ventilation MRI and Inhaled Corticosteroid Deposition in Severe Asthma
Ashutosh Thakar, McMaster University

O11-3: Feasibility of Simultaneous Whole-Lung Ventilation-Perfusion Imaging with Volumetric CT in Non-Small Cell Lung Cancer
Heather Young, Western University

O11-4: Evaluating CT Imaging Structural Changes in Cystic Fibrosis Responders and Non-Responders Following CFTR Modulator Therapy
Gaurav Veer Singh, Ryerson University

Oral 12
Image-Guided Intervention and Surgery
Zoom Meeting Room 2

Chairs: Hareem Nisar and Ali Tavallaei

O12-1: Impact of Real-Time Magnetic Resonance Thermometry Motion Compensation on Focused Ultrasound Controlled Hyperthermia in a Small Animal Model
Suzanne Wong, The Hospital for Sick Children

O12-2: Combining Colour and Ultrasound Video for Central Venous Catheterization Workflow Recognition
Rebecca Hisey, Queen's University

O12-3: Identifying Tissues for Task Recognition in Training of Open Inguinal Hernia Repairs
Elizabeth Klosa, Queen's University

O12-4: Development of a Mini Stereotactic Guidance System for Percutaneous Liver Tumour Ablation
Joeana Cambranis Romero, Robarts Research Institute

14:20 - 14:25 **Break**

14:25 - 14:55

Pitch 11
Lung Imaging
Zoom Meeting Room 1

Chairs: Alicia Cronin and Sarah Svenningsen

P11-1: Comparison of Computed Tomography Texture-Based Radiomic Features with Machine Learning for Predicting Chronic Obstructive Pulmonary Disease
Kalysta Makimoto, Ryerson University

P11-2: Intra-Visit and Inter-Visit Repeatability of 129Xe Multiple-Breath Washout MRI in Children with Stable Cystic Fibrosis Lung Disease
Faiyza Alam, University of Toronto

P11-3: The Use of the 129Xe MRI vADC Approach for the Emphysema Progression Evaluation
Elnaz Parniyany, Western University

P11-4: Fractal Dimensions of Airway Surfaces from Computed Tomography
Jason Bartlett, Ryerson University

P11-5: The Use of Two De-Noising Methods in Healthy Rats for 129Xe Diffusion-Weighted and 19F/129Xe Dynamic-Ventilation MRI Imaging
Elise Woodward, Western University

P11-6: Optimization of Tube Voltage for Xenon-Enhanced Dual-Energy Radiography for Imaging Lung Function
Fateen Basharat, Ryerson University

P11-7: Inter- & Intra-Visit Reproducibility of Free-Breathing Magnetic Resonance Imaging in Stable Pediatric Cystic Fibrosis Lung Disease
Samal Munidasa, University of Toronto

P11-8: The Use of 3D Hyperpolarized 129Xe Lung MRI for Deep-Learning-Based Automated Quantification of Ventilation Defects and Heterogeneity
Tuneesh Ranota, Western University

Pitch 12
Image-Guided Intervention and Surgery
Zoom Meeting Room 2

Chairs: Michael Daly and Leah Groves

P12-1: Recognizing Needle Insertion Attempts in Webcam Video for Skill Assessment in Central Venous Catheterization Training
Catherine Austin, Queen's University

P12-2: Toward Automated Three-Dimensional Ultrasound Image Guidance of Gynecological Brachytherapy Treatments
Tiana Trumpour, Robarts Research Institute

P12-3: Feasibility of a Video-Based Skill Assessment Method for Central Venous Catheterization
Olivia O'Driscoll, Queen's University

P12-4: Machine Learning the Assessment of Surgeon Technical Skill for One Handed Surgical Knot Tying
Kevin Kasa, Sunnybrook Research Institute

P12-5: Deep Learning Based Vessel Segmentation from Ice Imaging: Towards an Ultrasound-Based Vascular Navigation Image Guidance System
Hareem Nisar, Robarts Research Institute

P12-6: Determining the Location of Tumor Classifications in Breast Cancer Surgery
Josh Ehrlich, Queen's University

P12-7: Catheter Tracking Error Characterization for MRI-Guided Interventions
Arjun Gupta, University of Toronto

P12-8: Semi-Supervised Cautery Detection with Preprocessing in Basal Cell Carcinoma Surgical Videos
Lucas March, Queen's University

14:55 - 15:35 **Meet-and-Greet** — Gathertown

Poster Viewing — Pitch Sessions 11 & 12 Presenting

15:35 - 16:35 **Medical Imaging in Global Health: Challenges and Opportunities for Collaboration** — Zoom Meeting Room 1

Chairs: Helma Heidari and Parvin Mousavi
Speakers: Udunna Anazodo, Western University
Carlos Torres, University of Ottawa
Panelists: Gabor Fichtinger, Queen's University
James Lacefield, Western University

16:35 - 17:00 **Awards** — Zoom Meeting Room 1

Judging and Awards Coordinators: Corey Baron and Dan Xiao

Closing

ImNO Chairs: Gabor Fichtinger and Tina Khazaee

Oral and Pitch Abstracts (in order of the talks)

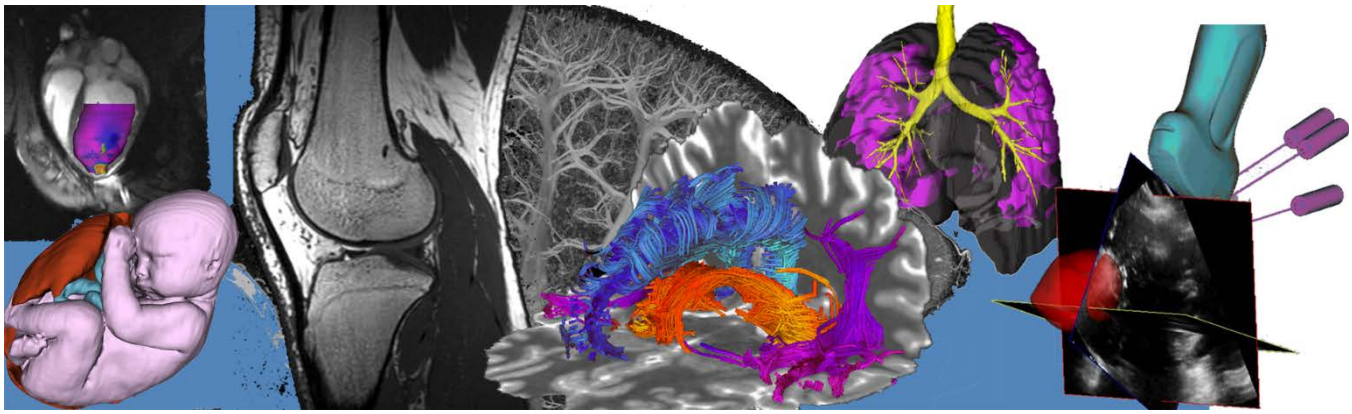

Oral Session 1:

Cancer Imaging –

Therapy Response

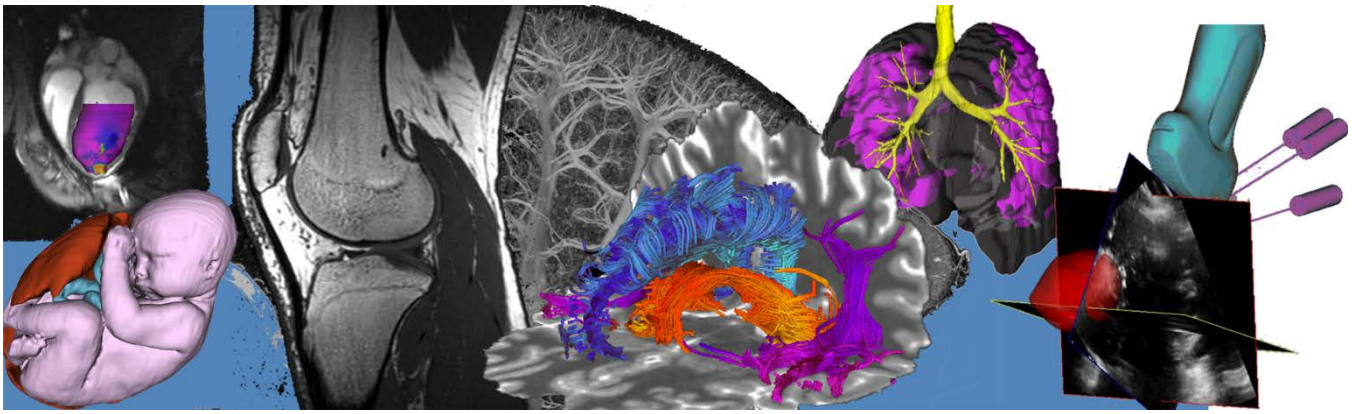

Predicting Recurrence Risk in Lung Cancer using Multi-Modal Radiomics and Random Survival Forest

Jaryd R. Christie[1], Omar Daher[2], Mohamed Abdelrazek[2], Perrin Romine[3], Richard A. Malthaner[4], Mehdi Qiabi[4], Rahul Nayak[4], Sandy Napel[5], Viswam Nair[6] and Sarah A. Mattonen[1].

[1] Department of Medical Biophysics, Western University, London, ON; [2] Department of Medical Imaging, Western University, London, ON; [3] Division of Medical Oncology, University of Washington, Seattle, WA, USA; [4] Division of Thoracic Surgery, Department of Surgery, Western University, London, ON; [5] Department of Radiology, Stanford University, Stanford, CA, USA;[6] Division of Pulmonary, Critical Care & Sleep Medicine, University of Washington, Seattle, WA, USA

Introduction: Lung cancer is the leading cause of cancer death worldwide with nearly 50% of early-stage lung cancer patients recurring within 5 years following surgery [1]. This disease is one of many cancers at the forefront of the artificial intelligence (AI) surge to use quantitative imaging to predict outcomes in patients. Currently, computed tomography (CT) and positron emission tomography (PET) are used for staging, the current gold standard for predicting the likelihood of recurrence. However, studies have shown that these medical images hold more information that can be used to improve tumor characterization and prognosticate treatment outcomes [2]. Radiomics aims to utilize AI on large amounts of advanced quantitative imaging features for applications in treatment selection and response assessment [3]. A multi-modality radiomics approach incorporating quantitative and qualitative features from the tumour and its surrounding regions, along with clinical features, has yet to be explored for recurrence risk stratification. Therefore, the aim of this study was to develop a model to significantly improve risk-stratification of non-small cell lung cancer (NSCLC) patients compared to cancer stage alone.

Methods: A dataset of 135 patients with early-stage NSCLC who underwent primary surgical resection from the retrospective NSCLC-Radiogenomics cohort (obtained from TCIA) was analyzed [4]. The tumour and peri-tumoural regions on both the pre-operative CT and PET scans were segmented. Additionally, the vertebral bodies L3-L5 were segmented on PET to assess bone marrow uptake. PyRadiomics was used to compute shape, size, first-order, and texture radiomics features on both the original and wavelet-filtered images [5]. These radiomic features were concatenated with clinical and qualitative CT features, which resulted in 5092 total features. Least absolute shrinkage and selection operator (LASSO) was performed to select the top features to predict time to any recurrence in the training cohort (n=94). A random survival forest model implemented in Python was built using these top performing features and evaluated on the testing cohort (n=41). Model performance was assessed using the concordance index and compared to a clinical stage-only model to determine its incremental value in predicting time to recurrence. Kaplan-Meier curves were generated to separate patients into high- and low-risk groups using the median risk score in the training cohort.

Results: A total of six features were selected as the top performing features to predict recurrence. Four of these features were wavelet features (one CT tumour, one CT peri-tumoral, one PET peri-tumoural and one PET tumour plus peri-tumoural) with the remaining two features being a textural bone marrow feature on the original image and cancer stage. The radiomics model achieved concordances of 0.75 and 0.74 on the training and testing cohorts respectively. The radiomics model significantly outperformed the stage-only model (testing cohort; concordance=0.63, p=0.02). The model was also able to significantly stratify patients into high- and low-risk groups in the training (n=94, p=0.006) and testing (n=41, p=0.01) cohorts (Figure 1).

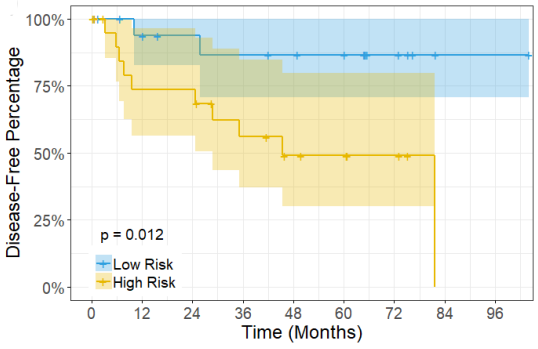

Figure 1. Kaplan-Meier curve for the radiomics model in the testing cohort.

Conclusions: Our radiomics-based random survival forest model outperformed the stage-only model when stratifying NSCLC patients into high- and low-risk of recurrence. These results demonstrate that CT and PET radiomics have the potential to augment staging information in a clinical setting and could aid physicians in more accurately identifying patients who are at higher risk of treatment failure for more personalized treatment options.

References: [1] Ellison, L., Health Rep. 29(9):10, 2018 [2] Christie, J., CARJ. 72(1):86, 2020 [3] Rizzo, S., Eur Radiol Exp. 2(1):36, 2018 [4] Bakr, S., Sci Data. 5(1):1, 2018 [5] Griethuysen, J., Cancer Res. 77(21):e104, 2017

Glioma regions with low apparent diffusion coefficient: correlation between volumetric changes during chemoradiation and progression-free and overall survival

Liam S. P. Lawrence,[ab] Rachel W. Chan,[a] James Stewart,[a] Mark Ruschin,[a] Aimee Theriault,[a] Sten Myrehaug,[a] Jay Detsky,[a] Pejman J. Maralani,[a] Chia-Lin Tseng,[a] Greg J. Stanisz,[ab] Arjun Sahgal,[a] Angus Z. Lau[ab]

a. Sunnybrook Health Sciences Centre, Toronto, ON b. Medical Biophysics, University of Toronto, Toronto, ON

Introduction: High-grade (III/IV) gliomas carry poor prognosis. Patient survival might be extended by escalating the radiotherapy (RT) dose. Possible targets are regions of low apparent diffusion coefficients (ADC) on diffusion MRI, since low ADC indicates tumour of high cell density [1]. To validate low-ADC regions as dose escalation targets, the prognostic value of these regions should be demonstrated. The volumetric change of low-ADC (<1.25 $\mu m^2/ms$) regions at 3 weeks following RT initiation was previously shown to be prognostic of overall survival [2]. We hypothesized that the change at other time points would be prognostic for progression-free and overall survival.

Methods: High-grade glioma patients ($N = 49$) were treated with 54-60 Gy in 30 fractions over 6 weeks and concurrent temozolomide. MRI (1.5T Philips Ingenia, 16-channel head coil) was performed at four time points: treatment planning, fractions 10 (2 weeks) and 20 (4 weeks), and one-month post-RT (10 weeks). Follow-up imaging occurred every 3 months thereafter; tumour response was evaluated using RANO criteria. Patients were followed for 3.9 years. Scans included DWI (TR/TE=7720/74 ms, 1.1×1.5×5.0 mm^3 voxels, 200×240×170 mm^3 FOV) and pre- and post-Gd T_1-weighted (T_1w) images (TR/TE_1/TE_2=6.2/1.97/4.1 ms, 1.0×1.0×2.0 mm^3 voxels, 240×192×200 mm^3 FOV). The gross tumour volume (GTV), comprising residual gross tumour and surgical cavity, was contoured on the post-Gd T_1w image at each session. Images were rigidly co-registered. ADC maps were computed from b-values of 0 and 1000 s/mm^2. The "low-ADC region" was defined as the largest connected component inside the GTV with ADC < 1.25 $\mu m^2/ms$ [2]. The relative difference (ΔV_{rel}) between the low-ADC region volume at a given time point (V) and at planning (V_0) was computed as $\Delta V_{rel} = (V - V_0)/V_0$. Progression-free/overall survival (PFS/OS) Kaplan-Meier curves were estimated from the times between RT planning and tumour progression/death. At each time point, patients were stratified according to whether ΔV_{rel} was above or below the median; survival curves were compared using the log-rank test. *P*-values were adjusted for the six multiple comparisons using Holm's method; *p*-values <.05 were considered significant.

Results: The median ΔV_{rel} at fractions 10, 20, and one-month post-RT were $-30\%, -43\%$, and -67%, respectively. Patients with ΔV_{rel} below the median (more shrinkage of low-ADC region) at fraction 10 had longer PFS and OS (**Figures A, B**) ($p < .001, N = 46$ and $p < .001, N = 46$, respectively). The same associations were true for ΔV_{rel} at fraction 20 (PFS: $p = .033, N = 44$, OS: $p = .022, N = 44$). No correlation was found at one-month post-RT in PFS or OS ($p = .11, N = 39$ and $p = .11, N = 38$).

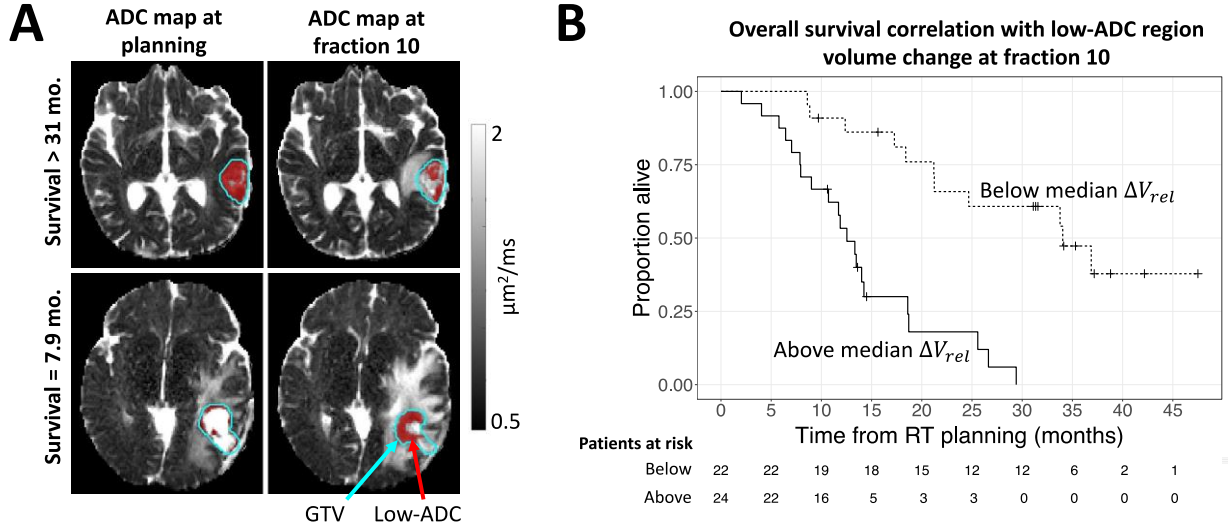

Conclusions: Volumetric changes in low-ADC regions of high-grade gliomas are prognostic for progression-free and overall survival at 2 weeks and 4 weeks from RT initiation, in concordance with other studies showing intra-treatment ADC changes correlate with outcome [1,2]. The therapeutic benefit of escalating the radiation dose to regions of low ADC and adapting the target to changes in this region should be investigated in a clinical trial.

References: [1] Patterson et al., *Nat Rev Clin Oncol*, 2008. [2] Chenevert et al., *Tomography*, 2019.

The effects of stereotactic body radiotherapy on tumour microvasculature: insights from optical coherence angiography towards adaptive radiation medicine

Nader Allam[1,2], W. Jeffrey Zabel[1,2], Valentin Demidov[1,3], Blake Jones[1], Luuk van der Pol[4], Warren Foltz[2], Costel Flueraru[5], Edward Taylor[2,6] and I. Alex Vitkin[1,2,6]

[1]Department of Medical Biophysics, University of Toronto.
[2]Radiation Medicine Program, Princess Margaret Cancer Centre.
[3]Geisel School of Medicine, Dartmouth College.
[4]Department of Medical Engineering, Eindhoven University of Technology.
[5]National Research Council Canada, Information Communication Technology.
[6]Department of Radiation Oncology, University of Toronto.

Introduction: *Stereotactic body radiotherapy* (SBRT) shows promise for increasing local tumour control for many of the most lethal cancer types including *pancreatic ductal carcinoma* (PDA), compared to conventional radiotherapy. Yet SBRT radiation fractionation schedules may still be improved as its mechanism of action remains largely unknown. It has been suggested that this accelerated hypofractionated treatment benefits from vascular damage (in particular of blood capillaries ~10-30 μm in diameter). We therefore hypothesize that monitoring radiation-induced microvascular changes will (1) yield insights into SBRT's radiobiological effects, and (2) enable predictions of long-term tumour response.

Methods: We addressed these hypotheses pre-clinically in PDA human xenografts grown in immunocompromised mice in a dorsal skinfold window chamber model. We monitored both micro- (via optical coherence angiography (OCA)) and macro- (via dynamic contrast enhanced magnetic resonance imaging (DCE-MRI)) vascular responses to irradiation over time. We first studied responses to single fraction irradiation (0, 10, 20, 30 Gy, n=18), and then to a full typical clinical SBRT regimen (e.g, Fig. a) 3x12 Gy, n=5) delivered via a small animal irradiator. Candidate predictive vascular biomarkers of radiobiological relevance were derived from 3D OCA microvascular networks (micro-scale response) and correlated with the DCE-MRI functional metrics relating to the transport of an MRI contrast agent (macro-scale response). The longitudinal trajectories of both were measured before, during and following treatments. Herein we focus primarily on the DLF_{150} and λ metrics from OCA which describe the microvascular heterogeneity and molecular transport efficiency. These measure the proportion of tissue at the *short* (~average intervascular separation) and *long* (>~150 μm, the typical diffusion distance of oxygen in tumour tissue) distance from the nearest vessels throughout the tumours respectively. To assess the predictive power of the various metrics, their temporal trends were compared to the macroscopic tumour response (volume and viability). Efforts are ongoing to train neural networks for this time series analysis.

Results: Both metrics exhibited a gradual increase up to 2-3 weeks post-irradiation with maxima positively correlated with the single-delivered dose, before gradually returning to pre-irradiation levels (the normalization ref.). Conversely λ and DLF_{150} for the unirradiated controls steadily decreased, likely due to unaltered continued chaotic vascular growth. Their temporal dependencies appear to precede those of the macroscopic tumour response (volume, and viability via fluorescence intensity) by up to 2 weeks (Fig. b)), indicating that they may be good candidates for early predictive biomarkers. These trends are still being investigated in the context of SBRT.

Conclusions: The combined OCA and DCE-MRI insights should yield a better understanding of tissue functional response to high doses of radiation employed in SBRT and help develop improved SBRT fractionation schedules (dose and time combinations) towards personalized and adaptive radiation therapy.

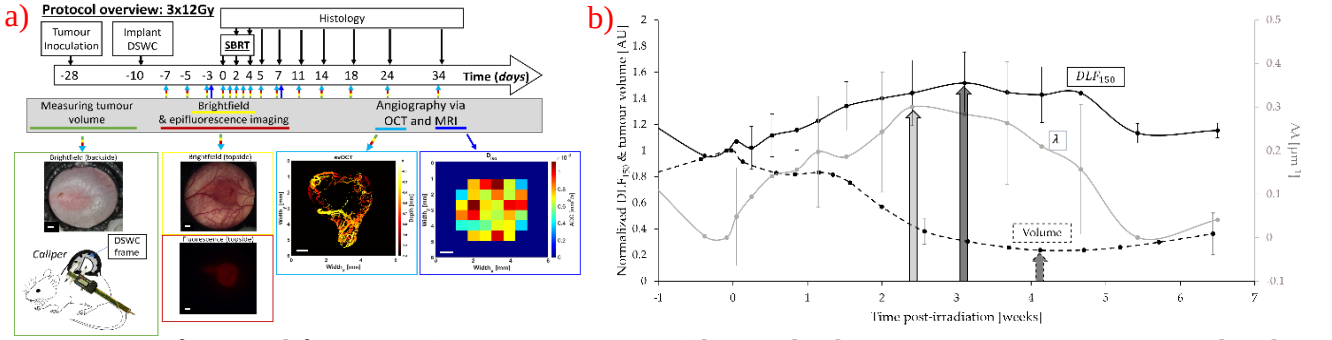

a) Overview of protocol for SBRT (e.g., 3x12 Gy, MWF) longitudinal response monitoring via optical and MR modalities. b) The global maxima in DLF_{150} and λ vascular metrics appear to precede the global minimum macroscopic tumour response to single high dose irradiation (shown: 1x30 Gy (n=6)) by ~ 2 weeks (see arrows).

Tumour cell clusters surviving after radiotherapy can be detected via texture analysis of optical coherence tomography images to predict treatment outcome

Natalia V. Demidova [1, 2,*], Valentin Demidov[3], Costel Flueraru[4], I. Alex Vitkin[1, 5]

1. *Department of Medical Biophysics, University of Toronto, Toronto, Canada;* ***2.*** *Department of Chemical and Physical Sciences, University of Toronto, Mississauga, Canada;* ***3.*** *Geisel School of Medicine, Dartmouth College, Hanover, USA;* ***4.*** *Information Communication Technology, National Research Council Canada, Ottawa, Canada;* ***5.*** *Princess Margaret Cancer Centre, University Health Network, Toronto, Canada;*
*****natalia.demidova@mail.utoronto.ca*

20th Imaging Network Ontario Symposium, March 2022

Introduction: Radiotherapy is widely used for cancer treatment, alone or in combination with other therapies. During its weeks-long course, tumour response is assessed by changes in tumour volume which is only loosely related to treatment outcome; the ~millimeter spatial resolution of such imaging modalities is insufficient to visualize subtle micron-scale changes in tumours early into the treatment course. Noninvasive evaluations of treatment response are currently being explored, but reliable data about the early radiation-induced tumour changes is difficult to obtain at the microscopic level longitudinally without biopsy intervention. Here we propose a method for detection of early changes in irradiated tissues with optical coherence tomography (OCT), an emerging imaging modality capable of depth-resolved label-free 3D visualization of cancerous tissues *in-vivo* at micron-scale resolutions [1]. For this, we combine (1) our recently developed volumetric tumour delineation method [2], (2) microvascular imaging technique [3], and (3) our emerging texture-analysis-based viable tumour-cell-cluster detection approach for longitudinal monitoring of subtle radiation-induced tumour changes.

Methods: We used human-derived BxPC-3 pancreatic adenocarcinoma grown subcutaneously in dorsal-skin window chambers implanted on the backs of immunocompromised NRG mice. Animals were monitored and imaged prior to and for 5 weeks following radiotherapy treatment of 10, 15, 20 and 30Gy doses. As proof-of-concept, n=3 animals were chosen for each of 4 treatment doses, including a non-irradiated set of control animals to total n=15. Using this data, we develop a method capable of segmenting out viable tumour cell clusters, where their discrimination from surrounding tissue relies on differences in optical scattering properties between different cell types and their radiotherapy-induced alterations. Texture analysis of volumetric OCT utilizes histograms of OCT speckle intensity fitted with the gamma distribution, a method previously shown to detect changes in tissue scattering properties in high frequency ultrasound and OCT. Parametric volumes made from extracted gamma-fitting parameters are thresholded within a range of specific values to delineate only the surviving viable cell nests within the irradiated tumours. This novel approach is validated with epi-fluorescence imaging, confocal fluorescence microscopy and histology, then applied to reveal the radiation-induced longitudinal changes in surviving tumour cell clusters after treatment for up to 5 weeks.

Results: OCT-detected quantified proportions of viable cell populations scale with dose, correlate well with histology, and may serve as predictors of the treatment end point (e.g., volume growth delay for these single-dose radiotherapy treatments). Results demonstrate that the early microscopic changes captured by OCT texture analysis may predict treatment outcome (e.g., growth delay) as early as the first week after irradiation.

Conclusion: Optical coherence tomography detects surviving tumour cell clusters following irradiation *in-vivo,* thus opening the new exciting ways for (i) aiding in our understanding of basic tumour radiobiology, including size and location of treatment-resistant subpopulations, (ii) providing quantitative data for judicious radiotherapy treatment planning, and (iii) enabling response monitoring for potential treatment course corrections.

References: [1] van Manen et al, "The clinical usefulness of optical coherence tomography during cancer interventions," *J Cancer Res Clin Oncol* **144** 1967–90 (2018); **[2]** Demidov et al, "Volumetric tumour delineation and assessment of its early response to radiotherapy with optical coherence tomography," *Biomed Opt Exp* **5** 2952-67 (2021); **[3]** Demidov et al, "Preclinical longitudinal imaging of tumour microvascular radiobiological response with functional optical coherence tomography," *Sci Rep* **8** 38 (2018).

Oral Session 2: Neuro Imaging

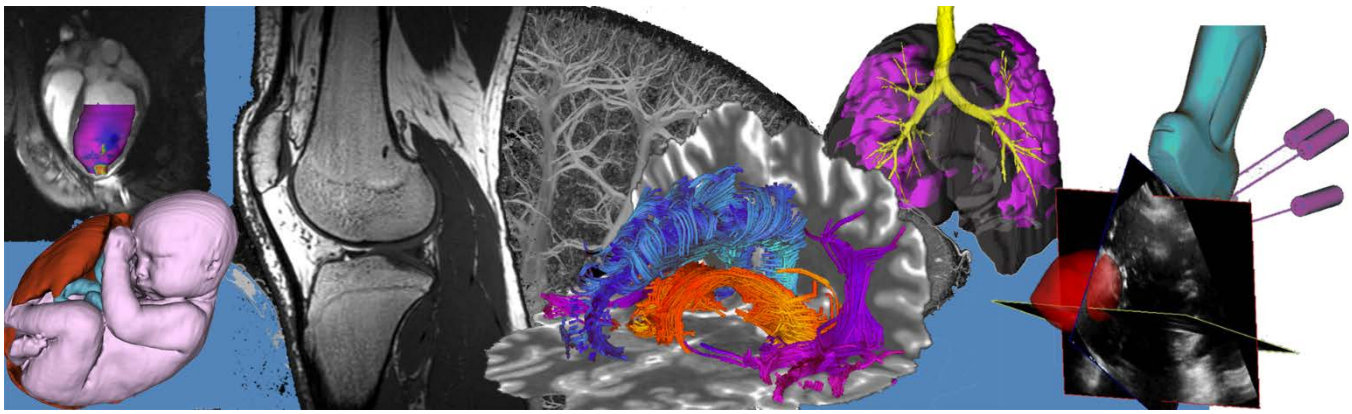

Lower amyloid-PET signal in white matter lesions is associated with increased free water: a multi-center mixed cohort of small vessel disease and Alzheimer's pathology

Authors: J Ottoy[1], M Ozzoude[1], K Zukotynski[1], MS Kang[2], S Adamo[1], C Scott[1], J Ramirez[1], W Swardfager[3], B Lam[4], A Bhan[1], P Mojiri[1], A Kiss[5], S Strother[6,7], C Bocti[8], M Borrie[9], H Chertkow[10], R Frayne[11], R Hsiung[12], R Laforce[13], MD Noseworthy[14], FS Prato[9], DJ Sahlas[15], EE Smith[16], PH Kuo[17], JA Chad[6,7], O Pasternak[18], V Sossi[12], A Thiel[10], JP Soucy[2], JC Tardif[19], SE Black[1,4], M Goubran[1,6]

[1]Hurvitz Brain Sciences Program, SRI, University of Toronto, Canada; [2]Montreal Neurological Institute, McGill University, Canada; [3]Pharmacology & Toxicology, University of Toronto, Canada; [4]Neurology, University of Toronto, Canada; [5]Research Design and Biostatistics, SRI, University of Toronto, Canada; [6]Medical Biophysics, University of Toronto, Canada; [7]The Rotman Research Institute Baycrest, University of Toronto, Canada; [8]Medicine, Université de Sherbrooke, Canada; [9]Lawson Health Research Institute, Western University, Canada; [10]Jewish General Hospital, McGill University, Canada; [11]Radiology and Clinical Neuroscience, University of Calgary, Canada; [12]DM Center for Brain Health, BC University, Canada; [13]Clinique Interdisciplinaire de Mémoire, Université Laval, Canada; [14]Department of Electrical and Computer Engineering, McMaster University, Canada; [15]Medicine, McMaster University, Canada; [16]Hotchkiss Brain Institute, University of Calgary, Canada; [17]Medical Imaging, University of Arizona, Tucson, USA; [18]Brigham and Women's Hospital, Harvard Medical School, USA; [19]Montreal Heart Institute, Université de Montréal, Canada

Introduction: Positron emission tomography (PET) with amyloid-β ligands recently gained interest for evaluating white matter (WM) pathology[1]. Prior studies hypothesized that the amyloid-PET signal in the WM may reflect myelin health based on its association with diffusion metrics such as fractional anisotropy[2]. However, these *single*-compartment diffusion metrics are contaminated by vascular/inflammatory processes from extracellular free water[3]. Here, we investigated the neurobiological underpinnings of the amyloid-PET signal in the WM using *multi*-compartment diffusion MRI in a mixed cohort of small vessel disease and Alzheimer's disease pathology.

Methods: The study included 58 participants with moderate-to-severe white matter hyperintensity (WMH) burden from dementia and stroke-prevention clinics at 7 sites across Canada (MITNEC-C6 cohort). Additionally, the study included 57 participants with mild-to-moderate WMH burden from ADNI. They underwent diffusion MRI, ^{18}F-AV45 amyloid-PET, and cognitive testing (MMSE). We calculated diffusion metrics of the WM including fractional anisotropy (FA) and mean diffusivity (MD). In addition, we applied a bi-tensor diffusion MRI model[3] that differentiates between extracellular (free water fraction) and tissue-specific (free water-adjusted FA) compartments of the WM. We tested associations of all diffusion metrics with ^{18}F-AV45 standardized uptake value ratios (SUVR) in regions of WMH vs. normal-appearing WM, and with cognition. We further performed partial-least-square analysis to investigate how the closely related diffusion metrics as well as age, sex, education, WMH volume, and cortical ^{18}F-AV45 SUVR covary with ^{18}F-AV45 SUVR in the WM.

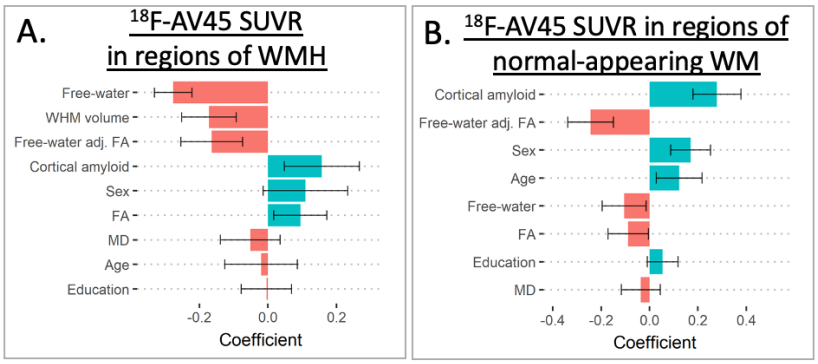

Fig1. Diffusion MRI metrics covary in predicting ^{18}F-AV45 SUVR in WM. Contribution of the loadings to the first components of PLS analysis explaining most of the variance in ^{18}F-AV45 SUVR in regions of WMH (panel A; 24% variance) and in normal-appearing WM (panel B; 31% variance) in the MITNEC-C6 cohort.

Results: ^{18}F-AV45 SUVR based on amyloid-PET was significantly lower in regions of WMH compared to normal-appearing WM (t=25.08, P<0.0001). Within regions of WMH, lower ^{18}F-AV45 SUVR was associated with higher free water (β=-0.36±0.13, P=0.005) and lower FA (β=+0.24±0.12, P=0.046), but not with the tissue-specific metric free water-adjusted FA. Partial-least-square analysis further confirmed that free water had the most influence on ^{18}F-AV45 SUVR in regions of WMH (**Fig.1A**). In contrast, free water-adjusted FA had more influence on ^{18}F-AV45 SUVR in the normal-appearing WM (**Fig.1B**). Last, correlation with cognitive impairment was higher for free water than for free water-adjusted FA, both in regions of WMH ($\beta_{\text{free water}}$=-0.40±0.13, P=0.003; $\beta_{\text{free water-adjusted FA}}$=0.14±0.09, P=0.11) and in normal-appearing WM ($\beta_{\text{free water}}$=-0.30±0.11, P=0.01; $\beta_{\text{free water-adjusted FA}}$=0.21±0.09, P=0.02).

Conclusion: In a mixed AD population with vascular comorbidities, reduced amyloid-PET uptake in WM lesions may largely reflect the appearance of extracellular free water, while changes in normal-appearing WM may more closely reflect tissue-specific damage. Our study supports free water and amyloid-PET as potential markers to detect WM abnormalities in Alzheimer's and small vessel disease pathology.

References: [1] Bodini 2016 *Ann Neurol;* [2] Moscoso 2021 *EJNMMI;* [3] Pasternak 2009 *Mag Res Med*

Greater Monoamine Oxidase B Distribution Volume in the Prefrontal Cortex in Traumatic Brain Injury with Persistent Symptoms: An [^{11}C]SL25.1188 PET Study

Y. Koshimori[1], M.D. Cusimano[2], P. M. Rusjan[3], N. Vasdev[1], S. Houle[1], E. Thomson[1], I. Boileau[1], S. Kish[1], S. Morguchi[1], I. Husain[1], T. Chao[4], Z. Nasser[1], J.H. Meyer[1]

[1] Brain Health Imaging Centre and Campbell Family Mental Health Research Institute, CAMH, and Department of Psychiatry, University of Toronto, Toronto, Canada

[2] Neurosurgery, St. Michael's Hospital, University of Toronto, Toronto, Canada
[3] Douglas Research Center, Department of Psychiatry, McGill University, Montreal, Canada
[4] Institute of Mental Health, Department of Psychiatry, University of British Columbia, Vancouver, Canada

Introduction: Traumatic Brain Injury (TBI) is an important public health problem affecting 1 to 2% of the general population. Over 90% of traumatic brain injury (TBI) cases are community based and mild to moderate at time of injury. Most symptomatic burden is consequent to the persistent symptoms, which may be more severe than the initial symptoms, that follow in one third of cases. Despite the high prevalence of TBI, there are no pharmacological intervention strategies for persistent TBI symptoms. Whether the inflammatory response of astrogliosis, a potentially therapeutically targetable process, occurs in such situations is not established. It seems plausible that reactive astrocytosis could be present in TBI with persistent symptoms since it occurs in humans with chronic traumatic encephalopathy (CTE) and animal studies simulating TBI. Reactive astrocytosis is also associated with greater expression of monoamine oxidase B (MAO-B). Recently [^{11}C]SL25.1188, a new PET MAO-B radiotracer was validated which demonstrated outstanding characteristics including high brain uptake values, high selectivity, excellent ratio of specific binding to free and non-specific binding for many brain regions and a lack of brain penetrant radioactive metabolites.

The primary hypotheses were that greater MAO-B V_T, a PET index of MAO-B density would occur in prefrontal cortex (PFC) and other cortical regions in TBI cases with chronic symptoms recruited from the community as compared to healthy controls. It was also hypothesized that greater PFC MAO-B V_T would be associated with slower cognitive speed, since astrogliosis in the PFC is associated with slower cognitive speed.

Methods: Seventeen participants with TBI and 23 healthy controls underwent [^{11}C]SL25.1188 PET scanning. None smoked cigarettes nor had a substance abuse disorder. A two tissue compartment model was applied. A repeated measures analysis of variance (rANOVA) assessing effect of diagnosis with region as the repeated variable, was applied to the subregions of the prefrontal cortex in one analysis and grey matter regions across the brain in the second analysis. Relationship of MAO-B V_T in PFC and its subregions to cognitive speed in TBI was investigated.

Results: Patients with TBI had significantly greater MAO-B V_T in the PFC (ANOVA, $F_{1,38}$=10.8; p=0.002) and throughout the cortex regions assessed (ANOVA, $F_{1,38}$=10.8 to 6.1; p=0.002 to 0.01). Effect sizes of differences in MAO-B V_T between TBI and healthy were substantial with the mean MAO-B V_T of TBI participants typically being about 1 standard deviation greater than controls. The correlation between PFC MAO-B V_T and t score of the Comprehensive Trail Making Test (1 to 3) was significant (r=0.64, p=0.006).

Conclusions: Greater MAO-B V_T, throughout cortical regions is strongly supportive of astrogliosis in community based samples with mild to moderate TBI. Therapeutics to modify astrogliosis towards curative phenotypes should be tested in this population. Given the substantive effect size, [^{11}C]SL25.1188 PET is a promising biomarker to stratify cases and/or assess target engagement for putative therapeutics to modify; or reduce astrogliosis in TBI. MAO-B itself may be a promising target in TBI.

A Digital Brain Perfusion Phantom to Test the Performance of CT Perfusion Software

Kevin J. Chung, Ting-Yim Lee

Department of Medical Biophysics, University of Western Ontario, London, Ontario;
Robarts Research Institute and Lawson Health Research Institute, London, Ontario

Introduction: Acute ischemic stroke is caused by a clot that restricts blood flow to the brain. As a result, cerebral blood flow (CBF) is a sensitive indicator of brain injury during acute ischemic stroke. CT perfusion (CTP) allows efficient estimation of CBF by analyzing the passage of x-ray contrast in brain tissue relative to the brain arteries through rapid CT scanning and contrast injection. This analysis (deconvolution) is dependent on CTP scan parameters such as noise and scan interval. In this study, we describe the development of a fully digital brain CT perfusion phantom that can be used to test the performance of CTP software at various CTP scan parameters. Specifically, we investigated the effect of varying CTP scan interval over a fixed scan duration and radiation dose.
Methods: A digital head CT phantom was generated by assigning expected CT numbers to head structures delineated from a high-quality brain MRI of a normal human subject. Using corresponding delineations of the grey and white matter, and a manually segmented region of ischemic brain injury, physiological perfusion values were assigned to create a ground truth CBF map. Using an arterial time-density curve (TDC) from a normal large brain artery of a stroke patient and assumed ground truth tissue perfusion parameters, tissue TDCs were simulated by convolving the arterial TDC with the assumed tissue residue function. Tissue TDCs were added to the digital head CT phantom to create a dynamic brain CT perfusion phantom. Realistic CT noise was independently added to each dynamic image by adding Poisson noise to simulated projections of the dynamic CT images, and reconstructing with standard filtered back projection. A 60 s CTP scan was simulated at scan intervals of 0.5, 1, 2, 3, 4, and 8 s with constant scan dose simulated by modulating the strength of added noise (e.g., 4× more noise at 0.5 s than 8 s). A model-based deconvolution algorithm developed in our lab was used to calculate CBF maps for each simulated CTP phantom. Relative CBF maps were calculated by normalizing CBF maps by the median CBF in the normal brain hemisphere. Infarct was identified by a standard threshold of relative CBF less than 30% for comparison with the ground truth.
Results: The Figure shows simulated CT images and CBF maps of a section of the digital brain perfusion phantom. The ground truth infarct volume was 3.9 ml. Using relative CBF<30%, infarct volume was estimated as 3.3, 1.9, 2.8, 2.1, 1.7, and 0.8 ml using 0.5, 1, 2, 3, 4, and 8 s CTP scan intervals. The ischemic region can qualitatively be identified with even 8 s scan interval but accuracy in the estimated infarct volume deteriorates.
Conclusions: We described a fully digital brain perfusion phantom in which its physiological and scan parameters can be freely adjusted to test the performance of CTP software. This phantom may help guide the design of novel CTP scanning protocols without radiation risk to stroke patients.

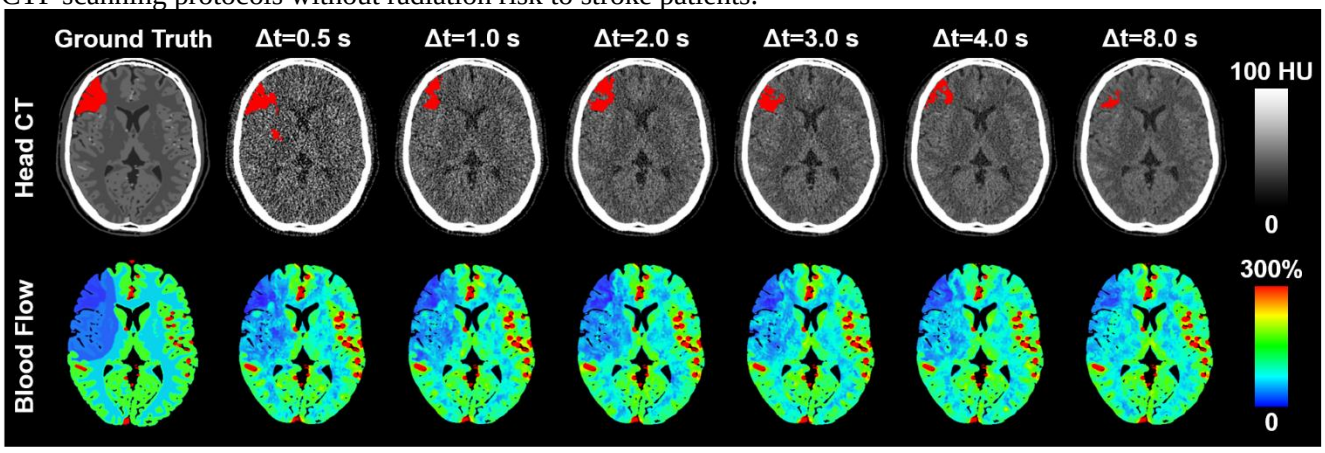

Figure. Pre-contrast head CT (top row) and relative CBF maps (bottom row, relative to the mean CBF in the normal brain hemisphere) derived from the digital brain perfusion phantom. Ground truths are in the leftmost column. Simulated infarct is delineated in red on CT. CT image noise decreases with longer scan intervals Δt (and fewer dynamic images), simulating a fixed scan dose. Calculated CBF maps appear qualitatively similar and match the ischemic region shown in the ground truth (region with decreased CBF in the right brain hemisphere). The ischemic region can even be seen at 8 s scan interval albeit with poorer contrast to normal CBF.

Physiological and functional brain changes in adults recovering from COVID-19

William S.H. Kim[1,2]; Xiang Ji[3]; Nicholas J. Luciw[1,2]; Eugenie Roudaia[4]; J. Jean Chen[1,4]; Asaf Gilboa[4,5]; Allison Sekuler[4–6]; Fuqiang Gao[2,3]; Zhongmin Lin[1,7]; Aravinthan Jegatheesan[1,7]; Mario Masellis[2,3,8]; Maged Goubran[1,2,7]; Jennifer Rabin[8–10]; Benjamin Lam[2,3,8]; Ivy Cheng[11–13]; Robert Fowler[13,14]; Chris Heyn[2,15]; Sandra E. Black[2,3,8]; Simon J. Graham[1,2,7]; Bradley J. MacIntosh[1,2,7]

[1]Department of Medical Biophysics, University of Toronto, Toronto, ON, Canada; [2]Hurvitz Brain Sciences Program, Sunnybrook Research Institute, Toronto, ON, Canada; [3]LC Campbell Cognitive Neurology Research Group, Sunnybrook Health Sciences Centre, Toronto, ON, Canada; [4]Rotman Research Institute, Toronto, ON, Canada; [5]Department of Psychology, University of Toronto, Toronto, ON, Canada; [6]Department of Psychology, Neuroscience & Behaviour, McMaster University, Hamilton, ON, Canada; [7]Physical Sciences Platform, Sunnybrook Research Institute, Toronto, ON, Canada; [8]Division of Neurology, University of Toronto, Toronto, ON, Canada; [9]Harquail Centre for Neuromodulation, Sunnybrook Research Institute, Toronto, ON, Canada; [10]Rehabilitation Sciences Institute, University of Toronto, Toronto, ON, Canada; [11]Evaluative Clinical Sciences, Sunnybrook Research Institute, Toronto, ON, Canada; [12]Integrated Community Program, Sunnybrook Research Institute, Toronto, ON, Canada; [13]Department of Medicine, University of Toronto, Toronto, ON, Canada; [14]Emergency & Critical Care Research Program, Sunnybrook Research Institute, Toronto, ON, Canada; [15]Department of Medical Imaging, University of Toronto, Toronto, ON, Canada

Introduction: Although coronavirus disease 2019 (COVID-19) manifests primarily as a respiratory illness, multi-organ pathology may occur in some cases. In particular, there are many reports of neurological and psychiatric symptoms during and beyond acute stages of infection. Whereas the consequences of the virus on the brain have been studied extensively from structural magnetic resonance imaging (MRI) of hospitalized patients, much less is known regarding physiological and functional brain changes, especially in adults who are recovering from acute stages of infection. As part of the Toronto-based NeuroCOVID-19 study, we sought to investigate brain physiology, function, and structure through MRI of adults recovering from COVID-19 (hospitalized and self-isolating) relative to controls who had flu-like symptoms. Arterial spin labeling (ASL) and blood-oxygenation level-dependent (BOLD) functional MRI are two pulse sequences that can yield measures of cerebral blood flow (CBF) and fractional amplitude of low-frequency fluctuations (fALFF), a proxy measure of brain activity. We hypothesized that adults previously infected with COVID-19 would exhibit altered CBF and fALFF relative to controls.

Methods: 56 adults from the NeuroCOVID-19 study were investigated. Participants were no longer infectious and belonged to one of three groups: 1) those hospitalized due to COVID-19 (n = 8), 2) those who self-isolated due to COVID-19 (n = 35), and 3) controls with flu-like symptoms (n = 13). Group designation was established by COVID-19 diagnosis. Image processing was performed with open-source tools from FSL and AFNI. Voxelwise comparisons of CBF, fALFF, and grey matter volume (GMV, as derived from available T1-weighted data) were assessed between COVID-19 and control groups using two-sample t-tests, after adjusting for age and sex. Cluster-extent thresholds were used for a family-wise error corrected $p < 0.05$. To further assess the effects of severe illness (e.g., hospitalization, ventilator effects), we performed a sensitivity analysis whereby hospitalized participants were omitted from the COVID-19 group.

Results: The three groups were matched for age, ethnicity, and sex. Hospitalized participants were imaged significantly later after end of quarantine than the self-isolating participants ($p = 0.04$). Relative to controls, the COVID-19 group exhibited significantly decreased CBF in one cluster encompassing the thalamus, orbitofrontal cortex, and regions of the basal ganglia as well as decreased fALFF in four clusters encompassing various limbic and frontal regions. Omitting hospitalized participants did not alter the pattern of results, suggesting that the observed CBF and fALFF reflect a more general systemic alteration induced by infection. No group differences in GMV were observed.

Conclusions: In this study, we investigated CBF, fALFF, and GMV in adults recovering from COVID-19 and observed physiological and functional changes in the absence of structural changes. Many of the implicated regions, encompassing frontal, basal ganglia, and limbic regions, have been highlighted in previous COVID-19 imaging studies; are possibly related to COVID-19 symptomatology; and may be involved in posited routes of neuroinvasion. Future work will investigate the persistence of these brain changes at longitudinal assessments.

Pitch Session 1: Machine Learning I

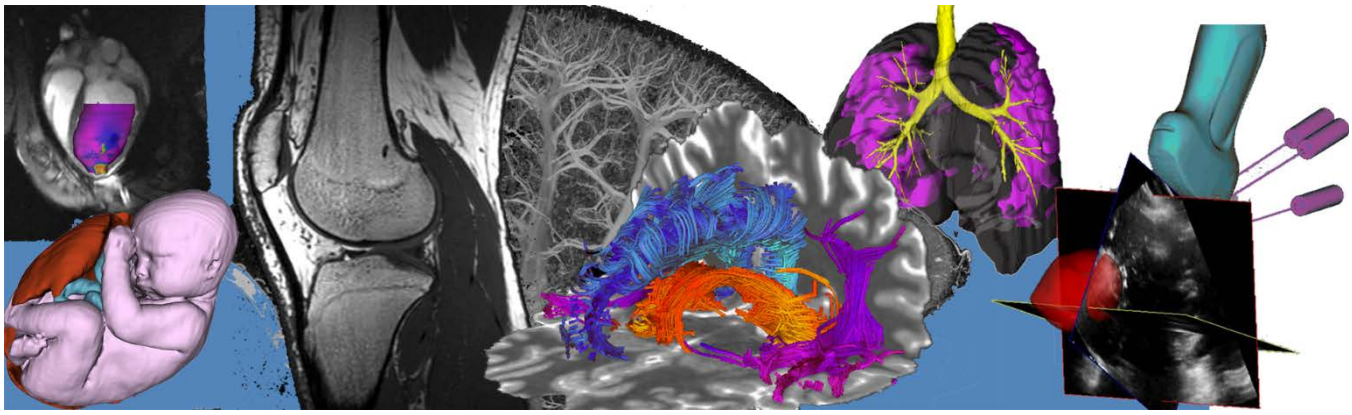

Domain Transfer through Image-to-Image Translation in Prostate Cancer Detection

Meng Zhou[1], Amoon Jamzad[1], Jason Izard[2], Alexandre Menard[2], Robert Siemens[2], and Parvin Mousavi[1]

[1]School of Computing, Queen's University, Kingston, ON, Canada
[2]Kingston Health Sciences Research Centre, Kingston, ON, Canada

Introduction: Prostate Cancer (PCa) is one of the most common types of cancer among males. Magnetic Resonance Imaging (MRI) is one of the effective ways to detect PCa in the early stages. While MRI with magnetic strength of 1.5 Tesla (T) is widely used in clinical settings and medical centers, 3.0 T MRI is used in research settings due to its higher image quality and spatial resolution [1]. Deep learning-based models have been proven to be efficient for the PCa classification task. However, training such models often requires a vast amount of data and it is infeasible to obtain in local clinical centers with low patient throughput. Publicly available data may be acquired by different equipment and settings, and therefore could not directly be used due to domain shift problem. To address this, we propose a generalized image translation model. In this work, we took the 3.0T MRI images from the " ProstateX" challenge; translated to 1.5T-like MRI images based on the CycleGAN framework [3]; and trained a classifier for PCa classification on translated images for PCa classification to use in the local 1.5T MRI dataset.

Method: Our data consisted of public ProstateX 3.0T (204 patients) and private local 1.5T (104 patients) volumetric MRI images. The dataset contains the PCa detected in both Transitional Zone (TZ) and Peripheral Zone (PZ). First, the 3.0T images had to be transformed to 1.5T, prior to the main cancer classification task. As a baseline, we replicated an implementation of **S**patial **D**ecomposition **Net**work, recently introduced by *Grebenisan et al.* [2] for domain transfer. To further improve the result from [2], we aimed to adopt the concepts of Adversarial Consistency Loss GAN [3] to the domain transfer of prostate MRI data. The input of GAN is the 2D slice of MRI images from both modalities. The primary network architecture consisted of generators to produce fake images between two modalities, and discriminators to distinguish between synthetic and real images. The adversarial consistency loss is utilized in the loss function, and it is crucial to preserve the anatomical features of the images while transferring the domain. An attention mask is used to retain the background of source images during the transferring process. After the domain transfer of 3.0T to 1.5T, a 3D-Convolutional Neural Network (CNN) was trained for the main task of PCa classification.

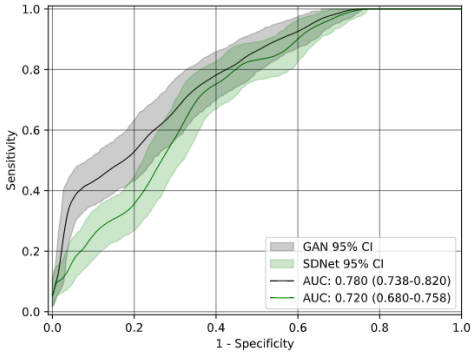

Result: The result is shown in the figure on the right. The proposed GAN (black line) has proven to be a feasible approach for the domain adaptation task in PCa, and it further overperformed the SDNet method (green line). The current result for GAN demonstrates the effectiveness of image translation method in the domain transfer of prostate MRI images.

Conclusion: The result demonstrates the feasibility of the domain adaptation in the PCa classification task. Based on the experiments and the reported AUC, the proposed image translation approach could perform translation between two different modalities and exceed the state-of-the-art performance in PCa classification.

Reference: [1] M. Ladd, et al. "Pros and cons of ultra-high-field mri/mrs for human application." Prog Nucl Magn Reson Spectrosc, 109:1-50, 2018. [2] A. Grebenisan, A. Sedghi, et al. "Spatial decomposition for robust domain adaptation in prostate cancer detection." ISBI, 1218-1222, 2021. [3] Yihao Zhao, et al. "Unpaired Image-to-Image Translation using Adversarial Consistency Loss." ECCV 2020.

Computer-Aided Methods to Predict Prostate MRI Quality via Rectal Content Estimation

Abdullah Al-Hayali[1], Amin Komeili[2], Azar Azad[3], Nicola Schieda[4], Eran Ukwatta[1]

[1]School of Engineering, University of Guelph; [2]Department of Mechanical and Manufacturing Engineering, University of Calgary; [3]AI. Vali. Inc.; [4]Department of Medical Imaging, The Ottawa Hospital

Introduction - In 2020, the Canadian Cancer Society estimated that 1 in 7 men are diagnosed with prostate cancer (PCa), which constitutes to 10% of all cancer-related deaths. Prostate MRI has become the standard of care in the PCa diagnostic pathway. Prostate MRI is now performed before biopsy as a less invasive alternative for PCa detection. Prostate MRI image quality is a key determinant of a diagnostic test's performance. MRI quality is inversely proportional to the amount of rectal distension and rectal gas. A low-quality MRI image may lead to repeat examinations, inefficiencies in the clinical workflow, and delayed diagnosis. In this work, we propose the use of MRI localizer sequences (a pre-scan MRI sequence that takes 20 seconds to acquire) to estimate rectal content and predict the quality of the subsequent prostate MRI image. The determined quality would assist the MRI technologist on the decision of whether a prostate MRI should proceed, or if the patient requires rectal evacuation to remove rectal gas.

Methods - The dataset consists of 213 prostate sagittal T2-weighted MRI localizer images manually labelled by an expert radiologist. Each MRI image contains 7 2-D slices of the patient, accompanied by a ground truth mask of the rectum for each slice. Along with the masks, rectal content at the time of scan for each patient was provided in CSV format. The labels in the CSV file are four: empty, fluid, fluid + gas, and gas. The data was split 70% and 30% for training and testing. Segmentation methods were based on U-Net, a convolutional neural network (CNN) consisting of an encoder and a decoder with concatenation layers between them. The original U-Net model was utilised, along with other variants, including U-Net++, different encoder formulations, and different pre-trained weights. The encoders used were ResNet-34 (R-34) and VGG-16, and the pre-trained weights were of ImageNet which were broken into two segments (ImageNet 1 and 2) for computational efficiency. The models tested were: U-Net; U-Net (R-34 encoder); U-Net (R-34 encoder + ImageNet 1 weights); U-Net (R-34 + ImageNet2 weights); U-Net (VGG-16 encoder with ImageNet weights); U-Net++; and UNet++ (R-34 encoder + ImageNet weights).

The generated rectum segmentation masks were used to classify rectal content. Three classifiers were designed based on rectal diameter and volume, radiomic features of the rectum, and CNNs. The determination of the scan's quality and usability will be based on the classification outcome. The assignment of quality will be non-usable if the outcome of the classifier is gas or fluid + gas, otherwise, the image would be usable if the classification outcome is empty or fluid. Dice similarity coefficient (DSC) and Area Under the receiver operating characteristic Curve (AUC) were used for segmentation and classification evaluation, respectively.

Results – The dice score coefficient (DSC) of all methods was computed and shown in Table 1. Relative to other U-Net variants, U-Net (R-34 + ImageNet2 weights) performed best. Of the several classification models tested, the best three performing models of each category were selected. The CNN classifier achieved an AUC value of 0.85 ± 0.05, while the rectal diameter and volume classifiers achieved an AUC of 0.73 ± 0.06. Lastly, the radiomics based classifier achieved an AUC of **0.90** ± 0.05, which is the best performing classifier.

Table 1: DSC results for segmentation models

Model	U-Net	U-Net (R-34 encoder)	U-Net (R-34 encoder + ImageNet 1)	U-Net (R-34 encoder+ ImageNet 2)	U-Net (VGG-16 encoder + ImageNet)	U-Net++	UNet++ (R-34 encoder + ImageNet)
DSC (Mean ± SD)	0.79 ± 0.07	0.83 ± 0.04	0.84 ± 0.06	**0.85** ± 0.07	0.84 ± 0.04	0.80 ± 0.05	0.84 ± 0.05

Conclusion – We implemented an automatic quality assurance pipeline to evaluate prostate MRI image quality using segmentation and classification methods. It was found that the U-Net (R-34 + ImageNet2 weights) outperformed all other U-Net variants for image segmentation. Using the segmentation masks generated, the radiomics based classifier achieved the highest AUC score. Further work will utilize classification results to generate a prediction of what the final image quality would be.

Effects of Feature Type and Multiple Scanners on Brain Metastasis Treatment Outcome Prediction

D. DeVries[1,2], F. Lagerwaard[3], J. Zindler[4,5], T. Yeung[6], G. Rodrigues[7], G. Hajdok[1], A. Ward[1,2]
[1]Department of Medical Biophysics, Western University, London, Ontario; [2]Gerald C. Baines Centre, London Regional Cancer Program, London, Ontario; [3]Department of Radiation Oncology, Amsterdam UMC, Amsterdam, The Netherlands; [4]Department of Radiation Oncology, Haaglanden Medical Centre, Den Haag, The Netherlands; [5]Holland Proton Therapy Centre, Delft, The Netherlands; [6]RefleXion Medical, Hayward, California; [7]Department of Oncology, Western University, London, Ontario

Introduction

Many types of cancers are known to spread, or metastasize, to the brain to form brain metastases (BMs). An established treatment for BMs is stereotactic radiosurgery (SRS). SRS delivers high doses of radiation in 1 to 3 sessions that are highly conformal to the BMs. To ensure accurate treatment, pre-treatment T1-weighted contrast-enhanced magnetic resonance imaging (T1wCE MRI) is used for targeting. There is a need for tools to support clinician decision-making on how to best prescribe SRS. One such tool could be a machine learning classifier that predicts SRS treatment outcomes, given pre-treatment clinical and MRI features. Previous research has shown links between BM MRI appearance and treatment outcomes [1], and presented initial results of using machine learning classifiers [2,3]. This study seeks to explore crucial aspects of SRS treatment outcome prediction relevant to clinical translation by examining three novel aspects: 1) the prediction of multiple treatment outcomes, 2) the effect of feature type, and 3) the effect of MR scanner variability.

Methods

The study population consisted of 91 SRS patients, across which n = 110 BMs were individually analyzed. A total of 7 clinical features were available per patient, including patient sex, age, BM location, SRS parameters, and primary cancer data. Patients had MRI performed across 5 models of scanner, though 93% of the patients were scanned on 3 primary models (Siemens Avanto, Expert, and Vision). The pre-treatment T1wCE MRI was used to extract 635 radiomic features from each BM clinician defined region of interest (ROI) including shape, size, 1st order statistical, gray-level co-occurrence matrix, and gray-level run-length matrix features. The same features were also extracted from a 5 mm dilated ROI to examine any information provided beyond the BM ROI, such as microscopic disease or mass effect. Before feature extraction, intensity normalization to the mean brain voxel value and interpolation to a common voxel size were performed on the T1wCE MRI to account for scanner variability. The treatment outcomes investigated were in-field progression, out-of-field progression and 1-year overall survival. Follow-up MRI defined in-field progression (a treated BM growing in size) and out-of-field progression (the appearance of new BMs). A 1000-bootstrap machine learning experimental design was used with a random decision forest classifier and both embedded feature selection and Bayesian hyper-parameter optimization. Multiple experiments were performed for different outcomes and available features, as well as performing leave-one-scanner-out analysis.

Results

As shown in the figure to the right, for all outcomes, the use of radiomic features provided the highest area under the receiver operating characteristic curve (AUC). Only for predicting in-field progression was the combination of clinical and radiomic features optimal. Features from the dilated ROI were found to not increase AUC. In-field progression was predicted with the highest accuracy of the three outcomes with an estimated AUC of 0.70. When the patients imaged on the Avanto scanner were restricted to the testing set, in-field progression AUC fell to 0.48. In contrast, when the patients imaged on the Expert and Vision scanners made up the testing set, the AUC rose to 0.74 and 0.79, respectively. This demonstrates that even after pre-processing, the texture features from the Avanto scanner are in a different domain than the other scanners.

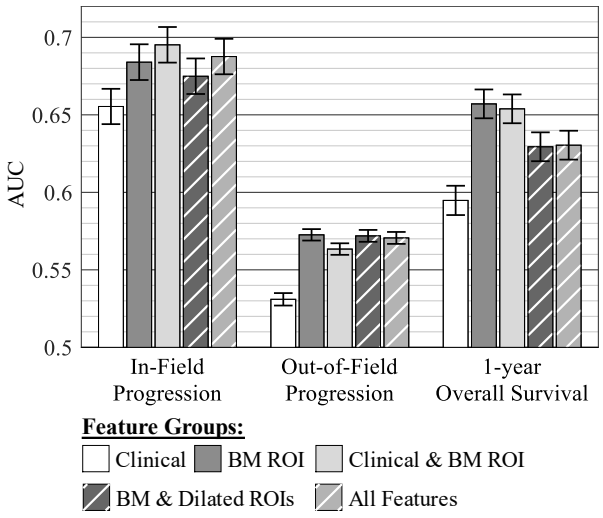

Conclusions

This study demonstrates that in-field progression, out-of-field progression and 1-year overall survival can all be predicted to some degree, with in-field progression being most accurately predicted. The clear utility of radiomic features was also demonstrated, along with the synergistic relationship of radiomic and clinical features and ineffectiveness of radiomic features from the dilated ROI. The effect of scanner model on prediction accuracy was found to be mixed, though the extremely poor performance on the Avanto scanner points towards possible difficulties during clinical translation, where mixed MR scanner models would be expected. The exploration of enhanced MR scanner normalization techniques is therefore a critical next step before clinical translation.

[1] *Rodrigues et al., Oncologist, 2013.* [2] *Mouraviev et al., Neuro-oncology, 2020.*
[3] *Karami et al., Sci. Reports, 2019*

Unsupervised Learning for Classification of Prostate Cancer Severity

A Perera-Ortega[1], F Fooladgar[2], NNM To[2], A Jamzad[1], P Mousavi[1], P Abolmaesumi[2]
[1]Medical Informatics Laboratory, School of Computing, Queen's University, Kingston, Canada
[2]Robotics and Control Laboratory, The University of British Columbia, Vancouver, Canada

INTRODUCTION: Prostate cancer (PCa) is the third leading cause of death from cancer in Canadian men [1]. Transrectal ultrasound (TRUS) guided core needle biopsy is the current practice for diagnosis of PCa. However, this method can miss clinically significant cancer since it is blind to intraprostatic pathology. After biopsy, a pathologist assigns the core a Gleason Score (GS), which is the gold standard for PCa grading. Since ultrasound is a widely accessible and inexpensive imaging modality, it would be beneficial if it could be used to assess where to biopsy as opposed to solely for navigation. To achieve this, the association of signatures of various Gleason grades of tissue in ultrasound and their pathology must be learned. However, such learning is difficult since labels are assigned to entire biopsy cores whereas ultrasound data is acquired at much higher resolutions. The objective of this study is to use unsupervised clustering to learn the Gleason signatures and address the issue of noisy data and labels to ultimately use ultrasound for biopsy location assessment.

METHODS: The original dataset consists of 258 biopsy cores from 70 patients that underwent TRUS-guided biopsy at Vancouver General Hospital. A CNN was trained using an evidential method approach proposed by Sensoy et al. to distinguish between benign versus cancerous cores. From that model, latent features were extracted from cores which had an involvement of at least 40%. Involvement is denoted as the percentage of signals in a core that are cancerous. This resulted in a split of 152, 57, and 55 cores for train, validation, and testing respectively. A Gaussian Mixture Model (GMM) was used to perform unsupervised clustering in the feature space. Within a GMM, each point is associated with a probability that it belongs to that cluster. The model separated the features into four clusters, intended to represent the benign, less severe cancer (GS <= 3+4), severe cancer (GS >= 4+3), and outlier classes. To visualize the resulting clusters, the latent feature space was reduced from 128 dimensions to 2 dimensions using an autoencoder model.

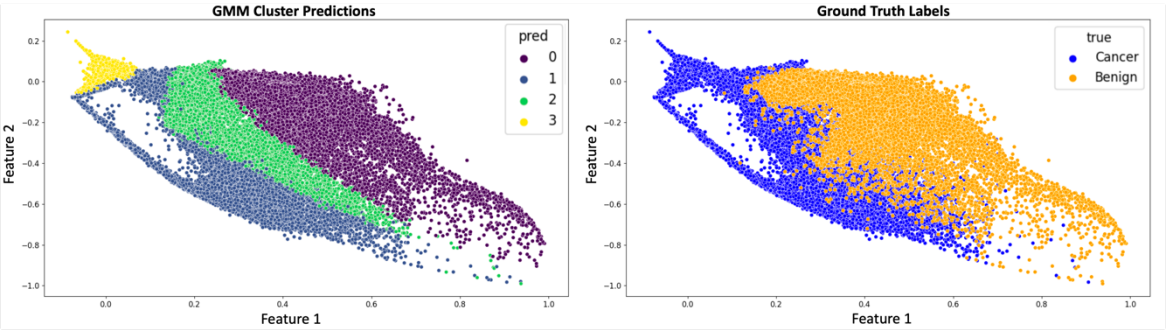

Fig. 1: A comparison between the GMM cluster predictions (left) and the ground truth labels (right).

RESULTS: Figure 1 shows that the model can find clusters that represent Gleason grades in the latent space. On the left figure, the blue, green, and yellow clusters seem to encompass cancerous signals, as it looks similar to the blue cluster (cancerous) when compared to the ground truth labels (right). The purple cluster on the left (predicted) appears to represent benign signals, as does the orange cluster on the right (true labels). More experimenting will be done to plot the ground truth labels in terms of Gleason 3, 4, and 5 groups to further assess the model's capability to separate Gleason signatures. Note that currently there are no Gleason 3+3 cores in the train data set (only Gleason 3+4), so the model may have difficulties separating Gleason 3 and 4 signatures.

CONCLUSION: A novel approach to visualize the signatures of various Gleason grades of tissue using ultrasound data was investigated. Determining the best visualization approach of the clustering space of the GMM is a challenge in and of itself. Future work will incorporate more data, specifically more Gleason 3+3 cores, into the dataset. Techniques to remove out of distribution and outlier signals will also be investigated.

REFERENCES:

[1] Canadian Cancer Statistics Advisory Committee. Canadian Cancer Statistics 2021. Canadian Cancer Society; 2021. **[2]** Javadi, G. et al. Towards targeted ultrasound-guided prostate biopsy by incorporating model and label uncertainty in cancer detection. IJCARS (2021). **[3]** Sensoy, M. et al. Evidential deep learning to quantify classification uncertainty. NeurIPS (2018).

Comparison of Radiomic Features for Bounding Box and Traditional Segmentation Methods of Axillary Lymph Node Metastases from Breast Cancer on CT

Matthew Van Oirschot[1], Mark Barszczyk[2], Grey Kuling[2], Anne Martel[2], Belinda Curpen[2], Naomi Matsuura[3], Navneet Singh[2]

[1]Division of Engineering Science, University of Toronto [2]Department of Medical Imaging, Sunnybrook Health Sciences Centre [3]Institute of Biomedical Engineering, University of Toronto

Introduction: The automated segmentation of metastases is a complex task that is highly dependent on 'ground truth' manual segmentations created by physicians (1). These manual segmentations are subject to both intra- and inter-observer variability, which can negatively affect machine learning models (1). This project proposes an alternative segmentation method using oriented bounding boxes, where the region of interest (ROI) is encapsulated by a rectangular prism such that the ROI is contained in the smallest possible volume. This method of segmentation may be less sensitive to intra- and inter-observer variability, but it is unknown whether the radiomic features used to differentiate between malignant and benign lymph nodes for traditional segmentations can also be used for bounding box segmentations. This preliminary study aims to compare the performance of radiomics-based classification for bounding box and traditional segmentation methods. The analysis was performed on axillary lymph node metastases (ALNMs) from breast cancer on computed tomography (CT), as part of a study aimed at developing a radiomics-based approach for the detection of ALNMs from breast cancer.

Methods: Patients identified as part of a dedicated database were included in this study (n = 75). Inclusion criteria included stage IIIA-IIIC breast cancer, an ultrasound-guided biopsy-proven ALNM, and an available contrast-enhanced CT chest scan. For each patient, a biopsy-proven ALNM and contralateral negative control node underwent manual 3D segmentation using 3D Slicer software. Radiomic feature extraction was performed using the PyRadiomics 3D Slicer extension. A total of 111 features were extracted. Oriented bounding boxes for each manual segmentation were generated using the Python scripting capabilities of 3D Slicer. The same 111 radiomic features were extracted for the bounding box segmentations, and the results were compared to that of the manual segmentations. To evaluate intra- and inter-observer variability, a subset of 15 patients were re-segmented twice, once by the original primary observer, and again by a secondary observer.

Results: Several radiomic features demonstrated excellent area under the receiver operating characteristic curve values (AUC > 0.9) and statistical significance ($p < 0.01$) when differentiating between malignant and benign lymph nodes for both manual (23 features) and bounding box segmentations (21 features). However, intra- and inter-observer variability was reduced for the bounding box segmentations, as shown by increased intraclass and interclass correlation coefficients (maximum = 1). The table below features three sample features and the associated comparison results. Large Dependence High Gray Level Emphasis (LDHGLE) is a measure of image homogeneity; Least Axis Length is the smallest axis length of the ROI; Run Entropy is a measure of randomness in stripes (runs) of colour within the image.

	Manual Segmentations			**Bounding Box Segmentations**		
Feature	**AUC**	**Intraclass CC**	**Interclass CC**	**AUC**	**Intraclass CC**	**Interclass CC**
LDHGLE	0.946	0.64	0.83	0.935	0.81	0.82
Least Axis Length	0.943	0.74	0.97	0.910	0.98	0.98
Run Entropy	0.905	0.73	0.88	0.947	0.98	0.97

Conclusions: Oriented bounding box segmentations have the potential to be substantially equivalent to traditional manual segmentations for the purposes of differentiating between malignant and benign axillary lymph nodes on CT using radiomic features. This segmentation method is less susceptible to the intra- and inter-observer variability that affects many other auto-segmentation and classification studies.

(1) Wong J, Fong A, McVicar N et al. Comparing deep learning-based auto-segmentation of organs at risk and clinical target volumes to expert inter-observer variability in radiotherapy planning. *Radiotherapy and Oncology*. 2020;144:152-158. doi:10.1016/j.radonc.2019.10.019

Using deep learning to predict tumour mutational burden in lung squamous cell carcinoma from 20 centres

Salma Dammak[1], Matthew Cecchini[2,3], Aaron D. Ward[1,4]

Western University: [1]School of Biomedical Engineering, [2]Department of Pathology and Laboratory Medicine, [3]Schulich School of Medicine & Dentistry, [4]Department of Medical Biophysics

Introduction: Immunotherapy is a novel anti-cancer treatment that has shown significant improvements in outcomes for lung cancer patients. However, this treatment has the potential for substantial side effects in a minority of patients, and many lung cancer patients do not benefit from it. High programmed-death ligand-1 (PD-L1) expression in tumour cells is currently the main biomarker used to identify those who might benefit, but it is not very accurate, with a 45% response rate[1]. Tumour mutational burden (TMB) is a biomarker that improves prediction accuracy substantially, with lung cancers having more than 10 mutations/megabase in addition to high PD-L1 having a 75% response rate[1]. However, TMB is obtained through extensive genetic sequencing, which is too resource-intensive to be implemented in the clinic in addition to PD-L1 testing. It is more expensive, slower, and requires tissue with high tumour cellularity, which is not always available as part of routine care.

Several studies in digital histopathology have shown that genetic information can be successfully estimated from standard-of-care hematoxylin and eosin (H&E)-stained slides containing the cancer tissue obtained during resections or biopsies[2]. H&E slides are routinely obtained in the clinic, and using scanned slides as the only input to a system predicting TMB would enable more straightforward translation to clinical practice. Based on this, we hypothesize that TMB can be predicted in lung squamous cell carcinoma from histopathology slides of tissue from surgically resected specimens prepared and scanned at different centres.

Methods: To test this hypothesis, we obtained digitized histopathology slides of resected lung squamous cell tumours from 30 patients and 20 centres through the National Cancer Institute's Genomic Data Commons (TCGA). The slides were all formalin–fixed, paraffin-embedded, and stained using H&E. As these slides are much larger than typical available graphics processing unit (GPU) memory sizes, we split them into non-overlapping tiles of 224 × 224 pixels (56 μm x 56 μm) and only used the tiles that overlapped with two different regions of interest (ROI) contoured by a pathologist: all cancer, and viable cancer only. We obtained the ground truth label of whether TMB was more than 10 mutations/megabase from the TCGA. To predict this label, we performed transfer learning using three different networks that have been shown to perform well in transfer learning scenarios: NASNetLarge, XceptionNet, and VGG-16[2]. We used 75% of the data for training, and the rest for validation, ensuring that no centre appeared in both training and validation. We trained each network, varying the image ROIs, learning rate (0.01, 0.1, 1), batch size (1,10,100), and augmentation (on, off), then measured the per-patient area under the receiver operator characteristic curve (AUC), error rate, false negative rate (FNR) and false positive rate (FPR) on the validation set.

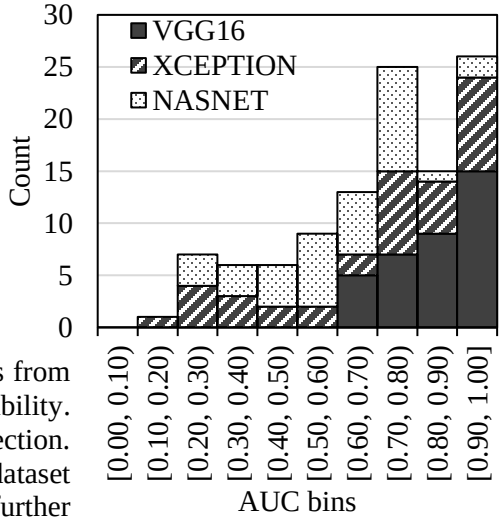

Results: The different ROI, network and parameter values yielded 108 trained models. The histogram of the per-patient AUCs on the validation set for these models is shown the figure (median = 0.70, inter-quartile range = 0.30). This performance indicates that the visual patterns for high TMB vs low TMB are likely to have high separability in visual feature space, as the prediction problem was solvable using several different pathways, with AUC values skewed towards 1.

Conclusions: This preliminary study (n = 30) shows that predicting TMB from digitized standard-of-care H&E slides of squamous cell carcinoma tumour resection tissue is possible on slides from centres on which a model has not trained previously, despite stain variability. These findings are promising for pursuing further work in this direction. However, a single model must be selected and tested on an unseen dataset and more data are needed to build a more robust system. With further development and external validation, such a system can act as an alternative to traditional genetic sequencing for patients with lung squamous cell carcinoma which will help physicians determine whether patients should be given immunotherapy with more accuracy. This will more effectively give access to immunotherapy drugs to those who need them and help spare others the toxicities associated with immunotherapy.

1. Carbone, D. P. *et al*. *New England Journal of Medicine* **376**, 2415–2426 (2017).
2. Srinidhi, C. L., Ciga, O. & Martel, A. L.. *Medical Image Analysis* **67**, 101813 (2021).

Prostate segmentation and reconstruction for integration in an ultrasound-guided prostate biopsy system for nationwide implementation in Senegal

Colton Barr[1], Leah Groves[1], Tamas Ungi[1], Babacar Diao[2], Ron Kikinis[3], Parvin Mousavi[1], Gabor Fichtinger[1]
[1]School of Computing, Queen's University, Kingston, Canada, [2]Cheikh Anta Diop University, Dakar, Senegal [3]Harvard Brigham and Women's Hospital, Boston, USA

INTRODUCTION: Transrectal ultrasound (TRUS)-guided biopsy is universally used in the diagnosis of prostate cancer. It involves systematic sampling of the prostate gland within its anatomical zones. One of the major technical difficulties of the procedure is that the zonal anatomy is not directly visible in TRUS. This issue is particularly daunting in Senegal, where prostate cancer is detected in only 30% of the biopsies despite 60% of patients having advanced disease [2], clearly indicating failures of proper sampling of the anatomical zones. Optical navigation (Fig. 1) was proposed to improve on TRUS-guided prostate biopsy, to be implemented in a national program in Senegal [3]. A key function of this system is deformable registration of a 3D anatomical atlas to the prostate capsule, enabling real-time overlay of the zonal anatomy on 2D TRUS (Fig.2) [4], which demands automated segmentation and reconstruction of the prostate gland; the objectives of the work reported in this paper.

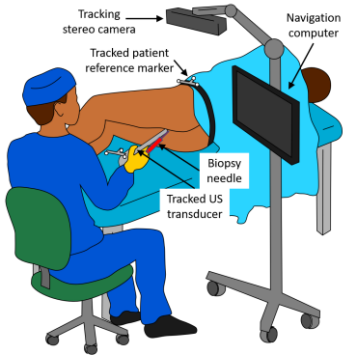

Fig. 1: Layout of optically navigated TRUS-guided prostate biopsy

METHODS: The proposed auto-segmentation module uses a 2D U-Net that has been previously trained on a large dataset of 2D TRUS slices [5]. The module is integrated in the previously mentioned prostate biopsy system being developed for nationwide deployment in Senegal [3]. We have tested the prostate auto-segmentation and reconstruction module on 3D TRUS volumes acquired from prostate biopsy patients. These volumes were captured by Orlando *et al.* using mechanical tracking and each include a ground truth segmentation of the prostate capsule [5]. For a given 3D TRUS volume, a series of 2D resliced images were generated at 15° intervals around a rotational axis to simulate the images expected in a real TRUS-guided biopsy situation. The resulting 2D ultrasound images were passed into the U-Net to generate prostate contours, which were then combined to compute a 3D surface representation of the prostate gland. To evaluate the real-time segmentation, we registered the reconstructed surface representation with the mechanically tracked ground truth model and computed the surface-to-surface distances. In 3D TRUS data from three patients, we recorded the framerate rate of segmentation and accuracy of prostate reconstruction.

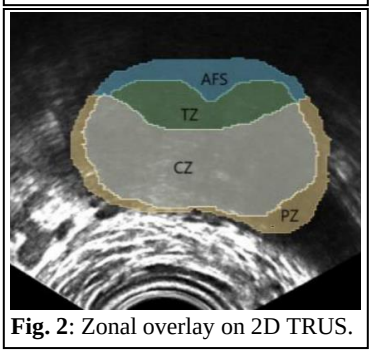

Fig. 2: Zonal overlay on 2D TRUS.

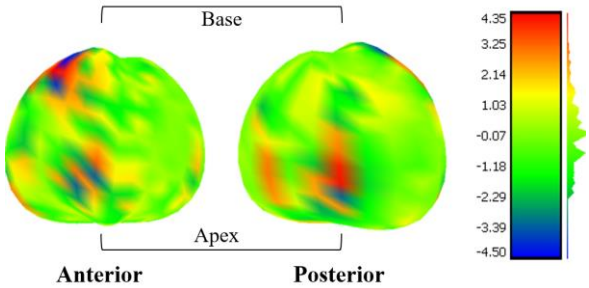

Fig. 3: Heat map for a 3D TRUS volume showing the surface distance between reconstructed and ground truth prostates.

RESULTS: The mean surface-to-surface distance between the reconstructed and the ground truth prostate models were 1.11mm ± 1.42mm, 1.53mm ± 1.75mm, and 2.49mm ± 2.72mm, respectively. Fig. 3 shows surface distances for a volume, projected onto the reference prostate volume as a heat map, where the scale shown on the right is in mm. The mean segmentation time for a 2D TRUS slice was 0.5 seconds, yielding a framerate of 2 frames per second.

CONCLUSIONS: Both the frame rate and accuracy are qualitatively sufficient for proceeding to patient trials. It must be noted that labeling of the zonal anatomy does not need to be highly accurate to aim a biopsy needle in the approximate middle of a zone and acquire a 20mm long tissue core. This allows considerable leeway in the required surface accuracy of the generated model of the prostate gland. This preliminary investigation indicates a level of reconstruction accuracy that is likely sufficient to align an anatomical atlas to better orient clinicians during a biopsy procedure. The next phase of the work will focus on working with clinicians to define protocols for re-slicing the pre-acquired 3D TRUS volumes as is being done in actual TRUS-guided prostate biopsy procedures.

REFERENCES: [1] C Presti (2007) Rev. Urol. 9(3). **[2]** L Niang, et al. (2011) ISRN Oncol. **[3]** G Fichtinger, et al. (2021) J. Img.7. **[4]** C Wu, et al. (2021) SPIE Med. Img. 11598. **[5]** N Orlando, et al. (2020) Med. Phys. 47(6).

Machine Learning Determination of the Relationship Between the µCT-Derived Visceral Adipose Tissue and Whole-Body Adipose Tissue in Rats

Joseph U. Umoh,[1] E. Turley,[2] T. Appleton,[3] M. Drangova,[1,4] and D.W. Holdsworth[1,4]
Ontario Pre-Clinical Imaging Consortium
[1]Preclinical Imaging Research Centre, Robarts Research Institute, [2]Depts. of Medicine and Biochemistry, [3]Depts of Physiology and Pharmacology, [4]Depts. of Medical Biophysics and Surgery, Western University, London, ON, Canada

Introduction: Accumulation of excess visceral adipose tissue is linked to different risks of obesity or diabetes. Research interest in adipose tissue is growing not only because investigators are seeking solutions to the problem of obesity but also because of the realization that adipose tissue in human is a potential reservoir of adult stem cells[1], which could be used in tissue repair and engineering. Clinical research in adipose tissue often begins in rat and mouse models. In this study, the mass of visceral adipose tissue (VAT) in the abdominal cavity and whole-body adipose tissue (WAT) were measured from micro-CT scans in rats. While WAT measurement is easily automated, VAT quantification requires manual segmentation and is time consuming. Our objectives are to apply Machine Learning to model the relationship between VAT and WAT in both male and female rats and to evaluate the performance of the model. The study will enable VAT to be easily estimated from WAT in these animals.

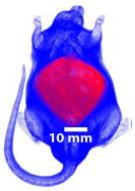

Fig.1: Micro-CT image-rendering of a whole-body (face-up) rat, showing the mass of visceral adipose tissue (red) and the rest of the adipose tissue (blue).

Methods: Ninety rats (50 male and 40 female) were used in this study. The animals were imaged using a *GE Locus Ultra* micro-CT scanner with the following scan protocol and reconstruction parameters: x-ray tube voltage 80 kV, tube current 55 mA, 1000 projections, exposure time 16 s, and 154 um 3D image voxels. Using the 3D micro-CT images, the abdominal cavity was manually segmented out for each animal. Lower (-380 HU) and upper (-30 HU) image threshold values of the adipose tissue were determined from the histogram plots of the whole animal image values. A software utility was written to compute volume and mass of the adipose tissue. Volume was calculated using pixel values between the two thresholds; and mass was calculated by multiplying the volume by a pre-determined density (0.90 g cm^{-3}) for adipose tissue.[2] Using the image of the whole-body, the program computed the mass of WAT for each animal. Similarly, using the segmented image of the abdominal cavity, the program computed the mass of VAT (Fig. 1). The relationship between WAT and VAT was determined using *Scikit-Learn* and *Pandas* Machine Learning libraries. Pandas was used to read the data into *Dataframe.* From *sklearn.model_selection, train_test_split* was imported to train, test and split the data into 80% training set, 10% validation set, and 10% test set. *LinearRegression* was used to model the data and validate the model performance.

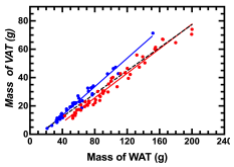

Fig. 2: Plot of the mass of the whole-body adipose tissue (WAT) against the mass of the visceral adipose tissue (VAT) showing the datapoints and the linear regression lines for male (red) and female (blue) rats

Results: Linear regression analysis between VAT (V) and WAT (W) showed (Fig. 2) that the two quantities could be expressed as $V = a\,W - b$. The slope $a_m = 0.44$ and $a_f = 0.49$ (subscript *m* for male and *f* for female rats). The intercept $b_m = 9.78$ and $b_f = 6.23$. The coefficient of determination R^2, which shows the model performance were $R^2_m = 0.95$ and $R^2_f = 0.98$. The mean-square error (estimated from the test dataset) were 15.50 and 1.68 for male and female model respectively. The large error in the male dataset might be due to the variability in the large values of the computed male visceral adipose tissue. The accuracy (estimated from the validated dataset) were 0.92 and 0.97 for male and female model respectively.

Conclusions: The Machine Learning implementation of the *Scikit LinearRegression* has been applied to determine a linear relation between the whole-body adipose tissue and visceral adipose tissue in male and female rats. The regression model parameters have been found to be different in male and female rats. The model performs highly with R^2 greater than 95% in both male and female rats, and can confidently be used to predict visceral adipose tissue using whole-body adipose tissue.

References: [1] Zuk *et al.* Mol. Biology of the Cell 2002; 13: 4279-4295.

[2] Wong, D., Umoh, JU, Holdsworth, DW *et al. J. Alzheimers,* 2021; 81(1): 375-388.

Pitch Session 2: Neuro Imaging I

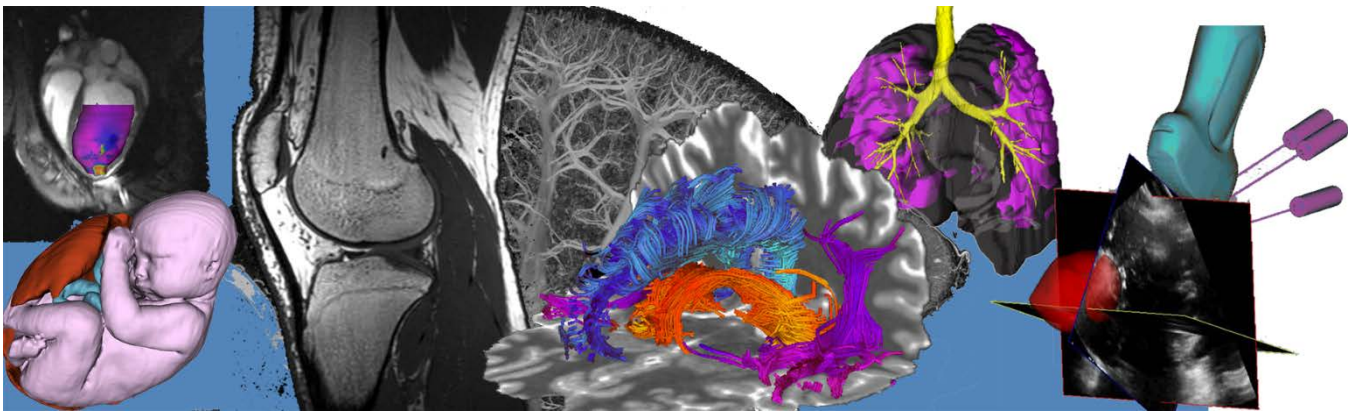

Updated radiosynthesis of three high demand positron-emitting radiotracers for neuroimaging

Stephen Oyeniran[a,b], Michael S. Kovacs[a-c], and Justin W. Hicks[a,b]
[a]Lawson Health Research Institute Cyclotron and Radiochemistry Facility. [b]Medical Biophysics and [c]Medical Imaging, Western University.

Introduction: To fully exploit the unrivaled sensitivity of positron emission tomography (PET) for in vivo molecular imaging, an effective radiotracer is required. PET radiotracer production must adhere to drug manufacturing regulations, but with added constraints of decaying product, high radiation, and minute mass. Through automation, radiochemists can develop predictable and traceable methods to remotely handle the one chance, last minute manufacturing of radiotracers. Optimizing these processes is a priority for our group to lower production costs and improve reliability. To illustrate this, we have selected three highly sought-after fluorine-18 (^{18}F; $t_{1/2}$ = 109.8 min) radiotracers for optimization. Automated synthesis of all three (Table 1) have been reported elsewhere[1,2,3] with improvement reported herein.

Method: A GE TRACERLab F_{XN} (*adjacent figure*) was used for automated radiolabeling (i.e. reagent additions, heating, HPLC purification, and reformulation). Prior to starting syntheses, the reaction vessel (*black column in figure center*) was dried by rinsing with acetone, then heating to 80°C under vacuum and helium flow for 15 min. A GE PETtrace 800 produced aqueous [^{18}F]fluoride via the ^{18}O(p,n)^{18}F nuclear reaction. The F_{XN} hoppers (*top row of red caps*) were charged with appropriate reagents, then the [^{18}F]fluoride solution was transferred to the reaction vessel. Automated radiolabeling proceeded according to our in-house F_{XN} program. Quality control testing of isolated radiotracers ensured their purity and identity.

Results: Our facility will typically see 10 – 15% of radiolabelings fail, leading to canceled imaging studies. The extra drying sequence prior to radiosynthesis improved this reliability, albeit with a small sample size for SynVesT-1 and flurpiridaz (Table 1). Radiochemical yields, purities, and specific activities matched those reported with a drastic improvement to the specific activity of flurpiridaz (200 MBq/μg reported[3]). Lastly, the synthesis time was reduced for each product by 10 min on average.

Table 1.	**[^{18}F]FEOBV[1]**	**[^{18}F]SynVesT-1[2]**	**[^{18}F]Flurpiridaz[3]**
Protein Target	Vesicular acetylcholine transporter (VAChT)	Synaptic vesicle glycoprotein 2A (SV2A)	Mitochondrial complex 1
Application	Cholinergic tone in neurodegeneration	Synaptic density in epilepsy, stroke, neurodegeneration	Blood flow, metabolism, oxidative stress
Yield[a]	37.2 ± 5.0%	15.2 ± 3.9%	9.1 ± 1.7%
Synthesis time[b]	59 ± 4	71 ± 5	55 ± 6
Purity	99.3 ± 0.7%	99.6 ± 0.5%	98.3 ± 0.8%
Specific Activity[c]	1663 ± 347	811 ± 255	4229 ± 2114
Success Rate	40/42 (96%)	11/11 (100%)	5/5 (100%)

[a] decay corrected to end of synthesis, [b] minutes, [c] MBq/μg.

Conclusion: Radiofluorination reactions are highly susceptible to water contamination. At the radiotracer level, a 1 μL water drop is 1000-fold excess compared to the 5 – 9 ng of [^{18}F]fluoride. Adding an acetone rinsing and drying step just before radiosynthesis appeared to improve reliability with >96% success (2/57 failed). We have demonstrated our automated processes to be equivalent or superior to reported methods. The next step is to translate these radiotracer productions for clinical use. With current quantities produced, there will be enough radiotracer to supply multiple concurrent clinical studies within London or to ship to regional collaborators (Windsor to Toronto).

Reference: 1) Mulholland *Synapse* 1998, 30, 263. 2) Li *ACS Chem Neurosci* 2019, 10, 1544. 3) Purohit *J Med Chem* 2008, 51, 2654.

Beta amyloid deposition and cognitive decline in Parkinson's disease: a study of the PPMI cohort

Alexander S. Mihaescu[1,2,3], Mikaeel Valli[1,2,3], Carme Uribe[1,2], María Díez-Cirarda[1,2,4], Mario Masellis[3,5,6], Ariel Graff-Guerrero[1,3], Antonio P. Strafella[1,2,3,7]

1. Centre for Addiction and Mental Health, Toronto, Canada **2.** Krembil Research Institute, Toronto, Canada **3.** Institute of Medical Science, Toronto, Canada **4.** Biocruces Bizkaia Health Research Institute, Barakaldo, Spain. **5.** Sunnybrook Research Institute, Toronto, Canada **6.** Hurvitz Brain Sciences Program, Toronto, Canada. **7.** Toronto Western Hospital, Toronto, Canada

Disclosures: All authors declare none.

Introduction: The accumulation of beta amyloid (Aβ) in the brain has a complex and poorly understood impact on the progression of Parkinson's disease (PD) pathology and much controversy remains regarding its role, specifically in cognitive decline symptoms. Some studies have found increased Aβ burden is associated with worsening cognitive impairment in PD, especially in cases where dementia occurs, while other studies failed to replicate this finding. Our study aims to elucidate this complex relationship by examining the effect regional Aβ burden in specific brain regions has on cognitive ability in PD, rather than measuring whole-brain amyloidpathy.

Methods: Our study used data from the Parkinson's Progression Marker Initiative (PPMI) cohort. We included 25 idiopathic PD patients and 30 healthy controls who all underwent [^{18}F]Florbetaben PET scans which measured the density of Aβ in 20 cortical regions of interest. We then followed this cohort post-scan for two years, measuring their Montreal Cognitive Assessment (MoCA) scores, a simple 30-point test for cognitive ability. This data was analyzed using IBM SPSS version 27 software with both 'top-down' stepwise linear regression modelling and 'bottom-up' hierarchical cluster analysis.

Fig.1a) Parkinson's disease 1b) Healthy Controls

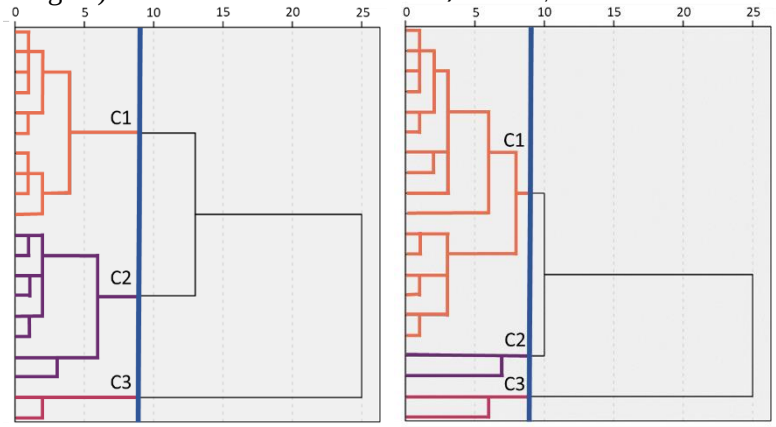

Table 1) Parkinson's disease

Regions of interest	R^2	Adjusted R^2	Standard Error of the estimate	*p*-value
MoCA at scan				
Left occipital cortex	0.183	0.148	2.269	0.033
MoCA one year after scan				
Left gyrus rectus, right parietal cortex, left anterior cingulum	0.564	0.495	2.298	0.001
MoCA two years after scan				
Right parietal cortex, right gyrus rectus	0.387	0.319	2.889	0.012

Figure 1. Dendrograms of the three cluster solution (cut-off shown with the blue line) for the hierarchical cluster analysis of the [^{18}F]Florbetaben standardized uptake value ratios for the 20 regions of interest.
Table 1. Stepwise linear regression models at each of the three years for the PD patient group.

Results: We found that Aβ clusters differently in PD patients compared to healthy controls. In the PD group, increased Aβ burden in cluster 2 was associated with worse cognitive ability, compared to deposition in clusters 1 or 3. We also found the strongest linear regression model one-year post-scan for the PD group, with an adjusted R^2 of 0.495 explaining 49.5% of the MoCA variance, encompassing the left gyrus rectus, the left anterior cingulate cortex, and the right parietal cortex.

Conclusions: Taken together, these results suggest regional Aβ deposition alone has a moderate effect on predicting future cognitive decline in PD patients. The patchwork effect of Aβ deposition on cognitive ability may be part of what separates cognitive impairment from cognitive sparing in PD. Thus, we suggest it would be more useful to measure Aβ burden in specific brain regions rather than using a whole-brain global Aβ composite scores and use this information as a tool for determining which PD patients are most at risk for future cognitive decline.

Evaluation of spinal cord registration for diffusion tensor imaging with pathological spine data

Vignesh Sivan[1], Michael Hardisty,[2,3] Alex Wong[1], Stewart McLachlin[1]

1. University of Waterloo, 2. Sunnybrook Research Institute, 3. University of Toronto

Introduction

Fiber tractography from magnetic resonance (MR) diffusion tensor imaging (DTI) enables the visualization of white matter fibers bundles using streamline tractography. In the presence of pathology, these bundles can be distorted and disconnected, which can reveal clinically significant information about the nature of the underlying pathology. A critical step in DTI analysis is the registration of the diffusion MR images to the structural space, allowing for localization of the tractography streamlines in the structural space. In this work we evaluate a previously developed atlas-based registration approach against a spinal cord MR dataset with pathology [McLachlin 2021]. We also empirically evaluate modifications to improve spinal cord registration.

Methodology

Dataset: The dataset consists of retrospectively collected spine MR-DWI from 12 subjects. The image volumes were obtained from a variety of MR scanners with varying scanning parameters informed by clinical indication.

Approach: The steps of the aforementioned registration pipeline are briefly described. Given a structural MR image volume (T1, T2) and a diffusion weighted image (DWI) volume, the pipeline first segments the spinal cord region in both the structural and diffusion volumes. The segmentations are then used to inform a deformable registration. The pipeline employs atlas-based registration, by computing the transform from diffusion→template→structural space. The atlas, as well as the segmentation and registration steps, make use of the Spinal Cord Toolbox (SCT) software package. We test various approaches to make registration more robust. We specifically investigate 1) cropping input volumes to the relevant spinal cord regions, 2) direct registration of diffusion and structural and 3) downsampling of inputs. These heuristics can be found in SCT's forums.

Results

Table 1 shows the mean fiducial error (MFE) for each subject in our dataset with the initial atlas-based registration (before) and the modified registration (after). It can be seen that the registration diverges in studies 1-6 (underlined). In these studies, it was found that the presence of pathology causes the registration to diverge from the target. The direct registration of diffusion and structural MRI and the downsampling of inputs was found to yield improved registration results. This result can be explained by the fact that direct registration of structural and diffusion MRI from the same subject can take advantage of the mutual information shared between the moving and target images. This information is not present in the spinal cord template. It was also found that cropping input volumes to the spinal cord region had no effect. While the registration was improved, registration artifacts persist, as can be seen in Figure 1.

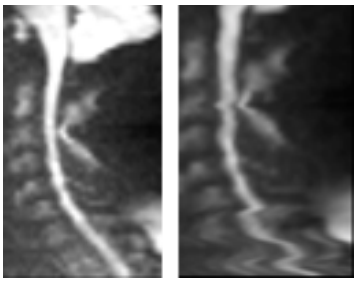

Figure 1: DMRI scan before (l) and after (r) registration with the modified pipeline.

Table 1: Mean fiducial registration error (MFE) before and after registration modifications.

MFE (mm)	1	2	3	4	5	6	7	8	9	10	11	12
Before	136.1	68.4	46.4	163.3	164.2	152.2	1.8	1.1	2.1	2	2.1	1.5
After	26.4	2.2	6.4	4.1	1.3	144.4	1.8	0.7	1.8	1.6	1.8	1.4

Conclusion

In this work we investigated registration for spine DTI against a clinical dataset with pathology and found that the previous approach is not robust to pathology. Registration preprocessing demonstrated improvements in the pipeline performance, but registration accuracy remained suboptimal. Future work will focus on improving registration for clinical evaluation and eventual translation of this work.

References: McLachlin et al. 2021 Neur Rad 63(3):373-380

Acknowledgements: Funding provided by the Centre for Bioengineering and Biotechnology, MITACS/Synaptive Medical, and NSERC Create.

Chemical Exchange Saturation Transfer (CEST) pH-Weighted MRI Optimization in the Spinal Cord

Alicia Cronin*,[1,2] Patrick Liebig,[3] Sarah Detombe,[4] Neil Duggal[1,4] and Robert Bartha[1,2]

[1]Department of Medical Biophysics; [2]Centre for Functional and Metabolic Mapping, Robarts Research Institute, The University of Western Ontario; [3]Siemens Healthcare GmbH, Erlangen Germany; and [4]Department of Clinical Neurological Sciences, University Hospital, London Health Sciences Centre

Introduction: Degenerative cervical myelopathy (DCM) is a degenerative disease of the spine that causes compression and neurological dysfunction.[1] Ischemia and hypoxia in the cord could impact recovery after decompression surgery but direct in-vivo evidence of such changes has been limited in humans. Chemical Exchange Saturation Transfer (CEST) is an MRI contrast derived from the transfer of magnetic saturation from selectively excited endogenous exchangeable protons to bulk water protons, causing a signal reduction in the observed water signal. Since exchange rate is pH-dependent, pH-weighted CEST contrast can be generated in the brain using a ratiometric method called amine/amide concentration-independent detection (AACID).[2] Previous studies have also found that changes in tissue pH may cause nuclear Overhauser enhancement (NOE) effects to be lower in tumours, but this relationship requires further study.[3] Both AACID and NOE CEST contrast in the spinal cord could provide a means to examine pH change, which is caused by hypoxia. The objective of this study was to optimize AACID and NOE CEST contrast in the human spinal cord, creating sufficient sensitivity and resolution to detect pH heterogeneity in DCM patients.

Methods: A prototype CEST sequence was used on a 3T Siemens MAGNETOM Prisma Fit MRI scanner, incorporating a single slice 2D gradient echo (GRE) readout. Pearson's correlation coefficient (r) was used to assess the linear dependence of optimized AACID and NOE effects on pH in egg white phantoms. In-vivo optimization was performed in the human brain (N = 3) to maximize both CEST contrasts. Saturation was performed using 30 Gaussian-shaped radiofrequency (RF) pulses (total saturation time = 3 s), applied at 132 offsets from -6.5 to 6.5 ppm. The RF pulse amplitude was varied to find the optimal B_1 value for AACID and NOE contrasts. Other relevant parameters include: TR/TE = 10.0/4.4 ms, voxel size = 2 mm x 2 mm, slice thickness = 5 mm, total scan time = 9.50 min. In the spinal cord, the respiratory cycle was monitored using the respiratory bellows to calculate respiration volume per unit time (RVT), defined by dividing the range of the cycle magnitude by the mean respiration time between peaks.[4] Non-saturated scans were interleaved throughout acquisition to account for variation of intensity due to the global effect of respiration. The RVT was scaled by the global effect to regress signal variation due to breathing out of the data.[4] One healthy subject was recruited to evaluate the respiratory corrected CEST effect in the spinal cord.

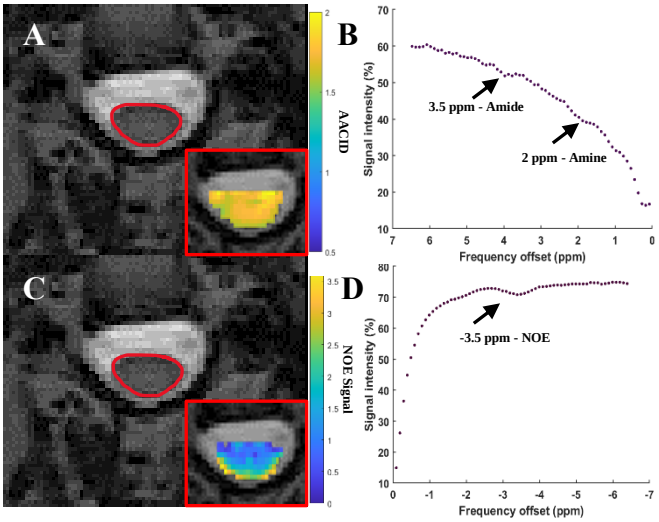

Figure 1: A: Axial T_2-weighted anatomical of healthy spinal cord with AACID map displayed on inset. **B:** CEST spectrum from a single pixel in the cord showing AACID effect. **C:** Axial of spinal cord with NOE map displayed on inset. **D:** CEST spectrum from a single pixel showing the NOE effect.

Results: In the egg white phantoms, both AACID ($p = 0.01$, $r = -0.94$) and NOE ($p = 0.04$, $r = 0.90$) CEST effects were found to be linearly dependent on pH. In the brain, the optimal amide CEST effect was achieved at a B_1 of 1.5 µT and the greatest NOE effect was observed at 0.5 µT. In the spinal cord, the average magnitude of the measured amide and NOE CEST effect was 1.34% and 2.55%, respectively (Figure 1).

Conclusion: The optimized CEST sequence produced high-quality images. Since both AACID and NOE values are pH-dependent, either could be used to investigate pH changes due to hypoxia at 3T. NOE contrast was more prominent in the spinal cord, shown by the higher magnitude, suggesting that it could be advantageous for the creation of pH-weighted contrast. In the future, further optimization in the spinal cord is needed to improve the fidelity of the measurements. To determine the reproducibility of the pH-weighted measurements, the two contrasts will be compared in the spinal cord of healthy subjects and DCM patients to examine pH heterogeneity at the compression site.

References: [1] Toledano, M. & Bartleson, JD. Neurol. Clin. 2013; [2] McVicar, N. et al. J. Cereb. Blood Flow & Metab. 2014; [3] Jones, CK. et al. NeuroImage. 2013; [4] By, S. et al. Magn. Reson. Med. 2018

Piloting a Methodology to Assess Functional Connectivity in Healthy Brain Aging

Abhijot S. Sidhu,[1-3] Kauê T N Duarte,[2-4] Cheryl R. McCreary,[2,3] and Richard Frayne[1-4]

[1]Biomedical Engineering Graduate Program, University of Calgary; [2]Departments of Radiology and Clinical Neurosciences, University of Calgary; Hotchkiss Brain Institute, University of Calgary; [3]Seaman Family MR Research Centre, Foothills Medical Centre; and [4]Calgary Image Processing and Analysis Centre, Foothills Medical Centre

Introduction: Resting-state functional magnetic resonance imaging (rs-fMRI) is used to investigate cortical gray matter connectivity. Correlations between regional changes in the blood oxygen level-dependent signal over time may indicate a functional connection between regions – functional connectivity (FC). The strength of functional connections in the brain are not static and change over the healthy adult lifespan, typically following a curvilinear trajectory with FC increasing from young-adulthood to middle-age, plateauing, then declining with more advanced age [1]. Previous rs-fMRI studies have predominately investigated FC changes using whole-brain (global) or singular network-level approaches with cross-sectional data that is sparsely distributed over the adult lifespan; longitudinal rs-fMRI studies that examine FC changes are scarce. The objective of this work was to pilot a methodology intended to observe the complex temporal trajectory of FC with age by investigating regional, network, and global changes across the healthy adult lifespan using age-balanced longitudinal data.

Materials and Methods: Data from the Calgary Normative Study (CNS), an ongoing, single-centre, longitudinal study collecting quantitative neuroimaging data across the adult lifespan, was used [2]. CNS data include T1-weighted structural MRI and rs-fMRI data acquired on a 3T MR scanner from ~450 presumed healthy participants aged 18 – 90+ y with an approximately equal distribution by sex and by age decade. MR data (single scan/subject) from an arbitrary sample of four participants representing young, middle, and advanced age (34 y F, 43 y M, 61 y F, and 75 y F) were used to pilot the rs-fMRI pipeline. The pipeline is composed of five steps: 1) *Structural Processing*: Freesurfer was used to parcellate the cortical regions of T1-weighted images into 400 regions based on the Yeo-Schaefer seven-network atlas [3] [4]; 2) *Functional Preprocessing*: Raw rs-fMRI data (200 volumes/subject) were processed using FSL including skull-stripping, motion and interleaved slice timing correction, and temporal high-pass filtering (> 0.01 Hz) [5]; 3) *Independent Component Analysis*: Classification and removal of noise components using FSL (ICA + FIX) [6]; 4) *Denoising*: Additional physiological and motion nuisance variables were regressed out and high motion volumes were omitted from further analyses. 5) *Generation of the FC Adjacency Matrix*: Based on the cortical parcellation, time-series were extracted from co-registered and cleaned rs-fMRI data. Pearson correlation coefficients were used to assess similarity (connectivity) between extracted time-series and plotted in a 400×400 adjacency matrix. Absolute values for appropriate Pearson correlation coefficients were averaged to assess global and network-level FC.

Results: The preliminary results from our pipeline for global FC displayed a complex temporal trajectory and network level changes in FC with age varied amongst the seven resting state networks (Figure 1).

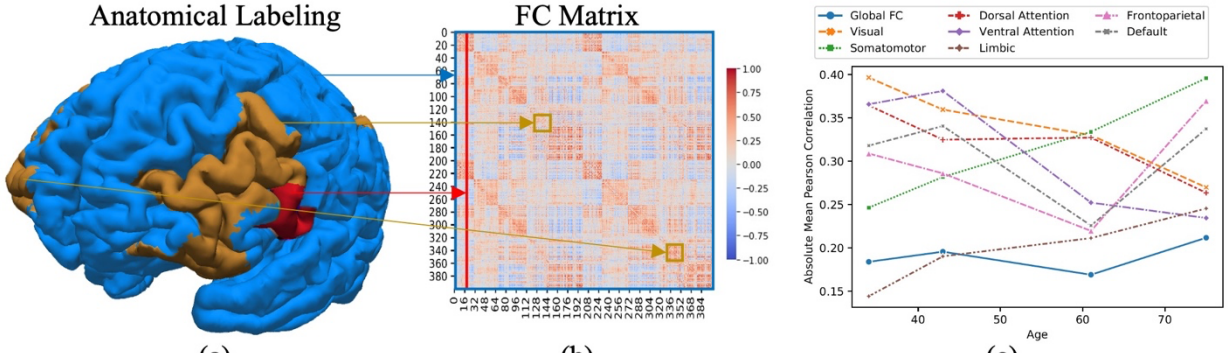

Figure 1: (a) The Yeo-Schaefer seven-network atlas was used to parcellate gray matter into 400 cortical regions (not shown). Cortical regions can be examined individually (red) to conduct a region-specific FC analysis; grouped together (yellow) for a network-level FC analysis; Grouping all 400 cortical regions together (blue) enables a global FC analysis. (b) FC adjacency matrices were constructed by extracting the correlation coefficients between cortical regions (labelled 0-399) over time. From the FC adjacency matrices, changes in FC can be examined on varying scales: global (large blue box), network (smaller yellow box), and single cortical region (vertical red line). (c) As a proof of concept, FC measured using the Pearson correlation coefficient (absolute mean) globally and across seven resting-state networks is plotted against age using the sample dataset.

Conclusion: By examining changes in FC at varying scales (regional, network, and global), our pipeline has the potential to elucidate a more comprehensive understanding of FC changes across the healthy adult lifespan.

References: [1] Edde M. *J Neurosci Res* 2020. [2] McCreary CR *BMJ Open* 2021. [3] Fischl B. *Neuroimage* 2012. [4] Schaefer A. *Cereb Cortex* 2018. [5] Jenkinson M. *Neuroimage* 2012. [6] Salimi G. *Neuroimage* 2014.

Investigating the Effect of Thrombotic Thrombocytopenic Purpura on Neurocognitive Function

Fahad Hannan[1], Michael Jurkiewicz[2], Jonathan D Thiessen[1, 3], Susan HS Huang[1, 4, 5]

[1]Department of Medical Biophysics, Western University, London, ON, Canada [2]Department of Medical Imaging, Western University, [3]Lawson Health Research Institute, [4]Department of Medicine, Schulich School of Medicine & Dentistry, [5]The Lilibeth Caberto Kidney Clinical Research Unit

Introduction: Thrombotic Thrombocytopenic Purpura (TTP) is a rare blood disease with a high untreated mortality rate (>90%) [1]. It is characterized by a reduced activity in the protein ADAMTS13 (A disintegrin-like and metalloprotease with thrombospondin type 1 repeats 13) which regulates the buildup of platelets and clots in the blood. The reduced activity of ADAMTS13 results in spontaneous clotting throughout the microvasculature, disrupting oxygen flow to vital organs [2]. Symptoms include fever, renal failure, low platelet count, and destruction of red blood cells. These can be treated using plasma exchange with or without immunosuppressants. However, patients in remission have high risk of cognitive impairment and depression despite the disease being in a state of remission. This project aims to gain a better understanding of the structural changes caused by TTP on the brain using multi-component driven equilibrium single pulse observation of T1 and T2 (mcDESPOT) MRI to generate T1, T2, and myelin water fraction (MWF) maps [3]. We hypothesize we will see increases in T1, T2 relaxation times, and decreases in MWF in brain regions corresponding to neurocognitive function.
Methods: A 3T MRI scanner (Biograph mMR, Siemens Healthineers, Erlangen, Germany) with a 32-channel head-only receive coil was used to acquire MRI in 23 TTP patients 30 days after remission. Standard-of-care (SOC) MRI, including T1-weighted, T2-weighted, diffusion-weighted, and susceptibility-weighted images, were read by a radiologist to assess gross pathology and determine regions of interest (ROI). mcDESPOT was acquired to determine T1 relaxation, T2 relaxation, and MWF maps with Quantitative Imaging Tools [4]. Additional testing included a cognitive assessment from Cambridge Brain Sciences (CBS) [5] and a Montgomery-Åsberg Depression Rating Scale (MADRS) [6] depression test to correlate with MRI findings.
Results: Significant T1 and T2 relaxation times are found in the cingulate cortex and frontal lobe (Figure 1). Results from depression scores indicate 91% of patients reporting concentration difficulties and 68% reporting lassitude which correlate with the frontal lobe and cingulate cortex respectively. Results from the cognitive assessment show a decreased score in short-term memory games which correlates with the frontal lobe. No significant increases/decreases were found in MWF maps. 91% of patients showed findings from SOC MRI. Findings include white matter hyperintensities, atrophy, infarcts, and aneurysms.
Conclusions: Correlations between the cognitive assessment, depression scores, and MRI findings may be attributed to neuroinflammation and subsequent white matter degradation in the cingulate cortex and frontal lobe. Patients will be scanned again at 6 months and 12 months to investigate the progression of white matter damage. Further testing with additional quantitative techniques such as Diffusion Tensor Imaging (DTI) and Arterial Spin Labeling (ASL) will help to better understand the extent of white matter damage caused by TTP.

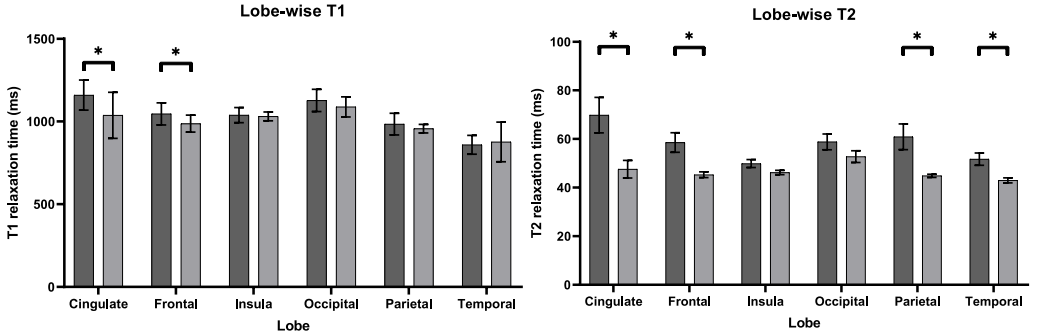

Figure 1: T1 and T2 relaxation times between patients and controls for each lobe. Significant differences ($P < 0.05$) are indicated by *.

References: [1] Levandovsky et al., J. Hematol. Oncol. (2008) **1.1**:23. **[2]** Lancellotti et al., Mediterr. J. Hematol. (2013) **5.1**. **[3]** Deoni el al., Magn Reson Med (2008) **60.6**:1372. **[4]** Wood., J. Open Source Softw. (2018) **3.26**:656. URL https://github.com/spinicist/QUIT. **[5]** Hampshire et al., Neuron (2012) **76.6**:1225. **[6]** Montgomery et al., Br J Psychiatry. (1979) **134.4**:382.

First-in-human PET imaging of [^{18}F]SDM-4MP3: A detour on the synaptic imaging journey, and cautionary note

Kimberly L. Desmond[1,2], Anton Lindberg[1], Armando Garcia[1], Junchao Tong[1,2], Elena Dobrota[1], Kelly Smart[1,3], Carme Uribe[1], Jeffrey H. Meyer[1,2], Sylvain Houle[1,2], Antonio Strafella[1,4], Henry Huang[3], and Neil Vasdev[1,2]

1. Brain Health Imaging Centre, CAMH, Toronto, Ontario. 2. Department of Psychiatry, University of Toronto, Ontario. 3. PET Center, Department of Radiology and Biomedical Imaging, Yale University, New Haven, Connecticut, USA. 4. Krembil Brain Institute, University Health Network, University of Toronto, Ontario.

Introduction: [^{18}F]SynVesT-1 (previously known as [^{18}F]SDM-8 or [^{18}F]MNI-1126) is a promising PET radiopharmaceutical that binds to the synaptic vesicle protein 2A (SV2A), serving as a new biomarker of synaptic density with clinical research applications in psychiatry and neurodegeneration. The initial goal of this study was to concurrently conduct PET imaging studies with our collaborators at the Yale University PET Center [1]. The inadvertent first-in-human PET imaging study of [^{18}F]SDM-4MP3 was discovered during our investigation of anomalous imaging data.

Methods: [^{18}F]SynVesT-1 radiolabeling precursor was obtained from ABX GmbH (Radeberg, Germany) and radiotracer was synthesized according to the published method [2]. Two healthy female participants (70 and 44 y) were scanned on a GE Discovery MI PET-CT. The radiotracer (~200 MBq) was delivered via bolus injection, and emission data was acquired for 120 min. Low dose CT images were used for attenuation correction, and dynamic image reconstruction used filtered back-projection. Arterial blood was collected via automated blood sampler (ABSS), and manual samples for plasma metabolite correction. PET images were registered to the subject's corresponding T_1-weighted anatomical MRI and time-activity curves (TACs) measured for regions of interest (ROIs) according to the Hammers-N30R83 atlas using the PNeuro module in Pmod 4.2. Regional volume of distribution (V_T) was estimated using 1-TCM, and non-displaceable binding potential (BP_{ND}) was calculated using centrum semiovale as the reference region. Rodent PET was acquired on a Mediso nanoScan PET/CT. LC-MS was performed on a Advion Expression L MS and NMR spectroscopy was acquired at the CSICOMP NMR Facility, University of Toronto.

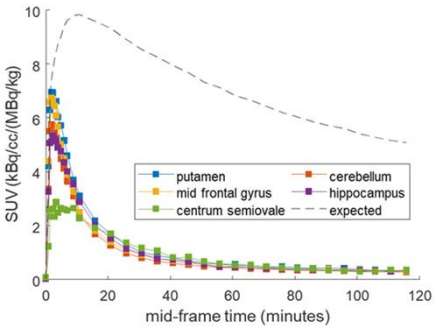

(Fig. 1) Time activity curves in selected regions of interest. Dotted line shows estimated expected TAC for middle frontal gyrus.

Results: Despite high initial brain penetration with an SUV of ~7, the TACs for both participants (Partic. 1 in **Fig.1**) showed rapid clearance with little evidence of specific binding, in sharp contrast to that expected based on human PET data from Yale and despite typical-appearing arterial input function. Concordantly, metrics of tissue binding, V_T and BP_{ND} (data not shown), were at least a factor of 10 lower than expected. Rodent PET revealed a similar difference between images obtained with tracers produced from Yale and ABX precursors. An investigation comparing the precursor from ABX with that synthesized at Yale and purchased from PharmaSynth AS (Tartu, Estonia) showed that although all three precursors had the same molecular mass of 449.3 (M+H) with characteristic isotope pattern associated with tin and fluorine in LC-MS, their ^{1}H- and ^{13}C-NMR spectra were different. The ABX precursor differed from that of Yale/PharmaSynth in the aromatic region (notably between 155-140 ppm on ^{13}C-NMR and 8.5-8.3 and 7.2-7.0 ppm on ^{1}H-NMR (**Fig.2**)). As the peaks at 8.5-8.3 in the ^{1}H-NMR spectra can be assigned to the *ortho*-protons on the pyridinyl ring, it could be determined that the substituents on the pyridinyl ring must be different. This was confirmed by ^{1}H-^{1}H COSY NMR and the ABX precursor was determined to have a *4*-methyl-pyridinyl instead of the desired *3*-methyl-pyridinyl moiety. Recent *in vitro* binding assays revealed a loss of affinity to SV2A for the 4-methyl analogue [3] and corroborated our *in vivo* imaging results.

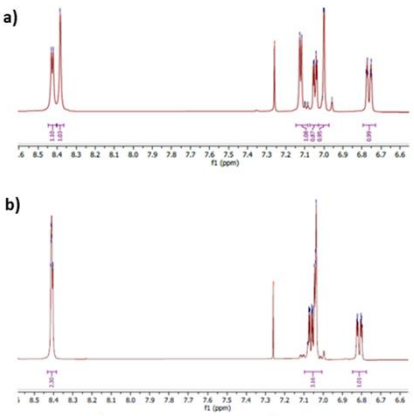

(Fig. 2) a) ^{1}H-NMR spectrum of ABX precursor **b)** ^{1}H-NMR spectrum of Pharmasynth precursor.

Conclusions: Anomalous imaging results from an [^{18}F]SynVesT-1 PET study spurred the discovery of incorrectly synthesized precursor material from a commercial vendor, resulting in an inadvertent first-in-human trial of the 4-methyl-pyridinyl analogue, [^{18}F]SDM-4MP3. **References:** [1] Naganawa M, et al. *J Nucl Med* **2021**;62(4):561-7. [2] Li S, et al. *ACS Chem Neurosci* **2018**;10(3):1544-54. [3] Pracitto R, et al. *ACS Omega* **2021**;6(42):27676-83.

Investigating the Effect of Tissue Heterogeneity on NIRS Monitoring of Cerebral Oxidative Metabolism

Natalie Li[1] and Mamadou Diop[1,2,3]

[1]*School of Biomedical Engineering, Western University, London, Ontario*
[2]*Department of Medical Biophysics, Western University, London, Ontario*
[3]*Imaging Program, Lawson Health Research Institute, London, Ontario*

Introduction: Near-infrared spectroscopy (NIRS) is a non-invasive technique that can monitor cerebral oxidative metabolism by measuring changes in the redox state of cytochrome-c-oxidase (ΔoxCCO)[1,2]. The most common approaches are based on continuous-wave NIRS (cwNIRS) technology[1,2], which relies on reference values to estimate the wavelength dependence of the optical pathlength that is required to determine ΔoxCCO. However, the optical pathlength changes with anatomy (i.e., tissue heterogeneity; inter-subject variability) and even tissue blood oxygenation (intra-subject variability)[3,4]. We hypothesize that ΔoxCCO estimated using reference values of optical pathlength will be inaccurate because tissue heterogeneity is ignored. This hypothesis was tested with *in-silico* data obtained from both a homogeneous and a 3-layer infant head model.

Methods: cwNIRS simulations were conducted using an open-source finite-element method toolbox for modeling near-infrared light transport in tissue (NIRFAST). The *in-silico* experiments were conducted on both a homogeneous (brain tissue) and 3-layer (extracerebral layer; ECL, cerebral spinal fluid; CSF, and brain tissue) infant head model to test the effect of tissue heterogeneity on the accuracy of the estimation of ΔoxCCO. Brain oxCCO concentration was varied linearly while ECL and CSF properties were held constant. The true optical pathlength was obtained from the times-of-flight of the photons and the estimated pathlength was determined using published reference values[3]. Data from each model was analyzed using the modified Beer-Lambert law with both an accurate and estimated optical pathlength. Recovered versus inputted ΔoxCCO was plotted for each model/analysis combination and linear regression was performed to obtain a line of best fit. The slopes and intercepts of each were compared to the ground truth (slope=1, intercept=0).

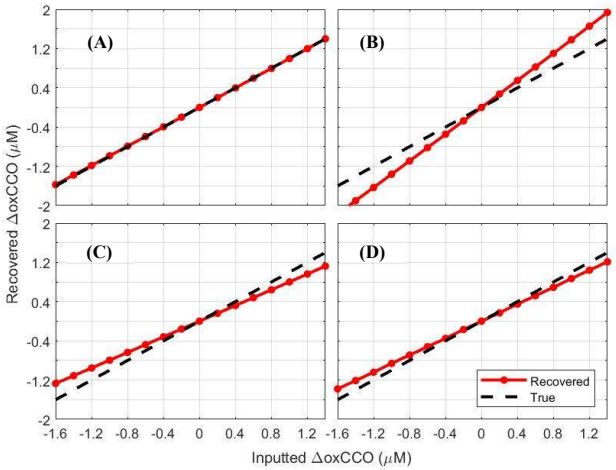

Figure 1 Recovered ΔoxCCO from a homogeneous model using **(A)** an accurate pathlength and **(B)** an estimated pathlength. Recovered ΔoxCCO from a 3-layer model using **(C)** an accurate pathlength and **(D)** an estimated pathlength.

Results: For the homogeneous model, the slope and intercept with the accurate pathlength method were identical to the ground truth (slope=0.99, intercept=0). When the pathlength was estimated, ΔoxCCO was overestimated (slope=1.37, intercept=0.01). For the 3-layer model, the slope and intercept with the accurate pathlength method were 0.80 and 0, respectively, indicating underestimation of ΔoxCCO. When the pathlength was estimated, ΔoxCCO was underestimated (slope=0.86, intercept=0) but with error less than when the pathlength was accurate.

Conclusions: Consistent with our hypothesis, accurate recovery of ΔoxCCO in the homogeneous model was achieved using an accurate but not an estimated pathlength. This suggests that reference values of optical pathlength may not be generalizable to all patients due to inter-subject differences in tissue heterogeneity. In the 3-layer model, brain ΔoxCCO was underestimated when the superficial layers remained constant despite the use of an accurate pathlength, which is consistent with previous findings of the limited depth sensitivity of cwNIRS[5,6]. However, when the estimated pathlength was used to recover ΔoxCCO from the 3-layer model, the result was closer to the ground truth than when the accurate pathlength was used. This is likely a fortuitous result caused by overestimation introduced when estimating the pathlength counteracting the underestimation due to the limited depth-sensitivity of cwNIRS. The results suggest that current cwNIRS methods have limited accuracy and methods like time-resolved NIRS that can measure the patient-specific optical pathlength and have better depth-sensitivity should be used for more accurate estimation of ΔoxCCO.

References: [1] Rajaram A., et al. *Brain Sciences* **10**(7), 1–13 (2020), [2] Bale G., et al. *Biomedical Optics Express* **5**(10), 3450 (2014), [3] Essenpreis M., et al. *Applied Optics* **32**(4), 418–425 (1993), [4] Matcher S.J.et al. *Physics in Medicine and Biology* **39**(1), 177– 196 (1994), [5] Milej D., et al. *Neurophotonics* **7**(04), 045002 (2020), [6] Strangman G. E., et al. *NeuroImage* **85**, 136–149 (2014)

Oral Session 3:
MR Imaging I

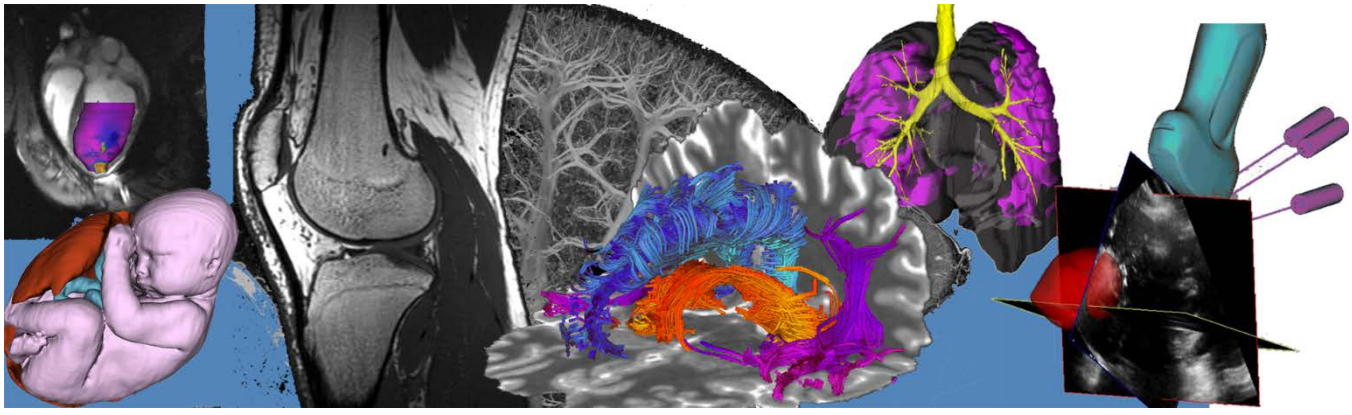

Correcting for gradient non-linearity in concurrent field monitored MRI data

Paul I. Dubovan[1,2], Kyle M. Gilbert[1,2], Corey A. Baron[1,2]
[1] *Department of Medical Biophysics, Western University, London, Ontario, Canada*
[2] *Centre for Functional and Metabolic Mapping, Western University, London, Ontario, Canada*

Introduction: MR image quality suffers from effects such as eddy currents, heating, and mechanical vibrations, which induce spatial and temporally varying field perturbations during MR acquisitions. Field monitoring (FM) is a strategy that aims to improve image quality using NMR probes to measure and account for field perturbations up to higher order spatial dependence.[1] FM can be performed sequentially, where field probes characterize field dynamics in an empty scanner, and the measurements are used to correct images from a subsequent identical acquisition.[2] Alternatively, concurrent FM is performed simultaneous to patient scanning, and has the advantage of tracking patient-induced perturbations, while also improving user workflow.[3] Concurrent FM is made possible by integrating field probes into a radiofrequency (RF) coil. Due to coil design and spatial constraints, the field probes may require placement in the non-linear region of the gradient coil. This can have adverse effects on probe data integrity, as probe signals decay quicker. As a result, higher order field perturbations become erroneous, and images reconstructed with unreliable FM data degrade image quality. In this work, we propose a three-part correction algorithm that aims to improve the integrity of concurrent FM data. Correction A accounts for the true gradient field distribution inside the scanner in image reconstructions.[4] Secondly, instead of computing all the field dynamics simultaneously, each order is solved one at a time (Correction B). Lastly, probes are inversely weighted based on spatial position in subsequent calculations of the field perturbations (Correction C).

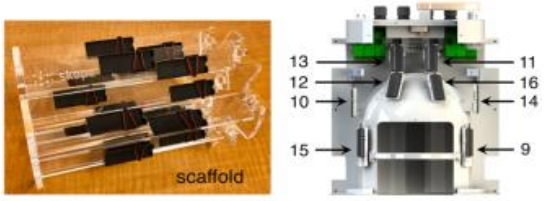

FIG. 1. Field probe scaffold (left) and CAD drawing of RF head coil with integrated field probes (right).

Methods: A healthy patient was scanned on a 7T head-only MRI (Siemens). Diffusion-weighted spiral trajectory acquisitions were acquired using the following imaging parameters: (FOV: 192 x 192 mm^2, in-plane resolution: 1.5 x 1.5 mm^2, slice thickness: 3 mm, number of slices: 10, TE/TR: 33/2,500 ms, b = 0 s/mm^2 acquisitions: 1, diffusion directions: 6, b-value: 1000 s/mm^2). FM was performed simultaneously using 16 transmit/receive ^{19}F commercial field probes (Skope) that are integrated into a 32-channel RF head coil (Fig. 1).[5] Image reconstruction was performed in MATLAB using in-house developed software. Images were reconstructed using full third-order FM data with and without correction, as well as using subsets of the three steps of the correction to determine each component's efficacy. For comparison to sequential FM correction, images were corrected using FM data from an identical acquisition acquired when field probes were on the manufacturer's scaffold (Fig. 1).

Results: In Figure 2, full correction of a diffusion weighted image (DWI) showed significant improvement in image quality, while the correction improvement for the scaffold case was incremental. Figure 3 illustrates for a DWI the effectiveness of each correction technique, with the addition of the first two correction steps noticeably reducing the error relative to the "gold standard" fully corrected image. Correction B showed substantial improvement in image quality, suggesting that it provides the largest benefit of the three strategies employed.

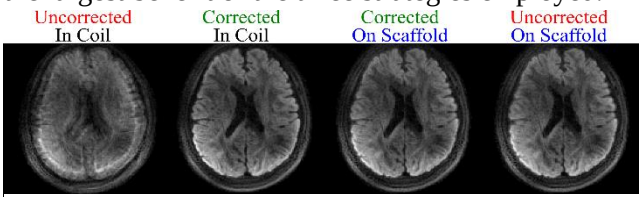

FIG. 2. Comparison between corrected and uncorrected images for a single diffusion direction DWI.

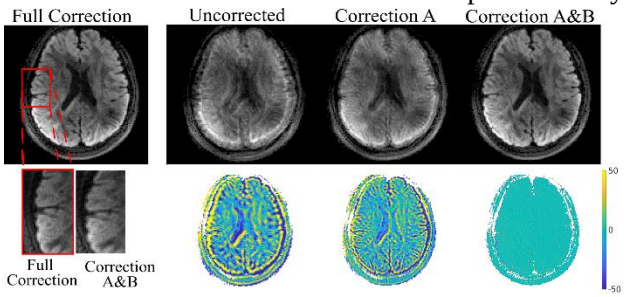

FIG. 3. Comparison between fully corrected DWI, uncorrected, and different correction subsets. Relative difference images calculated with respect to the fully corrected image are shown.

Conclusions: A correction algorithm that successfully improves the reliability of higher order concurrent FM data is presented and validated. This motivates the production of reproducible images for anatomical and functional imaging, as shown by high quality spiral DWI in this work.

References: [1]Wilm BJ et al. *MRM* (2011). [2]Dietrich BE et al. *MRM* (2016). [3]Kennedy M et al. *MRM* (2018). [4]Janke A et al. *MRM* (2004). [5]Gilbert KM et al. *bioRxiv* (2021).

Tissue Equivalent Agarose/$MnCl_2$ MRI Relaxation Phantom for MR Studies

Daniel Sare[1,2], Eunyoung Cho[1,2], Logi Vidarsson[3], Greg Stanisz[4], Dafna Sussman[1,2,5]

[1]Departments of Biomedical Physics and of Biomedical Engineering, Ryerson University, Toronto; [2]Institute for Biomedical Engineering, Science and Technology (iBEST) at Ryerson University and St. Michael's Hospital, Toronto; [3]Diagnostic Imaging, The Hospital for Sick Children, Toronto; [4]Department of Medical Biophysics, University of Toronto & Sunnybrook Research Institute, Toronto; [5]Department of Obstetrics and Gynecology, Faculty of Medicine, University of Toronto, Toronto, Canada.

Introduction: Magnetic resonance imaging (MRI) phantoms play a crucial role in medical imaging research and development, including testing and calibrating hardware performance, pulse sequence development, reconstruction techniques, and motion correction methods. The objectives of this work are to develop a solid 3T MRI phantom material capable of simulating a wide range of human tissues having accurate (1) anatomical structure, and (2) 3T MRI relaxation values (T_1 and T_2). This novel MRI phantom design will act as a valuable tool in advancing our understanding of biomedical systems.

Methods: Objective (1) was addressed using a carrageenan hydrogel due to its ability to retain geometrical shape and volume when cast from a 3D mould. To achieve objective (2), tissue-mimicking materials were synthesized using carrageenan (gelatinizer), $MnCl_2$ (T_1 modifier), agarose (T_2 modifier), NaCl (conductivity modifier), and glutaraldehyde (antiseptic). Relaxation curves were built using samples with varying concentrations of $MnCl_2$ and agarose. T_1 and T_2 values were measured using a 3T MRI utilizing an inversion recovery sequence and a multi-spin echo sequence, respectively. From the measurements, the relaxivities (r_1 and r_2) of $MnCl_2$ (M) and agarose (A) were calculated. The following equation was used to describe the relaxation values of the material given the concentrations and the material's inherent relaxation rate without any modifiers present ($1/T_1^0$ or $1/T_2^0$).

$$\frac{1}{T_i} = \frac{1}{T_i^0} + r_{iM}[M] + r_{iA}[A]\,;\; i = 1, 2$$

Results: An MRI phantom material was synthesized to simulate a wide range of tissues with relaxation times between 240-2165ms for T_1 and 23-499ms for T_2. Utilizing the equation, the appropriate concentrations of relaxation modifiers were selected to create tissue-equivalent relaxation phantoms and the total range of this material's possible relaxation values are visualized in Figure 1.

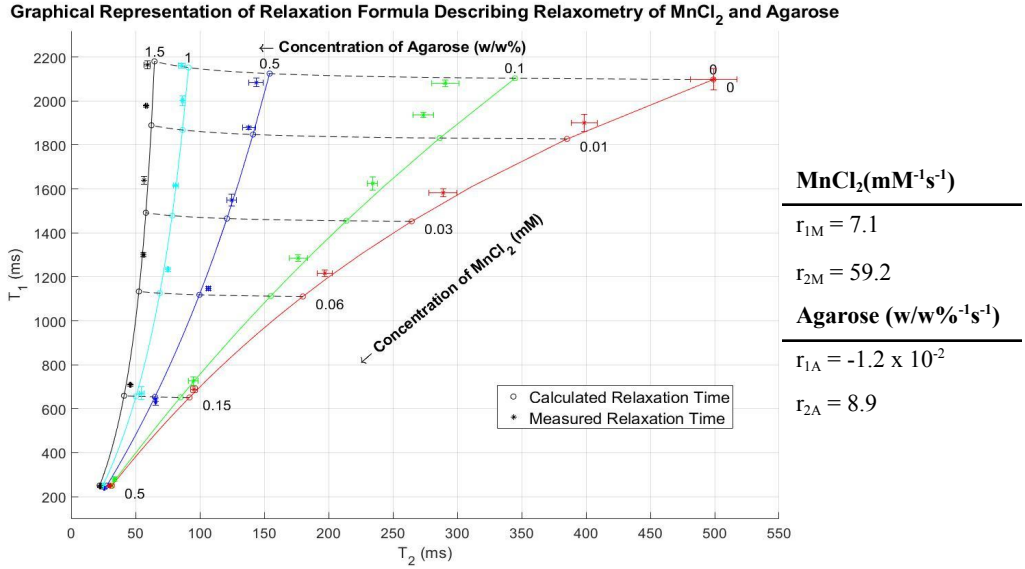

Figure 1 - Graphical representation of the T_1 and T_2 relaxation values for the varying concentrations of agarose and $MnCl_2$. Each line represents the relaxation times of each concentration of agarose over varying concentrations of $MnCl_2$ between 0-0.5 mM. The concentrations of agarose vary between 0-1.5 w/w %. The X and Y error bars represent the standard deviation of the T_2 and T_1 relaxation times, respectively.

Conclusion: This phantom material exhibited relaxation times that simulated a broad range of tissue types previously not possible. This novel material will provide the unique ability to efficiently produce solid MRI phantoms with desired relaxation times within the given range, furthering MRI research.

Real-time rigid motion detection for brain MRI using spherical navigators

Miriam Hewlett,[1,2] Junmin Liu,[1] and Maria Drangova[1,2]
[1]Robarts Research Institute, The University of Western Ontario, Canada
[2]Department of Medical Biophysics, The University of Western Ontario, Canada

Introduction: As many as 1 in 5 subjects require a repeat MRI due to motion artifacts [1], yet motion correction techniques are still not widely used for brain imaging. Prospective approaches which correct for motion during the scan itself can prevent the irrecoverable loss of information which may occur using retrospective correction techniques; however, they require real-time motion information throughout the scan. Spherical navigators (SNAVs) can be used to measure motion in 6 degrees of freedom with a relatively short acquisition time (10's of ms), making them especially suited for real-time motion measurement. Previous work in our lab has shown promise using spherical navigators for retrospective motion correction [2]. The objective of this work was to implement SNAVs for the real-time measurement of intra-scan motion required for prospective correction.

Methods: A 3D fast low angle shot (FLASH) sequence was modified to include SNAV acquisitions for real-time motion measurement. SNAVs were acquired in two shots (each under 15 ms), following which motion parameters were calculated online (Image Calculation Environment, Siemens Healthcare, Germany) and returned to the sequence as real-time feedback. All data was acquired on a 3T MRI scanner (Siemens Prisma, Siemens Healthcare, Germany) using a 32-channel head coil and the following imaging parameters: matrix size = 256x256x80, FOV = 24x24x16 cm, TE/TR = 1.04/20 ms, flip angle = 25 degrees. In order to assess the impact of the navigators on image quality with no motion present, a pineapple was scanned with and without SNAV acquisition. SNAV motion estimation was validated by manually displacing (n = 4) the pineapple between scans and assessing the quality of image registration (quantified using mutual information, MI, paired t-test) using SNAV data. Human scans with intra-scan motion were also performed for qualitative assessment.

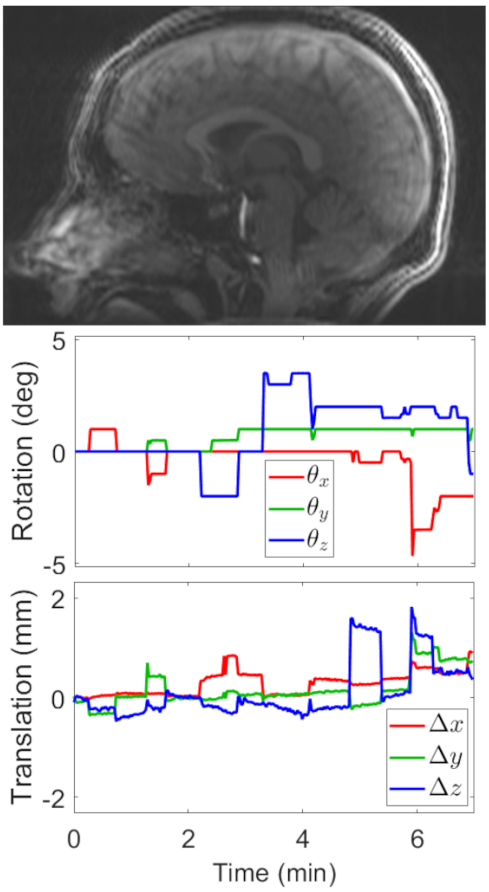

Figure 1. Sagittal view of the brain in the case of stepwise motion throughout the scan, along with SNAV motion estimates.

Results: Images acquired with and without SNAVs showed no apparent effect on image contrast. Registration of pineapple scans using SNAV motion estimates following inter-scan motion showed good alignment and led to a significant increase in MI ($p = 0.0019$). SNAV estimates of intra-scan motion appeared as expected, e.g., rotation in the sagittal plane in the case of head nodding. Shown in Figure 1 are the measured motion trace and corresponding image acquired during stepwise motion. Real-time motion estimates were returned to the sequence with a delay of 38 ms.

Conclusion: This work is the first implementation of SNAVs for real-time intra-scan motion measurement. SNAVs can measure motion more rapidly than image-based navigator approaches, which often require 100's of ms for acquisition and motion estimation [3], and without the need for external hardware as with optical approaches [4]. Future work will use these intra-scan motion estimates for prospective correction. Improved motion correction methods would reduce the need for repeat scans, which increase costs and can delay diagnosis in a clinical setting.

References: [1] Andre JB et al. *J Am Coll Radiol*. 2015;**12**:689-695. [2] Johnson PM et al. *Magn Res Imaging*. 2016;**34**:1274-1282. [3] Simegn GL, et al. *Magn Res Med*. 2019;**81**:2600-2613. [4] Frost R, et al. *Magn Res Med*. 2019;**82**:126-144.

MRSI Processing and Simulation using the FID Appliance (FID-A) Toolkit

Brenden Kadota[1], Bernhard Strasser[2], Wendy Oakden[1], Jamie Near[1]
[1]Physical Studies Research Platform, Sunnybrook Research Institute, Toronto, Canada
[2]High Field MR Centre, Medical University of Vienna, Vienna, Austria

Introduction: Magnetic resonance spectroscopic imaging (MRSI) non-invasively maps the spatial distribution of metabolite concentrations in vivo. Our lab previously developed the open-source FID appliance (FID-A), for processing and simulation of magnetic resonance spectroscopy data[1]. However, the original version of FID-A was not capable of processing MRSI data. Here, we present an extension to the MATLAB-based FID-A toolkit to enable processing, simulation and visualization of MRSI data.

Methods: *Processing toolbox*: Once loaded, a sequence of operations can be used to process and reconstruct MRSI data. The processing toolbox also allows for non-cartesian reconstruction using the discrete ”slow” fourier transform and density compensation using Voronoi diagrams. Finally, the toolbox contains a visualization feature to overlay either an MRSI spectral grid or an LCModel output metabolite concentration map onto an anatomical MRI using spm12’s MRI image function (**Figure 1**). MRSI data for **Figure 1** were acquired on a Siemens 3T scanner (MAGNETOM Prisma) using a semi-LASER MRSI sequence. *Simulation toolbox*: Users can create custom k-space trajectories or use pre-existing trajectories provided. An in-silico phantom is provided based on the MNI152 atlas with 2 mm isotropic resolution which has been segmented into grey matter, white matter, cerebrospinal fluid, and skull. The segmented areas contain metabolite and lipid concentrations based on previous published work. B0 or B1 inhomogeneity can readily be incorporated into the simulations to assess their effects on MRSI image quality.

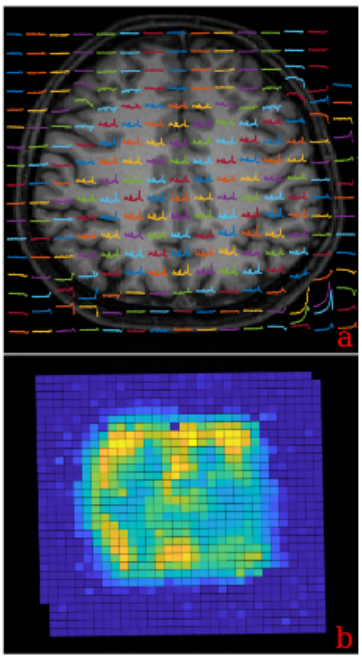

Figure 1: a) Plotting spectrum over MRI. b) Plotting LCModel concentration heatmap over MRI.

Results: **Figure 2** shows the results of two simulations using the MNI 152 MRSI phantom with conventional phase encoded MRSI: a low-resolution simulation with an 8x8 matrix and a high resolution simulation with a 32x32 matrix. Both signals were zero-filled to a resolution of 64x64. The magnitude of each voxel’s spectra was integrated from -1 ppm to 1 ppm to illustrate lipid contamination (**Figure 2b,c**), and from 2.2-2.4 ppm to illustrate the glutamate distribution (**Figure 2e,f**). These simulations illustrate that increased scan resolution effectively mitigates lipid contamination throughout the brain, due to improvements in point spread function.

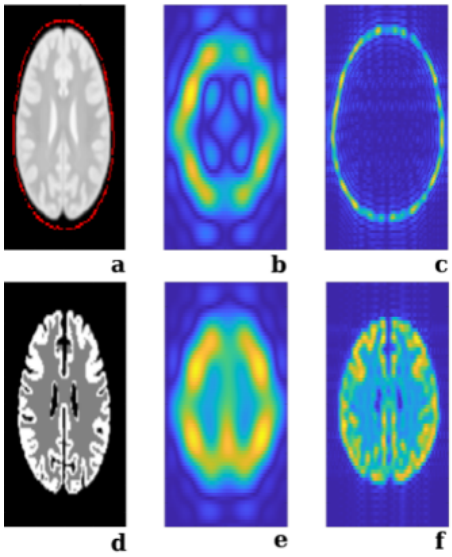

Figure 2: Ground truth maps of lipids (a) and Glutamate (d). Simulated low (b,d) and high (c,f) resolution MRSI maps of lipids (top row) and Glutamate (bottom row)

Conclusions: The MRSI extension of FID-A can process MRSI data and simulate experiments on an *in-silico* brain phantom. The processing toolbox can correct for B0 inhomogeneities, combine coils, and perform density compensation for non-cartesian trajectories. The simulation toolbox can quickly simulate MRSI trajectories and identify lipid contamination. Future work will increase the functionality to import different vendor’s data and export to different fitting tools.

References: Simpson R, Devenyi GA, Jezzard P, Hennessy TJ, Near J. Advanced processing and simulation of MRS data using the FID appliance (FID-A)-An open source, MATLAB-based toolkit. Magn Reson Med. 2017 Jan;77(1):23-33

Oral Session 4:

Device, Hardware and System Development

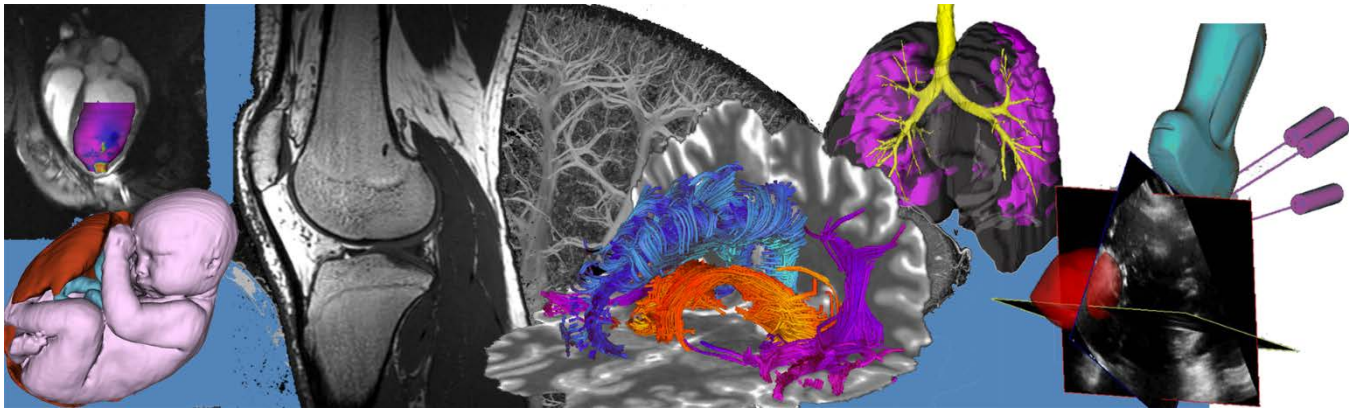

Cautery state classification for navigated iKnife surgery

Joshua Ehrlich, Mark Asselin, Amoon Jamzad, Martin Kaufmann, Jessica Rodgers, John Rudan, Tamas Ungi, Parvin Mousavi, and Gabor Fichtinger.
Queen's University, Kingston ON, Canada

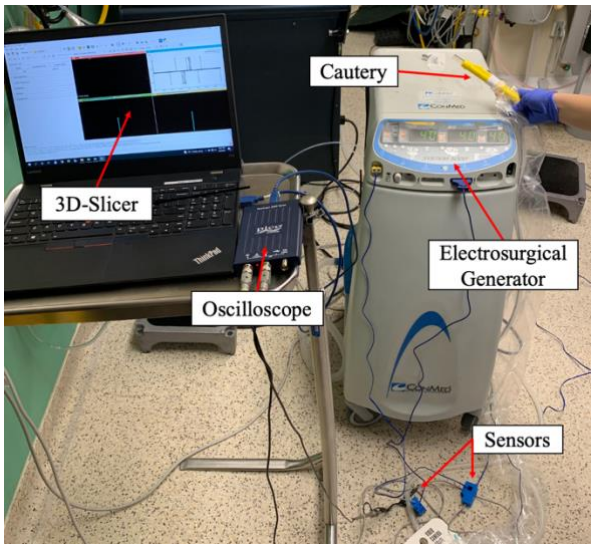

Figure 1: Experimental set-up

Introduction: Mass spectrometry (iKnife) has been proposed to improve the localization of cancerous tissue during breast cancer surgery by recognizing the tissue being cut in real-time [1]. Navigated iKnife combines the iKnife with a spatial tracking system, like Electromagnetic (EM) tracking. Tissue recognition combined with tumour position tracking will enable the surgeon to navigate back to locations where residual tumour needs to be excised [2]. To accurately synchronize tissue classification and position tracking, we must automatically detect a surgical incision's start and end time. This requires us to identify the electrosurgical cautery mode ("cut" or "coagulate") and when the cautery is activated and touches a patient, referred to as the "energy event." The energy event is difficult to isolate because surgeons often activate the cautery in the air prior to making an incision. Therefore, to locate surgical incisions, we must identify five different cautery *states*: powered on-not activated, activated cut-air, activated cut-tissue, activated coagulate-air, and activated coagulate-tissue. This study presents a method for detecting the cautery state during lumpectomies, a step toward fully navigated intra-operative mass spectrometry tissue analysis.

Methods: In our previous work by Asselin et al. (2019) and Carter et al. (2016), we attached SCT-013 current sensors to the live and return electrodes of the cautery. A PicoScope P2204A USB oscilloscope (Pico Technologies, St Neots, UK) digitized the electrical signal and streamed voltage data into 3D Slicer via the Plus toolkit (Figure 1) [3, 4]. We performed in-vitro testing on grocery-grade meat and in-vivo testing during breast surgery. In-vitro, we recorded voltages during each of the cautery states for 5 seconds to create a total of 250 samples. In-vivo, we collected data by recording the cautery states during the operation. Both in-vitro and in-vivo data were converted into an array to be used as model training data. To cluster our data, we applied a Fourier Transform (FFT) to each cautery state and extracted the maximal amplitude and corresponding frequency (Figure 2). A Support Vector Machine (SVM) was trained on the mean, minimum, maximum, and standard deviation of the voltage signals. We trained the model with a linear kernel, degree of 3, C of 5, scaled gamma, and used a train-test split of 80/20, respectively, to evaluate our model. We tested the system by displaying cautery state classifications in real-time while making incisions. Integration of voltage data, training the SVM, and classifying the cautery state intra-operatively in real-time was built within an open-source 3D-Slicer module (Github repository: https://github.com/SlicerIGT.git).

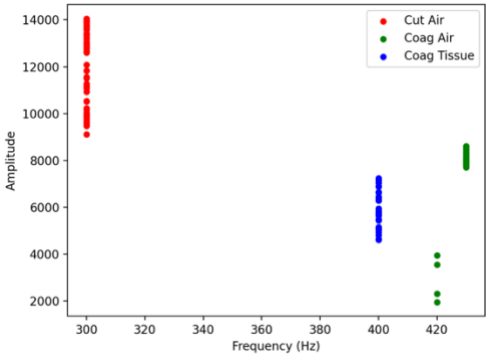

Figure 2: Clusters from in-vivo FFT analysis

Results: The system accurately classifies cautery states, with an SVM classification accuracy of 97%. The iKnife and oscilloscope classification is completed at a rate of 1Hz and 10Hz, respectively.

Conclusions: Accurately classifying cautery states will enable real-time identification of the start and endpoint of a surgical incision. By performing majority voting on the cautery classifications during an iKnife classification, we may be able to reduce the model error in detecting the cautery state. Detecting the cautery mode enables the analysis of the differences in mass spectra signatures based on the cautery mode. By combining accurate surgical incision times with position tracking, we can localize the origin of tumour signals detected by iKnife.

1. Balog, J., et al. *Science Trans Medicine*. 2013; 5(194): 194ra93.
2. Ungi T., et al. *IEEE Trans Biomed Eng*, vol. 63, no. 3, pp. 600-606, March 2016.
3. Asselin, M., et al. *Hamlyn Symposium on Medical Robotics.* 2019.
4. Carter, K., et al. *SPIE: Medical Imaging.* 2016

Continuing Design and Developments of a Forward-Looking Ultrasound Catheter

Alykhan Sewani,[1,2] Carlos-Felipe Roa,[1,3] James J. Zhou,[1,2] Amaar Quadri,[1,4] Rene Gilliland-Rocque,[2] Emmanuel Cherin,[1] Christine Démoré,[1,3] Graham A. Wright,[1] M. Ali Tavallaei[1,2]

[1]Sunnybrook Health Sciences Centre, [2]Ryerson University, [3]University of Toronto, [4]University of Waterloo

Background: Many catheter-based procedures have high technical failure [1]-[3] and complication rates [4]-[6]. This is partially due to navigation and visualization issues stemming from the difficulties of remote navigation from outside the body, mechanical engagement of the flexible device and anatomy, and 2D X-ray guidance for 3D operations. Minimally invasive procedures such as chronic total occlusion (CTO) recanalization require the surgeon to cross the occlusion using a guidewire. Due to the poor soft-tissue contrast and projection view of X-ray imaging, the surgeon is blind to the morphology of the occlusion. Forward-looking ultrasound can be used to image the occlusion and facilitate navigation to the penetrable sites (e.g., microchannels or soft tissue). One approach to create a forward-looking ultrasound catheter is to use capacitive micromachined ultrasound transducer (CMUT) arrays that require high power consumption (with corresponding safety concerns) and suffer from low SNR [9][10]. An alternative approach relies on the use of single element (SE) PZT transducers in conjunction with mechanical steering and tracking systems. However, such approaches suffer from reduced tracking accuracy in tortuous anatomy, leading to poor image reconstruction [7][8]. We have recently developed a high-precision steerable catheter that provides the interventionalists with reliable control and position tracking of the catheter tip regardless of the path tortuosity (CathPilot) [11]. The objective of this work is to characterize the CathEye, which integrates an ultrasound transducer with the CathPilot, for imaging applications.

Figure. 1: Distal end of deployed CathEye with transducer.

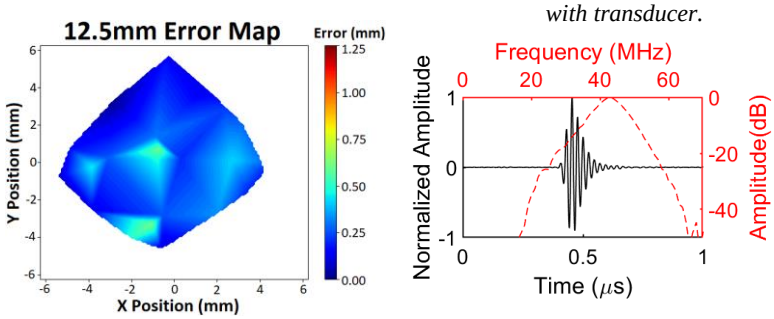

Figure 2: (a) Heatmap of CathEye positional error at 12.5mm expansion, (b)Pulse-echo and frequency response for 40 MHz transducer.

Methods: The system uses an expandable cable-driven parallel mechanism to provide for localized control of the device relative to the anatomy (Fig. 1). The catheter tip position was measured with a camera positioned perpendicular to the frame. The tracking error was characterized by calculating the Euclidean distance between the measured and predicted positions, averaged over 87 samples. An SE-PZT transducer with a centre frequency of 40MHz and a diameter of 900µm was designed for this application. A pulse-echo experiment was performed using a quartz reflector to characterize the transducer. The transducer was excited using a 40MHz Gaussian pulse with 100% fractional bandwidth. The waveforms were filtered with a 5th order Butterworth filter (20-60MHz) and processed into envelopes with a Hilbert transform.

Results: At an expansion size of 12.5mm, the CathEye has an average tracking error of 0.27±0.17mm (Fig. 2a). The transducer was characterized with a centre frequency of 43MHz and a fractional bandwidth of 25% (Fig. 2b). The received pulse envelope (-6dB) gave an axial resolution of 95µm.

Conclusions: The positional accuracy of the CathEye is acceptable for precise tracking of the transducer during imaging. The transducer was designed at the size of a guidewire and can be inserted and removed into the CathEye seamlessly during a procedure. The high frequency of the transducer will allow for high-resolution imaging of the occlusion morphology. Further integration between the CathEye position tracking and transducer pulsing electronics is required for imaging. Images generated with the CathEye will be created with respect to the expandable frame (i.e., anchored to anatomy). They will be inherently co-registered to the reference frame of the steering system. This allows for visualization of the surgical tool with respect to the obtained ultrasound images and can potentially help in various minimally invasive cardiovascular interventions and specifically CTO crossing.

References: [1] Bradbury et al., *J Vasc Surg*, 2010. [2] Hsu et al., *J Am Heart Assoc*, 2013. [3] Al-Hijji et al., *Am Heart J*, 2016. [4] Daye et al., *Cardi. Diag. & Ther.*, 2018. [5] Gupta et al., *Circ Arr. Elec.*, 2013. [6] Brilakis et al., *JACC Card. Interv*, 2015. [7] K. H. Ng et al., *Circ.*, 1994. [8] J. Janjic et al., *IEEE TBME*., 2018. [9] A. Nikoozadeh et al., *IEEE Ultrason.* 2010. [10] D.T. Yeh et al., *IEEE Trans Ultrason.*, 2006. [11] Roy et al., *J Vasc Surg*, 2019.

Design of a Radio-Ultrasound-Guided System for Breast Cancer Surgery

Sydney Wilson[1,2], Claire Park[2,3], Kevin Barker[2], Hristo Nikolov[2], Aaron Fenster[1,2,3], David Holdsworth[1,2,3,4]
[1]School of Biomedical Engineering, [2]Robarts Research Institute, [3]Dept. of Medical Biophysics, Schulich School of Medicine and Dentistry, [4]Dept. of Surgery, Schulich School of Medicine and Dentistry, Western University

Introduction: Non-imaging gamma probes are routinely used in breast cancer surgery to localize radiolabeled tumours and sentinel nodes. Unfortunately, this technique does not provide proper visualization or precise margin assessment and as a result, many patients must undergo a revision surgery. To address these limitations, we propose a new, hand-held, dual-modality image guidance system that combines a previously developed focussed gamma probe [1] with an ultrasound transducer for simultaneous acquisition of molecular and anatomical data. The focussed gamma probe is key to realizing this new hybrid system; unlike existing single-hole collimated gamma probes that suffer from poor resolution at a distance from a source, the highly convergent collimator of our focussed gamma probe positions the point of highest resolution in a remote focal region. The objective of this work is to create a computer aided design (CAD) for our proposed hybrid image guidance system, the radio-ultrasound-guided system, to assess its feasibility, resolution, and sensitivity.

Methods: The outer geometry of the convergent collimator, and thus the focussed gamma probe from [1], was reconfigured into a rectilinear geometry, Figure 1a, to maximize the detector area alongside the ultrasound transducer. The gamma probe had a 45 mm focal length and a 20 mm by 40 mm cesium iodide scintillation detector. The resolution and sensitivity of the gamma probe was simulated using a previously validated model in a Monte Carlo simulation software called GEANT4 Application for Tomographic Emission (GATE, OpenGATE) [2]. A 140 keV Technetium-99m point source was placed in the ideal focal plane, 45 mm from the tip of the probe, and the resulting two-dimensional point spread function was fit to an elliptical Gaussian function using non-linear regression (MATLAB, MathWorks).

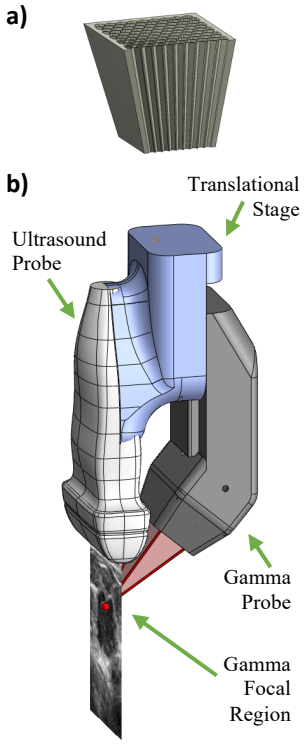

Figure 1: (a) cross-sectional CAD model of rectilinear collimator and (b) CAD model of the new radio-ultrasound-guided system.

To realize our radio-ultrasound-guided system, a receptacle was designed that coupled an ultrasound transducer with the focussed gamma probe. For simultaneous acquisition, the focal region of the gamma probe was positioned within the ultrasound plane and a single degree of freedom was required to allow for a variable focal depth. A CAD model of the radio-ultrasound-guided system was created in Solidworks (Dassault Systèmes, France).

Results: The radio-ultrasound-guided system, shown in Figure 1b, connects an ultrasound transducer to the focussed gamma probe through a custom-designed holder. By angling the head of the gamma probe, the focal region was placed in the ultrasound imaging plane and the translational stage allowed the gamma focal region to be positioned at axial depths of up to 3 cm in the breast tissue. Given that the hybrid system incorporates a commercially available ultrasound transducer, the resolution and sensitivity of the anatomical images will be consistent with manufacturer specifications. The focussed gamma probe was found to have a simulated full width at half maximum resolution of 3.5 mm in its 45mm focal plane while maintaining a sensitivity of 7.8 cps/kBq.

Conclusions: The CAD model for the radio-ultrasound-guided system demonstrates that it is possible to simultaneously acquire molecular data and anatomical images from a focussed gamma probe and ultrasound transducer, respectively. The single degree of freedom in the hybrid system would allow the clinician to accurately assess breast lesions and lymph nodes, which are usually only a couple of centimeters deep. The remote focal region on the focussed gamma probe is a crucial component of our design because we have achieved a high-resolution, overlapping assessment region while both probes sit side-by-side exterior to the breast tissue. In addition, since there is no physical overlap between the probes, there should not be any risk of image degradation in the hybrid system. To the best of our knowledge, the radio-ultrasound-guided system would be the first intraoperative image guidance system that simultaneously acquires data from a gamma probe and an ultrasound transducer in real-time, enabling clinicians to assess breast tumour margins more accurately during surgery.

References: 1. D. W. Holdsworth, *et al.*, "3D-printed focused collimator for intra-operative gamma-ray detection," Proceedings SPIE 10132, 2017. **2.** S. Wilson *et al.*, "Highly Focussed Collimators for Increased Resolution of Hand-Held Gamma Probes," in *19th Annual Symposium Imaging Network Ontario*, 2021.

Development of photoacoustic tomography to monitor photothermal therapy of localized prostate cancer
Ivan Kosik (University Health Network), **Robert Weersink** (Institute of Biomaterials and Biomedical Engineering, Radiation Oncology, U of Toronto), **Brian Wilson** (Medical Biophysics, U of Toronto)

Introduction: Photothermal therapy (PTT) is a minimally invasive treatment comprising thermal tumor destruction using near-infrared laser light delivered via interstitial optical fibers. PTT of focal PCa, offers a safe and cost-effective treatment option. Our ongoing phase I/II clinical trial has reported no cases of erectile disfunction, incontinence or perioperative complications following image guided PTT of localized PCa, with 75% of patients released same day. However, the clinical studies to date reveal two limitations: (1) guidance of PTT using MRI-based thermometry as currently used is not sufficiently reliable and accurate, and (2) confinement of the treatment to the tumor is compromised by thermal diffusion. These factors have resulted in some 30% of patients being undertreated to ensure that there is no damage to critical tissues, particularly near the rectal wall where tumors are most common. To address factor 1, we are developing frequency-optimized photoacoustic tomography (PAT) for near-real-time imaging and scale specific contrast (SSC). To address heat diffusion, we are employing tumor-localizing porphyrin-lipid nanoparticles (Porphysomes) developed at Princess Margaret to increase optical absorption in the tumor and thereby provide thermal confinement. We hypothesize that the exquisite sensitivity of PAT to both tissue temperature and Porphysome concentration will enable effective PTT treatment planning and monitoring resulting in ideal dose delivery while maintaining thermal confinement and minimizing risk. **Methods:** The most critical component of a PAT system is the detector array whose design specifications define the range of attainable imaging targets. To enable detection of both high-frequency signals originating from high contrast targets like Porphysomes as well as low-frequency signals from bulk tissue during PTT, we are developing a multifrequency transducer array. Specifically, the system shown in Figure 1 allowed an acoustic power spectrum analysis of photoacoustic signals originating from representative phantoms and tissues. This information guided the development of detectors optimized for scale specific contrast imaging.

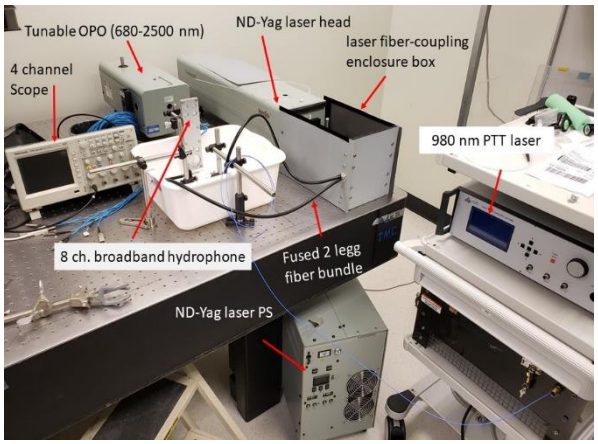

Fig 1. Photograph of experimental photoacoustic system for acoustic power spectral analysis

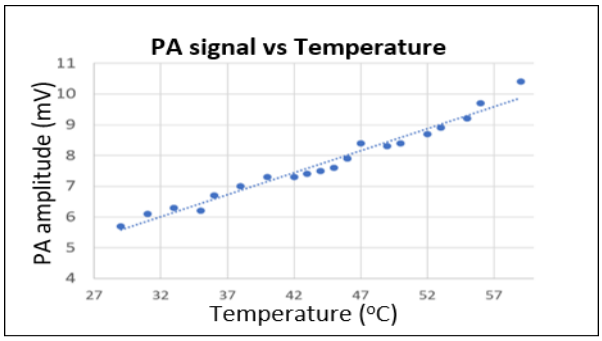

Fig 3. PAT signal amplitude as the temperature inside a tube is increased indicating linear trend within PTT therapeutic range.

Results: Figures below show photoacoustic measurements on polyethylene tubes ranging in diameter from 1.3 mm to 8.5 mm performed with our multifrequency detector array. Fig 2 left panel shows signal from a 1.3 mm tube measured with the high-f detector and the right shows 1.3 mm, 3.5 mm and 8.5 mm signals measured with the low-f detector. Note the reduced amplitude and inaccurate diameter estimate of the low-f measurement on the 1.3 mm tube compared to the high-f detector. Conversely, the low-f detector accurately estimated the bulky tubes for which the high-f detector failed (*not shown*). The sensitivity to bulk tissue changes (e.g. photothermal lesion) *and* focal features (e.g. blood vessels, Porphysomes), combined with signal-temperature linearity, shown in Fig 3, highlights the importance of detector frequency optimization for SSC in PAT.

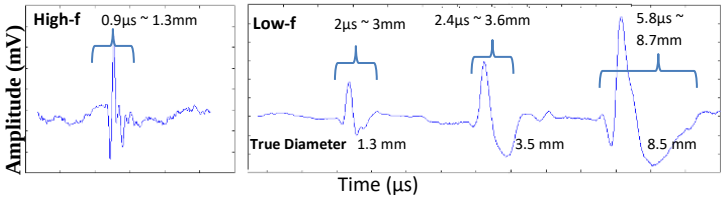

Fig 2. Time-resolved PAT signals from 1.3 mm, 3.5 mm and 8.5 mm tube diameters along with time-of-flight estimated diameters

Conclusion: We recently started characterization of a hand-held prototype photoacoustic imaging probe and are looking forward to sharing results of PTT treatment guidance in terms of thermometry, Porphysome uptake quantification, and heat-induced tissue changes. We hope these developments catalyze translation towards real patient benefit in the clinic.

Pitch Session 3: MR Imaging

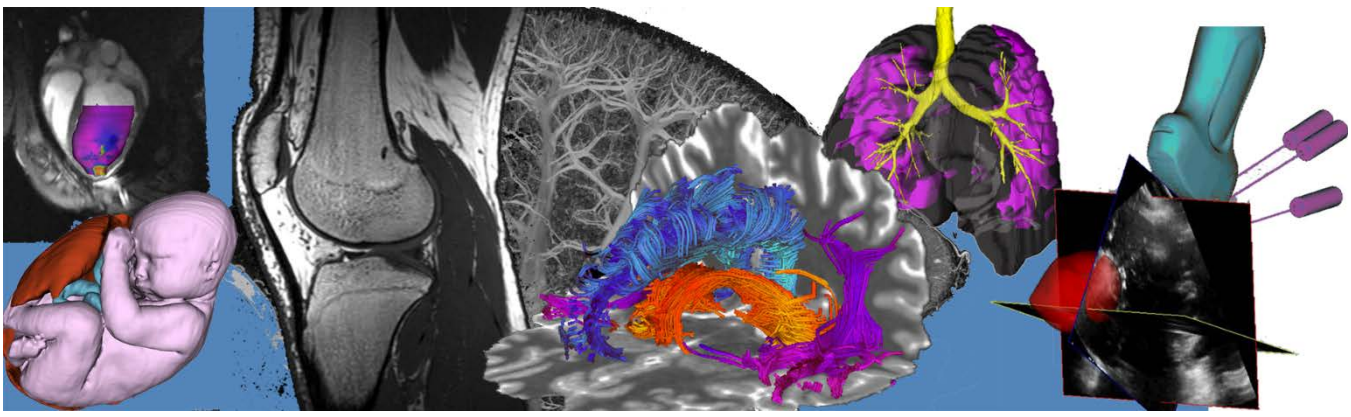

Monitoring the Effect of Cariporide on Intracellular Acidification by CEST-MRI

Maryam Mozaffari[1,2], Nivin Nystrom[1,2], Alex Li[2], Miranda Bellyou[2], Timothy Scholl[1,2], Robert Bartha[1,2]
[1] Department of Medical Biophysics, [2] Robarts Research Institute, University of Western Ontario

Introduction: In malignant tissues, there is an inversion of the normal pH scheme, where the intracellular pH (pH_i) becomes slightly more alkaline while the extracellular pH becomes strongly acidic. Na^+/H^+ exchanger isoform 1 (NHE1) is an acid-extruding membrane transport protein that has been directly linked to pH regulation.[1] Tumor acidification is a recognized therapeutic strategy and could be achieved by blocking the NHE1 transporter and consequently decreasing pH_i. Cariporide inhibits NHE1 and could modify tumor pH_i. This drug has not been clinically tested in cancer.[1] We have previously shown that cariporide selectively acidifies U87MG gliomas in mice.[2] However further studies are needed to examine the effect of cariporide on different tumor models. Chemical exchange saturation transfer (CEST) MRI contrast is sensitive to tissue pH_i. A CEST-MRI technique called amine and amide concentration-independent detection (AACID) was previously developed as an indicator of tissue pH.[3] The AACID value is inversely related to the tissue pH. The goal of this study was to track changes in the tumor pH_i over time to determine whether cariporide can selectively acidify rat C6 glioblastoma following cariporide injection. We hypothesized that blockage of NHE1 by cariporide would selectively acidify this tumor model as observed in U87MG tumors.

Methods: 10^6 C6 glioma cells were injected into the right frontal lobe of six 8-week-old male rats. MR imaging was performed on a 9.4T small-animal scanner. To evaluate the effect of cariporide on tumour pH_i, rats received an intraperitoneal injection of cariporide (dose: 6mg/kg in 2ml) two weeks after tumour implantation. Three CEST images were acquired at baseline. Animals then received the drug inside the scanner and eight CEST images were acquired during the following 160 minutes. CEST images were acquired for the slice of interest using a fast-spin-echo pulse sequence. The CEST spectrum from each pixel in the image was analysed using custom software in MATLAB to generate parametric maps. A paired t-test was performed to measure differences in AACID values between tumor and contralateral regions following the drug injection.

Results: Figure 1.a shows the average AACID value in the tumor and contralateral regions over time. The three pre-injection CEST spectra were summed to increase signal-to-noise ratio. Twenty minutes after drug injection, the average AACID value in the tumor increased and reached a first maximum. It then declined to a minimum about an hour after the injection. A second increase occurred at hundred minutes after which the average AACID value decreased again. The average AACID value in the contralateral tissue followed the same trend. At the first maximum, the average AACID value in tumor post-injection was 5.9% higher compared to pre-injection, corresponding to a 0.28 lower pH_i. However, at the second maximum it was 3.8% higher compared to pre-injection, corresponding to a 0.18 lower pH_i (Fig. 1.b).

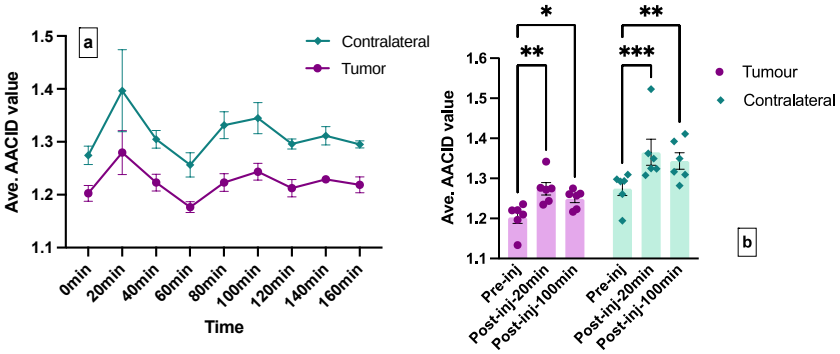

Figure 1. a) The average AACID value in the tumor and contralateral regions a) over time, b) pre-injection of cariporide and 20 minutes and 100 minutes after. Error bars represent the standard error of the mean. The asterisks indicated $p<0.05$ in the paired t-test.

Conclusion: Surprisingly, we did not observe *selective* tumor acidification following injection as had previously been observed in the mouse U87MG glioma model.[2] Instead, acidification occurred in the tumor and in the contralateral tissue. The reason for this discrepancy may be related to differences in tumor vasculature compared to the U87MG model that may have limited the ability of cariporide to infiltrate the tumor.[4] The C6 glioma model is more aggressive and proliferating than U87MG. Thus, the bulk effect of the tumor on day 14 could also have impacted contralateral tissue pH and the uptake of cariporide.[4] Future work will examine the effect of cariporide on healthy brain tissues in the rat.

References: [1] J Transl Med 2013; 11(282):1-17, [2] Int J Clin Oncol 2018, 23:812-819, [3] J Cerebral Blood Flow & Metabolism 2014, 34:690-8, [4] J Magn Reson Imaging. 2010; 32(2):267-75.

ExTE-HERMES: an MR spectroscopy acquisition for detection of GABA and GSH in the human brain

Peter Truong[1] and Jamie Near[1,2]

[1]Physical Sciences Research Platform, Hurvitz Brain Sciences Program, Sunnybrook Research Institute, Toronto, Canada; [2]Department of Medical Biophysics, University of Toronto, Toronto, Canada

Introduction: Magnetic resonance spectroscopy (MRS) offers a noninvasive way to observe brain metabolites *in-vivo*. However, some metabolites, such as Gamma-Aminobutyric acid (GABA, an inhibitory neurotransmitter), and glutathione (GSH, an antioxidant), are only present in low concentrations and are obscured by larger metabolite resonances. Thus, J-difference editing techniques, such as MEGA-PRESS[1], are often used to detect these metabolites individually. The HERMES sequence[2] builds upon this by allowing simultaneous detection of GABA and GSH. One limitation for HERMES is that the echo time (TE) can only be optimized for one metabolite at the expense of the other with it set at 80ms, which is neither ideal for GABA (68ms) nor GSH (120ms)[3].

Previously, Extended TE (ExTE) MEGA-PRESS has shown the possibility of acquiring J-difference edited GABA spectra at longer TEs while maintaining optimal editing efficiency[4]. Here, we propose to combine the ExTE concept with HERMES to enable optimal GSH editing efficiency with a TE of 120ms while still providing efficient GABA editing.

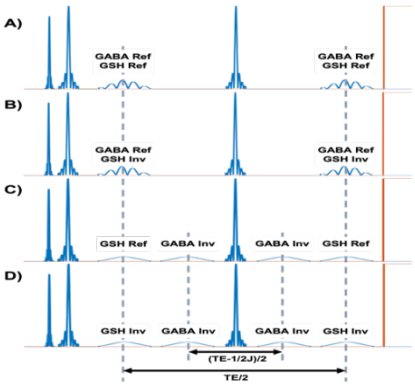

***Figure 1**: Editing scheme for ExTE-HERMES:*
***A)** "GABA and GSH refocused"*
***B)** "GABA refocused and GSH inverted"*
***C)** "GABA inverted and GSH refocused"*
***D)** "GABA and GSH inverted"*

Methods: The ExTE-HERMES pulse sequence, shown in **Figure 1**, is composed of 4 experiments: A) a simultaneous "GABA and GSH refocused" scan (editing at 1.88 ppm and 4.56 ppm, respectively) using dual-band editing pulses with TE/2 spacing; B) a simultaneous "GABA refocused and GSH inverted" scan (editing at 1.88 ppm and 7.5 ppm, respectively) using dual-band editing pulses with TE/2 spacing; C) a sequential "GABA inverted and GSH refocused " scan using single-band editing pulses at 1.88 ppm and 4.56 ppm with (TE-68ms)/2 and TE/2 spacing, respectively; D) a sequential "GABA and GSH inverted" scan using single-band editing pulses at 1.88 ppm and 7.5 ppm with (TE-68ms)/2 and TE/2 spacing, respectively.

Phantom Scans: A 3T Siemens Prisma-XR (Erlangen, Germany) was used to perform HERMES and ExTE-HERMES scans on a 500mL phantom containing 50mM GABA and 50mM GSH in water (pH = 7.1). 14ms Gaussian shaped single- and dual-banded editing pulses were utilized. Parameters used for both scans were: TR = 2400ms; spectral width = 2000 Hz; number of points = 2048; number of averages = 32. HERMES sequences were run with TE=80ms and TE=120ms, and ExTE-HERMES was run with TE=120ms.

Processing: All processing was performed using FID-A (**github.com/CIC-methods/FID-A**). Peak integration was used to estimate GABA- and GSH-edited peak areas from 2.5 to 3.25 ppm.

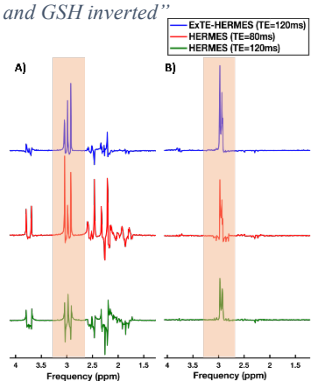

***Figure 2**: Phantom scans showing GABA-edited (**A**) and GSH-edited (**B**) spectra using ExTE-HERMES(TE=120ms) (blue), HERMES (TE=80ms) (red), and HERMES (TE=120ms) (green).*

Results: Phantom scan results are shown in **Figure2**. GABA peak areas of 5.47, 8.12, and -3.40 were calculated for ExTE-HERMES and HERMES with TE=80ms and TE=120ms, respectively (**Figure3**). With GSH, ExTE-HERMES had a larger peak area of 9.90 compared to HERMES with TE=80ms and TE=120ms at 4.34 and 6.34, respectively.

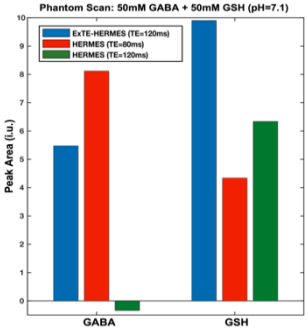

***Figure 3**: GABA- and GSH-edited peak areas from phantom scans for ExTE-HERMES (TE=120ms) (blue), HERMES (TE=80ms) (red), and HERMES (TE=120ms) (green).*

Conclusions: ExTE-HERMES enables optimal J-difference editing efficiency of both GABA and GSH signal. Compared with HERMES (TE=80ms), phantom scans show a small decrease in GABA peak area using ExTE-HERMES, which could be due to T2 decay. However, ExTE-HERMES shows a significant increase in GSH signal compared to both HERMES scans. Future work will involve a) testing and validation of the ExTE-HERMES sequence in human brain in vivo, and b) application of ExTE-HERMES to study GABA and GSH levels in brain disorders.

References: 1. Mescher M., et al. NMR Biomed, 1998. **2**. Saleh M.G., et al. Neuroimage, 2016. **3.** Chan K.L., et al., MRM, 2017. **4.** Near J., et al. [Poster] 23rd ISMRM Annual Meeting, 2015, May 30–June 5.

MR Image Resolution Enhancement using Real-ESRGAN

Shawkh Ibne Rashid[1], Elham Shakibapour[1], and Mehran Ebrahimi[1]
[1]Faculty of Science, Ontario Tech University, Oshawa, ON, Canada

Introduction: Higher quality Magnetic Resonance (MR) images are valuable for early detection and accurate diagnosis of various medical conditions. Acquiring higher resolution MRI requires higher image acquisition times, and can be costly. Super-resolution (SR) techniques are alternative ways to improve the spatial resolution of images by producing a High Resolution (HR) image given a Low Resolution (LR) one. While most image resizing techniques rely on interpolation methods such as linear or cubic, interpolated images blur or degrade important edge information of images. Recent advances in Super Resolution Generative Adversarial Network (SRGAN) is aimed to recover fine texture details and edge information even at large upscaling factors. This motivated us to apply a recent extension of the method called Real Enhanced Super-Resolution Generative Adversarial Networks (Real-ESRGAN) that achieves high perceptual quality for 2D real-world images [1]. Our specific focus in this work is to apply Real-ESRGAN [1] to resolution enhancement of 2D slices of 3D MR images.

Method: We have applied Real-ESRGAN [1] to enhance the spatial resolution of 2D MR images. Real-ESRGAN is a generative-adversarial network designed with 16 identical Residual-in-Residual Dense Blocks (RRDB) in the generator network and a UNET model in the discriminator network [1]. In our approach, the pre-trained Real-ESRNET applied on 2D real-world images is used as an initialization for the network's weights and is then fine-tuned on the Brain Tumor Segmentation Challenge (BraTS) 2018 dataset [2]. The dataset contains 285 MRI volumes with a depth of 152 slices which are converted to 2D image slices. In this work, 257 MRI volumes are used for fine-tuning the pre-trained model, i.e. 257x152=39,064 of 2D MR image slices. The remaining 28 MRI volumes, i.e., 28x152=4,256 of 2D MR image slices are used for testing. The LR images are created by down-sampling the images by a factor of 4 in each x-y direction.

Results and Conclusions: The generated 2D HR MR images using Real-ESRGAN are compared with images created using linear and cubic interpolation techniques. The SSIM (structural similarity index measure) values are measured instead of PSNR (peak signal to noise ratio) as a perceptually relevant measure. The mean SSIM values for the linear, cubic and generated images over all of the test data are 0.87, 0.83 and 0.87, respectively. The obtained SSIM values for the generated images are similar to the linear interpolation and slightly higher than cubic interpolation. However, the generated images are perceptually and qualitatively superior compared to the interpolated ones as shown in Fig 1. It can be observed that the interpolated images are blurry with ghosts and shadows around the boundaries with suppressed sharp edge information. Although the GAN model is performing better in enhancing the resolution of the low-resolution MR images, some of the information from the ground truth MR images are missing in the generated images. In summary, we fine-tuned the Real-ESRGAN model using 2D MR images derived from the BraTS dataset and compared them with the common linear and cubic interpolation methods. Future work will involve extending the model to use larger imaging datasets and comparing the model with the state-of-the-art SR models applied to medical imaging data.

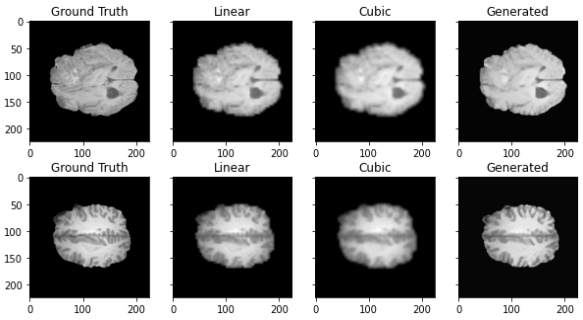

Fig 1. First column is the ground truth 2D MR image slice, second column is the linear interpolated image, third column is the cubic interpolated image, and fourth column is the generated image using the fine-tuned Real-ESRGAN

References:

[1] X. Wang, L. Xie, C. Dong and Y. Shan, " Real-ESRGAN: Training Real-World Blind Super-Resolution with Pure Synthetic Data," in proceedings of IEEE/CVF International Conference on Computer Vision Workshops (ICCVW), pp. 1905-1914, 2021, doi: 10.1109/ICCVW54120.2021.00217.

[2] S. Bakas, H. Akbari, A. Sotiras, M. Bilello, M. Rozycki, J. S. Kirby, J. B. Freymann, K. Farahani and C. Davatzikos, " Advancing The Cancer Genome Atlas glioma MRI collections with expert segmentation labels and radiomic features," in Nature Scientific Data, September 2017, doi: 10.1038/sdata.2017.117.

Retrospective Frequency and Phase Drift Correction in Rosette MRSI Data using Spectral Registration

Sneha Vaishali Senthil[1,2] , Brenden Kadota[1] , Jamie Near[1,2,3]

1.Sunnybrook Research Institute, Toronto, Ontario; 2.McGill University, Montreal, Quebec; 3.Department of Medical Biophysics, University of Toronto, Ontario

Introduction: Magnetic Resonance Spectroscopic Imaging (MRSI) is a non-invasive in-vivo technique for mapping tissue concentrations in clinical and neuro-scientific research. Although, in vivo MRSI has made significant progress; frequency and phase drifts owing to the heating of gradient coils and passive shimming, in the acquired data are still a persisting problem. This results in signal to noise (SNR) losses, spectral peak broadening, and deformities in metabolite line spectra.[1] Different methods have been proposed to correct for these drifts. However, drift correction of MRSI data is more challenging as multiple repetitions often do not share any common k-space points that can be used for estimating drifts thereby requiring separately acquired navigator echoes. There is no current solution available for common sampling trajectories as multiple repetitions collected using these methods often do not share any common k-space points that can be used for estimating drifts. The objective of this work is to demonstrate how a Rosette-MRSI acquisition overcomes these shortcomings by capturing the k-space center during each repetition thus acting as a self-navigator for estimating the frequency and phase drift at each scan.

Methods: A Rosette-MRSI sequence was implemented on a 3T Prisma Siemens MR scanner. Each repetition consisted of a circular trajectory originating at the center of k-space and rotated about the origin during each repetition until full k-space coverage was obtained. Phantom experiments were performed using a GE"Braino" phantom. Rosette-MRSI was implemented following a 15-min diffusion tensor imaging (DTI) scan. The parameters used were: 300 mm² field of view (FOV); 32 shots, 9 averages, repetition time (TR) =1200ms, echo time (TE) =1.6ms, flip angle=90°. Data processing and reconstruction were performed using the FID-A toolkit[2]. K-space density compensation was performed using the Voronoi method.[3,4] Free Induction decays (FIDs) from the k-space center were isolated from each repetition and then, using the first k=0 FID as reference, frequency and phase offsets for each repetition were estimated using time-domain spectral registration[1]. After estimating the offsets for each k=0 FID, the corresponding corrections were applied to all FID signals (not only the k=0 extracted FIDs), to achieve a frequency and phase drift correction across the whole of k-space.

Results: The resonant frequency drifted approximately linearly by a total of 4.6Hz and the phase drift ranged from -3° to 4.8° across all scans. Spectral registration resulted in a noticeable improvement in the alignment of k=0 FIDs and spectral peaks (Figure 1). Figure 2 shows spectra from a voxel following water removal, both with and without frequency and phase drift corrections. Frequency and phase drift correction resulted in a visual improvement in the line shape of glutamate, N-acetylaspartylglumate (NAA) and lactate peaks. Future work will involve implementing water suppression and drift correction in in-vivo data to capture the additional motion-related frequency and phase variations which are not seen in phantom results. Following that, this project aims at implementing Rosette-MRSI in clinical population to capture alterations in brain glucose metabolism and apply the above-mentioned drift correction before analysing the MRS spectra.

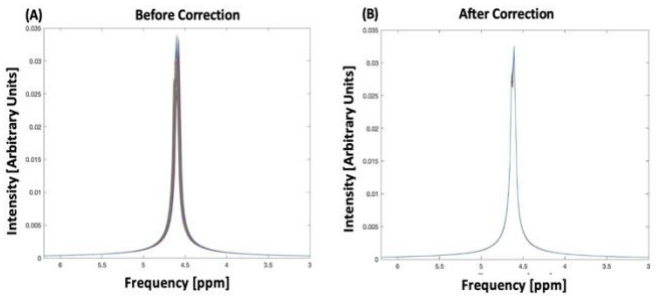

Figure 1: The spectra of the FIDS at the center of k-space are plotted for all scans ((A) and (B)) before (left) and after (right) frequency correction using spectral registration.

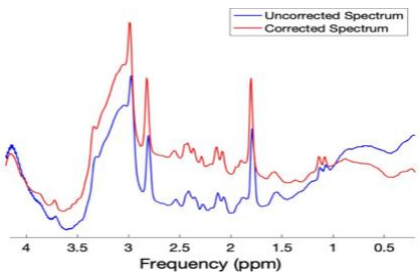

Figure 2: Drift corrected (blue) and uncorrected (red) MRS spectra plotted after Hancel Lanczos singular value decomposition (HLSVD) water removal.

Conclusion: Frequency and phase drifts can unfavorably affect the processing of acquired MRS data. We developed a rosette-MRSI sequence and demonstrated the use of spectral registration to correct frequency and phase drifts in the acquired data. The results obtained highlight the advantages of self-navigated rosette trajectories for drift correction.

References: 1. Near J, et al. (2015) *Magn Reson Med*. 2. Simpson R, et al. (2017) *Magn Reson Med*. 3. Bagchi S, et al. (1996) IEEE Trans Circuits Syst II Analog Digital Signal Process. 4. Rasche V, et al. (1999) IEEE Trans Med Imaging.

A Numerical Bloch Solver with Dynamic Relaxation Calculations for Low-Field MRI Modeling

John Adams[1,2], William Handler[1,2], Blaine Chronik[1,2]

[1] *Department of Physics and Astronomy, Western University, London, ON;* [2] *xMR Labs, London, ON*

Introduction: Low-field magnetic resonance imaging (MRI) is a growing field as a solution to the high cost and inaccessibility of MRI [1]. In addition to its practical benefits, shifting to lower field strengths may enable pre-clinical MRI techniques such as $T_{1\rho}$ imaging to be adopted as part of clinical practice [2]. To evaluate and optimize these techniques for low-field scanning, we have developed the Numeric Integrator for the Bloch Equations (NIBLEs); a Python 3 based tool designed to allow users to realistically simulate the signal from an MR pulse sequence by solving the Bloch equations with minimal assumptions[3]. In this abstract, we present our initial work implementing field-dependent relaxation effects into NIBLEs.

Methods: The details of the base NIBLEs solver have been presented in detail previously[3]. Equations for field-dependent relaxation values, as derived by Bloembergen, Purcell, and Pound for dipole-dipole interactions[4], were coded into the Bloch equations used by the NIBLEs solver to simulate sample magnetization. To appropriately simulate the signal from tissue, we implemented a 2-component model[5], where the water in the simulated tissues is split into two components; one describing free water and another describing protein-bound structured water.

Verification was performed on simulated white matter, with correlation times of 2×10^{-10} s and 7×10^{-8} s for free and bound water, respectively, with a 9 to 1 free to bound water ratio[5]. T_2 relaxation times were evaluated using a CPMG pulse train (TE1 = 15ms, TE2 = 30ms), while T_1 relaxation times were evaluated with an inversion-recovery sequence composed of an inversion pulse followed by a free induction decay (T_{IR} ranging from 0.5s to 4s in 0.5s increments). To verify that our simulator reliably translated calculated relaxation times to simulated signal, we compared the relaxation time calculated from simulated MR signal from NIBLEs, to the output of our relaxation model implemented outside the NIBLEs solver, and to literature relaxation values.

Results: Results from the simulated tissue model are shown in Table 1. The T_1 values measured from our simulated signal are consistent with both literature values and the values output by our relaxation model. The T_2 values output show a slight increase in our model and simulated outputs, compared to a significant decrease in the literature values. This is anticipated; the decrease in T_2 values with field strength is due to non-dipole-dipole interactions not included in our implemented model, such as diffusion through local magnetic susceptibility gradient [5].

Table 1- Comparison of T_1 and T_2 Values From Literature and Model

Field Strength (T)	Literature T_1[5] (s)	Relaxation Model Output T_1 (s)	T_1 Measured from Simulation (s)	Literature T_2[5] (ms)	Relaxation Model Output T_2 (ms)	T_2 Measured from Simulation (ms)
0.5	-	0.79	0.82 ± 0.15	-	72	70 ± 15
1.5	0.85 ± 0.05	0.93	0.96 ± 0.10	80 ± 10	73	71 ± 13
3	1.05 ± 0.10	1.00	1.02 ± 0.08	60 ± 10	74	71 ± 10
4	1.13 ± 0.08	1.07	1.14 ± 0.30	50 ± 10	74	72 ± 10
7	-	1.35	1.40 ± 0.12	-	74	72 ± 7

Conclusions: We have successfully implemented a simple model for calculating relaxation times into a pulse sequence simulation tool. Work on implementing field-dependent relaxation is ongoing. We aim to implement a more robust relaxation calculation method based on Redfield relaxation theory which will enable us to simulate $T_{1\rho}$ relaxation and evaluate its utility as a biomarker at low field.

References:

[1] A. Panther *et al*., "A Dedicated Head-Only MRI Scanner for Point-of-Care Imaging," *Proc. Annu. Meet. Int. Soc. Magn. Reson. Med.*, 2019.

[2] I. A. Gilani and R. Sepponen, "Quantitative rotating frame relaxometry methods in MRI," *NMR Biomed.*, vol. 29, no. 6, pp. 841–861, 2016, doi: 10.1002/nbm.3518.

[3] J. Adams, W. B. Handler, and B. A. Chronik, "Development of a Numerical Bloch Solver for Low-Field Pulse Sequence Modeling," 2021.

[4] N. Bloembergen, E. M. Purcell, and R. V. Pound, "Relaxation effects in nuclear magnetic resonance absorption," *Phys. Rev.*, vol. 73, no. 7, pp. 679–712, 1948, doi: 10.1103/PhysRev.73.679.

[5] R. A. DeGraaf, *in vivo NMR Spectroscopy*, 2nd ed. John Wiley & Sons, Ltd, 2007.

Improving Volumetric Magnetic Resonance Arrythmia Substrate Characterization in Cardiac Sequences with Non-Cartesian Gradients

Saqeeb Hassan[1], Jaykumar Patel[1,2], Graham Wright[1,2]

[1]Physical Sciences Platform, Sunnybrook Research Institute [2]Medical Biophysics, University of Toronto

Introduction: The current clinical standard in MR-guided scar mapping for arrhythmia substrate characterization is 2D Cartesian LGE with slice thicknesses greater than 5mm, but the increased through plane resolution in 3D Cartesian scans has been shown to improve the identification of re-entry circuits[1]. However, current high resolution 3D Cartesian techniques with full ventricular coverage typically require scans in the range of 10-20 minutes[1]. This is long enough for acquisitions to suffer from contrast agent washout and gross patient motion. Full coverage of the heart in under 5 minutes with a T1-weighted acquisition is possible using non-Cartesian sequences such as 3D cones and stack-of-spirals, which take full advantage of gradient hardware limits and cover k-space more efficiently. The 3D cones trajectory has been shown to scan 3-8 times faster than equivalent cartesian trajectories[2], while low resolution stack-of-spirals LGE can cover the whole ventricle in a single breath hold[3]. We propose a non-Cartesian imaging approach to obtaining high isotropic resolution 3D LGE volumes faster than tradition Cartesian methods, with image quality and T1 measurement validation done using phantom images.

Methods: Cartesian, 3D cones, and stack-of-spirals LGE sequences were developed and their imaging times were compared in Fig 1. Five phantoms made of fluids with various T1s reflecting blood and pre/postcontrast scar and myocardium were prepared to model different tissue types relevant to LGE. To measure image sharpness, the modulation transfer functions (MTF) were calculated along four lines crossing the contrast boundary in a phantom with postcontrast scar and myocardium fluids, and the effective spatial resolution was calculated as the inverse of the spatial frequency where the averaged MTF was reduced to 1/10 of its maximum value (Fig 2). T1 characterization accuracy was measured by creating T1 maps of all five phantoms for each sequence by applying a least squares curve fit to each MR[illegible]

Results: The effective sharpness across the contrast boundary was 2.2mm in all three images. The average T1s of each vial in the T1 mapping experiment were compared across sequence types and it was found that the 3D cones underestimated the value of the T1s in the postcontrast scar and myocardium phantoms by over 20% relative to the Cartesian values. The T1s from the stack-of-spirals T1 map agreed with the Cartesian map.

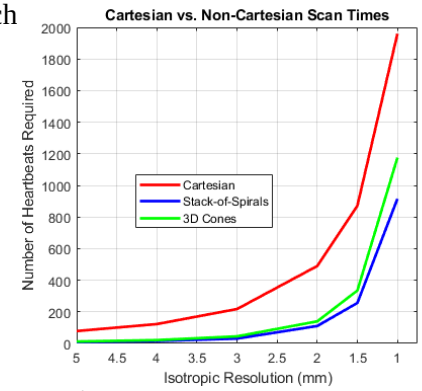

Figure 1: Scan time comparison, FOV=28x28x14cm^3.

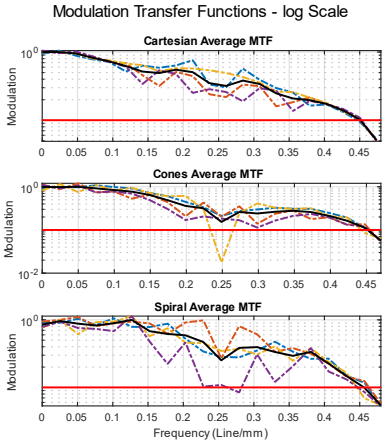

Figure 2: MTFs, black line is the average. Red indicates 1/10 maximum.

Conclusions: Two non-Cartesian imaging techniques, 3D cones and stack-of-spirals were developed for rapid cardiac-gated T1 mapping for the purpose of VT substrate characterization. The MTFs from each volume indicate no sharpness loss from the non-Cartesian trajectories. Off-resonance blurring is often a concern with these techniques, where longer readout durations with center-out trajectories and time-varying gradients can cause a spatial spread of signal. In this case, the effect of the blurring is smaller than the prescribed resolution. The 3D cones appear to have worse T1 accuracy than stack-of-spirals. This was expected, as the 3D cones trajectory samples the k-space origin with every readout, thereby averaging the inversion contrast throughout the acquisition window. The ideal contrast only lasts for a short period after the prescribed TI, and averaging the contrast causes the phantom images for each TI to appear brighter than they should, which in turn causes the T1 fitting to model a faster recovery. This may be avoided by discarding some central k-space data[4]. The stack-of-spirals trajectories only capture the k-space origin in a small fraction of acquisitions, allowing readouts to be timed appropriately to capture the ideal contrast.

References: [1] Andreu, D. et al. EP Europace. 2015. [2] Gurney, P.T. et al. Mag Res Med. 2006. [3] Shin, T. et al. J Mag Res Imaging. 2013. [4] Subashi, E. et al. Med Phys. 2013.

Quantitative Susceptibility Mapping of Brain Regions to Assess Metal Deposition Following Total Hip Arthroplasty and Hip Resurfacing Arthroplasty

Shahnaz Taleb[1], Gabriel Varela-Mattatall[1], Abbigail Allen[2], Chaithanya Nair[1], Roy Haast[1], Ali R. Khan[1], Vishal Kalia[1], Steven J. MacDonald[2], Ravi S. Menon[1], Brent A. Lanting[2], Matthew G. Teeter[1]
[1]*Western University, London, Canada,* [2]*Lawson Health Research Center, London, Canada*

Introduction: Wear and corrosion of implants used in total hip arthroplasty (THA) and hip resurfacing arthroplasty (HRA) release metal ions which can cause adverse local tissue reactions and travel via the bloodstream to distant organs. Cobalt and chromium, in particular, can get past the blood-brain barrier to deposit in the brain, leading to neurological disorders.[1] Magnetic resonance imaging (MRI) and positron emission tomography (PET) scans have reported changes in brain anatomy and metabolism after exposure to heightened levels of cobalt from metal-on-metal (MoM) and metal-on-polyethylene (MoP) hip implants.[2] Quantitative susceptibility mapping (QSM) is an emerging MRI technique used to non-invasively measure the magnetic susceptibility of tissues. Since cobalt and chromium metal ions are paramagnetic, inducing measurable levels of susceptibility in MR images, QSM can be leveraged to study the presence of these ions in the brain. The objective of this study is to use QSM to quantifiably measure the spatial distribution of susceptibility levels in the brains of patients with long-term THA and HRA implants in comparison with age- and sex-matched controls. We hypothesized that susceptibility would be positively correlated with blood ion levels of cobalt and chromium.

Methods: Ethics approval from the institutional review board and informed consent from participants were obtained. Subjects included have had a THA or HRA implant for a minimum time of eight years or have been referred to undergo a THA or HRA but have not yet received an implant. Five deep brain structures were identified from case reports describing anatomical changes in THA patients with implant wear-related cobalt toxicity: caudate, putamen, pallidum, amygdala, and hippocampus. Subjects were examined using 3T MRI (Siemens Prisma Fit). Blood ion levels of cobalt (Co) and chromium (Cr) were measured at the time of imaging in subjects with implants. The Montreal Cognitive Assessment (MoCA) test was performed. A T1-weighted, magnetization-prepared rapid acquisition gradient-echo (MPRAGE) sequence ($1.0\times1.0\times0.9$ mm^3 resolution) was used to segment brain regions using FreeSurfer (v7.1). Susceptibility between anatomical regions was compared using a Friedman test. Correlation between susceptibility and blood levels of Co and Cr was computed using a Spearman correlation. The effect of brain regions and the presence of an implant on susceptibility was assessed using a two-way ANOVA.

Results: A total of 31 subjects were recruited. Implant types consisted of MoM THA (n = 16), dual-modular neck MoP THA (n = 5), MoM HRA (n = 2), and ceramic-on-metal (n = 1). Partial recruitment (n = 7) of matched controls was completed. Mean age was 67 years (range 56-79) and 64 years (range 58-75) for the implanted and control group, respectively. Mean device implantation was 13 years (8-20 years). Mean Co was 6.5 μg/L (0.2-40.0 μg/L) and mean Cr was 2.2 μg/L (0.3-7.4 μg/L). Four subjects had Co levels above 7.0 μg/L. The mean MoCA score was 26 (19-30). Susceptibility varied both between brain regions ($p < 0.0001$) and between implanted subjects and controls ($p = 0.0154$). Left and right brain susceptibility levels were greatest in the pallidum and lowest in the amygdala. Differences between these regions were present for implanted subjects ($p < 0.0001$) and controls ($p < 0.003$). No correlation was found between susceptibility and blood ion levels of cobalt or chromium for any region.

Conclusions: Although susceptibility was significantly greater in implanted subjects than controls, there were fewer subjects in the control group. Full recruitment of age- and sex-matched controls is required before a conclusion can be determined with respect to metal ion deposition in the brain. Susceptibility was found to vary similarly between different anatomical regions of the brain in both implanted subjects and controls, consistent with ageing patterns.[3] There was no correlation between blood ion levels and brain susceptibility. Only 4/24 implanted subjects had blood Co levels >7.0 μg/L which is considered the risk threshold for toxicity. Most subjects have well-functioning implants, despite some devices being recalled from the market.

References: [1] Clark et al., AJNR Am J Neuroradiol, 2014. [2] Bridges et al., Eur J Nucl Med Mol Imaging, 2020. [3] Burgetova et al., Quant Imaging Med Surg, 2021.

Multi-metabolite-selective single-voxel spectroscopy sequence using ultra-high field proton magnetic resonance spectroscopy

Kanagasabai, K[1]; Palaniyappan, L[1,2,3]; Théberge, J[1,2]

1. Medical Biophysics, Schulich School of Medicine and Dentistry, London, Ontario, Canada
2. Lawson Imaging, Lawson Health Research Institute, London, Ontario, Canada
3. Robarts Research Institute, London, Ontario, Canada

Introduction: Psychiatric and neurocognitive disorders are described to be a complex network of abnormal neurotransmission involving neurotransmitters such as gamma-aminobutyric acid (GABA) and glutathione (GSH), and glutamate (GLU). Proton magnetic resonance spectroscopy (1H-MRS), a non-invasive in-vivo imaging modality, can quantify the chemical composition of a voxel in a human brain to study the abnormal neurotransmission. To date, no single-shot 1H-MRS pulse sequence has provided high-quality measurements of GLU, GABA, and GSH simultaneously. This is due to GABA's extremely low in-vivo concentrations, strongly coupled spins of GLU and glutamine in their spectral signature, and interference of neighboring signals. Therefore, there is an unmet need to implement an effective technique to quantify all three neurotransmitters accurately and simultaneously to understand the pathophysiology of several psychiatric and neurocognitive disorders. One promising technique involves the use of an advanced 1H-MRS pulse sequence known as Delays Alternating Nutation Tailored Excitation Point RESolved Spectroscopy (DANTE-PRESS). DANTE-PRESS uses a narrow-band radiofrequency pulse to selectively isolate the signal of a molecule of interest in the human brain spectrum. In addition to this highly selective pulse sequence, the use of a higher field strength scanner will increase the sensitivity of all three neurotransmitters. The primary objective is to develop, test and validate DANTE-PRESS at 7 Tesla to target GLU, GABA and GSH simultaneously in a human brain. The second objective is to compare spectral signatures of DANTE-PRESS with PRESS.

Methods: To complete this, DANTE-PRESS was programmed within the software environment of the 7 Tesla MR scanner at Robarts Research Institute at Western University. An interactive user interface was created to allow users to adjust bandwidth, amplitude modulation, and other features of their pulse sequence in real time to isolate metabolites of interest. An inline display of adjustment loops, to generate accurate frequency profiles to avoid magnetization transfer between metabolites, is a work in progress. Ongoing work involves comparing spectral signatures of GLU (2.35ppm), GABA(1.89ppm), and GSH (3.77ppm) at various echo times (50-150ms) using DANTE-PRESS and PRESS. The next step involves using DANTE-PRESS to isolate multiple metabolites simultaneously using phantoms containing high and in vivo concentrations of GABA, GSH, and GLU and a brain mimicking phantom.

Results: DANTE-PRESS was able isolate metabolites of interest while suppressing unwanted signals that would have contributed to chemical shift displacement errors. Furthermore, the suppression from DANTE-PRESS can effectively suppress signal from water such that water suppression is not required. Pre-analyzed single spectral signatures of GLU, GABA, and GSH appear to be detected at shorter echo times than PRESS.

Conclusion: It is crucial to develop a single shot pulse sequence that can obtain high-reliability measurements of low in-vivo metabolites and highly coupled spins. In the absence of spectral-editing, this will provide accurate in vivo human evidence to test GABA's role in models of psychiatric and neurocognitive disorders involving the simultaneous action of excitation or inhibition imbalance along with oxidative stress. Future work involves implementing DANTE-PRESS towards a longitudinal study to understand the pathophysiology of schizophrenia where clinicians can identify biomarkers of treatment resistance and the appropriate line of treatment.

Pitch Session 4:

Hardware, Software and System Development

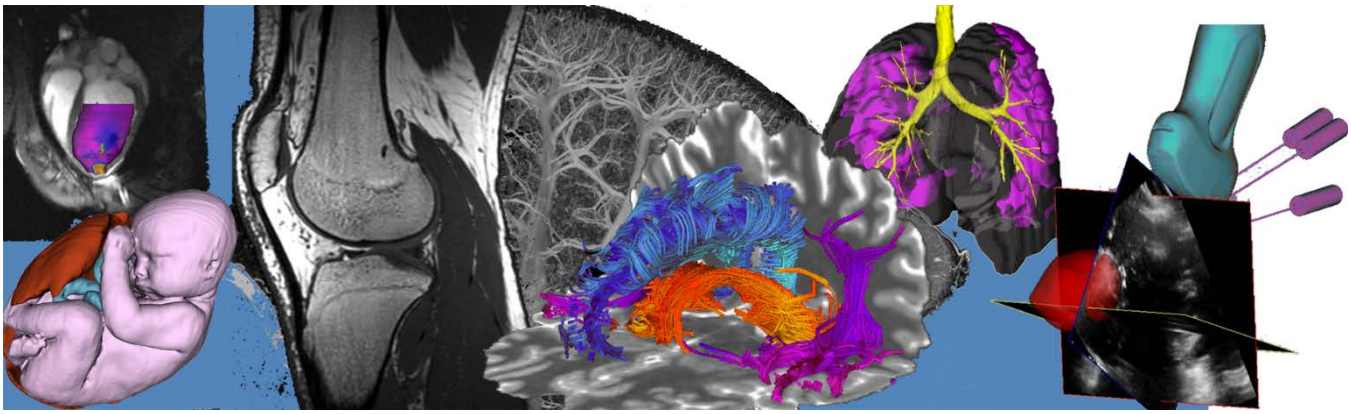

Feasibility of a spatially tracked three-dimensional ultrasound (3DUS) system for point-of-care whole-breast imaging

C. K. Park*[1,2], S. Xing[2,3], S. Papernick[1,2], N. Orlando[1,2], J. Bax[2], L. Gardi[2], K. Barker[2], D. Tessier[2], A. Fenster[1,2,3]
[1]Department of Medical Biophysics, Schulich School of Medicine and Dentistry, [2]Robarts Research Institute, [3]School of Biomedical Engineering, Faculty of Engineering, Western University, London, Ontario, Canada

Introduction: Early detection of breast cancer has reduced mortality in women through widespread screening mammography. However, challenges still exist in 40% of women with dense breasts, which reduces the sensitivity and detection of almost one-third of breast cancers.[1] Automated breast ultrasound (US) has enabled whole-breast imaging, 3D visualization, improved reproducibility, and reduction in operator-dependence, compared to handheld US.[2] However, ABUS still requires training for high-quality image acquisition, experienced interpretation, and are costly. We propose an alternative, adaptable, and cost-effective spatially tracked system for whole-breast 3DUS imaging. This work presents the system design, optimization of spatial tracking, assessment of spatial-based registration and fusion of acquired 3DUS images, demonstration of whole-breast 3DUS imaging in a tissue-mimicking breast phantom, and proof-of-concept whole-breast 3DUS imaging in two healthy volunteer studies.

Methods: The spatially tracked 3DUS system (Fig. 1) is composed of an in-house 3DUS scanner,[3] adaptable to any linear US transducer, and multi-jointed manipulator and counterbalanced stabilizer. The manipulator contains six 13-bit encoders (RMB20, RLS Merilna Tehnika) enabling 6D pose tracking and six degrees of freedom for motion. Tracking error was assessed for each joint (J_{1-6}) by comparing the measured spatially tracked position to its optically tracked position, using a custom stylus and optical tracking system (RMSE = 0.25 mm). Quadratic-based lookup table (LUT) corrections minimized the error in joints with suboptimal accuracy. Spatial-based registration and fusion of 3DUS images acquired in a tissue-mimicking phantom with fiducial spheres was assessed with the Target Registration Error (TRE) between corresponding pairs of overlapping fiducials. Whole-breast 3DUS imaging was demonstrated in a tissue-mimicking breast phantom.[4] The first proof-of-concept of the spatially tracked whole-breast 3DUS approach was demonstrated in a healthy male volunteer, to optimize acquisition protocol under ideal conditions without variable breast curvature and tissue deformations, and female volunteer study.

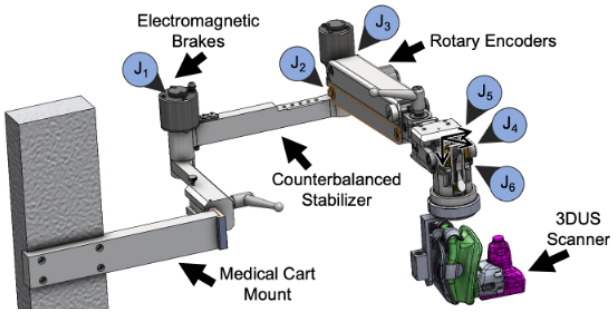

Fig. 1: Computer-aided design (CAD) of the spatially tracked 3DUS system for automated whole-breast 3DUS imaging.

Results: The mean tracking error (SD) was 0.87 ± 0.52 mm, 0.70 ± 0.46 mm, 0.53 ± 0.48 mm, 0.34 ± 0.32 mm, 0.43 ± 0.28 mm, and 0.78 ± 0.54 mm (N=4 position measurements, each) for J_{1-6}, respectively. Compound motions using all joints simultaneously resulted in a tracking error of 1.08 ± 0.88 mm (N=20) within the system's accessible workspace for bedside imaging. Spatial-based registration of acquired 3DUS images resulted in a mean TRE of 1.28 ± 0.10 mm. In the tissue-mimicking breast phantom, multi-image registration and fusion enabled whole-breast 3DUS imaging and multi-planar visualization in sagittal, axial, and coronal views. The first utility of the proposed spatially tracked whole-breast 3DUS approach was demonstrated in a healthy male (Fig. 2a) and female (Fig. 2b) volunteer study. In the male volunteer, a breath-hold at full-inspiration was employed for each 3DUS acquisition, which took 12 seconds per scan. In the female volunteer, a breath-hold at full-inspiration was not possible due to compression of the breast with the 3DUS scanner, thus, a breath-hold at half-full-inspiration was employed. However, breathing motion was still observed during the breath-hold, and post-acquisition translations (<4 mm) were applied to correct for the misregistration identified in whole-breast 3DUS image (Fig. 2b).

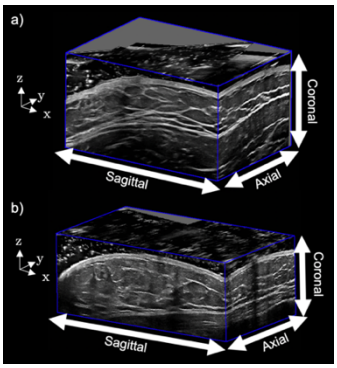

Fig. 2: Whole-breast 3DUS image of the healthy (a) male and (b) female volunteer study and standard multi-planar reconstruction views: axial, sagittal, and coronal view.

Conclusion: This work shows potential utility as an alternative, cost-effective bedside point-of-care (POC) approach for whole-breast 3DUS in women with dense breasts. Current work is focused on evaluating the quality of the whole-breast 3DUS images, developing a robust 3DUS acquisition protocol to address limitations in tissue deformations and motion, and performing a clinical feasibility study to evaluate its diagnostic performance accuracy as an alternative, whole-breast 3DUS method compared to screening mammography.

[1] S. Nazari, P. Mukherjee (2018) Breast Cancer. 25(3) 259–67. [2] S. H. Kim, H. H. Kim, W. K. Moon (2020) Korean J. Radiol, 21(4)15–24. [3] A. Fenster, G. Parraga, J. Bax (2011) Interface Focus. 2011. [4] D. W. Rickey, et al. (1995) Ultrasound. Med. Biol, 21(9) 1163–76.

An open-source testbed for developing image-guided robotic tumor-bed inspection

Laura Connolly, Amoon Jamzad, Arash Nikniazi, Rana Poushimin, Andras Lasso, Kyle Sunderland, Tamas Ungi, Jean Michel Nunzi, John F. Rudan, Gabor Fichtinger, Parvin Mousavi
Queen's University, Kingston Ontario

INTRODUCTION: Delineating tumor margins intraoperatively is a challenging task in many soft tissue cancer surgeries because of tissue deformation and mobility. We hypothesize that a combined approach of imaging, machine learning and cooperative robotics can help mitigate this challenge by enabling intraoperative tissue scanning of the tumor bed to identify and localize residual cancer cells. To realize this system, we develop an open-source testbed and demonstrate its viability with a combined optical and acoustic imaging approach for tissue scanning. Combining optical and acoustic imaging is beneficial in this application because it can help characterize the tissue at the surface layer while providing depth information about the anatomy being imaged [1]. For tumor bed inspection, this is necessary and make it possible to identify potentially residual cancer cells, and how far they penetrate the surrounding anatomy. In this study, we focus on the implementation of the imaging and analysis portion of the testbed and discuss its extension to a complete system.

METHODS: The goal of this testbed is to enable parallel flow of multiple imaging inputs that are spatially registered using robotics and temporally synched. To deploy this system, we make use of 3D Slicer for visualization as well as SlicerIGT (http://www.slicerigt.org/wp/) to stream imaging inputs (Figure 1). These tools also offer the flexibility to swap out the imaging modality in the system easily. Signal processing and data fusion can then be done with artificial intelligence (AI) tools in SlicerAIGT (https://github.com/SlicerIGT/aigt) which enables direct communication between AI models and imaging inputs in 3D Slicer. To demonstrate the technical viability and function of this testbed, we investigate the use of a combined temporally enhanced ultrasound (TeUS) imaging [2] and broadband spectroscopy to detect tissue heterogeneity in animal models. Tissue phantoms, made up of heterogeneous tissue (beef, turkey, beef on top of turkey and turkey on top of beef) are imaged with throughput broadband spectroscopy and ultrasound. Following this acquisition, the absorption of broadband light is computed to characterize the surface tissue optically. Additionally, the TeUS signals from the tissue are used to classify pixels in the US images according to their tissue type with a simple support vector machine (SVM).

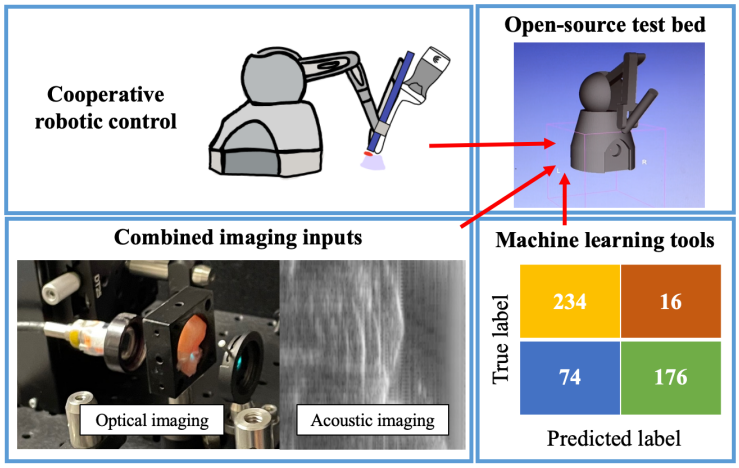

Figure 1: Concept for open-source testbed using combined optical and acoustic imaging as a sample use-case.

RESULTS: Using this test bed, we were able to successfully demonstrate a tumor bed inspection system that deploys combined optical and acoustic imaging with machine learning. More specifically, the absorption curve for each broadband acquisition showed distinct separability for every tissue phantom and our trained SVM could successfully classify 82% of the ultrasound pixels in the TeUS images according to their tissue type (Figure 1 – bottom right).

CONCLUSIONS: These preliminary results demonstrate the viability of this testbed for robotic tissue scanning in addition to the potential usage of combined optical and acoustic imaging for tissue recognition. To achieve this, we are currently working on using this imaging system as the input for the cooperative robotic control scheme.

ACKNOWLEDGEMENTS: L. Connolly is supported by an NSERC CGS-M award. G. Fichtinger is supported as an NSERC Canada Research Chair. This work was funded, in part, by CANARIE's Research Software Program.

REFERENCES:

[1] F. Geldof et al. "Combining diffuse reflectance spectroscopy and ultrasound imaging for resection margin assessment during colorectal cancer surgery," *Multimodal Biomed. Imaging XVI*, vol. 11634, no. 9, p. 116340K, Mar. 2021.

[2] S. Azizi et al., "Deep recurrent neural networks for prostate cancer detection: Analysis of temporal enhanced ultrasound," IEEE Trans. Med. Imaging, vol. 37, no. 12, pp. 2695–2703, Dec. 2018.

The CathPilot: Performance Characterization and Comparison to Conventional Catheters

James J. Zhou[1], Amaar Quadri[2], Alykhan Sewani[1], Yara Alawneh[1], Rene Gilliland-Rocque[1], Christopher Magnin[3], Andrew Dueck[4], Graham A. Wright[4], M. Ali Tavallaei[1,4]

[1]Ryerson University, [2]University of Waterloo, [3]Magellan Biomedical Inc., [4]Sunnybrook Research Institute

Introduction: Many catheter-based cardiovascular interventions have high failure (~20%) [1] and complication rates (~30%) [2]. This is primarily due to the challenges of accurate device steering and navigation. The long and flexible interventional devices (e.g., catheters and guidewires) engage with the tortuous anatomy along their length and are manipulated remotely from outside of the patient's body. This constrains the reachable workspace of the device tip and reduces its controllability. Visualization is also limited as the procedures are typically guided with 2D projection x-ray. To address these challenges our team has developed a new steerable catheter: the CathPilot. In this research, we evaluate the CathPilot's performance and compare it to conventional devices in an *ex-vivo* phantom model.

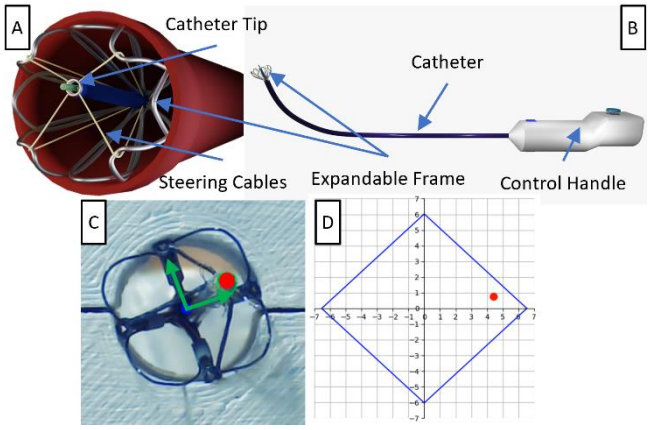

Fig. 1. CathPilot Concept. A) expandable frame deployed in the vessel lumen. B) complete Cath-Pilot device with the expandable frame, catheter, and control handle. C) Real-time position of the catheter tip with respect to principal axes measured with a camera. D) 2D position output from the CathPilot's tracking system to show device position within its workspace.

Methods: The CathPilot is a cable-driven parallel mechanism with an expandable frame that is delivered to the site of interest using a delivery sheath. Once extracted from the sheath, it expands and acts as a mechanical reference for local manipulation and tracking of the device (Fig. 1A-B). The CathPilot has a steering system that simultaneously adjusts the four cables with a single user input which permits remote manual operation. Rotary encoders with an accuracy of ±0.02º (0.0017 mm/cable) track the cable positions to provide feedback of the catheter position within the device's workspace [3] (Fig. 1C-D). We assess the device's reachable workspace and its position tracking accuracy using a camera (with 0.07 mm resolution) aimed at the device's workspace (Fig. 1C). To model different anatomies, the catheter shaft was constrained to three different shape profiles (i.e., straight, S shape, and 90º bend). For each profile, to simulate different vessel sizes, the frame was constrained to four different opening diameters of: 10 mm, 12.5 mm, 15 mm, and 17.5 mm. Ultimately, we compared the CathPilot's performance to both a non-steerable catheter as well as a steerable catheter within an occluded vessel phantom model. The occlusions placed at the end of the vessel model (I.D. 10 mm) contained a hole of 1.25 mm at various locations (four occlusions used) (Fig. 2A-B). Three users were blinded to the target hole locations and asked to cross them with the guidewire using each method (n=5). We compared crossing times and success rates.

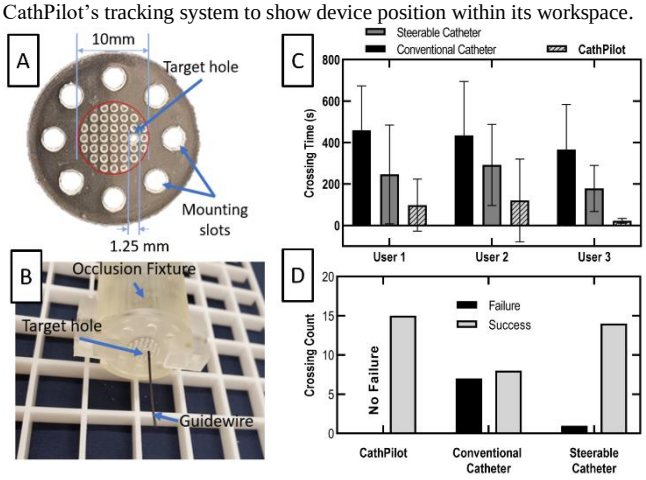

Fig. 2. A) angioplasty target with 10 mm ID and 1.25 mm target hole. B) occlusion fixed mounted at the end of artery phantom. C) average crossing time for different methods and users (n=5). D) success and failure rates for different devices.

Results: The CathPilot provides accurate steering with submillimetre accuracy irrespective of the path tortuosity and constraining vessel size with complete coverage of the expandable frame workspace shown in Fig. 1C. The average position tracking errors averaged for all catheter shaft profiles were 0.20 mm, 0.27 mm, 0.38 mm, and 0.35 mm for the 10 mm, 12.5 mm, 15 mm, and 17.5 mm vessel diameters, respectively. With the CathPilot, users were able to reach and cross the targets significantly faster ($p = 0.002$, two-way ANOVA, (Fig. 2C). In contrast to conventional methods, the users were always successful in reaching the targets with the CathPilot (Fig. 2D).

Conclusions: The CathPilot promises to overcome the major limitations in steering and navigation of conventional devices and allows for precise control and tracking of the device tip relative to the anatomy. In our ex-vivo validation experiments, the CathPilot significantly outperformed conventional devices.

References: [1] Bradbury *et al., J. Vasc. Surg.*, 2010. [2] Gupta *et al., Circ. Arrhythmia Eletrophysiol.*, 2013. [3] AS5048B, AMS, Premstaetten, Austria.

Design of a Novel Side-Looking Catheter for Fenestrated Endovascular Aneurysm Repair Procedures

Yara Alawneh[1,2], Andrew D. Dueck[1], Graham A. Wright[1], M. Ali Tavallaei[1,2]
[1]Sunnybrook Research Institute, Sunnybrook Health Sciences Centre, [2]Department of Electrical, Computer, and Biomedical Engineering, Ryerson University

Background: Fenestrated Endovascular Aneurysm Repair (FEVAR) is a very challenging catheter-based procedure that treats complex cases of thoracoabdominal aortic aneurysms (TAAA). This repair procedure has an increased risk of mortality and morbidity [1]. Patients undergoing this procedure are prone to developing various postoperative complications such as renal impairment and limb ischemia [2]. Fenestrated EVAR has been characterized as the highest-dose procedure performed by vascular surgeons [3]. Misalignment between the fenestration and targeted vessel can increase the length of the procedure and the number of catheter maneuvers needed to cannulate the vessel. To overcome these limitations, we have designed a novel side-looking catheter, *SideEye*, based on the **e**xpandable **ca**ble-**d**riven **pa**rallel **m**echanism (**X-CADPAM**) concept [4]. The expandable frame supports the cables that steer the inner catheter at different positions when tensioned (Fig. 1). The inner catheter lumen allows for the passage of a guidewire and other interventional devices.

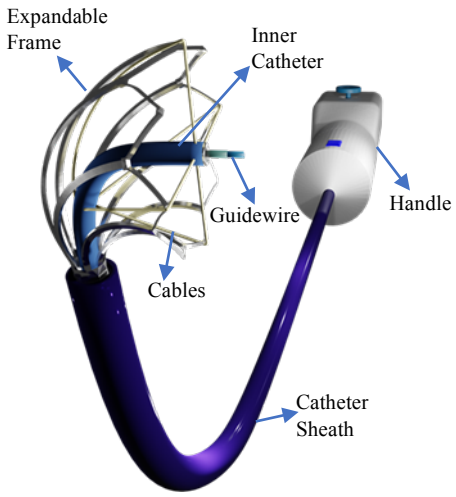

Fig. 1. SideEye Catheter

Methods: The expandable frame structure is made of a nitinol tube with a thickness of 0.3 mm. The stent cut on the nitinol tube was designed on SolidWorks then exported to ANSYS WB to start the shape setting process. The simulations consisted of first expanding the stent cut to an opening diameter of 15 mm, then deforming it at a 90-degree angle to get the desired shape. To validate the side-looking design, more simulations were performed to test for (1) the force-deflection relationship of the frame when cables are tensioned with a force of 2.84 N, and (2) the maximum force required for a 9F sheath to collapse the side-looking frame.

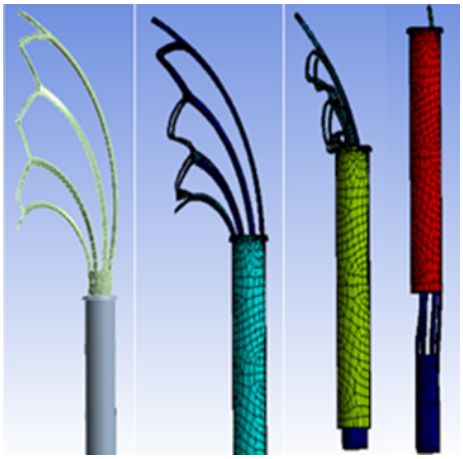
Fig. 2. 9F sheath collapsing the side-looking expandable frame with an opening diameter of 15 mm.

Results: The simulation results obtained from ANSYS WB showed a maximum deflection of 0.26 mm of the frame when cables are under tension. The maximum force required to retract the frame within the sheath and collapse the side-looking frame was 24 N (Fig. 2).

Conclusion: Simulation results demonstrated the feasibility of the design and proved that the expandable side-looking frame, at the size of 15mm, can maintain rigidity when the cables are actuated. It also revealed that a small-sized catheter sheath can smoothly collapse the widely expanded frame with a tolerable force.

Significance: The *SideEye* catheter promises improvements in accuracy and control over the device position, ultimately leading to reduced procedure times and increased success rates. Improving the efficiency of EVAR procedures will also lead to a significant reduction in postoperative complications and help reduce radiation dose and fluoroscopy time.

References: [1] Patel et al., *J Vasc Surg,* 2011.[2] Piffaretti et al., *J Vasc Surg,* 2012. [3] Kirkwood et al., *J Vasc Surg,* 2013. [4] Roy et al., *J Vasc Surg,* 2019

Open-Source Software for Analysis of Mass Spectrometry Imaging

Mackenzie Sharp, Amoon Jamzad, Parvin Mousavi
School of Computing, Queen's University, Kingston, ON, Canada.

Introduction: Mass spectrometry imaging (MSI) differs from most histochemical techniques as it differentiates molecular modifications, linking molecular data and the spatial distribution of analytes without requiring labels of targeted compounds [1]. Proteomic analysis relies on the use of MSI to identify specific disease markers or intervention targets. There is no user-friendly software solution for end-to-end analysis of MSI data. We propose a software implemented in a free and open-source 3D Slicer platform [2], enabling users without extensive background to run robust data exploration, visualization, and histopathology correspondence (preprocessing and tissue registration), build predictive models and visualize results, all in one environment. Users with technical background can customize the software according to their needs. We present the requirements of our software and demonstrate its advantages, compared to the current standard.

Methods: We are using 3D Slicer's environment, medical imaging processing software to implement the full analysis pipeline of DESI data as one of the MSI modalities [2]. Proposed software functionalities stem from needs of experts in the field, who exhibited a demand for a single platform solution. Required features of the developed module are data I/O, visualization, registration of MSI to pathology, and predictive model training and validation. First the user imports the DESI data in .txt format, along with the corresponding annotated histopathology images. Then mass spectra can be preprocessed and visualized as overlaid single-ion images, or a representative multi-ion PCA image. DESI images are then spatially correlated to annotations through landmark registration. The user then can segment regions of interest (ROI) based on the histopathology labels to generate a mass spectral dataset. The dataset and corresponding ROI masks can be exported for data backup, to be used in other platforms or further adjusted. The labels and corresponding DESI mass spectra can be used for training and evaluation of predictive models. The software provides the user with several predefined classification algorithms such as PCA/LDA and Random Forest for tissue identification. Lastly, models can be saved for deployment on prospective datasets.

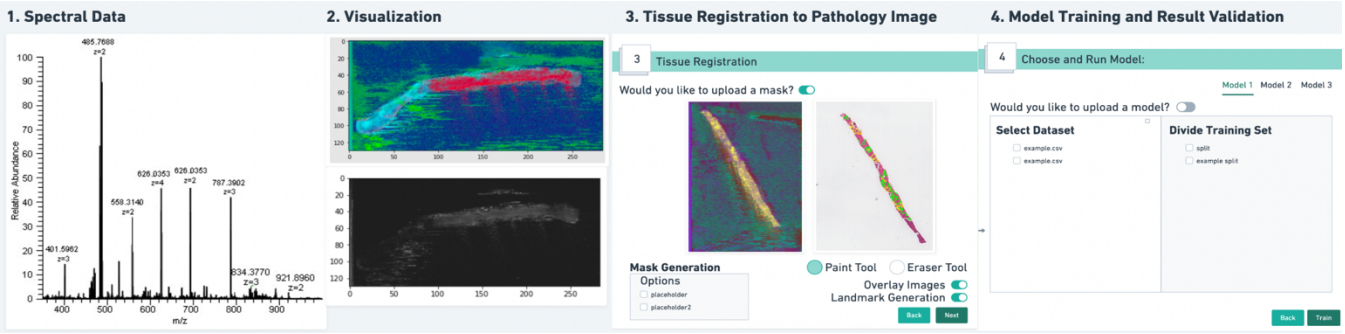

Fig 1: A schematic view of the software showing steps in order of use. Visualization tab shows current implementation visualization of DESI data as PCA and single ion image.

Results: As this is an ongoing project the current version has visualization and modelling functionality with work into tissue registration and dataset generation imminent. The single-ion visualization portion of the method will work like the available commercial software, while allowing multivariate representation of MSI data for more exploration. In addition, the spatial registration of MSI images and histopathology annotations (that is currently done in separate platforms by user's visual estimation) will be implemented in a single environment reducing spatial error. Also, in addition to exporting the paired mass spectra and pathology data, the software can export the pixel location of spectra, which is unavailable in commercial software. Development is coupled with consultations of experts in the field with end-user testing forthcoming.

Conclusion: This software allows utilization of open-source platform for end-to-end visualization, analysis of MSI data, adds flexibility and more robust features to the current pipeline such as dataset generation, and allows for frequent updates and a large client base. Improvements include removing the need for multiple platforms for various tasks and transition of data between them by providing all functionality in a single environment.
References: [1] D. R. Ifa *et. al.* Analyst, 135(4):669-81, 2010. [2] A. Fedorov *et. al.* Magn Reson Imaging, 30(9):1323-41, 2012. [3] N. Morse *et. al.* Lab Invest, 99(10):1561-1571, 2019.

Building a Platform for Medical Imaging Federated Analysis

Jenny Lee (a), Brandon Driscoll (a), Michael Andersen (a), Ever Liu (b), Xun Lin (a), Carlos Uribe (b,c,d), Julia Publicover (a) Bradley Wouters (a)

(a) QIPCM, Techna Institute, University Health Network, Toronto. (b) QURIT, BC Cancer Research Institute, Vancouver (c) Functional Imaging, BC Cancer, Vancouver. (d) Department of Radiology, UBC, Vancouver

Introduction: The Digital Health and Discovery Platform (DHDP) initiative focuses on bringing together health researchers and scientists from across Canada to enable data-driven discoveries for personalized medicine. This can result in cures for cancer and other diseases. Medical imaging is a key component to extract biomarkers that can be used to create predictive models for therapy outcomes. However, given the nature of the data, it is not always feasible for different institutions to share it and have access to a larger dataset that will benefit the creation of the models. QIPCM and BC Cancer have been prototyping a platform for medical imaging federated analysis. We aim to provide a learning opportunity on how to deploy a broader vision for data sharing and collaborative research where each institutions maintains governance of their own data. Here, we study and present the server architecture and software components required to build this platform.

Methods: Key requirements to enable this federated data analysis platform include: (1) the use of open-source software, (2) standardized DICOM communication and identity authentication protocol on modern secure web-based applications, (3) each institution maintaining governance of its own data, (4) single sign-on using own institution credential, (5) responsibility of patient health identifier (PHI) risk at each institution, and (6) network security measures. The OHIF viewer (OHIF.org) is a basic radiological web-based image viewer and it does not require installation on a user's workstation. OHIF is an open source extensible imaging platform where we added PET/CT fusion functionality.

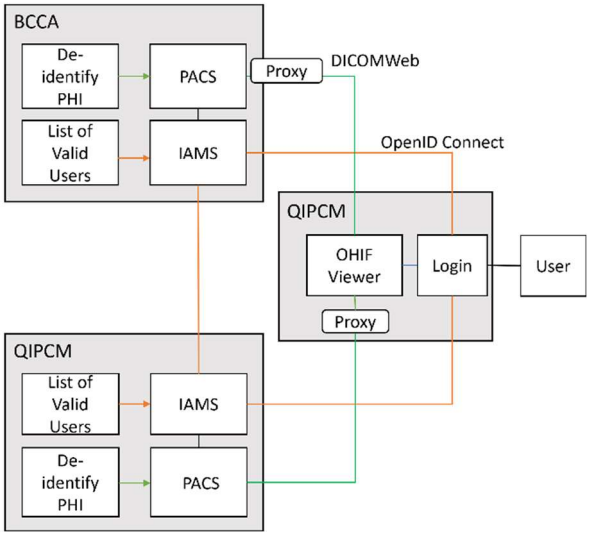

Figure 1: Diagram of the architecture.

Results: Figure 1 summarizes the proposed architecture. Communication between the Picture Archiving and Communication Servers (PACS) and the OHIF viewer was implemented using the DICOMweb protocol. Each center is responsible for removing patient identifier from data before storage at PACS. Each center is also capable of granting user access to its data cohorts through an identity access management system (IAMS) that is protecting their individual PACS. Thus, the IAMS contains a list of valid users from each institution. OpenID Connect is used as the identity authentication protocol, which features federated identity management to enable user to sign on once and gain access to PACS across both institutions. Network security measures include data encryption and the use of proxy servers hiding the PACS from the end-user viewer. We have successfully implemented this architecture. To test this platform, each institutions creates 3 different data cohorts with access granted to all members, granted to own institution's member only, and granted to other institution's member only. Our testing demonstrates members can sign-on from our OHIF viewer website using their institution's credential only once, and then members can view images stored on other institution's PACS according to our planned test cases.

Conclusions: The proposed architecture is a successful working prototype. Technical expertise in DevOps tools and IT support at each center are important to install and maintain software and configure servers. Next steps include contouring functionality on the viewer, prepacking a tool suite for the onboarding of new centers, and review for PHIPA compliance.

Open Health Imaging Foundation (OHIF) V3: Workflow-centric Web-based Medical Imaging Platform

Alireza Sedghi[1], Erik Ziegler[1], James Hanks[1,2], Daniel Rukas[1,2], Trinity Urban[1-4], Danny Brown[1], James Petts[1], Steve D. Pieper[1], Rob Lewis[1], Chris Hafey[1], and Gordon J. Harris [1-4]

[1]Open Health Imaging Foundation, Boston, MA, [2]Massachusetts General Hospital, Boston, MA, [3]Tumor Imaging Metrics Core, Boston, MA, [4]Precision Imaging Metrics, Boston, MA

Introduction: Open Health Imaging Foundation (OHIF) provides an extensible open-source framework to build zero-footprint web applications that can be used to perform various cancer imaging tasks such as lesion annotation and image segmentation. The user-centric design of OHIF facilitates quick adoption among end users, which are accustomed to efficient tools with user-friendly interfaces.

Methods: As of its current version, v2, OHIF provides functionality to the application via "extensions"; as a result, each time an OHIF application is customized for a particular use case and user interface, the developers need to fork the OHIF codebase. To address this limitation, the latest version of OHIF (v3) has been re-architected to support the development and sharing of task-specific workflow "modes". In OHIF v3, "modes" group extensions and custom UI into a specific route in the browser, and multiple modes (routes) can be present within a single application.

Results: An example of PET/CT mode within OHIF v3 (registered at a specific route such as `/pt-ct`) is illustrated in Figure 1, where the hanging protocol engine hangs the study series according to a predefined layout. Each column has synchronized Pan/Zoom tools, and the PET maximum intensity projection (MIP) can be seen on the right. In addition, other use cases can be presented at the same time as part of the same application (e.g., prostate review mode at `/prostate` with a different layout, panel, etc.) and the user can open a study in a desired mode.

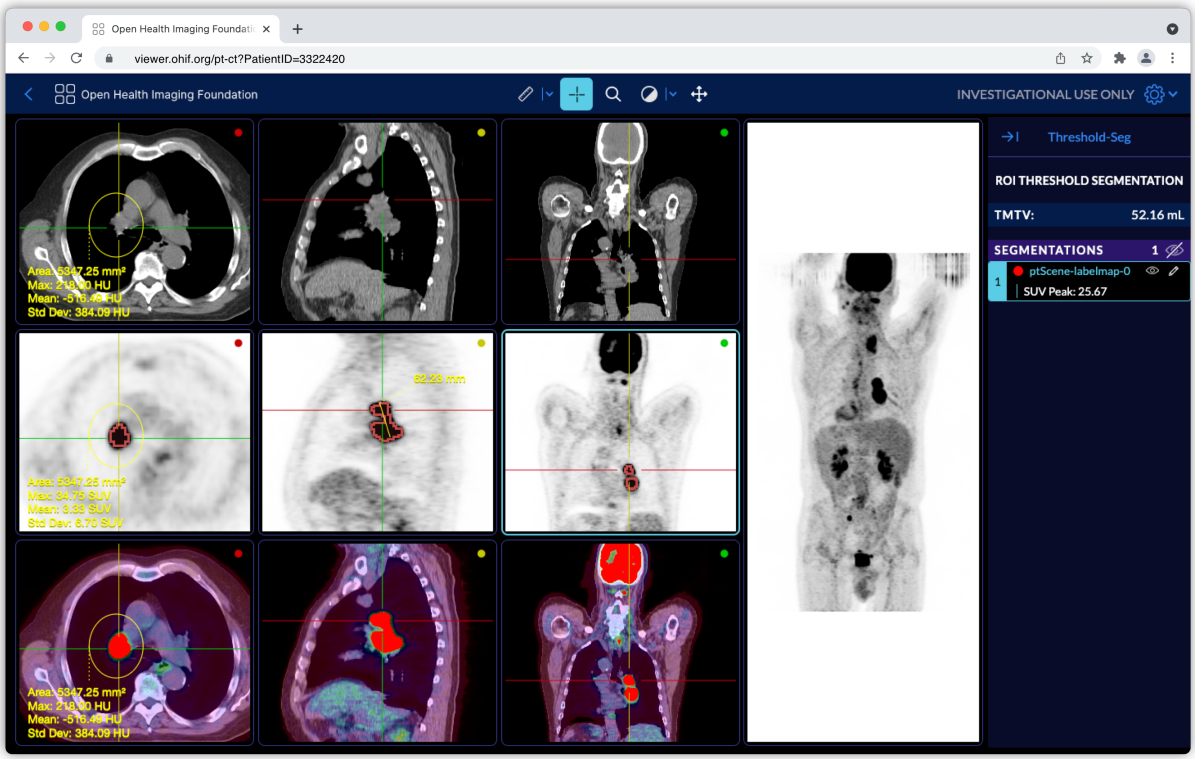

Conclusion: In order to facilitate community contribution and reduce the barriers of development, OHIF-v3's architecture is designed to make components easily interchangeable according to specific workflow and use case requirements. More information can be found in OHIF's documentation page at `https://v3-docs.ohif.org/`.

Review of research tools for computer-assisted interventions

Zaiba Amla, Elodie Lugez
Ryerson University

Introduction: The interest in Computer-Assisted Interventions (CAI) continues to grow significantly. As a result, various commercial and research-only software tools have been developed. Due to the large number of software available and the wide range of functionalities they enable, this paper aims to review some of the most widely used tools by the CAI research community. The tools to be reviewed are 3D Slicer and ITK-SNAP, which are free applications, and Analyze, a paid FDA-approved software. This paper will examine the features of the tools to aid others in choosing the appropriate program for their needs. We aim to compare these three tools based on their standard functionalities, strengths, weaknesses, user-friendliness, documentation, online support, licensing, extensibility, feature set, and efficiency.

Methods: Google Scholar was used to systematically search literature relevant to 3D Slicer, ITK-SNAP, and Analyze. Keywords include segmentation, registration, 3D imaging, and documentation, along with the respective software names. Although 3D Slicer and ITK-SNAP are both free, we included Analyze, a paid application, to compare their differences. Furthermore, we tested each software for the main functionalities they enable, including the following: segmentation and registration as well as additional tools the application provided. We recognized the applications for their user-friendliness, efficiency, effectiveness, and reliability. We uploaded an abdominal magnetic resonance image (MRI) in .dcm file format [1][2] to test our criteria. Segmentation was tested manually using the threshold function in 3D Slicer, ITK-SNAP and Analyze. To test registration, we aligned two MR images of the same subject. User-friendliness was established by evaluating the applications' ease of downloading and navigation. Efficiency and effectiveness were rated based on the interaction of the functionalities, and any discrepancies were noted. Reliability was evaluated by testing functionality and performing the same task several days later to see if we could replicate the results.

Results: In ITK-SNAP, segmentation can be done pixel by pixel, ensuring accuracy. 3D Slicer provides a 'drag and hold' function, making segmentation effortless. All softwares performed registration, but it was the easiest to do with 3D Slicer. As a first-time user, 3D Slicer was difficult to use and required experience for users to understand the software. ITK-SNAP and Analayze's interface was laid out neatly and was easier for users to navigate. 3D Slicer and ITK-SNAP made it easier for users to use features simultaneously, whereas Analyze has different windows for different functions. 3D Slicer proved to be very reliable; indeed, results could be replicated when performed days apart, as users can make modules for automating tasks. 3D Slicer took the longest to upload the MR image, around 20 seconds, compared to ITK-SNAP and Analyze, whose upload times were under 5 seconds each. Due to the popularity of 3D Slicer, there is widely available documentation for users, including active online forums and community support. ITK-SNAP does not have a full documentation suite but has sufficient information for its primary functions. Analyze provides complete documentation of their tool, outlining the use of every tool and icon. 3D Slicer has been extensively used in research projects, such as implant placement surgery [3]. Many studies have also been conducted using ITK-SNAP, including research for placenta placement surgery [4] and stroke-related lesions [5]. The versatility of Analyze has allowed for the benefit of 3D printed models of kidney carcinomas for surgeries [6].

Table 1: Rating of software based on proposed criteria

	3D Slicer	ITK-Snap	Analyze
Segmentation	2	3	1
Registration	3	1	2
User Friendliness	1	2	3
Efficiency & effectiveness	3	2	1
Reliability	3	2	1
Upload time	1	2	3
Documentation	3	1	2

Conclusion: This paper evaluated two free and open-source research tools and one with paid features. 3D Slicer provides an extensive collection of modules and should be used for complex tasks. ITK-SNAP is convenient for performing simple tasks such as segmentation and registration. Analyze is a user-friendly tool that is great for beginners but is not free of charge. Our findings provide insight to fellow researchers into selecting the appropriate tool for conducting their CAI projects.

References and acknowledgments:

[1] Linehan, M. et al. The Cancer Imaging Archive. (2016).
[2] Clark K, et al. Journal of Digital Imaging, Volume 26, Number 6, pp 1045-1057. (2013).
[3] Chen, X., et al. 10.1016/j.medengphy. 2017.01.005. (2017).
[4] Lu, T., et al. Translational andrology and urology, 9(2), 258–266. (2020).
[5] Pertsovsky, S. The University of Arizona. (2020)
[6] Lupulescu, C., and Sun, Z.. Australasian Medical Journal (Online) 14.8: 211-222. (2021).

The results published here are based upon data generated by the TCGA Research Network: http://cancergenome.nih.gov/."

Oral Session 5: Machine Learning

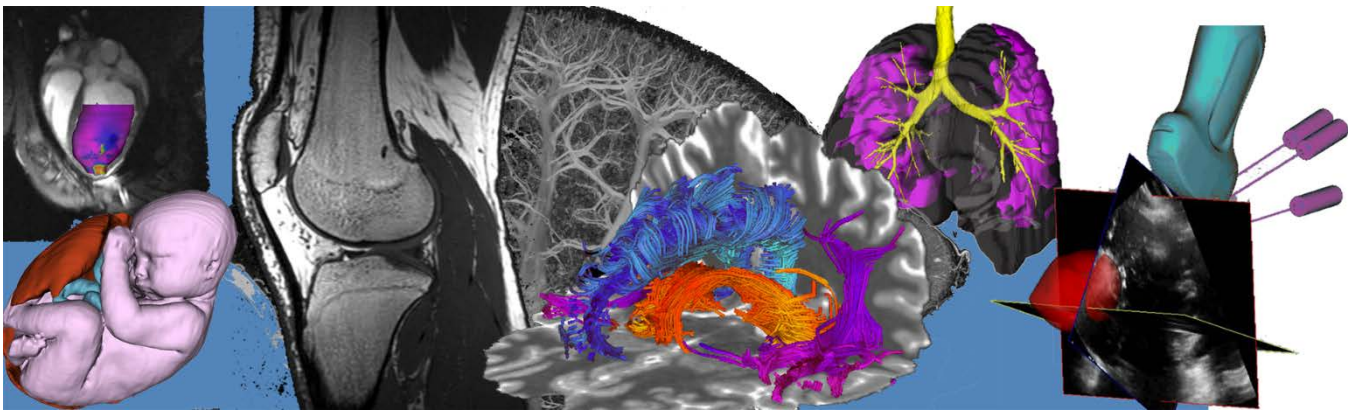

Fully Automated Multi-Organ Segmentation of Female Pelvic MRI using Transfer and Active Learning

Fatemeh Zabihollahy[1], Akila N. Viswanathan[1], Ehud J. Schmidt[1,2], Junghoon Lee[1]
[1]*Department Radiation Oncology and Molecular Radiation Sciences, Johns Hopkins University*
[2]*Department of Cardiology, Johns Hopkins University*

Purpose: Brachytherapy (BT) combined with external beam radiotherapy (EBRT) is the standard treatment for cervical cancer and has been shown to improve overall survival rates compared to EBRT only. Magnetic resonance (MR) imaging is used for radiotherapy (RT) planning and image guidance due to its excellent soft tissue image contrast. Rapid and accurate segmentation of organs at risk (OAR) is a crucial step in MR image-guided RT. In this study, we propose a fully automated two-step convolutional neural network (CNN) approach to delineate multiple OARs from T2-weighted (T2W) MR images.

Methods: We employ a coarse-to-fine segmentation strategy. The coarse segmentation step first identifies the approximate boundary of each organ of interest and crops the MR volume around the centroid of organ-specific region of interest (ROI). The cropped ROI volumes are then fed to organ-specific fine segmentation networks to produce detailed segmentation of each organ. A three-dimensional (3-D) U-Net is trained to perform the coarse segmentation. For the fine segmentation, a 3-D Dense U-Net is employed in which a modified 3-D dense block (DB) is incorporated into the 3-D U-Net-like network to acquire inter and intra-slice features and improve information flow while reducing computational complexity (Fig. 1). Two sets of T2W MR images (221 cases for MR1 and 62 for MR2) were taken with slightly different imaging parameters and used for our network training and test. The network was first trained on MR1 which was a larger sample set. The trained model was then transferred to the MR2 domain via a fine-tuning approach. Active learning strategy was utilized for selecting the most valuable data from MR2 to be included in the adaptation via transfer learning.

Results: The proposed method was tested on 20 MR1 and 32 MR2 test sets. Example segmentation results on MR2 are shown in Figs. 2. Mean±SD dice similarity coefficients (DSCs) are 0.93±0.04, 0.87±0.03, and 0.80±0.10 on MR1 and 0.94±0.05, 0.88±0.04, and 0.80±0.05 on MR2 for bladder, rectum, and sigmoid, respectively. Hausdorff distances (95th percentile) are 4.18±0.52, 2.54±0.41, and 5.03±1.31 mm on MR1 and 2.89±0.33, 2.24±0.40, and 3.28±1.08 mm on MR2, respectively. The performance of our method is superior to other state-of-the-art segmentation methods (Table 1).

Conclusions: We proposed a two-step CNN approach for fully automated segmentation of female pelvic MR bladder, rectum, and sigmoid from T2W MR volume. Our experimental results demonstrate that the developed method is accurate, fast, and reproducible, and outperforms alternative state-of-the-art methods for OAR segmentation significantly ($p<0.05$).

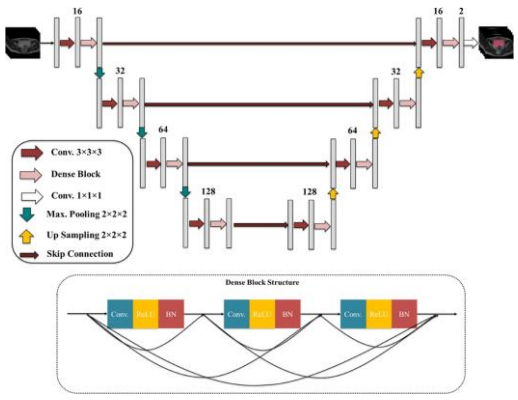

Fig. 1 The proposed three-dimensional (3-D) dense U-Net and dense block structures.

Table 1. Segmentation performance of three automatic segmentation methods compared to the expert radiation oncologist's manual segmentations.

	Bladder	Rectum	Sigmoid	Average of all three organs
3-D U-Net	0.85 ± 0.06	**0.87 ± 0.03**	0.78 ± 0.10	0.83 ± 0.03 ($p<0.05$)
3-D U-Net+DB	0.86 ± 0.13	0.87 ± 0.04	0.71 ± 0.12	0.81 ± 0.06 ($p<0.05$)
Proposed	**0.93 ± 0.04**	**0.87 ± 0.03**	**0.80 ± 0.10**	**0.87 ± 0.03**

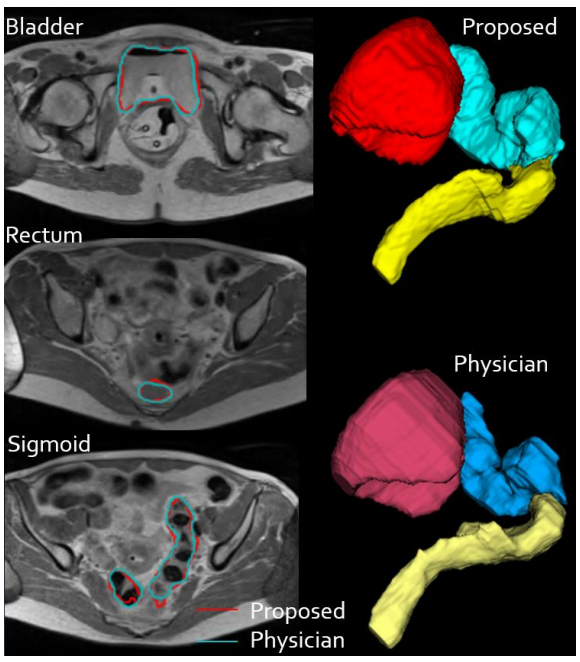

Fig. 2. Example segmentations and 3D renderings.

Automated fatty liver disease detection in Point-of-Care ultrasound B-mode images

Miriam Naim Ibrahim[123], Raul Blázquez Garcia[2], Adi Lightstone[2], Ahmed El Kaffas, B.Eng PhD[2], Mamatha Bhat, MD, MSc, PhD, FRCPC[3], Eran Ukwatta, PhD, P.Eng[1]

1. College of Engineering and Physical Sciences, University of Guelph, Guelph, ON 2. Oncoustics Inc., Toronto, ON 3. Division of Gastroenterology, Department of Medicine, University of Toronto, Toronto, ON

INTRODUCTION: Non-Alcoholic Fatty Liver Disease (NAFLD) is a global health concern, with a prevalence rate of 25.24% worldwide [1]. NAFLD is the most common chronic liver disease, affecting 20% of the Canadian population. The rising incidence of NAFLD, an asymptomatic condition, has occurred in parallel with the rise in diabetes and obesity [2]. NAFLD causes the liver to become vulnerable to further injury, including liver inflammation and scarring. Over decades, clinically significant non-alcoholic steatohepatitis (NASH) can silently progress to liver cirrhosis, associated with mortality and requiring consideration of liver transplantation. Thus, early diagnosis is crucial to implement therapeutic strategies that prevent further disease progression. Current diagnostic pathways rely on incidental findings, specialty level care where transient elastography is applied, or diagnostic ultrasound (US) performed by a trained radiologist [3]. However, the increasing prevalence of NAFLD warrants the need for screening tools in the primary care setting. The purpose of this research is to provide automated fatty liver detection using highly accessible Point-of-care ultrasound (PoCUS) and deep learning methods.

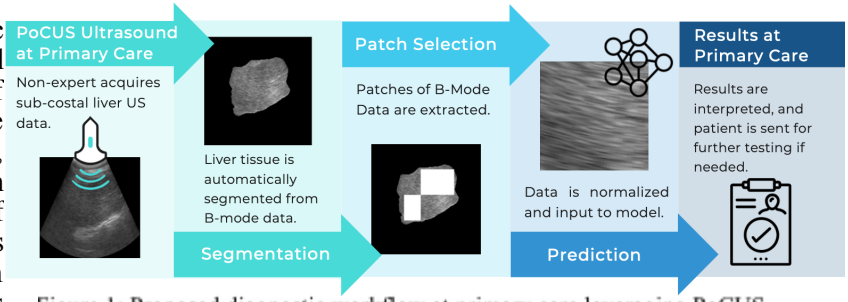

Figure 1: Proposed diagnostic workflow at primary care leveraging PoCUS

METHODS: The HIPAA-compliant dataset consists of 187 patients (BMI 23.4 ± 3.4, Age 41.9 ± 10.0), with five-second PoCUS videos recorded in four scan angles. All data was obtained through IRB-approved protocols at local data acquisition sites; all patients were consented before data acquisition. All PoCUS data was collected with standardized presets by Oncoustics (Toronto, Ontario), with 15cm depth, and 4 MHz frequency. Clinical standard assessment of steatosis was based on the controlled attenuation parameter (CAP) available on the FibroScan® elastography system (Echosens, France). Ninety-nine patients presented no steatosis with CAP values <238 and 86 patients had CAP values >290 suggesting S3 level steatosis. The subcostal scan angles were isolated, and 10 frames presenting optimal liver tissue visibility were manually selected for each patient. A basic U-Net segmentation algorithm (previously trained on 1400 labelled images from a similar PoCUS data-set) was used to segment liver tissue. A patch selection algorithm sectioned the tissue into 224x224 pixel images, yielding a total of 6009 patches. We considered 70% of patients for training and 30% for test data, with all samples from an individual patient assigned to either train or test. The Densenet-121 architecture was initialized with pre-trained ImageNet weights, and re-trained on the PoCUS dataset. The final classification layer was replaced with new layers including global average pooling, flattening, and batch normalization. Adam optimizer was used with a fixed learning rate of 0.00001 and a binary cross-entropy loss function was implemented. After obtaining initial classification results, majority voting was applied for patient-level results. The pipeline of our method is shown in Figure 1.

RESULTS: We achieved an AUROC of 0.93, accuracy of 92.7%, with 92.6% sensitivity and 92.9% specificity. To our best knowledge there are no comparable reports on the application of AI models with PoCUS images for the diagnosis of NAFLD. Similar studies utilizing expert acquired conventional US images and deep learning techniques include those by Che et al. [4], Constantinescu et al. [5] and Byra et al. [6], achieving AUROCs of 0.98, 0.93 and 0.97 respectively.

CONCLUSION: Our results demonstrate that a pre-trained deep learning network can reasonably classify steatosis from normal liver tissues in PoCUS B-mode images acquired by non-expert healthcare personnel (HCPs). The successful implementation of this software into PoCUS transducers would allow for early diagnosis through affordable and widely accessible screening, by a wide range of HCPs with minimal training. Future work includes incorporating radiofrequency (RF) data and CAP regression for tissue characterization.

REFERENCES: [1] Mitra, Souveek et al. "Epidemiology of non-alcoholic and alcoholic fatty liver diseases." Translational gastroenterology and hepatology vol. 5,16 (2020) [2] Mikolasevic, Ivana et al. "Nonalcoholic fatty liver disease and liver transplantation - Where do we stand?." World journal of gastroenterology vol. 24,14 (2018) [3] Pandyarajan, Vijay et al. "Screening for Nonalcoholic Fatty Liver Disease in the Primary Care Clinic." Gastroenterology & hepatology vol. 15,7 (2019) [4] H. H. Che, et al. "Liver disease classification from ultrasound using multi-scale CNN." International Journal of Computer Assisted Radiology and Surgery, vol. 16, 9 (2021) [5] E. C. Constantinescu et al. "Transfer learning with pre-trained deep convolutional neural networks for the automatic assessment of liver steatosis in ultrasound images," Medical Ultrasonography, (2020) [6] Byra, Michał et al. "Transfer learning with deep convolutional neural network for liver steatosis assessment in ultrasound images." International journal of computer assisted radiology and surgery vol. 13,12 (2018)

Evaluating Faster R-CNN for cataract surgery tool detection using microscopy video

H.Y. Lee[1], R. Hisey[1], M. Holden[2], J. Liu[3], T. Ungi[1], G. Fichtinger[1], C. Law[3,4]

[1]Laboratory for Percutaneous Surgery, School of Computing, Queen's University, Kingston, Canada
[2]School of Computing, Carleton University, Ottawa, Canada
[3]Department of Ophthalmology, Queen's University, Kingston, Canada

Introduction: Traditional methods of cataract surgery skill assessment rely on human expert supervision. This exposes the trainee to interobserver variability and inconsistent feedback. Alternative measures such as sensor-based instrument motion analysis promise objective assessment [1]. However, sensor-based systems are logistically complicated and expensive to obtain. Previous studies have demonstrated a strong correlation between sensor-based metrics and two-dimensional motion metrics obtained from object detection [2]. Reliable object detection is the foundation for computing such performance metrics. Therefore, the objective of this study is to evaluate the performance of an object detection network, namely Faster Region-Based Convolutional Neural Network (FRCNN), in recognition of cataract surgery tools in microscopy video.

Methods: Microscope video was recorded for 25 trials of cataract surgery on an artificial eye. The trials were performed by a cohort consisting of one senior-surgeon and four junior-surgeons and manually annotated for bounding box locations of the cataract surgery tools (Figure 1) The surgical tools used included: forceps, diamond keratomes, viscoelastic cannulas, and cystotome needles. A FRCNN [3] was trained on a total of 130,614 frames for object detection. We used five-fold cross validation, using a leave-one-user-out method. In this manner, all videos from one surgeon were reserved for testing and the frames from the remaining 20 videos were divided among training and validation. Network performance was evaluated via mean average precision (mAP), which is defined as the area under the precision/recall curve. Samples were considered correctly identified when the intersection over union (IoU) between the ground truth and predicted bounding boxes was greater than 0.5.

Table 1. Mean average precision (mAP) by tool

Tool	*mAP*
Forceps	0.61
Diamond Keratome	0.49
Viscoelastic Cannula	0.59
Cystotome Needle	0.96

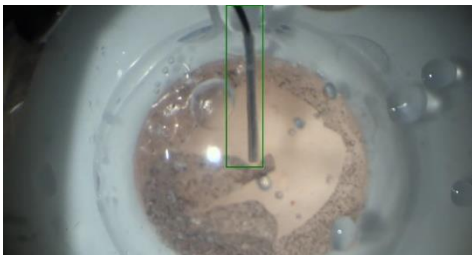

Figure 1. Manually annotated bounding box.

Results: The overall mAP of the network was 0.63. Tool-specific mAPs ranged between 0.49 and 0.96 (Table 1). The high accuracy in detection of the cystotome needle is likely due to the distinct size and shape of the tool tip. The diamond keratome had the lowest mAP of any of the tools recognized, however this may be attributed to variations in the appearance of the tool tip (Figure 2).

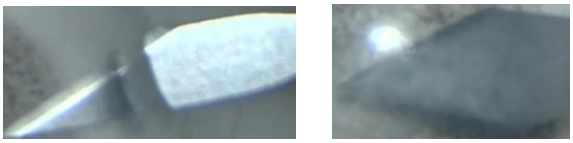

Figure 2. Right angle diamond keratome (left) and isosceles diamond keratome (right).

Conclusions: The FRCNN was able to recognize the surgical tools used in cataract surgery with reasonably high accuracy. Now that we know the network can sufficiently recognize the surgical tools, our next goal is to use this network to compute motion-based performance metrics. Future work seeks to validate these performance metrics against those obtained from sensor-based tracking and against expert evaluations. This serves as a first step towards providing consistent and accessible feedback for future trainees learning cataract surgery.

References:

[1] G. M. Saleh, et al, "Evaluating Surgical Dexterity During Corneal Suturing," *Archives of Ophthalmology*, vol. 124, no. 9, pp. 1263–1266, Sep. 2006.
[2] O. O'Driscoll *et al.*, "Object detection to compute performance metrics for skill assessment in central venous catheterization," in *SPIE Medical Imaging 2021*, Feb. 2021, vol. 11598, pp. 315–322.
[3] S. Ren, et al, "Faster R-CNN: Towards Real-Time Object Detection with Region Proposal Networks," *arXiv:1506.01497 [cs]*, Jan. 2016.

Magnetic Resonance T_1 Spectrum Analysis Using Neural Networks

Tristhal Parasram[1], Dan Xiao[1]
[1]Physics Department, University of Windsor, ON, Canada

Introduction: Quantitative analysis of the magnetic resonance (MR) relaxation time could reveal microscopic properties, and has significance in the study of the brain and related diseases, heart, and tumors [1]. A multi-component model, with a continuous relaxation spectrum, requires exponential analysis which is an intrinsically ill-posed problem. The traditional inverse Laplace transform (ILT) employs a nonnegative constraint and a user defined regularization parameter for spectrum smoothness. For T_1 analysis, it requires an additional phase correction pre-processing step. Extending our previous work using neural networks for exponential analysis [2], artificial neural networks (ANNs) have been trained to generate the multicomponent T_1 distribution spectra with low signal-to-noise ratio and only 8 input data points. The performance was evaluated across a large parameter range. In addition to superior computation speed, higher accuracy was achieved compared to the traditional method. This improved performance, with a significantly reduced number of input data points, will enable faster relaxation experiments.

Methods: Keras and NumPy were employed to create the networks, with an array of Inversion Recovery signal as input and the corresponding T_1 spectrum as output. The network was trained in a multi-step process alternating between simulated T_1 distributions consisting of narrow or wide peaks. Three log-normally distributed functions of random width, position and relative heights were summed to create T1 spectra of one, or two, or three peaks. 2 million simulated Inversion Recovery signals, with 8 inversion times (τ_1) logarithmically spaced across 3 orders of magnitude (10^3-10^6 μs), were employed in the training data. The signal equation is

$$s(\tau_1) = \left| \int_0^\infty a(T_1) \left(1 - 2e^{-\frac{\tau_1}{T_1}}\right) dT_1 \right| + \mathcal{E}(t),$$

where $a(T_1)$ is the spectrum to be solved, and ε is Rician noise. The signal magnitude was considered to eliminate the phase correction step as negative signals were expected with short inversion times. An example of the input and output is shown in figure 1. The loss function was the sum of mean squared errors of the T_1 spectrum, the T_1 decay signal compared to the ideal decay, a factor to punish negative values, and weighted total variation of the spectrum.

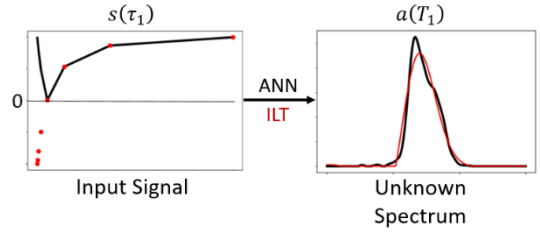

Figure 1. Inversion recovery data processing. Amplitude signal is used in ANN (black), while a phase correction is required ILT (red dots).

Results and Discussion: To analyze the performance across multiple T_1 values and determine the resolution limit of the ANN, spectra of varying peak positions were simulated with a fixed 1:1 area ratio. The individual peaks had a narrow width (0.2 log scale), which yielded the maximum resolution. The range of T_1 values was determined based on the range of inversion times. The shortest T_1 component should be no smaller than the first inversion time. Error maps for the log mean peak position and area were compared with the traditional ILT results, as shown in Fig. 2. The red line indicates the resolution limit below which two peaks can be distinguished. This resolution limit is approximately a factor of 3.5 for ILT and approximately 3.1 for ANN. Systematic errors occurred in ILT when the short T_1 component was below 3.35 (log scale) or the long T_1 component was above 5.65 (log scale), which were not apparent in the ANN results.

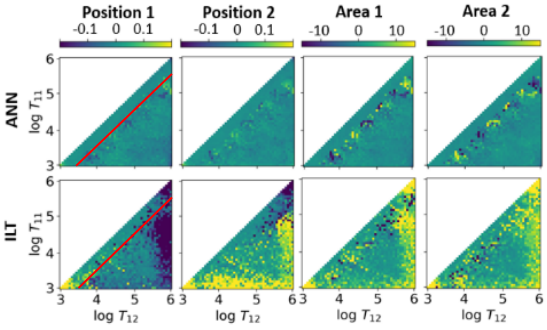

Figure 2. Error maps of simulated two-peak T_1 distribution with varying peak positions. The diagonal line represents two overlapping peaks. The red line is the resolution limit.

Conclusion: We demonstrated the effectiveness of ANNs for rapid analysis of continuous, multicomponent T_1 distributions with few datapoints in the presence of noise. The performance was evaluated across a large parameter space and was superior compared to the traditional ILT method without requiring phase correction. This technique can be extended to other multi-dimensional correlation analysis such as T_1-T_2-Diffusion correlation measurements and spatially resolved T_1 distributions for which few data points are essential to achieve reasonable experiment times.

References: [1] Cheng, JMRI, 36, 805-824 2012 [2] Parasram, JMR, 325, 106930, 2021

Oral Session 6:
Cellular and Molecular

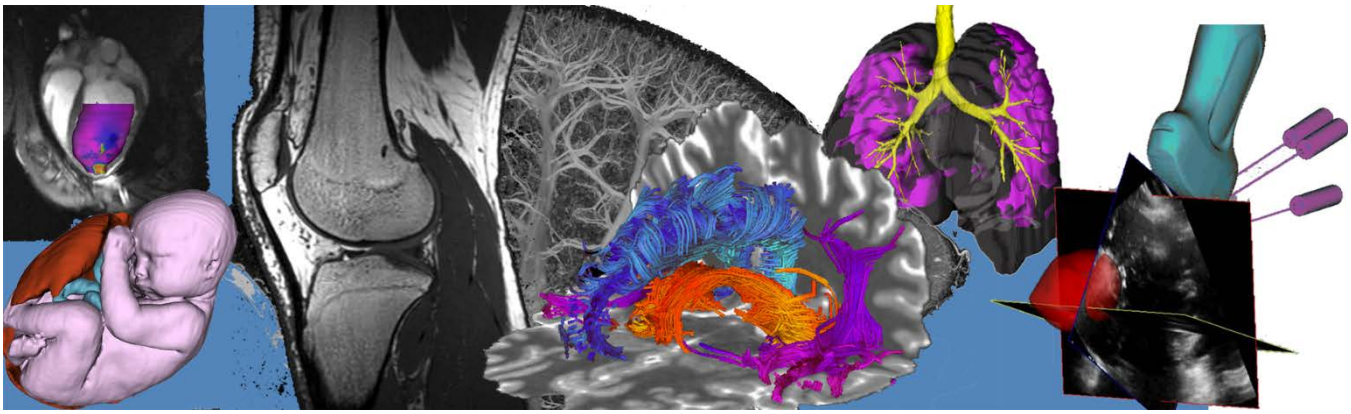

In vitro testing of novel manganese-derived paramagnetic contrast agents for MRI reporter gene imaging

McRae SW[1], Martinez F[2], Gale EM[3], Ronald JA[1,2], Scholl TJ [1,2,4]
1. Department of Medical Biophysics, Western University, London, Ontario
2. Robarts Research Institute, Western University, London, Ontario
3. Martinos Center for Biomedical Imaging, Massachusetts General Hospital, Boston, Maine
4. Ontario Institute for Cancer Research, Toronto, Ontario

INTRODUCTION: Preclinical models of disease have been invaluable for understanding the steps of disease progression, for discovering new mechanisms of disease spread, and for evaluating new therapies. There is a strong need for robust cellular imaging techniques that offer excellent spatial resolution and high sensitivity to support studies that require sensitive detection of engineered cells. Our group has shown that by means of cellular engineering with the MRI reporter gene OATP1 (organic anion transporting polypeptide 1), we can achieve highly sensitive detection of OATP-expressing cells in animal models over time. OATP1 facilitates intracellular localization of the gadolinium-derived paramagnetic contrast agent Gd-EOB-DTPA (*Primovist*) which leads to increased MRI signal of our engineered cells compared to surrounding tissues on T_1-weighted images (Nyström et al., 2019). Here we aim to further improve the detectability of engineered cells by developing and evaluating a novel suite of manganese-derived OATP1-targeted MRI probes (figure 1).

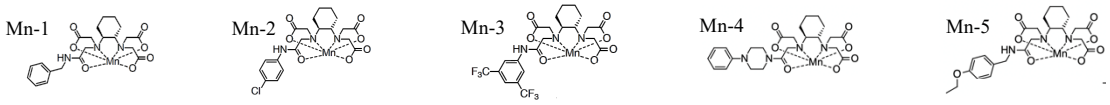

Figure 1: Structures of Mn-CDTA agents

METHODS: Human (MDA-MB-231) breast cancer cells were engineered with lentivirus encoding human OATP1B1 or OATP1B3. Upon confirming the function of the transporter, we completed high throughput testing of cell uptake of five novel manganese agents for comparison with Gd-EOB-DPTA. Cells were incubated in 1.6 mM of Mn-agent for 90 minutes with or without the agent and were then washed such that only intracellular manganese remained. Cells were then pelleted and imaged at 3T with a fast spin-echo inversion recovery (FSE-IR) sequence at fifteen inversion times to determine T_1. Additionally, we measured the T_1 relaxivity of the five novel manganese agents at low magnetic field strengths (0.23 mT – 1 T) using fast field-cycling relaxometry and at 3 T with FSE-IR. These data are analyzed to determine the best combinations of organic anion transporter (1B1 or 1B3), probe relaxivity (r_1), cellular uptake and preclinical dose for eventual *in vivo* imaging.

RESULTS: The average relaxivity of the five measured agents at 3 T was 2.99 ± 0.3 $mM^{-1}s^{-1}$, compared to the relaxivity of Gd-EOB-DTPA of 6.01 ± 0.1 $mM^{-1}s^{-1}$. Cells expressing the OATP transporter experienced moderate increases in R_1, with a preferential increase in transport through the OATP1B1 transporter. Agent uptake normalized to Gd-EOB-DTPA shows high uptake of Mn-1, Mn-2, and Mn-3 through OATP1B1 (figure 2).

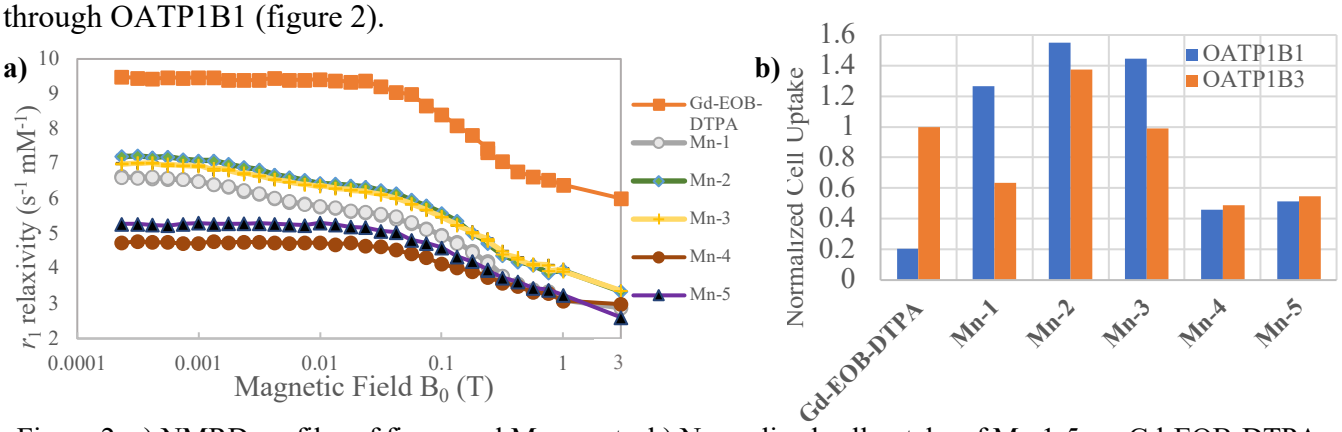

Figure 2: a) NMRD profiles of five novel Mn agents. b) Normalized cell uptake of Mn 1-5 vs. Gd-EOB-DTPA

CONCLUSIONS: Our *in vitro* data shows that despite the lower relaxivity of agents at 3 T, there was still strong uptake through OATP1B1. Moving forward, we hope to take advantage of the high uptake by administering agent *in vivo* at maximum safe preclinical doses. We aim to test the best reporter gene/probe combinations in mice bearing genetically engineered tumors to assess detection limits of this novel cell tracking technology and to measure liver uptake by endogenous OATP expression.

Imaging of Neuroinflammation in Chronic Traumatic Encephalopathy

Cassis Varlow,[1,2] Ashley C. Knight,[3] Paul McQuade[3] and Neil Vasdev[1,2]

[1]Azrieli Centre for Neuro-Radiochemistry, Brain Health Imaging Centre, Centre for Addiction and Mental Health, Toronto, ON., M5T 1R8; [2]Institute of Medical Science, University of Toronto, Toronto, ON., M5S 1A8; [3]Takeda Pharmaceutical Company, Cambridge, MA 02139, USA

Introduction. Chronic traumatic encephalopathy (CTE) is a neurological disorder associated with head injuries and is diagnosed upon autopsy. Positron emission tomography (PET) imaging of neuroinflammatory processes following brain injury could enable ante-mortem diagnosis of CTE for the first time, and critical insights into monitoring disease progression and therapeutic interventions. The goal of the present study is to evaluate four tritium-labeled PET tracers for neuroinflammatory targets: [^{3}H]PBR-28 for the 18 kDa translocator protein (TSPO), [^{3}H]L-deprenyl for monoamine oxidase-B (MAO-B), [^{3}H]CPPC for colony stimulating factor 1 receptor (CSF-1R) and [^{3}H]SMW-139 for the P2X7 purinergic receptor, using *in vitro* radioligand binding assays in pathologically diagnosed cases of human CTE brains.
Methods. Thin section (10 µM) autoradiography was employed to assess specific binding and tissue section distribution of [^{3}H]PBR-28, [^{3}H]L-deprenyl, [^{3}H]CPPC and [^{3}H]SMW-139 in post-mortem CTE frontal cortex. [^{3}H]PBR-28 activity was quantified by autoradiography and was correlated with TSPO expressing cells by immunohistochemistry. [^{3}H]L-deprenyl signal was detected by autoradiography and correlated with GFAP positive cells by immunofluorescence. TSPO cell-type expression was shown by immunofluorescent co-localization to Iba1, GFAP and CD68 positive cells. Target density (B_{max}) of TSPO and MAO-B in both CTE and healthy control (HC) tissue was quantified by saturation analysis in brain homogenates (25 µg tissue/reaction in a final assay volume of 1000 µL) where [^{3}H]PBR-28 and [^{3}H]L-deprenyl concentrations were increased from 0.05 nM to at least 10-fold the reported affinity.
Results. [^{3}H]CPPC demonstrated low specific binding (15.34 ± 8.12%; n = 4) and [^{3}H]SMW-139 had negligible radiotracer signal in fresh-frozen human post-mortem CTE tissues and were not further evaluated. [^{3}H]PBR-28 revealed high specific binding in both CTE (95.40 ± 1.87%; n = 11) and healthy controls (HC; 89.89 ± 8.52% , n = 3) and co-localized to TSPO immunostaining. TSPO expression was localized to Iba1, GFAP and CD68 positive cells, indicating microglial, astrocytic and macrophage expression in CTE. [^{3}H]L-deprenyl also displayed high specific binding in CTE (96.95 ± 1.43%; n = 12) and HC (93.24 ± 0.43%; n = 2), with the distribution co-localized to GFAP positive cells. Using [^{3}H]PBR-28 the B_{max} of TSPO in HC was 177.91 ± 56.96 nM (n = 7; mean ± SD) however, a highly variable B_{max} (345.84 ± 372.42 nM; n = 11; mean ± SD) was measured in CTE. [^{3}H]L-deprenyl quantified a MAO-B B_{max} of 304.23 ± 115.93 nM (n = 8; mean ± SD) in HC tissue and is similar to the B_{max} in CTE tissues (365.80 ± 128.55 nM; n = 12; mean ± SD). A two-sample t-test determined no significance in TSPO or MAO-B B_{max} values between HC and CTE (P > 0.05), albeit a trend of increased TSPO and MAO-B expression was observed in CTE compared to controls.
Conclusions. To our knowledge, this work represents the first *in vitro* evaluation of neuroinflammatory biomarkers for PET imaging in CTE tissue and reveals the variability in neuroinflammatory pathology of head injuries. PET imaging of TSPO and MAO-B in patients after head injuries could be used to quantify neuroinflammation and shows potential toward the ultimate goal of imaging CTE in the living human brain.

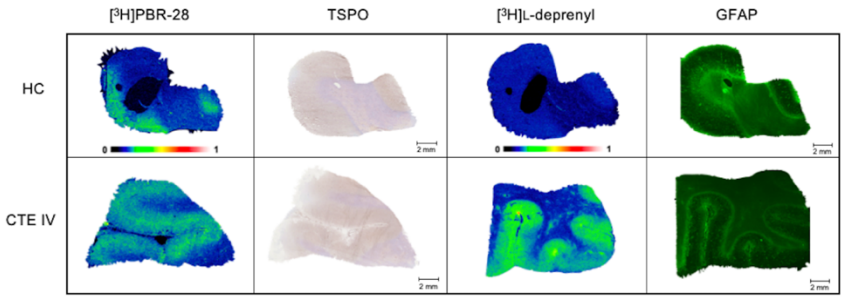

Figure 1. TSPO and MAO-B distribution in healthy control and CTE tissue by [^{3}H]PBR-28 autoradiography validated by TSPO immunostaining and [^{3}H]L-deprenyl autoradiography validated by GFAP immunostaining.

Analysis of Magnetic Resonance Relaxation Rates in Mammalian Cells Expressing Essential Magnetosome Genes

Q. Sun[1,2,3], P. Vivekanantha[1], S. Hassan[1], M. Ahmed[1], J. Yohans[1], N. Gelman[1,2], R.T. Thompson[1,2], F.S. Prato[1,2,3], D.E. Goldhawk[1,2,3]

[1]Imaging Program, Lawson Health Research Institute; [2]Medical Biophysics and [3]Collaborative Graduate Program in Molecular Imaging, Western University, London, Canada

Introduction: Magnetic resonance imaging (MRI) is ideal for non-invasively tracking cellular and molecular activities with high spatial and temporal resolution [1]. Nevertheless, enhancement of cellular contrast is required and may be achieved through manipulation of cellular iron [2]. For this, magnetotactic bacteria (MTB) possess genes that confer the ability to synthesize refined iron crystals within vesicles called magnetosomes [3]. Moreover, from this complement of bacterial genes, several are essential for magnetosome formation, including *mamE, mamI, mamL,* and *mamB* [4]. Using a mammalian cell model, we have shown that MamI and MamL co-localize and specifically interact within the intracellular compartment [5]. Here, we report the ability of essential magnetosome protein-protein interactions to potentiate the magnetic resonance (MR) signal.

Hypothesis: Essential magnetosome proteins interact in any cell type to form rudimentary magnetosome-like nanoparticles, providing a genetically-controlled contrast agent for molecular MRI.

Methods: MTB genes *mamE, mamI, mamL,* and *mamB* were previously cloned from *M. magneticum* sp. AMB-1 genomic DNA. EGFP-MamE, EGFP-MamI, and Tomato-MamL fluorescent fusion proteins were singly-expressed, and FLAG-MamL/EGFP-MamI were co-expressed, in the human MDA-MB-435 melanoma cell line using antibiotic selection. Appropriate protein expression was confirmed with western blotting and confocal microscopy, and protein-protein interactions were confirmed with the co-immunoprecipitation assay. Cells were cultured in the presence and absence of iron supplementation (250 µM ferric nitrate/medium). At harvest, cells were either mounted in a gelatin phantom for MRI at 3 Tesla (3T, Biograph mMR) [6] or analyzed by inductively-coupled plasma mass spectrometry (Analytical Services, London). Total cellular iron content was normalized to total cellular protein, quantified by the BCA assay. A custom MATLAB-based program (The Viewer) was used to obtain relaxation rates. Analysis of variance (ANOVA) and Tukey's post-hoc test were performed in GraphPad Prism 8.

Results: In the absence of iron supplement, total transverse relaxation rates (R2*) of mammalian cells expressing MamE, MamI, MamL, or MamI+MamL (Fig. 1) were no different than parental controls. However, in the presence of iron supplement (+Fe), cells expressing MamI or MamL showed a significant increase in R2* while their co-expression (MamI+MamL) or MamE alone did not.

Conclusions: Even when expressed in a foreign cell environment, the essential magnetosome-associated membrane proteins MamI and MamL each increase transverse relaxation rates in response to iron supplementation. Regardless, when co-expressed this contrast benefit is lost, suggesting that the interaction between MamI and MamL [5] may exert regulatory control over how iron is handled. Consistent with this possibility, MamE alone does not increase R2* although reported to have a role in iron-handling [7] and, like MamI, increases cellular iron content more than 20-fold over the parental control in response to iron supplementation (data not shown).

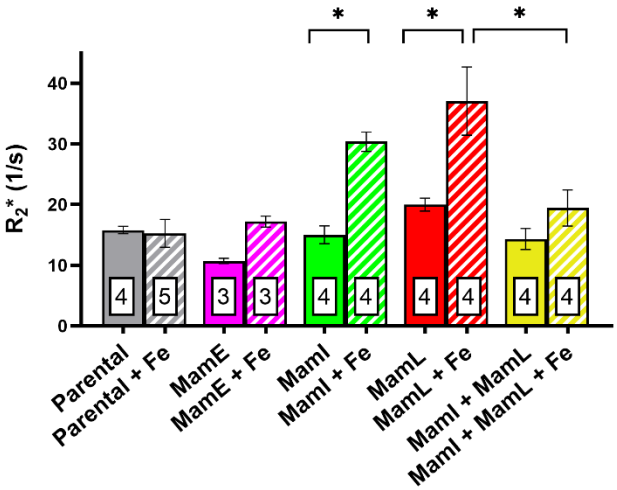

Fig. 1. Essential magnetosome genes influence transverse relaxation rates. Cells (Parental, grey; MamE, pink; MamI, green; MamL, red; MamI+MamL, yellow) were cultured in the presence (striped) or absence (solid) of iron supplementation prior to mounting in a gelatin phantom for 3T MRI. R2* values are the mean +/- SEM (n = 3-5 as shown within bars). * $p < 0.01$.

Future experiments will evaluate the MR signal in cells expressing all three genes (MamI+MamL+MamE) to determine whether their essential role(s) in magnetosome formation depend on complementary interactions.

References: [1] Goldhawk *et al* (2017) in Design and Applications of Nanoparticles in Biomedical Imaging, p. 187; **[2]** Alizadeh *et al* (2020) Sci Rep 10, 3163; **[3]** Goldhawk *et al* (2012) Nanomed Nanobiotechnol 4, 378; **[4]** Sun *et al* (2020) in Imaging by Light and Electromagnetics in Medicine and Biology, p. 201; **[5]** Sun *et al* (2021) ImNO 2021 **[6]** Sengupta *et al* (2014) Front Microbiol 5, 29; **[7]** Quinlan *et al* (2011) Mol Microbiol 80, 1075

CRISPR Editing of Chimeric Antigen Receptor T (CAR-T) Cells Expressing Human-Derived MRI and PET Reporter Genes

John J Kelly[1], Nourhan Shalaby[2], Ying Xia[1], Francisco Martinez[1], Justin Hicks[2,3], Timothy Scholl[1,2], John A Ronald[1,2,3]

[1]Robarts Research Institute and [2]Dept. of Medical Biophysics, University of Western Ontario, London, ON, Canada; [3]Lawson Health Research Institute, London, ON, Canada.

Intro: Chimeric antigen receptor T (CAR-T) cells have shown remarkable efficacy in treating blood-based cancers[1]. However, challenges of low effectiveness, accumulation in normal tissues, and insufficient migration into and treatment of solid tumours remain[2]. Translationally relevant imaging technologies could enable prediction of patient response, as well as better evaluation of new CAR-T designs. Our objective was to develop a highly efficient CRISPR system for integrating multiple transgenes at loci known to improve both safety (using targeted vs viral integration) and efficacy of human CAR-T cells, whilst also making them "visible" with clinically relevant imaging modalities. To improve efficacy, a CD19-targeting CAR was inserted at the *TRAC* locus, which simultaneously knocks-out the endogenous T cell receptor (TCR). For molecular-genetic imaging, human MRI, PET or preclinical bioluminescent reporter genes were incorporated into edited CAR-T cells.

Methods: T cells were nucleofected with ribonucleoprotein complexes and transduced with adeno-associated viral (AAV) particles. Each AAV contained a CD19CAR tagged with green fluorescent protein (GFP) and/or the organic anion transporting polypeptide 1B3 (*OATP1B3*) MRI reporter gene, sodium iodide symporter (*NIS*) PET reporter gene or *Akaluc* bioluminescent reporter gene. Editing efficiency was determined by flow cytometry and integration by PCR analysis. CD19+ human B cell lymphoma (NALM6) cells expressing firefly luciferase (*FLuc*) or Antares were engineered for CAR-T targeted *in vitro* and *in vivo* assays. Uptake of the PET tracer [18F]tetrafluoroborate ([18F]TFB) into CAR-T cells was measured with a gamma counter. Uptake of the MRI contrast agent Gd-EOB-DTPA was determined on a 3T clinical MRI scanner.

Results: We achieved >85% GFP+/TCR- editing efficiency when targeting CD19CAR-GFP to the *TRAC* locus (Figure 1) and ~21% for OATP1B3 and ~50% for NIS at a safe-harbor (*AAVS1*) locus, which increased to 80-95% purity post sorting. NIS- and OATP1B3-edited T cells showed significant uptake of their respective tracer ([18F]TFB) and contrast agent (Gd-EOB-DTPA) (Figure, 2A, B). Multiplexed editing with CD19CAR at *TRAC* and reporter genes at *AAVS1* together effectively killed NALM6-Fluc cells (Figure 3), showing that the CAR and reporter gene components were functional. To improve efficiency, "all-in-one" AAV vectors containing CD19CAR-OATP1B3, -NIS or -Akaluc were targeted to the *TRAC* locus. Correct integration and bioluminescence signal for CD19CAR-Akaluc edited cells was confirmed and edited T cells killed NALM6 cells *in vitro*. In addition, bioluminescent imaging confirmed that intravenous injection of CD19CAR-Akaluc cells homed to NALM6-Antares subcutaneous tumours *in vivo* (Fig. 4).

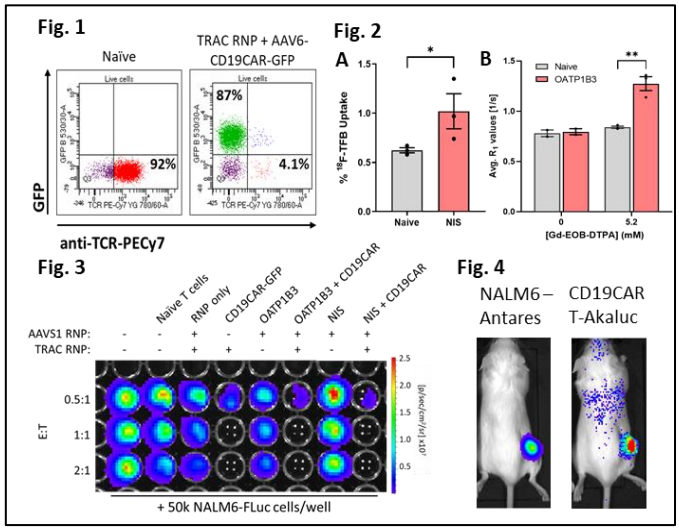

Conclusion: Our work demonstrates the first CRISPR-Cas system for highly efficient editing of cancer-killing CAR-T cells with clinically relevant human reporter genes. Ongoing efforts are extending these studies to MRI and PET of edited CAR-T cells in preclinical mouse cancer models. These advanced CRISPR tools should have broad utility for co-editing primary cells with therapeutic genes and reporter genes to make trackable therapeutic cells with improved efficacy and safety profiles.

References: *[1]Vitale, C. and Strati, P., Frontiers in Oncology, 2020; [2]Sterner, R.C. and Sterner, R.M., Blood Cancer Journal, 2021.*

Pitch Session 5: Machine Learning II

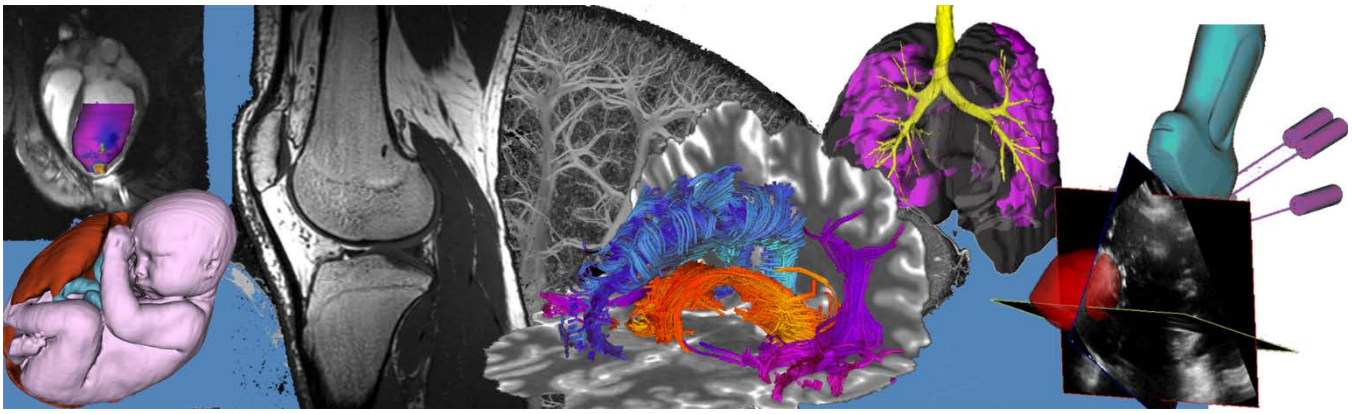

A CT-based radiomics model for predicting feeding tube insertion in oropharyngeal cancer

Tricia Chinnery[1], Pencilla Lang[2], Anthony Nichols[3], Sarah Mattonen[1,2]
[1]Departments of Medical Biophysics, [2]Oncology, [3]Otolaryngology, Western University, London, ON

Introduction: Oropharyngeal cancer (OPC) is the fastest-rising incident cancer in Canada, due to the rapidly increasing rates of oral infection with the human papillomavirus.[1] Nearly all patients with OPC treated with chemoradiation suffer treatment-related toxicities such as xerostomia (dry mouth) and dysphagia (trouble swallowing). Consequently, to combat nutritional deficiencies, approximately 30% of patients will require a feeding tube, an invasive procedure requiring hospital admission.[2] This may cause treatment delays or the need to forgo chemotherapy due to unanticipated hospital admissions and general deconditioning of patients, all potentially impacting the success of treatment. Currently, there are limited clinical prognostic factors to determine which patients will require a feeding tube during treatment.[3] Therefore, there remains an unmet clinical need for additional biomarkers to assist in identifying this patient population, who could benefit from prophylactic feeding tube insertion prior to the start of their treatment. Radiomics aims to extract quantitative image features that can be used to develop predictive machine learning models and provide a more comprehensive view of diseases. We hypothesize that CT-based radiomic features, augmented with clinical features, will significantly outperform traditional clinical features for predicting the need for feeding tube insertion, based on a significant increase in the area under the receiver operating characteristic curve (AUC).

Methods: A dataset of patients (n=343) with OPC treated with chemoradiation was used for this study. A total of 116 patients (34%) required a feeding tube during treatment. Primary tumour volumes were contoured on pre-treatment planning CT images as part of the routine radiation therapy workflow (Figure 1). PyRadiomics was then used to compute radiomic image features (n=1218) from these volumes of interest on the original, wavelet, and Laplacian of Gaussian (LoG) filtered images.[4] The dataset was split into independent training (n=244) and testing (n=99) datasets based on date of diagnosis. Linear regularization with a least absolute shrinkage and selection operator (LASSO) penalty was applied to select the optimal radiomic features to predict feeding tube insertion. A support vector machine (SVM), random forest (RF) classifier, and Naïve Bayes (NB) classifier were individually built using the selected radiomic features and three prognostic clinical features from the literature (body mass index, tumour stage, nodal stage). The combined models were built on the training dataset and performances were assessed in the testing dataset. A baseline model using only the clinical features was compared to the combined radiomic and clinical models. The AUC was used to assess the prognostic value.

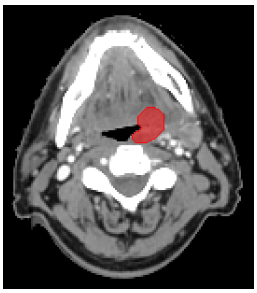

Figure 1: Tumour volumes contoured on pre-treatment CT.

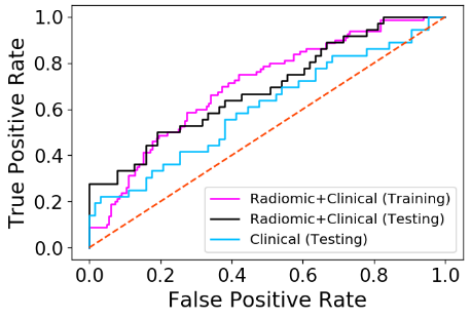

Figure 2: ROCs from evaluation of the Naïve Bayes and baseline clinical models.

Results: Through LASSO feature selection, seven predictive radiomic features were selected. This included one first-order feature from the wavelet filtered image, one textural feature from the wavelet filtered image, and five textural features from the LoG filtered images. The baseline model comprised of clinical features alone achieved an AUC of 0.61 [95% CI: 0.50-0.72] in the testing dataset. The NB was the top-performing radiomics model and achieved an AUC of 0.69 [0.59-0.79] in the testing dataset, which significantly outperformed the baseline clinical model (p=0.006) (Figure 2). The SVM and RF achieved AUCs of 0.62 [95% CI: 0.51-0.73] and 0.66 [95% CI: 0.54-0.77] in the testing dataset, respectively. Qualitatively, we found that patients who required a feeding tube tended to have more heterogenous texture in the primary tumour.

Conclusions: To the best of our knowledge, this was the first study to use radiomics to predict feeding tube insertion. These preliminary results demonstrate that a model integrating quantitative image features with clinical data has the potential to augment traditional information in a clinical setting. Future work involves exploring deep learning methods for the prediction of this supportive care intervention. Once validated, this model has the potential to assist physicians in identifying patients who may benefit from prophylactic feeding tube insertion, leading to reduced treatment disruptions and improved quality of life for patients with OPC.

References: [1] S. Habbous et al., CMAJ, 189(32), 2017. [2] C. Friedes et al., Cureus, 12(4), 2020. [3] J. P. Reddy et al., IJROBP, 105(1), 2019. [4] J. J. M. Van Griethuysen et al., Cancer Res. 77(21), 2017.

Deep Learning-Based MR Image Re-parameterization

Abhijeet Narang [1], Abhigyan Raj[1], Mihaela Pop[2], and Mehran Ebrahimi[3]
[1]Indian Institute of Technology (ISM), Dhanbad, Jharkhand, India; [2]Sunnybrook Research Institute, Toronto, ON, Canada; [3]Faculty of Science, Ontario Tech University, Oshawa, ON, Canada

Introduction: Image re-parameterization refers to generating a given MRI scan with a new set of parameters such as Repetition Time (TR) and Echo Time (TE) parameters. Acquiring new MRI scans with different acquisition parameters is time-consuming and costly; thus, using MRI re-parameterization to estimate an image with a new set of parameters can be an inexpensive alternative. While most current MRI simulators rely on complex biophysical models to simulate non-linearities [1], recent advances in deep learning (DL) techniques in medical imaging have motivated us to develop a novel DL-based model for MR image re-parameterization. Specifically, in this work, we propose Param-net, a coarse-to-fine fully convolutional network (CN) for MR image re-parameterization for TR and TE parameters. As this model is coarse-to-fine, our aim is to use image features extracted from an image reconstruction auto-encoder as its input instead of directly using the raw image, since this approach could make the proposed model more advantageous and robust to overfitting.

Method: For re-parameterization, we use a single MR image with default parameters (TE= 50ms, TR= 4.5s) along with the desired parameters as inputs to our architecture. The output of our model is the generated MR image corresponding to the desired parameters. Our architecture consists of 1) Auto-encoder: a feature extraction part for down-sampling the image; and, 2) Param-net: an up-sampling part used to retrieve the desired image. We relied on a general image reconstruction auto-encoder for feature extraction, since this technique is more robust to overfitting and can be generalized to other image-to-image translation tasks. The auto-encoder was trained on 5000 images from the Places365 dataset taken from [2] and then fine-tuned using the MR data. The default parameter image was fed to the auto-encoder, and the outputs of the 8 down-sampling layers of the auto-encoder were extracted to be used as image features. These features along with parameters of the desired output image were then fed to the param-net which constructs the output image. An Adam optimizer and mean square loss function were used, and an instance normalization and ReLU activation functions were applied at the end of each CN layer.

Results and Conclusions: The initial dataset was generated using MRiLab [1]. We generated MRI scans for 200 different pairs of {TE, TR} where TE is ranging from 20ms to 1s and TR is ranging from 1.2s to 10s. The T1 values were in range 0s to 4.5s while the T2 values were in range 0s to 2.2s. For each pair of {TE, TR}, we generated 24 different MR slices of a 3D brain scan, therefore in total we obtained 4800 MR slices. We used 1000 samples of these slices for training, while the rest were kept for testing. An exemplary result from our pipeline is displayed in Fig 1. Notably, we were able to successfully re-parameterize the MRI scans with a mean peak signal-to-noise ratio(PSNR) of 30.34 and PSNR Standard Deviation (SD) of 1.04. The difference between the ground truth and the generated image has a mean absolute value of 5.25 per pixel on a scale of [0, 255] with a SD of 1.74.In summary, our simulation study showed that DL-based methods can be used for MR image re-parameterization. Based on our preliminary results, we suggest that DL-based methods hold the potential to simulate MR scans with a new set of parameters. This approach could be also utilized for T1/T2 mapping, overall shortening the MR scans by requiring less acquisitions. Future work will focus on re-parameterization from any MRI parameter set instead of a default one.

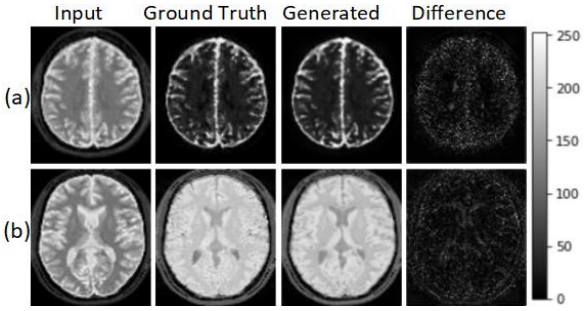

Fig 1. The {TE,TR} for the input image of (a) and (b) is {50ms, 4.5s}. For (a), {TE,TR} for generated image is {139ms, 8.4s}. For (b), the {TE,TR} for generated image is {38ms, 1.2s}

References:

[1] F. Liu, J. V. Velikina, W. F. Block, R. Kijowski and A. A. Samsonov, "Fast Realistic MRI Simulations Based on Generalized Multi-Pool Exchange Tissue Model," in IEEE Transactions on Medical Imaging.
[2] B. Zhou, A. Lapedriza, A. Khosla, A. Oliva and A. Torralba, "Places: A 10 Million Image Database for Scene Recognition," in IEEE Transactions on Pattern Analysis and Machine Intelligence.

Deep Learning Based Differentiation of Solid and Cystic Renal Masses using T2-Weighted MRI Images

Rohini Gaikar [1] *Azar Azad* [2] *Nicola Schieda* [3] *Eranga Ukwatta* [1]
rgaikar@uoguelph.ca azar@aivali.org nschieda@toh.on.ca eukwatta@uoguelph.ca

[1] *School of Engineering, University of Guelph, Guelph, Ontario, Canada,* [2] *A.I. Vali, Toronto, Ontario, Canada,* [3] *Department of Radiology, University of Ottawa, Ottawa, Ontario, Canada*

Introduction: Renal cell carcinoma (RCC) is the most common kidney cancer and represents 2% of the global cancer diagnosis and mortality [1]. Renal masses are commonly detected incidentally in patients undergoing MRI for other reasons; however, commonly detected incidental renal masses are benign cysts [2]. The subjective assessment often requires the use of contrast media which adds cost and time consuming in patients with multiple renal masses This study evaluates Convolutional Neural network (CNN) to differentiate solid renal masses (tumors) and benign cysts on routinely performed T2 Weighted (T2W) MRI images without contrast media.

Methods: The dataset consisted of 3D abdominal scans from 108 patients with benign and malignant solid kidney tumors including: renal cell carcinoma, oncocytomas, and fat poor renal angiomyolipoma (fpAML) and confirmed by surgery diagnosis. In dataset 43 patients had ≥1.0 cm simple or minimally complex benign Bosniak Type 1 or 2 cysts. The kidneys and renal masses were annotated by a fellowship-trained radiologist on axial MR images. The block diagram of semi-automated process of classification is shown in Figure 1. The training and test data is repapered in 80:20 split format and validation data is 20% of training data. In the first stage, we developed deep learning based U-Net model for kidney localization on T2W-MRI images. In the localized kidneys as region-of-interest (ROI), radiologists identified renal masses as tumors and cysts. The ROIs of renal masses prepared from 2D axial slices, resized to 78×78 to train two different CNN models for tumor vs cyst classification. To improve the classification accuracy, we performed weighted average ensemble of two models as mentioned in Table 1.

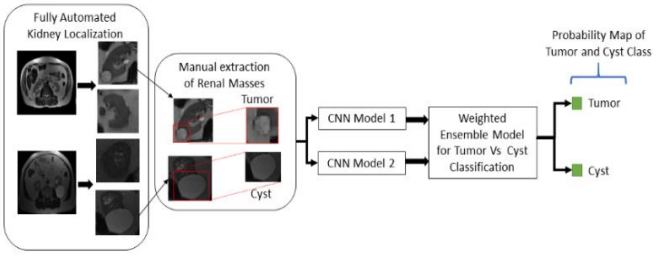

Figure 1: Block diagram of Semi-Automated Process of Tumor vs Cyst Classification

Table 1: CNN Models Training Summary

CNN Model 1	Filters: (32,64,128,512), Flatten Layer, Dense Layers: (128,32,1)
CNN Model 2	Filters: (32,32,64,64,128,128,256,256) Flatten Layer, Dense Layers: (256,128,1)
Optimizer	Adam (*lr =0.001)*
Focal Loss	(γ =2.0, α =0.25)
Ensemble Rule	Weighted Avg: 0.3T,0.8C

Result: The model is evaluated on 20 test cases containing 120 tumors and 110 cysts ROI which are confirmed through biopsy surgeries. The classification metrics of weighted average of CNN models are shown in Table 2 and confusion metrics in Figure 2. The plots of ROC-AUC and Precision-Recall are shown in Figure 3 with respect to No skill classifier which predicts a random class or constant class in all classes.

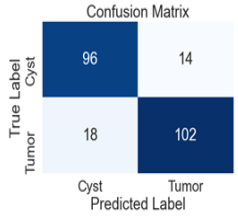

Figure 2: Confusion Matrix

Table 2: Classification Metrics

Metrics	Value (%)
Accuracy	86.08
Precision	87.93
Recall	85.00
F1 Score	86.44
ROC_AUC	86.13

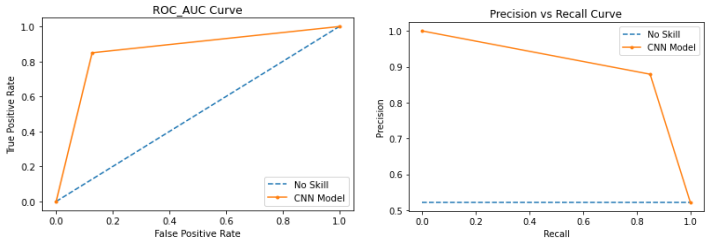

(a) **(b)**

Figure 3: (a) ROC Curve and (b) Precision-Recall Curve

Conclusion: The semi-automated process accurately differentiated solid renal masses and benign cysts using only T2W images without gadolinium. This method may increase clinician efficiency when interpreting renal MRI and reduce the need for contrast. This will help in characterization of renal masses without biopsy process.

1. R. M. Turner, T. M. Morgan, and B. L. Jacobs, "Epidemiology of the Small Renal Mass and the Treatment Disconnect Phenomenon," Urol. Clin. North Am. 44(2), 147–154 (2017) [doi:10.1016/j.ucl.2016.12.001].
2. D. C. Johnson et al., "Preoperatively Misclassified, Surgically Removed Benign Renal Masses: A Systematic Review of Surgical Series and United States Population Level Burden Estimate," J. Urol. (2015).

Automatic thyroid nodule detection and segmentation method based on Mask R-CNN

Ningtao Liu[1,2], Jaron Chong[4], Aaron Fenster[1,3,4], Shuiping Gou[2]
[1]Robarts Research Institute, Western University, London, ON, Canada
[2] School of Artificial Intelligence, Xidian University, Xi'an 710071, Shaanxi, China
[3]Department of Medical Biophysics, Western University, London, ON, Canada
[4]Department of Medical Imaging, Western University, London, ON, Canada

Abstract

Introduction. Thyroid nodules are very common, and ultrasound (US) is the primary method used to detect and classify them. In the clinical workflow of Computer-Aided Diagnosis (CAD), determination of the location and contours of the thyroid nodule is critical. In the traditional process, the position and contour of the thyroid nodule depend on the definition of experienced radiologists, which is time-consuming, labour-intensive, and subjective. Because of its full-automatic, high-efficiency, and human-independent characteristics, deep learning methods have been extensively studied in many modalities of medical image and clinical tasks. In this work, considering the great variation in the shape and size of thyroid nodules in ultrasound images, we developed a target detection and semantic segmentation model using an improved Mask R-CNN[2] to meet clinical needs.

Methods. Our work made use of the training data set TN-SCUI, which contained 3,644 thyroid images plus annotations of the thyroid nodules. The images and annotations were split into training, validation and test datasets in the ratio of 7:1.5:1.5. In this work, for the distribution of thyroid nodule size and aspect ratio, we improved the sampling scale of the anchors of the Mask R-CNN from (32, 64, 128, 256, 512) to (32, 64, 96, 256), and the sampling ratios from (0.5, 1.0, 2.0) to (0.5, 1.0, 1.5, 2.0), respectively. The model was trained on 2549 images using 547 validation images to optimize the hyperparameters and tested on 547 images. In addition, as a compromise between specificity and sensitivity, we considered multiple candidate detection and segmentation results and varied a probability threshold hyperparameter to find an optimal trade-off between sensitivity and specificity. All detection and segmentation results with predicted probabilities greater than this threshold were considered by examining the sensitivity to false negatives and tolerance of false positives. The workflow of our method is shown in Figure 1.

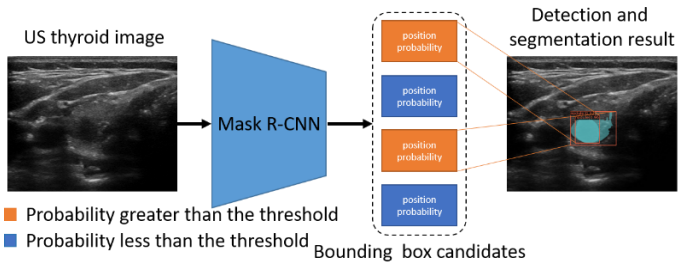

Figure 1 Workflow of our method

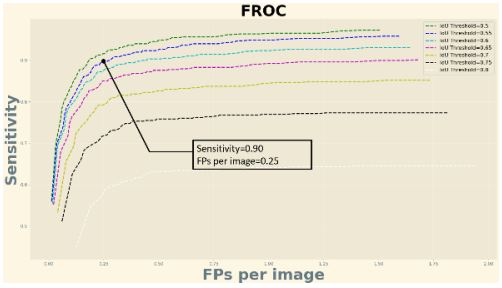

Figure 2 The FROC curves at different IoU thresholds

Results. Experimental results demonstrated that our method can detect and segment thyroid nodules well in a fully automated manner with a very low false-negative rate. Considering only the detection result with the highest predicted probability, the mean Intersection over Union (mIoU) of the segmentation result was 0.76, while the mIoU was 0.78 when the top two detections with the highest prediction probability were considered. This is better than the IoU obtained using the publicly available top-ranked 2-stage model of the TN-SCUI challenge (0.77). The mean average precision was 0.95 when IoU threshold was set to 50%, which is better than that of the basic Mask R-CNN (0.94), Fast R-CNN[3] (0.90) and Faster R-CNN[4] (0.89). As shown in Figure 2 the sensitivity of detection was 0.90 and the average number of false-positive detection results (FPs) per image was 0.25 when the IoU threshold was set to 0.55.

Conclusion & Significance. Our modified Mask R-CNN can segment and detect thyroid nodules sensitively and specifically.

References

1. https://tn-scui2020.grand-challenge.org/
2. He, Kaiming, et al. "Mask R-Cnn." Proceedings of the IEEE international conference on computer vision. 2017.
3. Girshick, Ross. "Fast r-cnn." Proceedings of the IEEE international conference on computer vision. 2015.
4. Ren, Shaoqing, et al. "Faster r-cnn: Towards real-time object detection with region proposal networks." Advances in neural information processing systems 28 (2015): 91-99.

Deep Image Clustering for Standardization of Radiological Workflows

Dhruv Patel[a], Erik Ziegler[b], Rob Lewis[b], Parvin Mousavi[a], and Alireza Sedghi[b]
[a]Medical Informatics Laboratory, Queen's University, Kingston, ON, Canada
[b]Radical Imaging, Boston, Massachusetts, USA

Introduction: Artificial Intelligence (AI) has played a major role in medical imaging, with applications such as disease detection and organ segmentation. However, AI models are typically trained for specific imaging tasks and require particular images as inputs (such as training a Prostate AI model with T2 Axial images from mp-MRI). At the deployment level, specific image characteristics (such as modality and body region) should be utilized to transfer the correct image series in a study to the AI engine, especially where several AI models are present, each requiring different input requirements. Although DICOM metadata provides some of these characteristics, it is inconsistent and non-standard in many tags. In this study, we present a deep learning-based unsupervised clustering algorithm to group and standardize radiological images solely based on their pixel data.

Methods: Images of different modalities, body regions, and orientations were obtained from 15 publicly available datasets from The Cancer Imaging Archive (TCIA), forming 19000 training images and 7000 testing images. Using Semantic Clustering by Adopting Nearest Neighbors (SCAN) [1], semantically meaningful features were extracted from each image, and the nearest neighbors of the image were calculated. The image and its neighbors were used as inputs for an unsupervised deep clustering network, which contained a ResNet backbone and novel loss function, to group images based on similarities in features. A total of 20 clusters were used to over-cluster and accommodate for the variability in image characteristics. Finally, manual annotation of each cluster was conducted, by examining the modality, body part, and orientation. During testing, the trained clustering model can be used to identify the group the image belongs to, which can then assign the consistent and correct metadata labels as annotated.

Results: Experimental evaluation showed that image clustering successfully occurred with a 94.2% accuracy without the use of labeled data. Our clustering algorithm substantially outperformed a K-means baseline (48.6% accuracy) and the state-of-the-art SCAN method (75.6% accuracy).

Conclusions: Our experiments show strong results for grouping medical images based on their pixel data. We envision our approach being utilized as a pre- processing step for a range of tasks that involve detecting the underlying characteristics of the data in the DICOM files, even if the metadata is incorrectly formatted.

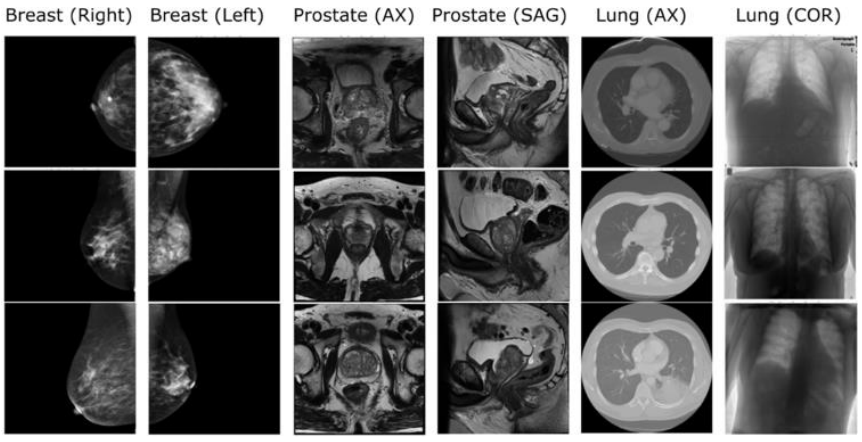

Figure 1: Sample clusters of images after performing unsupervised clustering. Images were successfully separated by modality, body region, and orientation.

[1]Van Gansbeke, Wouter, et al. "Scan: Learning to classify images without labels." *European Conference on Computer Vision*. Springer, Cham, 2020.

Automated Tumour Reconstruction for Real-Time Visualization in Breast-Conserving Surgical Navigation

Chris Yeung[1], Tamas Ungi[1], Zoe Hu[2], Gabor Fichtinger[1]
[1]School of Computing, Queen's University, Kingston, Canada
[2]School of Medicine, Queen's University, Kingston, Canada

INTRODUCTION: Breast cancer is the most common cancer in women worldwide. Most patients choose to undergo a lumpectomy, removing the tumour while conserving as much healthy tissue as possible. However, due to the lack of information on the tumour contour during surgery, the tumour may not be completely excised, increasing the chance of recurrence. In recent years, a navigation system has been developed to help visualize the tumour and its location relative to the cautery [1]. However, tumour contouring is still a manual process, increasing operation time and introducing human error. This work introduces an automated tumour contouring process by integrating a deep neural network into the surgical navigation system. The goal is to display the tumour contour at a frame rate that is clinically useful.

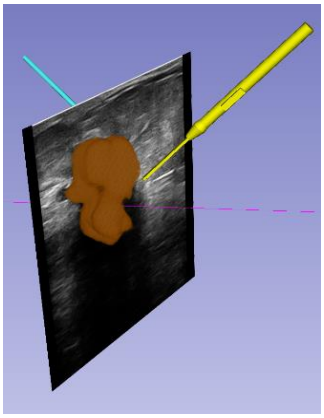

Figure 1. 3D view of an automatically reconstructed tumour (brown) along with the cautery (yellow) and localization needle (blue).

METHODS: This work was implemented in 3D Slicer, an open-source software for medical image visualization [2], using a segmentation module and a lumpectomy navigation module. As the ultrasound is scanned, the segmentation module continuously sends the images to a trained network, which generates a mask of the tumour. The lumpectomy navigation module then reconstructs the tumour using the mask and overlays the cross-section on the ultrasound image (Figure 1). For this task, an 8-layer UNet was trained using 7,218 ultrasound images from 33 lumpectomy patients. To assess the speed of the segmentation, the frame rate of the output prediction was compared when run on the same or a different process as 3D Slicer. Both modules can be found at https://github.com/SlicerIGT/aigt.

Table 1. Frame rate (FPS) of the live segmentation process.

Hardware Specifications	On 3D Slicer Process	On Separate Process
Ryzen 5 2600X, AMD RX 590	10.4	16.5
Core i7-8700K, NVIDIA RTX 2070	12.5	16.2

RESULTS: In addition to high performance on typically-used metrics, the majority of clinicians rated the segmentation to be useful in breast-conserving surgery [3]. When the tumour prediction was run on a separate CPU process, an FPS increase of around 30-60% was observed, irrespective of the sample used for testing (Table 1).

CONCLUSIONS: The ultrasound machine used in lumpectomy navigation displays images at 20 FPS, so the higher frame rate achieved using a separate process reduces the amount of information lost. Nevertheless, since the ultrasound probe is unlikely to be moved every 0.05-0.1 seconds, the frame rate should be more than sufficient for clinical use. The UNet can now be deployed as part of the surgical workflow rather than being used only as an experimental tool.

REFERENCES:

[1] T. Ungi *et al.*, "Navigated Breast Tumor Excision Using Electromagnetically Tracked Ultrasound and Surgical Instruments.," *IEEE Trans. Biomed. Eng.*, vol. 63, no. 3, pp. 600–606, Mar. 2016.
[2] A. Fedorov *et al.*, "3D Slicer as an image computing platform for the Quantitative Imaging Network.," *Magn. Reson. Imaging*, vol. 30, no. 9, pp. 1323–1341, Nov. 2012.
[3] Z. Hu, T. Ungi, J. Engel, G. Fichtinger, and D. Jabs, "Deep Learning-Based Automatic Tumour Segmentation in Breast-Conserving Surgery Navigation Systems," *Can. Assoc. Radiol. 2021 Virtual Annu. Sci. Meet.*, 2021.

Semi-Supervised Segmentation of 3D Ultrasound Images

Zachary Szentimrey[1], Abdullah Al-Hayali[1], Sandrine de Ribaupierre[2,3], Aaron Fenster[2], Eranga Ukwatta[1]
[1]School of Engineering, University of Guelph, Guelph, Ontario, Canada; [2]Robarts Imaging, University of Western Ontario, London, Ontario, Canada; [3]Department of Clinical Neurological Sciences, University of Western Ontario, London Health Sciences Centre, London, Ontario, Canada

Introduction: Intraventricular hemorrhaging (IVH) affects 20-30% of very low birth weight infants (<1500g). IVH can lead to post-hemorrhagic ventricle dilation (PHVD) (the abnormal enlargement of the ventricles) and developmental delays. Monitoring the changes of the ventricles obtained through fully automated segmentation is critical because it can provide clinicians with more information for choosing the best treatment to prevent further neurological degradation. However, given the difficulty and time-consuming process of manually segmenting the irregular ventricle shapes in the three-dimensional (3D) ultrasound (US) images, labelled data is scarce and may not capture variability in ventricle shapes. To this end, we are developing a semi-supervised learning (SSL) method for 3D US segmentation that can use unlabelled data and provide better generalizability and accuracy when compared to a fully supervised method with few labelled data.

Methods: The dataset consists of 75 labelled 3D US images, including images of both lateral ventricles and images with varying degrees of PHVD. The dataset was split between train/test where 50 images were used for training and 25 used for testing. Test images were not used during model training. In addition, 800 unlabelled 3D US images were used for SSL. The training set and unlabelled set did not contain images from the same patients as the test set. The images were collected by a motorized 3D US system developed specifically for cranial imaging of neonates. Manual segmentations were performed on the sagittal view at 1 mm intervals using multi-planar reformatting software. The baseline supervised learning (SL) method used a 3D U-Net architecture and is the backbone for the SSL methods including the dual-task consistency (DTC) and SASS-Net methods. These SSL methods use both labelled and unlabelled data to segment the images. We also compared these SSL methods to the state-of-the-art fully supervised 3D U-Net ensemble method developed previously for this problem that consists of three 3D U-Net variants. The Dice similarity coefficient (DSC), absolute volumetric difference (VD) and mean absolute boundary distance (MAD) were used for model evaluation and the Wilcoxon and paired t-test were used for statistical analysis.

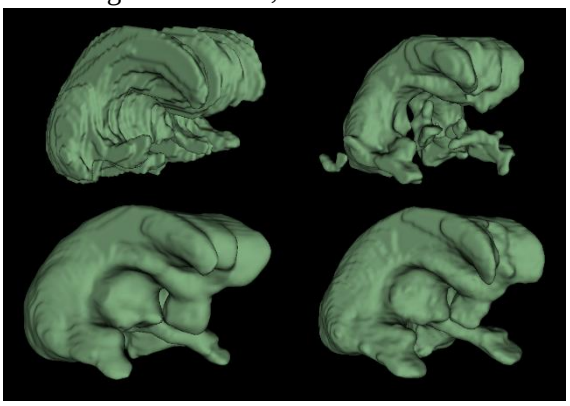

Figure 1: Example segmentation. Top left: ground truth. Top right: 3D U-Net. Bottom left: SASS-Net. Bottom right: DTC.

Results: The mean and standard deviation of the metrics were calculated and are shown in Table 1. The SSL methods outperformed the baseline 3D U-Net in terms of DSC and MAD but over segmented some images leading to a worse VD. Minimal difference between the DTC and SASS-Net models. When compared to the state-of-the-art ensemble method, the SSL techniques had similar DSC but yielded slightly worse VD and MAD. However, the SSL methods required approximately 1/3 the number of parameters and training time compared to ensemble. Example segmentations from the 3D U-Net, SASS-Net and DTC models are in Figure 1, including ground truth.

Table 1: DSC, VD and MAD results for each model tested.

Supervision	Method	Training Labelled	Training Unlabelled	Test Data	DSC ± SD	VD ± SD	MAD ± SD	Params. At Test
SL	3D U-Net	50	0	25	0.716 ± 0.074	2.3 ± 2.3	1.39 ± 0.55	23M
SL	Ensemble	50	0	25	0.739 ± 0.063	2.1 ± 1.8	1.02 ± 0.29	72M
SSL	SASS-Net	50	800	25	0.736 ± 0.076	3.6 ± 4.0	1.21 ± 0.64	23M
SSL	DTC	50	800	25	0.735 ± 0.063	3.5 ± 3.8	1.24 ± 0.51	23M

Conclusions: We implemented deep learning models to automatically segment 3D US images of neonatal cerebral ventricles using SSL techniques. We found the SSL methods yielded better results than the baseline 3D U-Net for two of the metrics used but yielded worse results than the 3D U-Net ensemble. Though it is worth noting that further experiments are being conducted with varying amounts of labelled and labelled data. The goal is to use a minimal amount of labelled data resulting in a notable difference in either results metrics or model performance.

An Advanced Acquisition/Reconstruction Method for ^{1}H and ^{129}Xe MRI with Deep Learning

Samuel Perron[1], Matthew S. Fox[1,2], and Alexei Ouriadov[1,2,3]

[1]Department of Physics and Astronomy and [3]School of Biomedical Engineering, The University of Western Ontario, London Canada; [2]Lawson Health Research Institute, London, Canada

INTRODUCTION: MRI is largely limited by the amount of magnetizable nuclei and their gyromagnetic ratios[1]. In certain cases, such as hyperpolarized gas lung MRI with naturally-abundant ^{129}Xe,[3] this low-sensitivity issue still poses considerable problems. It has recently been shown that accelerated MRI via Compressed-Sensing, combined with fitting to the Stretched-Exponential-Model, is able to provide considerable gains in SNR without increasing total scan-duration.[4] k-space is undersampled according to high acceleration factors (AF) and averaged together using a specific averaging pattern. If the SNR of this set of images is assumed to reflect the spin-density difference instead of the signal-level,[4] then the SNR dependency of these images can be fitted to the Stretched-Exponential-Model (SEM) equation.[5-8] The feasibility of this approach was demonstrated using retroactively undersampled phantom images.[4] We hypothesize that a convolutional-neural-network capable of minimizing reconstruction artefacts from the reconstructed images[9] can be developed using recent advancements in deep learning.[10,11] We have proactively acquired accelerated proton phantom images at low-field and non-accelerated ^{129}Xe human lung images using a small xenon dose at 3T to demonstrate this method's potential in human subjects and its ability to reduce image reconstruction artefacts in phantoms.

METHODS: ^{1}H MR was performed on a resolution phantom at 0.074T using the Fast-Gradient-Recalled-Echo (FGRE) pulse sequence. Nine undersampled images were acquired for three AFs (7, 10, 14) and subsequently averaged together for every unique combination without overlap (e.g., 2 combinations of 4 averages, etc.); the SNR dependency of the resulting 14 k-space images was plotted as a function of the image number and fitted to the SEM using the Abascal method.[4,6] A healthy volunteer with written informed consent underwent spirometry and ^{129}Xe MRI scanning: nine fully-sampled ^{129}Xe human-lung images were acquired at 3.0T (MR750, GEHC) using whole-body-clinical-gradients and a commercial, xenon-quadrature-flex human RF-coil[12] (MR Solutions). All images were acquired in breath-hold (<16s) after inspiration of 1L of gas (10/90 $^{129}Xe/^{4}He$ mix) from functional-residual-capacity, after which the previously discussed averaging pattern was applied. Hyperpolarized ^{129}Xe gas (35% polarization) was obtained from a turn-key, spin-exchange-polarizer system (Polarean-9820 ^{129}Xe polarizer).[13] The SNR decay was assumed to represent the decreasing gas density of ^{129}Xe after each wash-out oxygen breath.[14,15] The k-spaces of the 14 images were retroactively under-sampled for the same three AFs and for three sampling schemes (FGRE, x-Centric[16], and FE-Sectoral[17]) and fitted to the SEM as previously described.[4,6] The reconstructed images were assumed to be a superposition of the original (artefact-free) images and the artefacts themselves[9]. A 3-stage U-Net[18] was developed[9], and the artefact masks of 202 unrelated previously acquired phantom-images were generated and used as training data for the network.

RESULTS: Fig.1 shows the phantom reconstructions before and after applying the neural network, as well as retroactively undersampled human-lung image reconstructions using FE-Sectoral for all three AFs (SNR>21); FE-Sectoral showed much less artefacting compared to FGRE & x-Centric (not shown here).

CONCLUSION: The phantom reconstructions yielded significant SNR gains, albeit with considerable artefacts at higher acceleration-factors. The human lung reconstructions show a large improvement in SNR while using only a third of a typical ^{129}Xe dose. The neural network was able to remove artefacts in the AF=7 phantom reconstruction, but performance suffered at higher AFs. This sampling/reconstruction method could be implemented in existing MRI setups as it does not require additional hardware; when paired with a pulse-sequence featuring minimal artefacts (e.g., FE-Sectoral), this technique could become a valuable clinical-tool for diagnosing various pulmonary-diseases, with significant benefits in low-field systems.

We acknowledge the support of the NSERC, R5942A04.

REFERENCES: 1. Song, X.-x. et al. New J. Chem. (2014); 2. Stewart, N.J. et al. MRM. (2015); 3. Perron, S. et al. ISMRM (2021); 4. Westcott, A. et al. JMRI. (2019); 5. Abascal, J. et al. IEEE Trans Med Imaging. (2018); 6. Berberan-Santos, M.N. et al. Chemical Physics. (2005); 7. Parra-Robles, J. et al. ISMRM (2013); 8. Lee, D. et al. MRM. (2017); 9. Yang, Y. et al. IEEE Trans Pattern Anal Mach Intell. (2018); 10. Hammernik, K. et al. MRM. (2018); 11. Kaushik, S.S. et al. MRM. (2016); 12. Kaushik, S.S. et al. MRM. (2011); 13. Ouriadov, A.V. et al. MRM. (2015); 14. Santyr, G.E. et al. MRM. (2008); 15. Ouriadov, A.V. et al. MRM. (2017); 16. Khrapitchev, A.A. et al. JMR. (2006); 17. Ronneberger, O. et al. ArXiv abs/1505.04597 (2015).

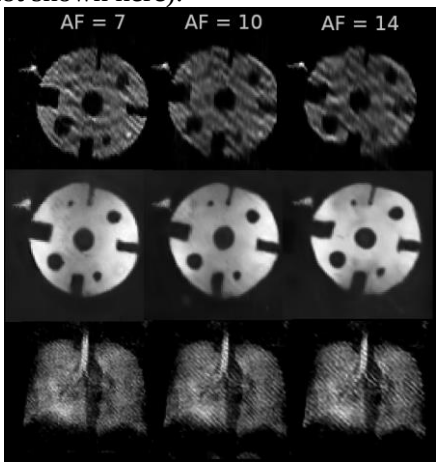

Figure 1. Phantom image reconstructions before (top row) and after (middle row) applying the Deep Learning network; representative ^{129}Xe human lung images obtained with FE-Sectoral (bottom row).

Pitch Session 6:

Cardiac, Cellular and Molecular

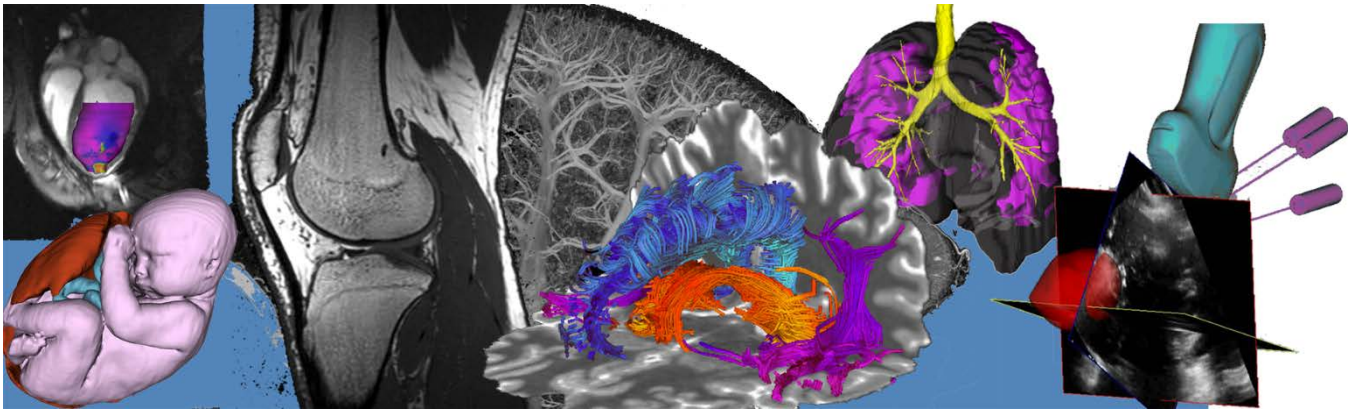

A highly modular activatable synthetic biology system to visualize in vivo cell-cell communication

TianDuo Wang[1,2], Yuanxin Chen[1], Nivin Nystrom[1,2], Shirley Liu[1,2], John. A. Ronald[1,2,3]
1. Robarts Research Institute – Imaging; 2. Department of Medical Biophysics, University of Western Ontario; 3. Lawson Health Research Institute, London, ON, Canada.

INTRODUCTION: In multicellular organisms, cell-cell communication is central to development and homeostasis. Cell-cell interactions have been leveraged to create cellular therapies for a variety of biomedical problems such as infectious diseases, autoimmune disorders, and cancer. Cellular cancer immunotherapies harness the innate tumour-homing ability of immune cells to better target and kill malignant cells. To improve cancer killing, immune cells can be engineered with targeting receptors, such as chimeric antigen receptors (CAR)[1], to recognize specific cancer antigens. CAR-T cells have already shown remarkable clinical success in treating B-cell cancers, with potential to treat other cancer types on the horizon. However, some patients still suffer from inadequate efficacy and/or serious side effects, thought to be due to sub-optimal tumour homing and off-targeting of normal tissues by immune cells. This study aims to develop a specific and non-invasive imaging tool to visualize when immune cells interact with its targeted antigen – the prerequisite for inducing cancer killing. The synthetic notch (SynNotch) receptor is a uniquely versatile system that signals cell-cell contact via activatable transcriptional expression of desired transgenes[2] (Fig. 1A). In this work, we engineered immune cells with a new SynNotch system that activates the expression of multimodal imaging reporter genes in response to cancer antigen binding.

METHODS: We engineered a human T cell line (Jurkat) via lentiviral transduction of two components: (1) SynNotch receptor directed against the B-cell surface antigen CD19[3], and (2) a response element containing tdTomato (tdT) for fluorescence, firefly luciferase (Fluc) for bioluminescence (BLI), and organic anion transporting polypeptide 1B3 (OATP1B3) for MRI[4] (Fig. 1A). Successfully engineered T cells were isolated using fluorescence activated cell sorting. For *in vivo* evaluation, Nod-scid-gamma mice were implanted with either CD19+ or CD19- Nalm6 leukemia cells subcutaneously. Once tumours reached >100mm^3, mice received an intratumoural injection of 10 million engineered T cells. BLI and gadolinium-enhanced T_1-weighted MRI was performed to assess Fluc and OATP1B3 reporter activation in tumours, respectively.

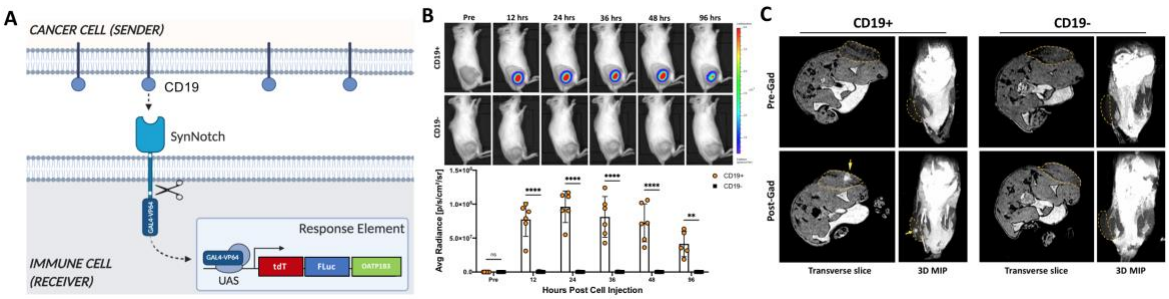

Figure 1. (A) Schematic of SynNotch system. CD19 binding by the CD19-targeted SynNotch receptor induces intracellular cleavage of a GAL4-VP64 transactivator, which binds to an upstream activating sequence (UAS) to initiate transcription of transgenes encoded in the response element. (B) Representative bioluminescence images with quantification of Fluc signal in subcutaneous tumours pre- and post-cell injection. (C) T_1-weighted MR images pre- and 5 hours post-injection of Primovist gadolinium agent. Enhanced regions (arrow) in tumours are marked on transverse slices and 3D maximal intensity projections.

RESULTS: BLI revealed minimal background Fluc in tumours prior to T cell injection (Fig. 1B). Excitingly, CD19+ tumours exhibited significantly higher Fluc signal compared to CD19- tumours at all timepoints post-cell injection. Following administration of the gadolinium agent Primovist, MRI revealed notable regions of contrast enhancement in CD19+, but not CD19- tumours, reflective of T cells that bind their target antigen (Fig. 1C).

DISCUSSION: We have developed a novel molecular imaging system to non-invasively visualize antigen-specific communication between immune and cancer cells for the first time. This SynNotch-driven system demonstrated antigen-dependent activation of reporter genes in immune cells when engaging CD19 on cancer cells, with minimal off-target activity. Further development of this technology will provide a broadly applicable tool for monitoring cellular immunotherapies and beyond. We posit these tools will ultimately improve our ability to develop better cell products, and to understand response/non-response and side effects in individual patients.

REFERENCES: [1] Maude et al., *NEJM*, 2014, 371: 1507-1517. [2] Morsut et al., *Cell*, 2016, 164: 780-791. [3]

Trimodal Tracking of Mesenchymal Stem cells (MSCs) with Magnetic Particle Imaging (MPI), Bioluminescence Imaging (BLI) and Positron Emission Tomography (PET)

Nourhan Shalaby[1], John Kelly [2], Olivia Sehl[1], Julia Geavert[1], Mathew Fox[3,5] ,Qi Qi[1,3,5], Jonathan Thiessen[1,4,5] , Justin Hicks[1,3,4] , Paula J Foster[1,2], Timothy J Scholl[1,2,6] , John A Ronald[1,2,3]

[1] Department of Medical Biophysics, Schulich School of Medicine and Dentistry, Western University
[2] Robarts Research Institute, Schulich School of Medicine and Dentistry, Western University
[3] Lawson Health Research Institute
[4] Lawson Cyclotron and Radiochemistry Facility
[5] Saint Joseph's Health Care
[6] Ontario Institute for Cancer Research

Introduction: Mesenchymal stem cells (MSCs) have been used for the treatment of many pathologies[1]. While remarkably successful, there are still major hurdles to overcome for optimum clinical potential. Current post-administration monitoring methods (blood tests and biopsies) are invasive and lack critical information on the number, biodistribution and viability of the administered cells [2]. With this work, we propose a non-invasive multi-modal approach to monitor mesenchymal stem cells using a multi-modal imaging technique comprising magnetic particle imaging (MPI), bioluminescence imaging (BLI) and positron emission tomography (PET). **Methods:** MSCs were transduced to express a lentiviral plasmid containing a tdTomatoe (tdT) fluorescence gene and a BLI reporter gene, Akaluc. MSCs were sequentially transduced with a second lentiviral plasmid containing genes for zsGreen (zsG) fluorescence protein and a Sodium Iodide Symporter (NIS) PET imaging reporter. These MSCs were labeled *in vitro* by incubation with a super-paramagnetic iron oxide, Synomag-D for detection with MPI. Mice (n=5) were injected with 10^6 tdT-Akaluc-zsG-NIS-MSCs in the hind limb muscle. Longitudinal imaging of these mice with MPI, BLI and PET was performed over a duration of 30 days. **Results:** At early time points, MPI and BLI showed high sensitivity while PET did not show significantly higher tracer uptake than background. MPI detection of iron-labeled MSCs declined over time, likely due to iron label dilution, and clearance. BLI and PET signals both showed similar early signal decreases (mainly due to initial cell death post-administration) and eventual increase of BLI and PET at later time points (Fig.1). We report correlation between MPI and BLI (R^2=0.677) at earlier timepoints. At later time points, MPI and BLI showed no correlation (R^2=0.002), while PET and BLI showed strong correlation (R^2=0.987). Thus, we show the feasibility of using MPI as an early cell detection technique, while PET can be used at later time points, for long-term tracking applications. **Conclusions:** MSCs were engineered with a BLI and PET reporter gene and iron-labeled to allow for MPI detection. We tracked biodistribution, viability and proliferation of MSCs with MPI, BLI and PET. MPI was successful in cell detection at earlier timepoints, while PET and BLI can be used for longitudinal tracking. We show that a multi-modal imaging approach allows for sensitive imaging over longer time frames with different unique advantages for each modality.

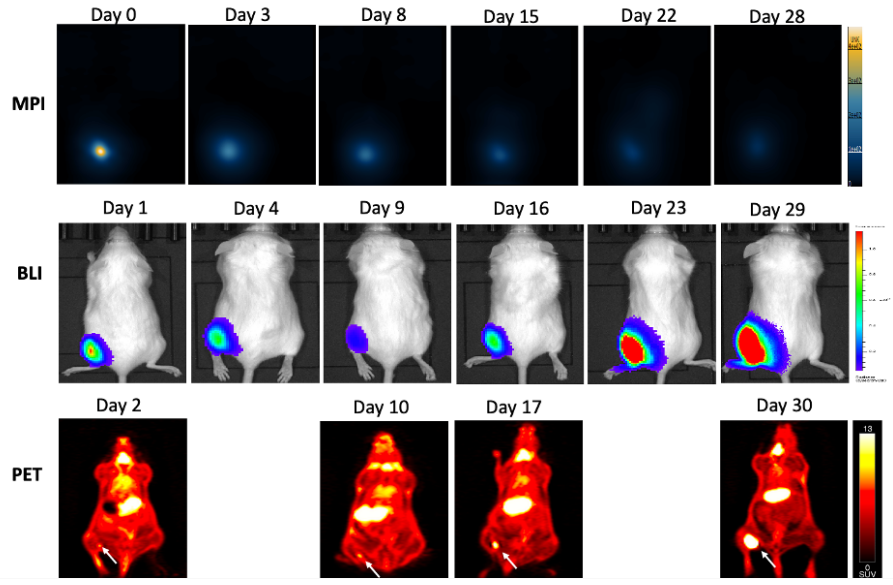

Figure 1: The detection of MSCs using MPI (top), BLI (middle) and PET (bottom) over a 30-day period in a representative mouse. Early time points show sensitive detection of MSCs with MPI and BLI, and later time points show PET and BLI detection, while MPI signal is diminishing at later time points.

Fluorine-19 MRI of Stem Cell-Derived Alveolar-Like Macrophages Tagged with Perfluoropolyether

Janny Kim[1,2], Michael Litvack[1], Daniel Li[1], Brandon Zanette[1], Martin Post[1], Giles Santyr[1,2]
[1]Translational Medicine Program, The Hospital for Sick Children, Toronto, ON, Canada.
[2]Department of Medical Biophysics, University of Toronto, Toronto, ON, Canada.

Introduction: Bronchopulmonary dysplasia (BPD) is a chronic lung disease diagnosed in ventilated preterm infants leading to compromised innate immune system. This can inhibit branching morphogenesis[1] and lead to long-term breathing complications. Stem cell-derived alveolar-like macrophages (ALMs) have been shown to be therapeutically effective by promoting gas exchange and tissue repair in a rodent models of lung disease[2]. For ALMs to be used as therapeutics, a non-invasive imaging modality to guide treatment and monitor improvement is essential. Magnetic Resonance Imaging (MRI), such as Fluorine-19 (^{19}F) MRI, is a non-invasive imaging technique, suitable for longitudinal monitoring of cells. Cells can be labeled with fluorinated compounds, such as perfluoropolyether (PFPE) to potentially make them visible in the lung in vivo[3]. In preparation for longitudinal in vivo studies, in vitro ^{19}F MRI was performed in different dilutions of PFPE, as well as PFPE-labeled ALMs to mimic in vivo experiments in rat lungs. ^{1}H images were also obtained to confirm registration of the ^{19}F images.
Methods: For ^{19}F labeling and detection, a commercially available PFPE-based reagent was chosen (CS-1000, CelSense Inc.). Various concentrations of PFPE with consistent total volume of 1mL were prepared in Eppendorf tubes: 100%, 70%, 40%, 20%, 8%, 4%, 2%, 1%. ^{19}F MRI was performed using a 3T clinical scanner (Philips Achieva) with a custom-built transmit-receive animal size birdcage coil tuned to the ^{19}F frequency. Imaging was done using a standard gradient echo pulse sequence with the following parameters: field of view=150x150mm, matrix= 192x192, slice thickness=30mm, flip angle (FA)=50°, TR/TE=20/2.2ms, number of signal averages=200. A human knee coil, provided by Philips, was used for proton MRI. Images and signal-to-noise ratio (SNR) of eight different PFPE solutions were processed and calculated using ImageJ and MATLAB. Relative SNR is the normalized SNR value, where each SNR value was divided by SNR from the stock PFPE solution (100%) and multiplied by 100. ALMs were produced and cultured following the protocols of Litvack et al[2] and Riberdy et al[4] respectively. The ALMs were co-incubated with 8% PFPE solution for four hours. 5 million PFPE-labeled cells were harvested (manually counted) and spun down in a pellet form.
Results: Figure 1 shows the SNRs measured from the eight different concentrations of PFPE solutions. The relationship between the relative SNR and PFPE concentration showed the expected linear trend with the slope of 1.002 and r-squared value of 0.992. The value of relative SNR measured from the cell pellet of PFPE-labeled ALMs is also shown in Figure 1 in blue. When the cell pellet was imaged, the linear relationship still held true with a slope of 1.009. Figure 2 shows the overlay image of the cell pellet with the three different PFPE solution tubes: 100%, 20% and 4% concentrations. The SNR was 1091, 212, 36.6 for 100%, 20% and 4% tubes respectively and 7.37 for the cell pellet. On the overlay image, only the fluorine signal coming from the cell pellet is shown in red, as indicated by the arrow.

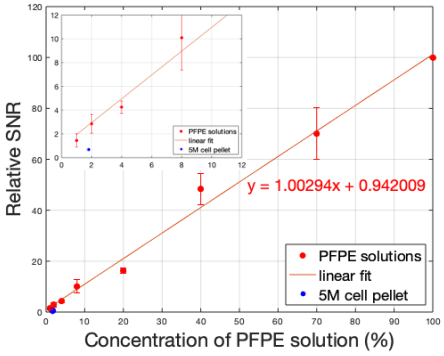

Figure 1. Averaged values of relative SNR plotted as a function of PFPE concentration with error bars. The equation of the linear fit is also shown.

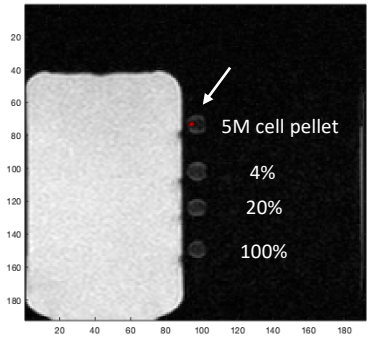

Figure 2. An overlay of ^{19}F image (red) and the ^{1}H image (grey-scale) of three PFPE solutions (bottom) and a PFPE-labeled cell pellet (top).

Conclusion: The linear relationship between SNR and PFPE concentration (Fig. 1) confirms the feasibility of visualizing PFPE down to 10µL (1mL of 1% PFPE) using ^{19}F MRI at 3T. This work further demonstrates the feasibility of detecting 5 million cells, a typical number of cells expected to be used for stem cell treatment, in rats. This work serves as a preliminary step toward in vivo MRI of ALMs instilled in the rat lung. Following successful detection of PFPE-labeled ALMs in rat lungs, considering the advantages ^{19}F MRI gives, longitudinal monitoring of biodistribution of ALMs may be possible. This will further benefit the clinical translation of ALMs as a stem cell therapy to treat chronic lung diseases, including BPD. **References**: [1] Blackwell, T. S. et al. *J Immunol*, 2011. [2] Litvack M. et al. Am J Respir Crit Care Med. 2016. [3] Fox, M. S. et al, *Magnetic Resonance Insights,* 2015 [4] Riberdy, V. et al, *Magnetic Resonance in Medicine*, 2019.

VivoTrax+™ improves the sensitivity and detection of cancer cells with magnetic particle imaging

Kyle J.T. Van Beek, Julia J. Gevaert, Olivia C. Sehl, Paula J. Foster
Robarts Research Institute, Department of Medical Biophysics, University of Western Ontario

Introduction: Magnetic particle imaging (MPI) is a non-invasive, non-ionizing, sensitive modality capable of tracking cells labeled with superparamagnetic iron oxide (SPIO) nanoparticles *in vivo*. MPI signal is proportional to iron content, which, combined with a measure of iron per cell, can be used to quantify cell number. As a tracer-based modality, the SPIO has a critical role in imaging cells. The ideal SPIO for cell tracking should label cells efficiently, without inducing cytotoxicity, and retain magnetic properties after cellular internalization. Iron core size has a direct effect on the magnetic relaxation of SPIOs and determines their sensitivity and resolution[1]. VivoTrax™ (Magnetic Insight Inc.), or ferucarbotran, is a commonly used MPI tracer and has been used to detect a variety of cell types. Although widely used, it is not considered optimal for MPI due to its bimodal size distribution, comprised of 30% ~25-30 nm cores and 70% ~5 nm cores[2]. The smaller cores do not magnetize sufficiently to produce signal, leaving a small fraction of particles that contribute to signal. Recently, Magnetic Insight released VivoTrax+™, a filtered form of VivoTrax™ that increased the fraction of larger cores to have improved MPI performance. The goal of this study is to directly compare the two agents by assessing their sensitivity, resolution, cell labeling efficiency, and *in vivo* imaging, to provide evidence of superiority for Vivotrax+ over Vivotrax for tracking cancer cells with MPI.

Methods: A2058 human melanoma cancer cells were labeled by coincubation in vitro with either VivoTrax+™ or VivoTrax™, both with and without addition of transfection agents (TAs). After labeling, Perls Prussian Blue (PPB) staining for iron was performed, samples containing 1 x 10^6 cells suspended in ~250 µL phosphate-buffered saline (PBS) were collected for MPI acquisitions. MPI relaxometry was performed on triplicate samples on a Momentum™ scanner (Magnetic Insight Inc.). To assess cellular sensitivity, samples containing 62.5K, 31.3K, 15.6K, and 7.8K (K = 1000) VivoTrax+™ or VivoTrax™ labeled cells were acquired. In vivo imaging was performed on nude mice 24 hours post intravenous injections of VivoTrax+™ (n = 3) and VivoTrax™ (n = 3).

Results: Relaxometry of free and intracellular VivoTrax+™ and VivoTrax™ is shown in Fig. A1. The MPI signal was ~2.4 times greater for VivoTrax+™ compared to VivoTrax™ (111.8 vs. 46.6). After cellular internalization, sensitivity was reduced by ~4 times with VivoTrax+™ and ~2 times with VivoTrax™. Reduced sensitivity could be explained by the confined intracellular environment, which causes aggregation and slower relaxation. As few as 15.6K VivoTrax+™- labeled cells were detected using 2D imaging (Fig. 1B). Overall, fewer cells were detected with VivoTrax+™ than VivoTrax™. Significantly more signal (Fig. 1.C2) was detected in the liver of mice with VivoTrax+™ (Fig. 1.C3) compared to VivoTrax™ (Fig. 1.C4), in agreement with relaxometry.

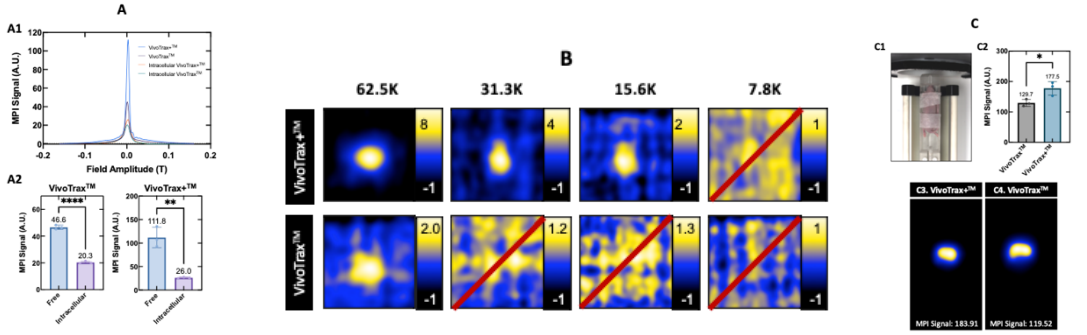

Figure 1: Relaxometry of VivoTrax+™ and VivoTrax™ showing MPI sensitivity before (free) and after cellular internalization **(A)**. 2D MPI of cell samples comparing VivoTrax+™ to VivoTrax™ **(B)**. In vivo MPI signal of VivoTrax+™ and VivoTrax™ after IV injections in nude mice **(C).**

Conclusion: This study demonstrates the improved performance of VivoTrax+™ and its potential use for cancer cell tracking applications. VivoTrax+™ had a higher labeling efficiency and cellular sensitivity than VivoTrax™. Significantly more MPI signal was detected in the liver of nude mice 24 hours post IV injection, demonstrating higher *in vivo* sensitivity. In the future, intracellular resolution will be analyzed, and histology of the liver will be assessed to confirm iron uptake.

References: [1] Tay, ZW. *et al*. *Biomed Phys End Express* **3**, 1–21 (2017). [2] Eberbeck, D. *et al. IEEE Trans Magn* ***49*****,** 269–274 (2013).

PET imaging of GLUT5 in rodent models of neuroinflammation

Amanda J. Boyle[1], Emily Murrell[1], Christin Schifani[1], Andrea Narvaez[1], Junchao Tong[1], Melinda Wuest[2], Frederick West[3], Frank Wuest[2], and Neil Vasdev[1].

[1]Azrieli Centre for Neuro-Radiochemistry, Brain Health Imaging Centre, Centre for Addiction and Mental Health, Toronto, ON

Departments of [2]Oncology and [3]Chemistry, University of Alberta, Edmonton, AB

Introduction: Fluorine-18 labeled 6-deoxy-6-fluoro-D-fructose (6-[^{18}F]FDF) was developed for PET imaging of fructose metabolism in breast cancer via the fructose-specific facilitative hexose transporter, GLUT5 **[1]**. In the brain, GLUT5 is predominantly expressed on microglial cells which are activated in response to inflammatory stimuli. The most common PET imaging biomarker of neuroinflammation is the 18 kDa translocator protein (TSPO) which is expressed on both activated microglia and astrocytes. We hypothesize that 6-[^{18}F]FDF will specifically image the role of microglia in neuroinflammation and neurodegeneration.

Methods: Automated radiosynthesis of 6-[^{18}F]FDF was performed as previously described **[2]** and evaluated in a) healthy control (HC) male Sprague Dawley rats and b) in a neuroinflammation model induced by intracranial injection of lipopolysaccharide (LPS) into the right striatum (males, 50 µg/animal) **[3]**. Evaluation of 6-[^{18}F]FDF was performed by dynamic PET imaging following tail-vein injection of the radiotracer. Experiments underway include PET imaging in female rats at low and high estrous phases of the menstrual cycle, PET imaging in LPS rodents with 2-[^{18}F]FDG, cellular uptake of 6-[^{18}F]FDF, and immunohistochemistry studies.

Results: PET/MR test-retest studies of HC male rats with 6-[^{18}F]FDF displayed steady accumulation of radioactivity in the brain that plateaued at ~80 min to an SUV of 1.63 ± 0.10 with no difference observed between the test-retest groups (p = 0.0732) or between left and right brain regions (p = 0.193). Despite bone uptake of ^{18}F in the skull that could potentially lead to spill over to adjacent brain regions (e.g., cerebral cortex), the partial volume effect is negligible in deep nuclei (e.g., striatum and thalamus). In LPS-treated rats, increased accumulation of radioactivity from 6-[^{18}F]FDF was observed in the ipsilateral striatum compared to the contralateral side at 48 hr post-LPS injection (1.25 ± 0.01 vs. 0.99 ± 0.03 SUV at 80-110 min; n=3, p = 0.0001; Fig. 1). Longitudinal PET/MR scans showed that the ipsilateral-contralateral difference in striatal 6-[^{18}F]FDF uptake was decreased at one-week post LPS injection and was no longer observed at two-week and one-month time points. In contrast, no significant differences in the SUVs were observed following administration of 6-[^{18}F]FDF between the right and left thalamus in the LPS-injected rats at any time points.

Conclusions: 6-[^{18}F]FDF is a promising PET radiotracer for imaging GLUT5 in the brain with applications for imaging neuroinflammatory and neurodegenerative diseases.

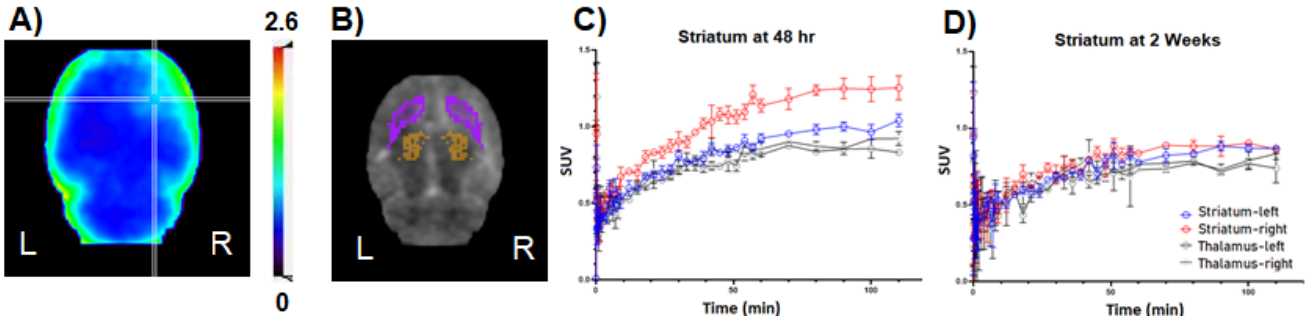

Fig. 1. A) Dynamic PET imaging of 6-[^{18}F]FDF LPS rat models of neuroinflammation (48 hr) and **B)** MRI indicating striatum (purple) and thalamus (orange), and associated time-activity curves in the left and right striatum and thalamus at **C)** 48 h, **D)** 2 weeks post-LPS injection.

References: [1] Wuest M, et al. Radiopharmacological evaluation of 6-deoxy-6-fluoro-D-fructose as a radiotracer for PET imaging of GLUT5 in breast cancer. *Nucl Med Biol*. **2011**;*38*:461-475. **[2]** Bouvet V, et al. Automated synthesis and dosimetry of 6-deoxy-6-[^{18}F]fluoro-D-fructose (6-[^{18}F]FDF): a radiotracer for imaging of GLUT5 in breast cancer. *Am J Nucl Med Mol Imaging*. **2014**;*4*:248-259. **[3]** Narayanaswami V, et al. Preclinical Evaluation of TSPO and MAO-B PET Radiotracers in an LPS Model of Neuroinflammation. *PET Clin.* 2021;16:233-247.

The environment surrounding iron oxide nanoparticles influences sensitivity and resolution for magnetic particle imaging

Maryam A. Berih[1], Olivia C. Sehl[1,2], Paula J. Foster[1,2]
[1] Imaging Research Laboratories, Robarts Research Institute, Canada
[2] Department of Medical Biophysics, University of Western Ontario, Canada

Introduction: Magnetic particle imaging (MPI) is an emerging imaging technique that directly detects superparamagnetic iron oxide nanoparticles (SPIO) using magnetic gradients and excitation fields[1]. There are exciting opportunities for cellular imaging with MPI, which involves labeling cells with SPIO, to learn about the fate of cellular therapies and cancer cells in preclinical models[2]. There is some evidence that the ability of the SPIO to respond to the changing magnetic fields is influenced by the nanoparticle's surroundings[3]. For imaging SPIO *in vivo*, where tissues have varying stiffness[4], it is not understood how surrounding tissue effects the sensitivity and resolution of MPI signal. **Our aim** is to measure changes in MPI sensitivity and resolution resulting from suspending SPIO and SPIO-labeled cells tissue-mimicking agarose phantoms.

Methods: 5.5 µg ferucarbotran (an SPIO) was suspended in saline, 0.5%, 2.5%, or 5% agarose (n = 3). These agarose phantoms mimic the Young's Modulus (stiffness) of liver, lung, and cartilage tissues, respectively[4,5]. Mesenchymal stem cells (MSC) were labeled by coincubation of ferucarbotran and transfection agents in culture[6]. 5 x 10^5 MSC were suspended in these same four conditions (n = 3). MPI relaxometry was used to characterize the sensitivity (maximum intensity) and resolution (full width half maximum, FWHM) using rf amplitude 20 mT and bandwidth ±160 mT. MPI images of these samples were acquired using 5.7 T/m gradient and 20 mT excitation.

Results: Comparing ferucarbotran in saline to 5% agarose, MPI relaxometry exhibited a 36% reduction in sensitivity and a 55% increase in FWHM ($p < 0.05$) (Fig. A and C). This can be visualized in MPI images (Fig E) as a reduction in signal amplitude from SPIO in 5% agarose, despite being the same amount of SPIO. For ferucarbotran-labeled cells, a similar trend is observed with MP relaxometry (Fig B and D). Compared to cells in saline, MPI sensitivity was reduced by 21% and resolution by 11% for cells in 5% agarose, however these results were statistically non-significant. The images of ferucarbotran-labeled cells in saline and 5% agarose produce similar observable MPI signal (Fig. F).

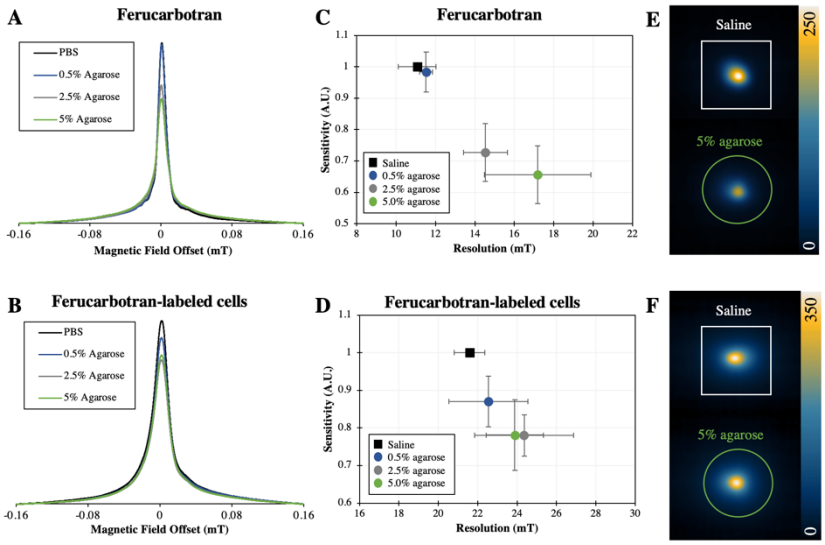

Figure: MPI relaxometry curves for ferucarbotran (**A**) and ferucarbotran-labeled cells (**B**) in saline, 0.5%, 2.5%, or 5% agarose. The adjacent plots show measurements of sensitivity and resolution from these curves (**C, D**). MPI images of ferucarbotran (**E**) in saline or 5% agarose also show differences in MPI signal intensity and resolution, but images of ferucarbotran-labeled cells (**F**) do not.

Conclusion: As agarose concentrations increase a relative reduction in MPI amplitude (sensitivity) and increase in FWHM (resolution) are observed for ferucarbotran. This is likely due to partial immobilization of SPIO within agarose suspensions that contribute to delayed magnetic relaxation[7]. Changes in sensitivity and resolution with agarose concentration were non-significant for ferucarbotran-labeled cells. We reason that cellular internalization of ferucarbotran may shield the SPIO from experiencing the surrounding environment. This work contributes to our understanding of how the surrounding environment can influence SPIO relaxation which has important implications for *in vivo* imaging (varying surrounding environments) using MPI.

[1] Saritas EU. *et al. J. Magn. Reson.* 229. (2013). [2] Sehl OC *et al. Tomography* **6**. (2020). [3] Utkur M *et al. Appl. Phys. Lett.* 115. (2019). [4] Salati MA *et al. Polymers* (Basel). 12. (2020). [5] Yang YHK *et al. J. Funct. Biomater.* 11, (2020). [6] Sehl OC & Foster PJ *Sci. Rep.* 11. (2021).[7] Arami H *et al. Med Phys.* 40. (2013)

Multi-view 3D echocardiography volume compounding for mitral valve procedure planning

Patrick Carnahan[1,2], Daniel Bainbridge[3], Elvis C.S. Chen[1,2,4], and Terry M. Peters[1,2,4]
[1]Imaging, Robarts Research Institute, London, CA,
[2]School of Biomedical Engineering, [3]Department of Anesthesiology, London Health Sciences Centre, [4]Department of Medical Biophysics
Western University, London, CA

Introduction: Current standard of care diagnostic imaging for mitral valve procedures primarily consists of transesophageal echocardiography (TEE) as it provides a clear view of the mitral valve leaflets and surrounding tissue.[1,2] However, TEE has limitations in signal dropout and artefacts, particularly for structures lying below the valve such as chordae tendineae. Although cardiac CT is capable of imaging the entire mitral valve structure, due to higher costs and exposure to ionizing radiation it is not employed for all patients as part of the standard of care. Our objective is to enable TEE imaging to provide detailed imaging of the entire mitral valve apparatus without the use of additional CT imaging. We propose a volume compounding system to fuse multiple TEE acquisitions to create a single volume containing the mitral valve and sub-valvular structures with a high level of detail.

Methods: Images are acquired during standard pre-operative imaging sessions using Philips Epiq TEE probes. One or more mid-esophageal volumes and four or more transgastric volumes with a high degree of overlap are acquired with ECG gating. These volumes are then rigidly registered with an image based group wise registration method[3] using the end-diastolic phase of the cardiac cycle. Following rigid alignment, for each frame in the image sequences, non-rigid registration is performed with a semi-simultaneous approach[3] to account for slight variation in cardiac phase between acquisitions. Then, each voxel in every volume is weighted according to a combination of distance from the image probe and a feature detector based on the monogenic signal. The volumes are then resampled onto a common isotropic grid, and voxel-wise weighted averaging is used to generate the final volume.

Results: We validated this image compounding approach on two excised porcine mitral valve units, a custom silicone phantom, and on two patient data sets acquired from University Hospital with REB approval. The porcine valves and silicone phantom were imaged according to our clinical acquisition procedure. The porcine valves were also stained with iodine and imaged with a CT scanner to provide ground truth data. The ultrasound images were then compounded using the described approach. The resulting compounded volumes were registered to the CT volumes to enable direct comparison for both the porcine models and phantom. The compounded volumes visually replicate the structures visible in the ground truth CT scan, and chordae measurements have an error of 0.6±0.5mm between modalities. Results of ultrasound compounding on human patient data sets are shown in Figure 1. Visual inspection shows clear delineation of the mitral valve leaflets, chordae tendineae, and papillary muscles.

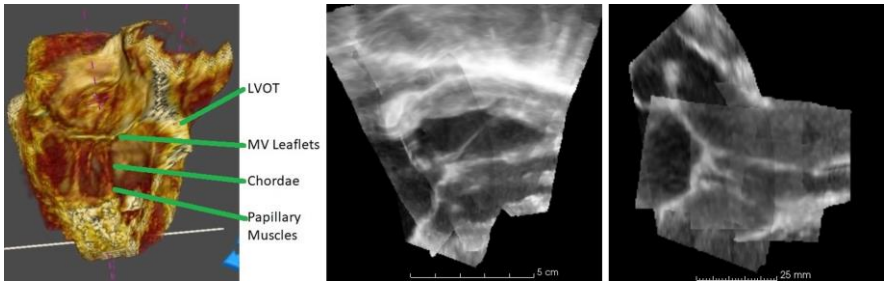

Figure 1: Visualizations of compounded TEE data from five different TEE volumes. Left, a volume rendered view. Middle, a commissure-commissure slice. Right, an AP slice.

Conclusions: We have described a workflow for capturing a series of images using a TEE probe during standard diagnostic imaging that can then be registered and compounded together. These compounded volumes capture the sub-valvular structures of interest for cardiac procedure planning including the left ventricular outflow tract and the chordae tendineae. Capturing the necessary additional volumes can be done with no added cost and only an additional ten minutes to the current standard of care diagnostic images. This method can provide clinicians with a single volume that captures the entire mitral valve apparatus without the use of cardiac CT, which will enhance the mitral valve procedure planning process.

References: 1. Shah, P. M, *Journal of Cardiology* 56, 125–133 (2010). **2.** Linden, A *et al., The Thoracic and Cardiovascular Surgeon* 65, S213–S216 (2017). **3.** Wachinger, C. et al., *MICCAI 2007* 327–335 (2007). **4.** Grau, V. et al., *MICCAI 2006* 612–619 (2006).

The Resurrection of Multi–Energy Subtraction Angiography

Lisa. M. Garland and Ian. A. Cunningham.
Robarts Research Institute, Western University, London Ontario, Canada.

Introduction: For decades, the leading cause of death globally has been cardiovascular disease (CVD). To detect CVD, an angiogram may be used. This invasive procedure images vasculature in the extremities, brain, and heart by imaging an injected contrast agent using X-rays. This procedure requires a high dose of radiation and the injection of contrast which can be uncomfortable for patients. Digital subtraction angiography (DSA) is a powerful method used in neuro angiography capable of suppressing the visibility of background structures. Though background suppression would be useful in other applications such as cardiac, due to the time delay required between the two subtracted images, DSA is not feasible for cardiac work. Multi-energy subtraction angiography allows for near complete background suppression with a total acquisition time of just milliseconds, making this protocol capable of cardiac imaging. The objective is to further develop this technique to reduce dose, iodine concentration, patient motion artifacts and supress background structures while still maintaining a reasonable signal to noise ratio (SNR) and current engineering of angiographic systems. To do so, we propose a multi-energy imaging technique where optimization of the k-edge effect of iodine is required, as well as high performance imaging detectors.

Methods: Based on MATLAB simulations, over a dozen parameters were optimized such as kV high, kV low, mAs, filter thickness, filter atomic number, iodine concentration, pixel area and many more. Low iodine concentrations were assumed because it is more important to maximize iodine SNR when iodinated structures are difficult to see in a noise-limited image. Using a Canon Alphenix angiography system, images of a chest phantom with contrast agent injected into simulated coronary arteries will be obtained to test the proposed k-edge multi-energy subtraction technique. Theoretical results have already been validated using the Rose SNR threshold and compared to DSA calculations, as well as to single image angiography, the gold standard method of cardiac angiography. These results will be experimentally confirmed using an iodine step wedge and chest phantom. Previous work in our lab used a spinning filter placed in front of the beam to attenuate the high energy spectrum only. In contrast, our work uses a stationary filter of optimal atomic number and thickness to attenuate approximately 50% of the transmitted air KERMA. A theoretical comparison of a static vs. dynamic filter has also been conducted. The underwhelming results demonstrated that a stationary filter makes an insignificant change in image quality and therefore, all experiments will be done using a stationary attenuation filter. A figure of merit (FOM) is used that is the SNR per root exposure (normalized by dose-gives SNR for a specified exposure) this is useful for comparing two methods to see which will yield the better SNR for the same dose to patient. Maximum tube heat loading, and cooling will also be considered, as this is a limitation in angiography due to the long procedures and constant wear on the X-ray tube.

Results: It was found that an mAs ratio of 10-20 would be acceptable for 20-30cm patients using multi-energy subtraction methods. Using a copper filter (Z=29) which is used in standard practise was also found to be ideal and is easily accessible, Cooper filter thickness of $0.2 g/cm^2$ for a patient of 40cm would yield a FOM for multi-energy of 0.41 compared to 0.71 for the gold standard single image acquisition. This is a significant decrease, but it is important to note that the benefits of background suppression compensate for the reduction in SNR and FOM. Similar decrease can be seen for DSA which has been very successful in clinical applications. Though detector readout noise was ignored for this simulation, heat loading was not. Similar to FOM, SNR was normalized per root heat units, where SNR was determined for a specified tube heat loading. It was found that by adding a $0.2 g/cm^2$ copper filter in front of the beam, the FOM increases by 34% but requires nearly double the tube heat loading to maintain the SNR per unit exposure. Experimental images produced by colleagues showed majority of background structures suppressed with enhanced visibility of iodine structures.

Conclusions: Multi-energy subtraction angiography is an alternative to conventional angiography and DSA. It could have application in cases where acquiring a mask image for DSA is not possible or results in unacceptable motion artifacts (uncooperative or cardiac patients). Multi-energy subtraction angiography can suppress background image structures and produce an iodine SNR of approximately 50% that of conventional single kV images for the same patient dose. Finally, multi-energy angiography can produce images with the same or better iodine SNR compared to conventional single kV images for the same tube heat loading. Once our chest phantom is obtained, theoretical results with be further validated. Success will be measured by how this may reduce procedure time and reduce both radiation exposure and contrast injection requirements.

Oral Session 7: Cancer Imaging

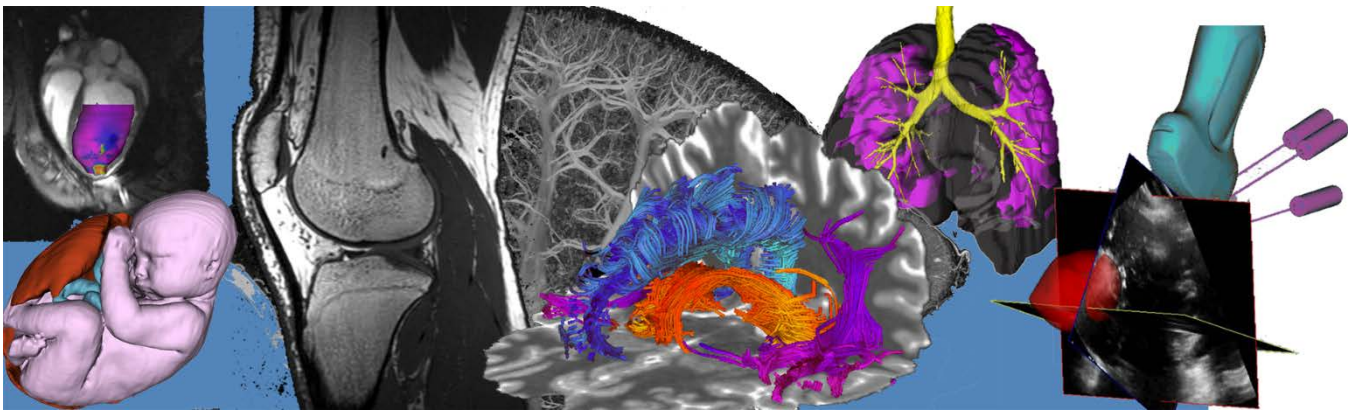

Quantification of the Tumor Microvascular Response to Stereotactic Body Radiation Therapy Using Optical Coherence Tomography Angiography and Dynamic Contrast Enhanced MRI

W. Jeffrey Zabel[1,2,†] , Nader Allam[1,†], Warren D. Foltz[2,3], Costel Flueraru[4], Edward Taylor[2,3], I. Alex Vitkin[1,2,3].

[1]Department of Medical Biophysics, University of Toronto, Toronto, Canada.
[2]Radiation Medicine Program, Princess Margaret Cancer Centre, Toronto, Canada.
[3]Department of Radiation Oncology, University of Toronto, Toronto, Ontario.
[4]National Research Council Canada, Information Communication Technology, Ottawa, Canada.
[†]These authors Contributed equally to this work

Introduction

Stereotactic Body Radiation Therapy (SBRT) is a cancer treatment that involves the delivery of much higher doses of radiation in fewer fractions than conventional radiation therapy. SBRT is being used more often in the clinic since it has shown improved tumor control in some sites. Despite the increased use of SBRT, the exact radiobiological mechanisms of tumor cell kill are not well understood. Preliminary evidence has suggested that the high doses associated with SBRT lead to vascular ablation. The tumor vascular response to SBRT may thus be an important determinant of treatment outcome. Monitoring the tumor vascular response to SBRT in the clinic may inform personalized SBRT treatment adaptions based on the structure and function of the vascular network.

Speckle Variance Optical Coherence Tomography (svOCT) allows for high resolution (~10 μm) 3D images of the vascular network in a tumor xenographt window chamber mouse model. Here we use svOCT to monitor the tumor vascular response to SBRT thus providing novel insight into the temporal dynamics of the microvasculature throughout SBRT.

Despite the excellent resolution afforded by svOCT, clinical implementation of this technology is limited by its modest depth penetration of ~1-2 mm. Dynamic Contrast Enhanced (DCE) MRI is a clinically applicable imaging modality however its limited spatial resolution (mm scale) may not be able to image the tumor microvasculature (μm scale). To overcome this 'resolution gap', we directly correlated high resolution svOCT images of the microvasculature to the comparably lower resolution DCE-MR images in the same animals. Successful discovery of correlates between svOCT derived microvascular information and DCE-MRI macrovascular metrics will support the use of DCE-MRI in the clinic for SBRT microvascular response monitoring potentially enabling personalized SBRT treatment adaptions.

Methods

n = 8 mice were subcutaneously injected with human pancreatic cancer cells (BxPC3 cell line). Plastic window chambers were 3D printed and sutured to the dorsal skinfolds of the mice enabling dual modality (svOCT and DCE-MRI) imaging. n = 6 mice (n = 2 controls) were exposed to a clinically relevant SBRT fractionation schedule (3 fractions of 10 Gy/fraction). svOCT and DCE-MRI was performed at regular intervals before, during and up to 1.5 months after SBRT to monitor the tumor microvascular response.

Results

Several micro-svOCT to macro-DCE-MRI linkages were quantified for pre-irradiation time points. The strongest correlation was found between svOCT's mean intervascular distance and DCE-MRI's time to peak contrast enhancement metric (Spearman correlation coefficient, $r = -0.81$, $P < 0.0001$). Data analysis for timepoints during and after SBRT is ongoing.

Conclusions

The microvascular insights afforded by svOCT are important for understanding the temporal dynamics the vascular networks response to SBRT. Linking svOCT microvascular images to DCE-MRI macro-vascular metrics provides a 'bridge' to the clinic so that microvascular information may be used to personalize/optimize a patients treatment plan.

Contrast Enhanced Endobronchial Ultrasound for Malignant Lymph Node Detection and Staging

Sean McGrath[1]*, Masato Aragaki[2], Alexander Gregor[2], Yamato Motooka[2], Yu-Jack Shen[3], Matthew Chen[3], Nicholas Bernards[2], Kazuhiro Yasufuku[2] and Naomi Matsuura[1,3,4]

[1]Institute of Biomaterials and Biomedical Engineering, University of Toronto, [2]Division of Thoracic Surgery, Toronto General Hospital, University Health Network, Toronto, [3]Department of Material Science and Engineering, University of Toronto, [4]Department of Medical Imaging, University of Toronto

Introduction: Determining malignant involvement in the lymph nodes is a significant prognosis factor for cancer survival [1,2,3]. Contrast-enhanced ultrasound (CE-US) is often employed for the determination of lymph node status, as CE-US can easily identify the level of vascularization [1,4]. Despite this, there have been no studies using CE-US on the mediastinal and hilar lymph nodes, important sites for lung cancer prognosis. This is partially due to the limitations of standard ultrasound systems, which cannot access the inner lung. Additionally, typical ultrasound systems capable of reaching those lymph nodes are not designed to detect the signals scattered by microbubbles (MBs). This barrier is overcome by using the EU-ME2 PREMIER ultrasound processor with BF-UC180F bronchoscope (Olympus, Japan), an ultrasound probe attached to the end of a bronchoscope, known as an endobronchial ultrasound (EBUS), which can display the harmonics emitted by MB contrast enhancement [5]. Although EBUS has been used to aid in lymph node biopsies, it has not been used with contrast enhancement outside of doppler imaging. This study determines the concentrations of MBs required for detection in-vitro and in-vivo and compares EBUS to a pre-clinical ultrasound system. Mouse models of lung cancer have been used to demonstrate the use of this system with contrast enhancement, as an analog for metastatic lymph nodes.

Methods: Lipid shelled MBs were synthesized in-house, with a number peak diameter of 1.1 ± 0.1 µm. The MB detection limit of the EBUS system was determined in-vitro by flowing MBs at 1.25, 7.5, and 12.5 x 10^5 MB/mL dilutions through a 3% agar phantom while imaging (MI = 0.06). Mouse models with differing levels of vascularization were used to simulate metastatic lymph nodes. In-vivo MB detection was assessed with the more vascular subcutaneous Murine AE17-OVA mesothelioma tumours (prepared by injecting 10^4 cells/µL into the flank) in C57Bl/6 mice (Taconic Bioscience, NY). For contrast enhancement, 100 µL of MBs were injected, followed by a 50 µL saline flush. EBUS and a VEVO2100 ultrasound system (Visual Sonics, Canada) were used with MBs to compare the EBUS systems perfusion curve to that of a preclinical system (Figure 1). CE-EBUS was compared to EBUS-doppler in a human A549 adenocarcinoma tumour model in athymic nude mice (prepared similarly, Taconic Bioscience, NY).

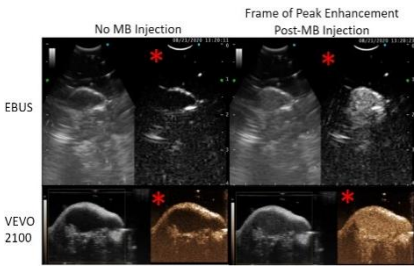

Figure 1: B-mode and contrast mode (*) images from EBUS and VEVO2100

Results: The minimum concentration of MBs visible under EBUS in-vitro was 2.5 x 10^5 MB/mL. The concentration in-vivo was higher, at 2.5 x 10^8 MB/mL. This was expected, as the dilution factor from the mouse blood was ~10x, however this increase may have been due to the tumours having low vascularity, resulting in significantly fewer total MBs being visible. This corresponds to 0.03 µL of perfluorocarbon gas per mL of blood, less than a clinically acceptable dose of Definity MBs (~0.05 µL/mL of blood, Lantheus Medical Imaging, USA). MB perfusion was measured over a region of interest, with EBUS having a similar curve to that of the VEVO2100 system (Figure 2). Additionally, CE-EBUS was able to detect blood flow that EBUS-doppler was unable to detect from.

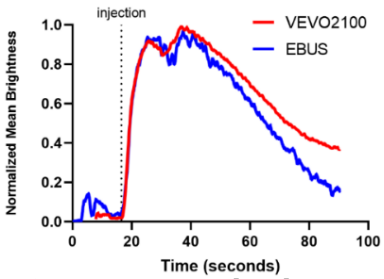

Figure 2: Normalized MB perfusion curves of EBUS and VEVO2100

Conclusion: This study applied CE-EBUS to mouse models as an analog for malignant lymph nodes. CE-EBUS was used on two different tumour models. Future work includes evaluating the EBUS system in conjunction with MBs using rabbit VX2 tumours to model bulky mediastinal lymph node metastasis [6].

References: [1] Y. Jin et al, Asian Pac J Cancer Prev. 2015;16(6): 2361-2368. [2] T. Nakajima et al, J Thorac Oncol. 2012;7: 1009-1014. [3] S. Yin et al, J Ultrasound Med. 2018;37(2): 385-395. [4] M. Mei et al, Cancer Manag Res. 2018;10: 4987-4997. [5] K. Yasufuku et al, Chest. 2004:126(1): 122-128. [6] T. Anayama et al, PLoS One. 2013:8(6): e67355

Ventilation heterogeneity assessed by V-SPECT and ^{129}Xe MRI in lung cancer patients prior to lung resection: An interim analysis of prevalence and clinical relevance

Nisarg Radadia[1], Mobin Jamal[1], Housne Begum[6], Chynna Huang[5], Katherine Radford[5], Nicola LaVigne[5], Norman B Konyer[7], Troy Farncombe[3,8], Christopher Marriott[3,7,8], Michael Noseworthy[3,4,7], Eldar Priel[2,6], Parameswaran Nair[1,5], Yaron Shargall[2,5,6], and Sarah Svenningsen[1,4,5,7]

[1]Division of Respirology, Department of Medicine; [2]Division of Thoracic Surgery, Department of Surgery; [3]Department of Radiology; [4]School of Biomedical Engineering; McMaster University, Hamilton, Canada. [5]Firestone Institute for Respiratory Health; [6]Division of Thoracic Surgery; [7]Imaging Research Center; [8]Department of Nuclear Medicine; St. Joseph's Healthcare Hamilton, Hamilton, Canada.

Introduction: Patients undergoing curative-intent lung cancer resection are at risk of developing postoperative pulmonary complications (PPC). It is possible that *pre-operative* identification and management to improve ventilation heterogeneity (consequence of factors including luminal inflammation, plugging, and emphysema) might reduce PPC and improve outcomes. In this proof-of-concept study, our objective is to determine the prevalence and clinical relevance of ventilation heterogeneity, assessed by Technegas V-SPECT/CT and ^{129}Xe MRI, in patients prior to lung cancer resection.

Methods: Adults undergoing anatomical lung resection for cancer underwent Technegas V-SPECT/CT and hyperpolarized ^{129}Xe MRI[1] to evaluate pre-operative ventilation heterogeneity. Spontaneous or induced sputum was collected to evaluate pre-operative luminal cellular inflammation. Ventilation heterogeneity was quantified as the ventilation-defect-percent (VDP)[2,3] and was considered abnormal if VDP was ≥ mean ±2 standard deviations of a control population. Luminal cellular inflammation was quantified by sputum cytometry and was considered clinically relevant if ≥2.3% eosinophils (or many free eosinophil granules) and/or ≥64%neutrophils with a total cell count of ≥9.7x106 cells/g were reported. PPCs (Ottawa TM&M definitions) and length of hospital stay (LOS) were reported. Herein we report the interim prevalence of pre-operative ventilation heterogeneity assessed by V-SPECT and ^{129}Xe MRI, and their association with postoperative outcomes. Between-group differences were evaluated using Mann-Whitney tests. Univariate relationships were evaluated using Spearman correlations.

Results: 27 patients (16F/11M; 64±8 years-of-age; n=7 never-smokers/n=12 former-smokers/n=8 current-smokers; n=5 asthma/n=10 COPD/n=12 no history of lung disease) have been evaluated pre-operatively and followed for post-operative outcomes. Abnormal ventilation was detected pre-operatively by V-SPECT and MRI for 44% (12/27) and 65% (17/26) of patients, respectively. In a subset of 13 patients in whom sputum was collected, 31% (4/13) had intraluminal inflammation (n=1 eosinophilic/n=2 neutrophilic/n=1 mixed-granulocytic). Intraluminal inflammation was concomitant with abnormal ventilation detected by V-SPECT and MRI for 33% (2/6) and 29% (2/7) of patients, respectively. A PPC occurred in 19% (5/27) of patients (n=4 atelectasis/n=1 pneumonia) and median LOS was 3 days (minimum of 1, maximum of 9). Figure 1 details four representative patients. Pre-operative V-SPECT$_{VDP}$ and MRI$_{VDP}$ were not different for patients with or without a PPC but were positively correlated with LOS (V-SPECT$_{VDP}$, r=0.50, p=0.008; MRI$_{VDP}$, r=0.67, p=0.0002).

Conclusions: Ventilation heterogeneity assessed by Technegas V-SPECT and ^{129}Xe MRI is prevalent prior to lung cancer resection and might be associated with a longer post-operative hospital stay. Ongoing work will determine if ventilation heterogeneity, assessed by Technegas V-SPECT and/or ^{129}Xe MRI, is a modifiable risk factor of poor outcomes following lung cancer resection.

[1]S Svenningsen et al. Acad Radiol 2021; [2]M Kirby et al. Acad Radiol. 2012; [3]C Farrow et al. J Appl Physiol. 2017.

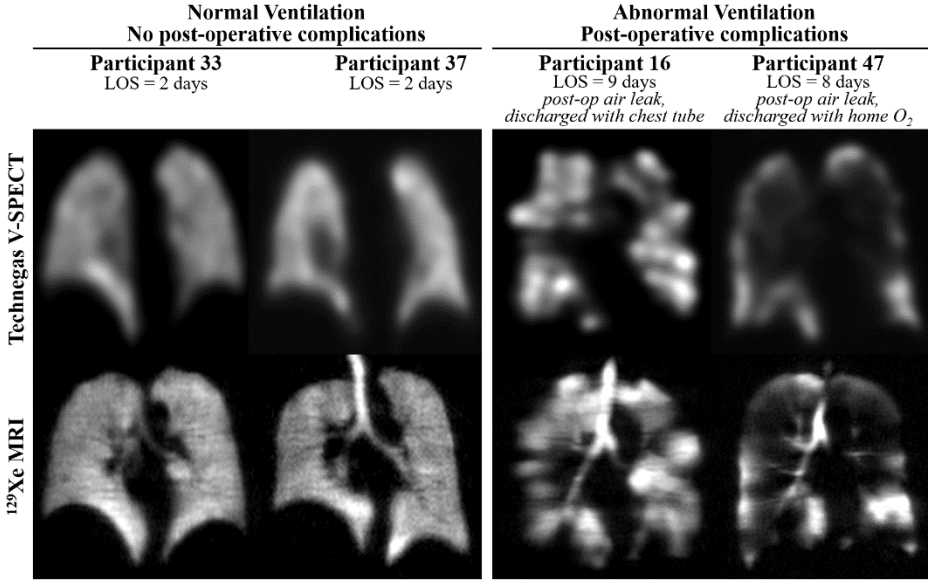

Figure 1. Representative coronal slices of pre-operatively acquired Technegas V-SPECT and ^{129}Xe MRI are shown for two patients with normal pre-operative ventilation and no post-operative complications and two patients with abnormal pre-operative ventilation and post-operative complications.

Optical identification of biomarkers for liquid biopsies

Matthew A. Chen,[1] Catherine Campbell,[1] Yiran Zou,[1] James Drake,[2] Adam Waspe,[2,3] and Naomi Matsuura[1,2,3]
[1]Dept. of Materials Science and Engineering, [2]The Hospital for Sick Children, [3]Dept. of Medical Imaging, [4]Institute for Biomaterials and Biomedical Engineering, University of Toronto

Introduction: Recent clinical studies have demonstrated the release of circulating tumour DNA (ctDNA) concentration from behind the blood-brain barrier in glioblastoma patients using focused ultrasound (FUS) and microbubbles (MBs)[1] however this technique still results in low concentrations of ctDNA. This study investigates the possibility of encapsulating biomarkers at their source, prior to dilution, for subsequent identification using echogenic MBs to improve tumourigenic DNA recovery. Our hypothesis is that insonating MBs can result in liposomes containing local biomarkers and co-injection with calcein can result these liposomes being fluorescent. These fluorescent liposomes could then be isolated optically (i.e. via fluorescence-aided cell sorting). Here, capture of calcein and free DNA after phospholipids MB exposure to focused ultrasound *in vitro* is evaluated.

Methods: PFB (C_4F_{10}) MBs were synthesized using phospholipids (DPPA, DPPC, DPPE-mPEG5k) and glycerol. DiI was included in certain formulations to optically track MB lipids. For cavitation experiments, MBs; DAPI-stained salmon sperm DNA, as a surrogate ctDNA; and calcein were flowed through a polyimide tubing (ø: 1.1mm) ultrasound phantom with applied FUS (1 MHz, 1% duty cycle, 550 kPa). MBs were measured for size and concentration; acoustic response was assessed with a clinical ultrasound system with an agarose phantom and MATLAB, and optical properties of liposomes were measured with fluorescence microscopy and flow cytometry.

Results: MBs were synthesized in-house (concentration: $8.2\pm0.7\text{x}10^9$ MBs/mL, peak diameter: 2.0±0.2µm). Colocalization between DAPI-stained DNA and calcein was observed using flow cytometry and calcein encapsulation in liposomes post-insonation was observed with fluorescence microscopy. MBs flowed without exposure to ultrasound resulted in debris in addition to the MB population.

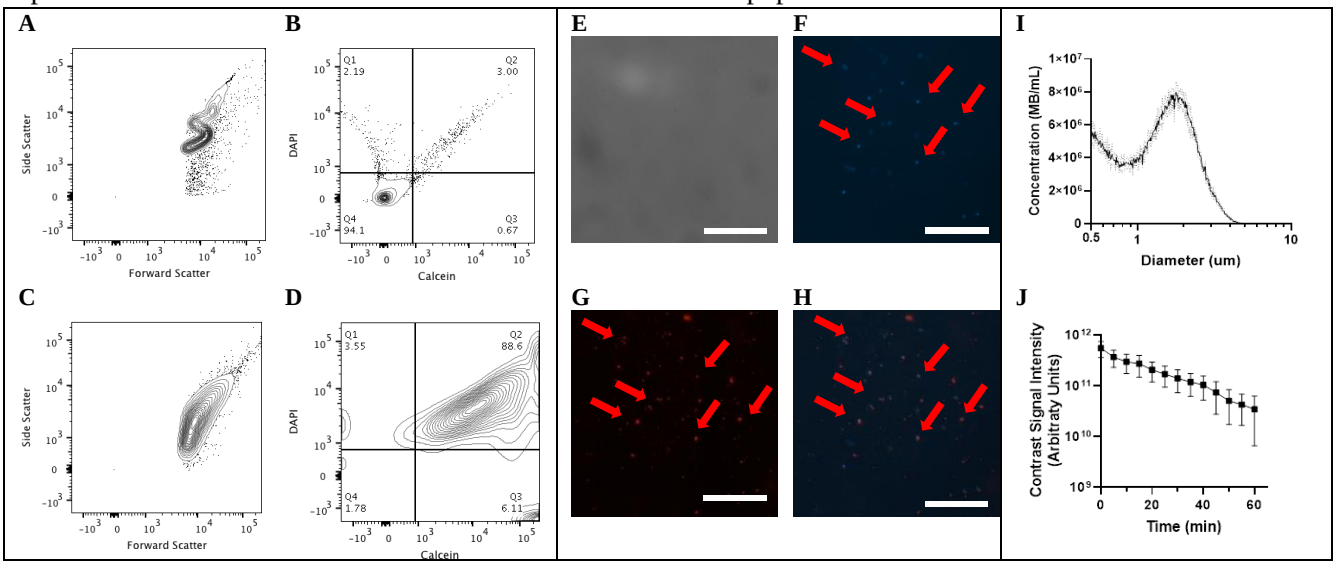

Figure. (A) The MB population under flow cytometry **(B)** did not express any native fluorescence, as shown in Q4 **(C)** Insonation at 1% duty cycle with a 1Hz pulse repetition frequency and 550kPA resulted destroyed MBs and an increased signal in both the **(D)** calcein channel and DAPI channel (Q2). Optical microscopy of sonicated DiI labelled MBs demonstrated **(E)** a destruction of MBs from the insonation. This resulted in particles exhibiting **(F)** DAPI (Ex/Em: 377±50/430±25) and **(G)** DiI (Ex/Em: 531±40/610±60) fluorescence. Scale bars are 29µm. **(H)** DiI and DAPI were found to be co-localized, suggesting that the surrogate DNA biomarker was encapsulated by MB lipids. **(I)** MB distribution was measured and (J) evaluated for acoustic response over time.

Conclusions: DAPI staining allowed surrogate biomarker and calcein detection optically through flow cytometry. DiI signal was colocalized with surrogate biomarker, indicating that MB lipids were colocalized with the fluorescent DNA surrogate biomarker. This suggests that fluorescently labelled particles could potentially be used with optical techniques (i.e. fluorescence aided cell-sorting) for isolation of these particles to collect ctDNA.

Reference: (1) Meng, Y. *et al.* MR-guided focused ultrasound liquid biopsy enriches circulating biomarkers in patients with brain tumors. *Neuro. Oncol.* (2021) doi:10.1093/neuonc/noab057

Oral Session 8: Cardiac and Vascular Imaging

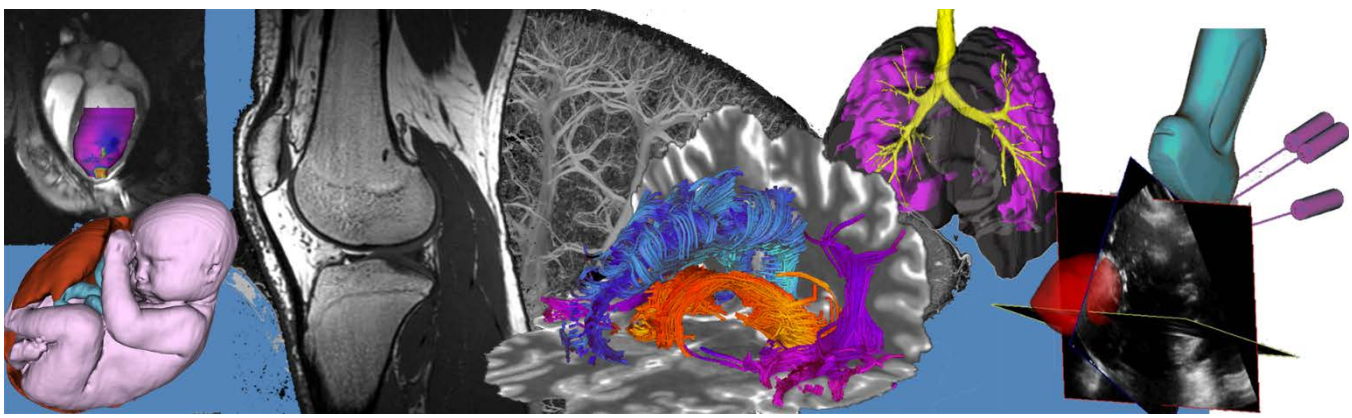

Assessing Acute Cardiac Inflammation after Left-sided Breast Cancer Radiotherapy with Hybrid PET/MRI

AUTHORS: O Chau[1,2], Ali Islam[2,3], Michael Lock[1,2,4], Edward Yu[1,2,4], Robert Dinniwell[1,2,4], Brian Yaremko[1,2,4], Muriel Brackstone[2,3,4], William Pavlosky[3,4], John Bulter[3], Heather Biernaski[3], Chantelle Graf[3], Gerald Wisenberg[2,3,4], Frank S Prato[2,3], Stewart Gaede[1,2,3,4]

[1] London Regional Cancer Program, London, ON, [2] Western University, London, ON, [3] Lawson Health Research Institute, [4] London Health Sciences Centre, London, ON,

INTRODUCTION: Adjuvant radiotherapy (RT) of the breast plays a vital role to breast cancer treatment and has shown to improve overall survival. However, patients with left-sided breast cancer are at an increased risk of coronary artery disease due to the proximity of heart to the radiated breast.[1] Using hybrid positron emission tomography (PET) and magnetic resonance imaging (MRI), cardiac abnormalities and coronary artery disease can be assessed in a non-invasive manner. ^{18}FDG/PET can identify an inflammatory reaction as the activated proinflammatory macrophages preferentially sequester glucose. A previous canine study done in our lab demonstrated that ^{18}FDG/PET detected a global myocardial inflammatory response after a low radiation dose exposure. These effects were detected as early as 1-week and confirmed with histology 1-year after radiotherapy.[2] These findings suggested that radiation induced cardiac effects are occurring at much lower radiation doses than previously believed. In this study, hybrid PET/MRI and serial blood work are used to detect early changes in response to radiation dose in patients receiving standard left-side breast RT.

METHODS: Fifteen left-sided breast cancer (stage T0-T3) patients enrolled in the RICT-BREAST study underwent hybrid PET/MRI cardiac imaging (mMR, Siemens Medical Systems) at baseline and 1-month after standard RT (42.5 Gy in 16 fractions). 11 patients received deep-inspiration breath-hold RT, while 4 patients received free-breathing 4D-CT-based RT.

PET scans were performed prior with heparin glucose suppression, followed by 60-minute list-mode scan of ^{18}FDG/PET bolus injection at 5MBq/kg. The ^{18}FDG/PET images were later dynamically reconstructed with 10-minute intervals. Two patients had insufficient glucose suppression at baseline. Myocardial inflammation was quantified by the change in the mean ^{18}FDG standard uptake based on body weight (meanSUV_{bw}) at 40-60 minutes post injection. Grouped based on the supplied artery (left anterior descending (LAD), left-circumflex (LCX) or right coronary (RC) artery, the standard uptake values of 1-month follow-up were compared to baseline following the AHA heart model.

Cardiac MR assessment, including LV functional and extracellular volume matrices (ECV), were extracted from T1 (pre and post- constant infusion of gadolinium) and cine images acquired simultaneously with PET. Cardiac disease and inflammation biomarkers measurements of troponin T, high sensitive C-reactive protein and erythrocyte sedimentation rate were compared at each timepoint.

RESULTS: Average age of patients, mean(Heart) and $V5_{Gy}$Heart were 60y/o (38-79), 1.79 Gy and 9.46%. Significant increase of ^{18}FDG/PET myocardial uptake at LAD segments ($p = 0.04$, 0.14, 10%) and ECV in slices of apex and bottom ($p \leq 0.02$, 6% and 5%) at follow-up were detected. Whereas, significant reduction of LV stroke volume (SV) ($p < 0.02$, -7%) was identified. Insignificant changes of all blood work measurements at 1-month follow-up were reported. None of the patients had clinically significant cardiac events at follow-up.

CONCLUSIONS: ^{18}FDG/PET myocardial uptake, functional MR, including SV and ECV were sensitive to changes at 1-month after left-side breast cancer RT. This may suggest an acute inflammatory response in the heart.

INNOVATION/IMPACT: In this study, we demonstrated the utility of ^{18}FDG/PET and functional MR to detect early inflammatory response, which varied comparing the cardiac radiation dose delivered to fifteen breast cancer patients underwent RT. Imaging microvascular inflammation in RICD will allow us to consider new techniques to minimize or eliminate heart complications to future cancer patients.

[1] Correa et al. Coronary Artery Findings After Left-Sided Compared with Right-Sided Radiation Treatment for Early-Stage Breast Cancer, J Clin Oncol, 2007; 25(21):3031-3037

[2] El-Sherif et al. [18F]FDG cardiac PET imaging in a canine model of radiation-induced cardiovascular disease associated with breast cancer radiotherapy. Am J Physiol - Hear Circ Physiol. 2019; 316(3):H586-H595

Imaging and Electrophysiological Biomarkers in a Novel Preclinical Pig Model of Doxorubicin-induced Cardiotoxicity

Lin P[1,2], Escartin T[1,3], Ng M[3], Li M[4], Larsen M[3], Barry J[3], Roifman I[3], Pop M[3]

[1]Medical Biophysics, University of Toronto; [2]University Health Network - Toronto; [3]Sunnybrook Research Institute - Toronto; [4]Institute of Biomedical Engineering, University of Toronto, Toronto, ON, Canada

INTRODUCTION: Cardiotoxicity is a major complication of doxorubicin (DXO)-based chemotherapy [1], leading in time to progressive electro-mechanical dysfunction; irreversible tissue remodeling (fibrosis); and, heart failure. However, current diagnostic methods (e.g. biopsy, echocardiography) fail to detect DXO-mediated myocardial injury in early phases post-DXO [2]. Here we present a novel preclinical DXO model, hypothesizing that MR and bipolar voltage maps can reveal biomarkers of early alteration of structure and function post-DXO.

METHODS: In this pilot study, 3 Yorkshire pigs underwent each 4 weekly intravenous injections of DXO (1mg/kg). Cardiac MRI was performed on a 3T GE scanner and included 2D scans at 1x1x5mm resolution (short/long-axis CINE, T1/T2/T2* mapping) and 3D late gadolinium enhancement LGE (1.4mm isotropic voxel, TE = 1.8ms, TR = 4ms). Images were acquired pre-DXO in all pigs and post-DXO (at: 1 week in all three pigs; 5 weeks in pigs #1 and #2; and, 9 weeks in pig#3), and then analyzed using *CVI 42* [3]. In pig#3, bipolar voltage maps were acquired endocardially to detect fibrosis (<1.5mV). Select tissue samples were histologically stained with Masson Trichrome to validate the presence of fibrosis, while H&E stain validated the presence of edema and hemorrhage.

RESULTS: Figure 1A shows selected results from the function assessment of left ventricle (LV), where ejection fraction (EF) was calculated at: baseline, 1 week, 5 weeks, and 9 weeks following the last DXO injection. Fig 1B shows post-DXO increase in % fibrosis calculated from LGE images identified by a 5SD threshold of signal intensity (SI) above healthy tissue. Fig 1C illustrates longitudinal evolution of T1, indicating a significant decrease in T1 signal after DXO therapy (P<0.05, t-test, Bonferroni correction). Furthermore, an increase in mean T2 and T2* values was observed between pre-DXO (T2=55±11ms, T2*=28.2±2ms) and 1-week post-DXO (T2=68±11ms, T2*=35.1±1.7ms). However, these values decreased close to baseline values at week 5 post-DXO (T2=61±16ms, T2*=28.9±1.1ms), suggesting that initial edema as well as hemorrhagic events (due the collapse of some capillaries) had notably resorbed within 5 weeks post-DXO, which was further confirmed by H&E histological observations.

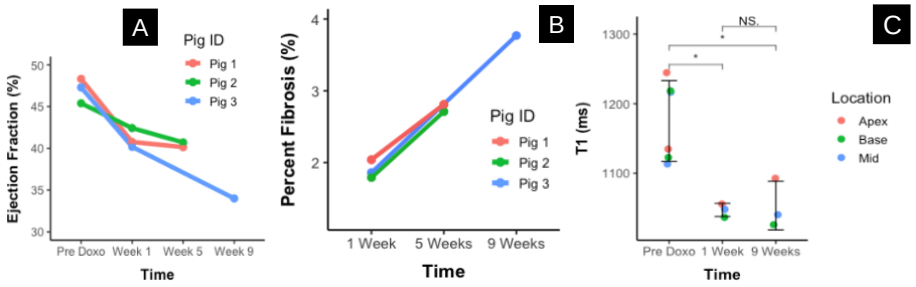

Fig. 1 Longitudinal MRI-based assessment of the LV, pre- and post-DXO therapy, respectively: (A) significant decrease in EF; (B) increase in % fibrosis; and (C) decrease in T1 values as calculated in select heart slices from the apex, mid and base.

Figure 2 shows examples of MR images, bipolar voltage map and histology results from pig#3 at 9w post-DXO. Specifically, Fig 2A shows the bipolar voltage points projected onto endocardial LV shell (fibrosis areas in green have >1.5mV). Fig 2B shows the result of LGE-based segmentation with fibrosis (in green) identified by a 5SD threshold of signal intensity (SI) above healthy tissue (in white). Representative recordings of abnormal and normal ECG waves and samples of histopathological stains as ground-truth, are shown in Fig 2C-D.

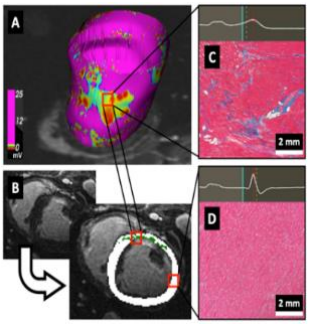

Fig. 2 Fused 3D LGE image with the endocardial bipolar voltage map acquired from the LV (using a CARTO3 system, J&J), along with examples of ECG waves as well as Masson Trichrome slides (note: fibrotic areas are stained in green and healthy tissue in red).

CONCLUSION: We successfully developed a novel translational pig model to study cardiotoxicity in sub-acute phases post-DXO by means of MRI. Our preliminary results demonstrate that there is a gradual decrease in EF post-DXO due to diffuse fibrosis as detected by LGE, T1 and voltage maps, and supported by histology. Future work will focus on extending the study to improve statistical analysis. The longitudinal evolution of MR biomarkers can be used to develop predictive models of the myocardial injury severity post-DXO, while early detection of these biomarkers could help clinicians design better cardioprotective strategies prior to and during DXO therapy.

REFERENCES: [1] Nebigil et al *Front Pharmacol* 2018; [2] McLellan et al *Circ Arr EP* 2014; [3] https://www.circlecvi.com.

Imaging Endothelial Cell Mechanosensory Response to Wall Shear Stress at Varying O_2 Tensions

Kevin R.J. Moore[1], Matthew W. Grol[6], David W. Holdsworth[1,2,7], J. Geoffrey Pickering[1,4,5], Tamie L. Poepping[3]

[1]Robarts Research Institute; Departments of [2]Medical Biophysics; [3]Physics & Astronomy; [4]Biochemistry; [5]Medicine; [6]Physiology & Pharmacology; [7]Surgery
The University of Western Ontario, London, Canada

Introduction: Atherosclerosis is a disease of the artery wall characterized by plaque formation at regions associated with flow disturbances. Blood flow through a vessel can become turbulent when passing through plaque-burdened regions within the vasculature. At sufficiently high wall shear stress (WSS) disturbances, endothelial cell dysfunction occurs, exacerbating the atherosclerotic characteristics of the vessel. Endothelial cell response to WSS has not been thoroughly investigated under physiological O_2 partial pressure. The objective of this study is to image endothelial cell response to WSS stimulations under varying oxygen tension.

Methods: A novel microfluidic device was manufactured from polydimethylsiloxane as it is optically clear, can be used as a cell scaffold, and is permeable to oxygen. The device consists of a small channel for fluid to pass over endothelial cells, with two perpendicular jets to create varying levels of multi-directional disturbed flow, simulating physiological WSS in disturbed flow regions of the vasculature. Particle image velocimetry measurements and analysis (DaVis 8.3, LaVision, Inc.) are used to determine the time variation in the instantaneous WSS throughout the device. The WSS maps demonstrate the variation in scrubbing effects experienced by cells in different regions, which can be correlated to the differential cell responses.

Transient cytosolic free-calcium, a by-product of the ATP signaling response, was measured via fluorescence microscopy (Nikon Eclipse TE2000-U, Tokyo, Japan). Fresh devices are pretreated with fibronectin to facilitate adhesion, then human umbilical vein endothelial cells (passage 4-8) were trypsinized from their culture dishes and seeded into a device to be imaged. Cells were loaded with 1.5 μM FURA-2 AM, then excited with 510 nm light, and the fluorescent emissions at 340 nm and 380 nm were imaged (Fig. 1). Extracting the ratio-time graphs for each cell gives insight to the intracellular calcium levels over the course of the experiment and are analyzed for total calcium response and time to recover.

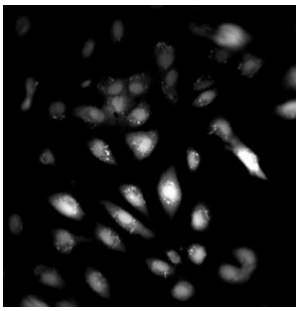

Figure 1: Intracellular Ca^{2+} imaging of endothelial cells exposed to laminar flow.

To control the oxygen tension throughout the experiment, the device is perfused with cell media pre-bubbled with 5% CO_2 and either 1%, 5%, or 21% O_2, representing hypoxic, normoxic, and hyperoxic conditions, respectively. The device is sealed with gas-impermeable nylon-6 film and used with glass syringes and high-density PTFE tubing to prevent atmospheric gasses passing into the imaging chamber. O_2 tension can be confirmed during the experiment by porphyrin dye, an oxygen-quenching material that produces phosphorescence dependent on O_2 concentration.

Results: A transient spike in cytosolic-free calcium was observed in a fraction of the cells when exposed to changes in laminar flow. A muted but much more sustained response was seen in nearly all cells exposed to multi-directional disturbed flow, indicative of activation of a different mechanosensitive pathway. It is anticipated that these responses will be more pronounced when studied under physiological oxygen tensions. The device was capable of maintaining oxygen-tension conditions for flow rates as low as 10 μL/hour, making it suitable as an imaging rig for controlled live-cell, oxygen-tension experiments.

Conclusion: We have successfully designed and manufactured a device capable of imaging live endothelial cells subjected to variations in WSS and oxygen tensions. The results of this experiment will contribute to the understanding of the differential response of endothelial cells to WSS. The characterization of endothelial cell responses to varying flow patterns is essential in strengthening the link between endothelial cell response to flow and atherosclerotic development.

Characterization of Myocardial Metabolism using a Novel Dual-Condition PET/MRI Protocol

Fayez Habach[1,2], Jennifer Barry[2], Melissa Larsen[2], Marne Jamieson[3], Amit Singnurkar[3], Michael Laflamme[4], Nilesh R. Ghugre[1,2,3]

[1]Physical Sciences Platform, Sunnybrook Research Institute, [2]Department of Medical Biophysics, University of Toronto, [3]Schulich Heart Research Program, Sunnybrook Research Institute, [4]Nuclear Medicine, Sunnybrook Health Sciences Centre; [5]McEwen Stem Cell Institute, University Health Network, Toronto, ON, Canada

Introduction: Characterization of myocardial infarction (MI) and the consequent structural remodeling are important to understand progression towards heart failure (HF).[1] Magnetic Resonance Imaging (MRI) can elucidate structure, function, and viability, and evaluate treatment efficacy[2], while Positron Emission Tomography (PET) can offer metabolic information and inflammatory state.[3] Clinically, glycolytic suppression is typically used to isolate inflammatory activity. Additionally, glucose loading can provide further information by inducing metabolite uptake within the myocardium.[1] Combining fasting and glucose loading protocols (dual condition) in one imaging session could have the advantages of reduced scan time and cost, while also providing differential metabolic information under different substrate conditions. The objective of this work was to develop a hybrid PET/MRI imaging protocol that will accurately and simultaneously reflect tissue state using a novel dual-condition protocol, in a preclinical model of MI.

Methods: A whole-body clinical PET/MRI scanner (Siemens mMR) and a validated porcine model[4] of MI (90 min LAD occlusion/reperfusion) was utilized. Fasting was induced by a 24 hour fast and injection of a heparin bolus (2000 IU). Glucose loading was induced by a 30-minute dextrose infusion (0.8 mL/min/kg). Imaging was performed at baseline, 10-, 31-, and 45-days post-MI (n=2). For MRI, a CINE sequence was used to assess anatomy and function and 3D Late Gadolinium Enhancement (LGE) (1x1x2 mm res.) was used to delineate scar tissue. For PET, a 1-hour dynamic list-mode acquisition (2 mm iso. res.) was performed concurrently with MRI, immediately following [^{18}F]-FDG dosing (2.5 mCi) in the fasted state. A 1.5-hour acquisition was then performed following glucose loading with a second FDG dose (7.5 mCi). PET standard uptake values (SUVs) were computed and corrected for the second imaging session by appropriate activity subtraction.

Results: Glucose loading induced almost 4-fold increase in tracer uptake immediately after dextrose infusion. Co-registered 3D LGE and ^{18}FDG-PET showed strong spatial correlations between infarct location and inflammatory cell activity (Fig. 1). Longitudinal tracking revealed metabolic remodelling post-MI (Fig. 2).

Conclusions: Dual dose protocol shows promise in inducing different metabolic states within the same imaging session, potentially reducing scan time and cost. Longitudinal metabolic, functional, and structural characterization with PET/MRI can potentially aid evaluation of novel therapies for MI-related HF.

[1]Taegtmeyer et al. Nat. Rev. Cardiol. 5,S42–S48(2008), [2]Naumova et al. Nat. Biotechnol. 32(8),804–818(2014), [3]Kunze et al. J. Cardiovasc. Magn. Reson. 20,33(2018), [4]Romagnuolo et al. Stem Cell Rep. 12(5),967-981(2019)

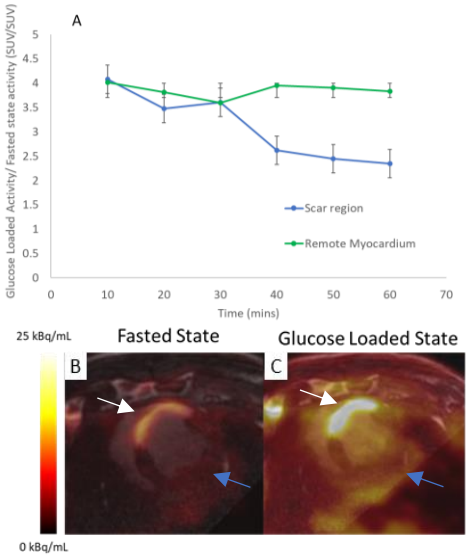

Figure 1: A) Division plot of ^{18}FDG uptake following glucose loading, divided by ^{18}FDG uptake following B) 24 hours fast, and C) 30 mins. dextrose infusion, within infarcted region (white) and remote myocardium (blue)

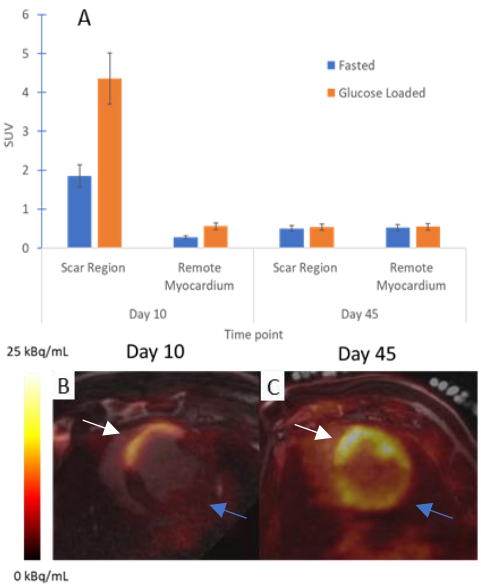

Figure 2: A) Longitudinal characterization of metabolic activity within infarcted region and remote myocardium, comparing B) 10 days and C) 45 days post-MI using dual-condition PET

Pitch Session 7: Cancer Imaging

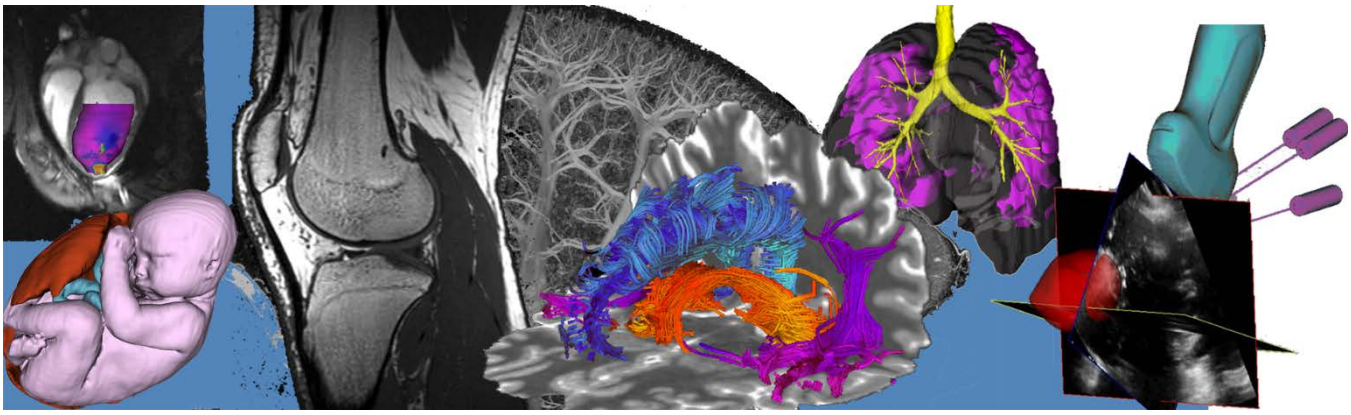

Vision Transformers for Prostate Cancer Detection from Ultrasound

Paul Wilson[1], Mahdi Gilany[1], Amoon Jamzad[1], Minh Nguyen Nhat To[2], Brian Wodlinger[3], Purang Abolmaesumi[2], Parvin Mousavi[1]

[1]Queen's University, Kingston, Ontario, Canada, [2] University of British Columbia, Vancouver, British Columbia, Canada, [3]Exact Imaging, Markham, Ontario, Canada

INTRODUCTION: Prostate cancer (PCa) is the most common cancer in Canadian men. The standard for PCa diagnosis is histopathology analysis of biopsy cores obtained by trans-rectal ultrasound (TRUS) guided biopsy. There have been significant efforts made towards using TRUS for direct tumor detection [1]. When applying large and complex classification models, it is critical that we are still able to obtain insight about how the model makes decisions. In this work we present a model based on the vision transformer (ViT) architecture [2]. ViTs use self-attention to selectively attend to and ignore regions of the input image. This provides direct access to their decision-making process and offers improved interpretability compared to conventional vision models.

METHODS: Our cohort includes 600 biopsy cores grouped into training, test, and cross-validation sets from 194 patients who underwent TRUS-guided prostate biopsy at a private practice urology clinic in Virginia Beach, VA (as part of protocol NCT02079025). The ExactVu ultrasound machine [4] was used. Prior to firing the biopsy gun, radio frequency (RF) echo signals were collected. The needle region of interest (ROI) was identified within the RF, and 43 patches were extracted. These patches correspond to a tissue area of 5mm by 5mm and have an overlap of 4.5mm (90%). They are resized to 256x256 pixels before being passed to our ViT-based neural network, which sequentially splits to 32x32 mini-patches, embeds the patches to vectors using a CNN, passes the embeddings to a transformer encoder module, and predicts a class based on encoder output. This pipeline is summarized in figure 1. The model is trained to minimize the cross-entropy loss between the predicted label for the patch and the histopathology label assigned to the core from which the patch is obtained. As in [3], co-teaching is used to reduce effects of label noise caused by applying coarse core-wise labels to every patch. At evaluation time, predictions per patch are averaged over each patch in a core to obtain an overall core-wise prediction. The model's attention maps can be overlaid over the input ultrasound image to estimate the spatial distribution of cancer.

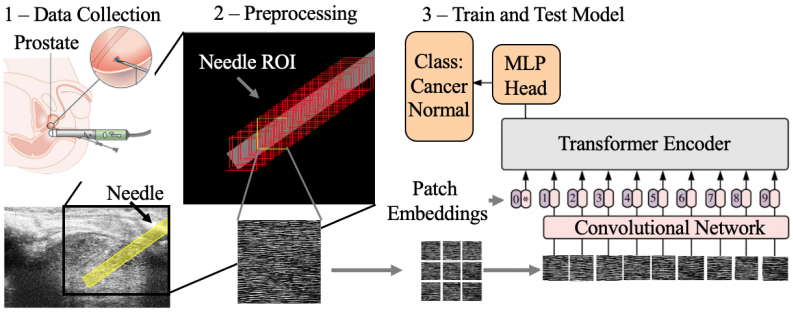

Figure 1: Left: data collection during TRUS-guided biopsy. Center: patch extraction from ROI. Right: Our model - patch embedding using CNN followed by transformer encoder and prediction

RESULTS: We compared our model to two variants of ResNet, a baseline convolutional network. Table 1 shows evaluation metrics on the test set following training. Our model is competitive with the baselines.

Table 1: Metrics of model performance

Model	Accuracy	Sensitivity	Specificity
ResNet-10	70.43	46.45	94.4
ResNet-18	59.80	20.00	**99.75**
ViT (ours)	**71.87**	**56.13**	87.6

CONCLUSIONS: To be useful in a clinical setting, a model should not only be accurate, but also provide insight into how it makes decisions. This study shows that ViT-based models are a promising option, providing good classification results and unlocking many interpretability tools from a growing body of research.

REFERENCES: [1] Azizi S et al., MICCAI 2016 [2] Dosovitsziy A et al., ICLR 2021 [3] Javadi G et al., MICCAI 2021 [4] Rohrbach D et al., Ultrasound in Medicine and Biology 2018

p53 immunohistochemistry interpretation based on digital image analysis for better prediction of mutation status in acute myeloid leukemia

Ting Xiao[1,2], Anne Martel[1,2], Raheem Peerani[3,4], Larissa Liontos[3,4]

[1]Department of Medical Biophysics, University of Toronto, Toronto, Canada; [2]Physical Science, Sunnybrook Research Institute, Toronto, Canada; [3]Department of Laboratory Medicine and Pathobiology, University of Toronto, Toronto, Canada; [4]Department Laboratory Medicine and Molecular Diagnostics, Sunnybrook Health Sciences Centre, Toronto, Canada

Introduction: TP53 mutations confer poor response to chemotherapy and rapid progression of disease in acute myeloid leukemia (AML). Determining TP53 mutation status at AML diagnosis is critical in selecting an appropriate chemotherapy. In routine practice, TP53 mutations are often identified by next-generation sequencing (NGS). However, NGS has a long turn-around time and may miss some mutations. Immunohistochemistry (IHC) of p53 protein on bone marrow biopsy samples can be helpful in identifying overexpression in some types of p53 mutation. IHC is fast and inexpensive, however, interpretation by the hematopathologist of what constitutes "positivity" is subjective and subject to individual lab variability. This study proposes a digital imaging-based algorithm to analyze p53 IHC and correlate it with mutational status.

Methods: 42 AML cases with bone marrow biopsy material were retrieved and selected based on the availability of NGS data from Sunnybrook Health Center. 21 cases (A) with a TP53 mutation and 21 cases (B) without mutations. For each patient, two ROIs are cropped from WSI and annotated by pathologists. 5 ROIs from five distinct cases are randomly selected to train a deep neural network Hover-net[1], the rest of the ROIs are used as test set. First, the Hover-net will segment and classify each nucleus into marker negative or marker weak (moderate, strongly) positive. Then, the model will quantify the nuclei positivity according to the segmentation and classification results. Last, we will compare the Hover-net-based quantification with the pathologist's manual quantification and correlate them in predicting the p53 mutations.

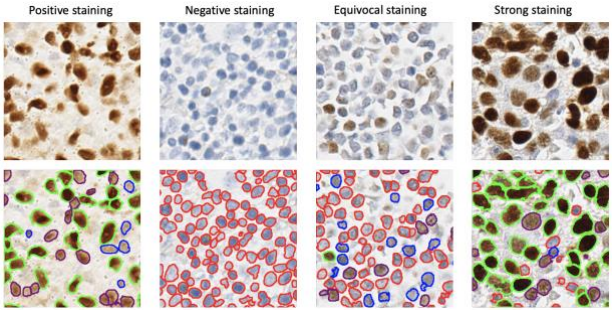

Fig. 1: Segmentation and classification results on positive, negative, equivocal, and strong staining cases. The different colors of nuclear contours highlight individual instances. Red, blue, purple, and green mean negative, weak, moderate, and strong staining.

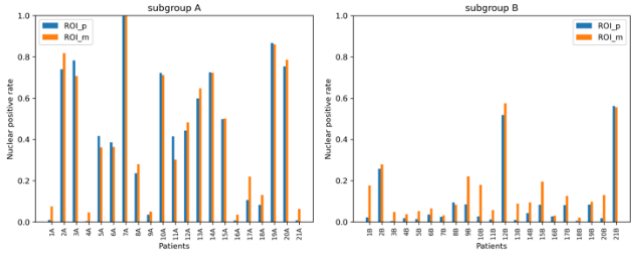

Fig. 2: Comparison between the model-based (ROI-m) quantification and manual quantification (ROI-p) in subgroup A with a mutation and subgroup B without mutations. In subgroup B, patients didn't identify a mutation, the nuclei positivity is expected lower than that in subgroup A.

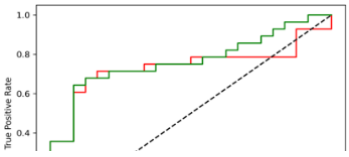

Fig. 3: ROC curve analysis for p53 mutation prediction. ROI-p is the quantification by pathologists and ROI-m is the model-based quantification. model-based quantification has better prediction ability.

Results: The trained model performs well on test images, as shown in fig.1. Whether it is positive or negative cases or some equivocal cases, the model can identify different types of nuclei. Fig.2 shows the model-based and manual quantification results in two subgroups. In subgroup B, patients didn't identify a mutation, the nuclei positivity is expected lower than that in subgroup A with a mutation. Model-based quantification shows a good correlation with manual quantifications. Fig. 3 shows the ROC curve analysis for the quantifications of model-based and manual quantifications in predicting whether a p53 mutation is presented or not. Results show that model-based quantification has better prediction ability than manual quantifications.

Conclusion: In general, our model demonstrated good performance in nuclei segmentation and classification on AML and MDS IHC images despite staining variations. Experiments showed good correlation between the digital algorithm and manual counting. Ongoing work includes automatic positive hot-pot area finding in WSIs, which may guide the pathologist to find the most interesting area.

References: [1]Graham S, Vu Q D, Raza S E A, et al. Hover-net: Simultaneous segmentation and classification of nuclei in multi-tissue histology images[J]. Medical Image Analysis, 2019, 58: 101563.

Visualization of cancer probability maps in micro-ultrasound guided prostate biopsy

H.Y.Lee[1], S.Sojoudi[2], M.Gilany[1], A.Jamzad[1], B.Wodlinger[3], P.Abolmaesumi[2,] P.Mousavi[1]

[1]Medical Informatics Laboratory, School of Computing, Queen's University, Kingston, Canada

[2]Department of Electrical and Computer Engineering, University of British Columbia, Vancouver, Canada

[3]VP, Engineer and Clinical, Exact Imaging, Markham, Canada

Introduction: Prostate cancer remains the most diagnosed cancer in Canadian men, accounting for 20% of all cases [1]. Transrectal ultrasound (TRUS)-guided prostate biopsy provides clinicians a real-time view of the prostate enabling sampling of potentially cancerous regions. However, sonograms are difficult to interpret due to their noisy appearance and the heterogeneity of prostate tissue. We previously presented deep learning-based frameworks for identification of probable cancer, using TRUS data [2]. It is critical that these cancer predictions are intuitive. Therefore, we seamlessly interlace the cancer probability maps with TRUS images to identify regions of cancer within the prostate boundary. In this study, we fine-tune a prostate segmentation model for integration with deep learning prostate cancer detection frameworks to visualize cancer probability maps using data from an ExactVu 29MHz ultrasound machine [3].

Methods: Conventional ultrasound machines are unable to run deep learning models due to incompatibility with Python and a shortage of compute power. We employ a client-server approach, computing deep learning inference on GPU servers. Data acquired on the ultrasound machine is split into three Google Remote Procedure Call clients (gRPC) based on task. Each client streams data to a matching gRPC server, residing on the GPU servers. The first client streams B-mode images to be used as the base TRUS image. The second client streams B-mode images to a dedicated gRPC server for prostate boundary segmentation. The prostate boundary is segmented by a fine-tuned U-Net model pre-trained on conventional ultrasound data. The last expansion block is trained on the rectangular beam ExactVu data. The segmented region is then overlayed on the base TRUS image using a toggle. The third client streams radio frequency (RF) data to a third gRPC server for cancer prediction. The cancer prediction model takes 256-by-256 RF patches and outputs a binary classification of prostate cancer for each patch. Output patches are combined to form a 2D heatmap that is overlaid on the base TRUS image.

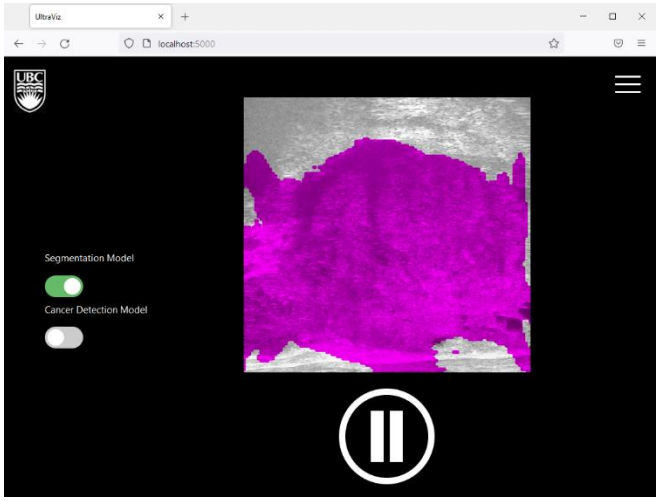

Figure 1. Screenshot of prostate segmentation. Deep learning models utilize B-mode images to segment prostate region.

Visualization: A blue and red heatmap will be overlaid on the prostate area in the TRUS image (Fig. 1). Blue would indicate benign regions while red indicates areas of probable cancer.

Conclusions: This pipeline is anticipated to enable intuitive visualization of cancer probability maps from deep learning models, integrating seamlessly with ExactVu 29MHz micro-ultrasound and add greater flexibility to the surgeon's workflow. The decision to fine tune rather than train a model from scratch stems from conventional ultrasound data being more available.

References:

[1] Canadian Cancer Statistics 2021. Toronto, ON: Canadian Cancer Society; 2021.

[2] Azizi, S., Van Woudenberg, N., Sojoudi, S. *et al.* Toward a real-time system for temporal enhanced ultrasound-guided prostate biopsy. *Int J CARS* 13, 1201-1209 (2018).

[3] "ExactVu™ Micro-Ultrasound System – Exact Imaging" https://www.exactimaging.com/exactvu-micro-ultrasound-system.

Discriminating optically turbid media by scatterer size and scattering coefficient using backscattered linearly and circularly polarized light

MICHAEL D. SINGH,[1] I. ALEX VITKIN,[1,2,3,*]

[1] Department of Medical Biophysics, University of Toronto, Toronto, ON, Canada
[2] Department of Radiation Oncology, University of Toronto, Toronto, ON, Canada
[3] Division of Biophysics and Bioimaging, Princess Margaret Cancer Centre, Toronto, ON, Canada

Introduction: Precancer-to-cancer progression in epithelial tissues is marked by cellular proliferation and nuclear pleomorphism (size / shape changes to nuclei), as well as connective tissue remodeling. These transformations have been shown to result in changes to (1) the tissue turbidity (quantified by the scattering coefficient) and (2) the average scatterer size. Importantly, the scatterer size and scattering coefficient are known to influence the backscatter response of polarized light. We thus study the ability of linearly and circularly polarized light to assess these important biophysical properties of turbid media by Stokes degree of polarization (DOP) analysis (DOP measures the amount of polarization coherence between photons).

Methods: The change in DOP of linearly and circularly polarized light after scattering in well-controlled microsphere suspensions of different sphere sizes and scattering coefficients was determined by taking the ratio of the light's incident DOP to scattered DOP. High signal-to-noise DOP measurements were enabled by a polarimetric system based on photoelastic modulation and phase-sensitive synchronous detection. Polarization-sensitive Monte Carlo simulations are also performed to corroborate the experimental trends and gain insight on backscattering through its tracked photon statistics.

Results: Circular DOP was found to be a sensitive marker of scatterer size, but due to helicity reversal effects (e.g., right-circular converts to left-circular polarization) the interpretation of its low values can be ambiguous due to the nature of Stokes analysis; the linear DOP appeared to be mostly dependent on the medium scattering coefficient. We exploit these trends to generate a DOP_C - DOP_L response surface which clusters turbid samples by scatterer size and scattering coefficient, as shown in **Figure 1**.

Conclusion: The novel polarimetric ability to noninvasively and simultaneously assess scatterer size and scattering coefficient of tissue-like turbid media may improve upon currently invasive skin cancer tests and other skin pathology assessment procedures.

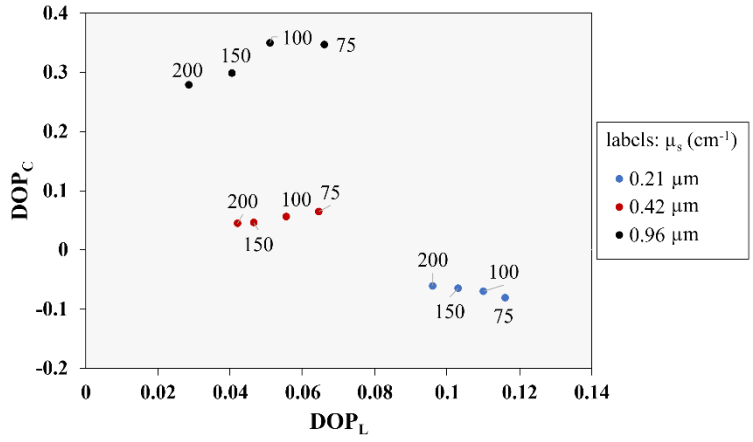

Figure 1. $DOP_{L/C}$ response surface for monodispersed microsphere suspensions with a given scattering coefficient (ranging from 50 cm^{-1} to 200 cm^{-1}) and mean sphere diameter (0.21 μm, 0.42 μm, and 0.96 μm). Clustering according to particle size (distinct along the DOP_C axis) and scattering coefficient (somewhat along the DOP_L axis) is evident.

Modelling the Radiation Distribution of Stereotactic Radiotherapy in the Treatment of Patients with Multiple Lung Lesions

Edward Wang[1,2], Sarah Mattonen[1-3], and Pencilla Lang[2,3]

[1] *Department of Medical Biophysics, Western University, London, ON, Canada;*
[2] *Baines Imaging Research Laboratory, London Regional Cancer Program, London, ON, Canada;*
[3] *Department of Oncology, Western University, London, ON, Canada*

Introduction: Stereotactic radiotherapy (SBRT) is a radiation technique that makes use of large, ablative radiation doses. Typically, SBRT is delivered in 1-5 fractions. The primary limitation of using SBRT to treat patients with multiple lung lesions is the toxicity associated with the cumulative radiation dose. In the lung, radiation toxicity manifests primarily as pneumonitis (leading to pain, dyspnea, need for supplemental oxygen and in severe cases death) and late fibrosis (leading to decreased long-term pulmonary function). Higher doses of radiation lead to improved disease control at the expense of increased risk for treatment associated toxicities. Therefore, the dose is constrained by the minimum dose to the tumour and maximum dose to the healthy lung. There are currently no guidelines for optimal dose to metastatic lung lesions. When evaluating a potential plan, radiation oncologists and medical physicists make use of metrics including the percentage of healthy lung receiving dose above a certain threshold. Due to their complexity, SBRT cases require extensive planning and quality assurance resources. Internal data at the London Regional Cancer Program shows an average of 7.5 hours to plan an SBRT lung case. If the plan does not meet dose constraints, either a re-plan is required, costing significant resources, or the patient is switched to an alternative treatment method, leading to increased mental burden. The goal of this project is to model the radiation dose received by healthy lung tissue in multi-lesion SBRT without utilizing the full planning workflow, thereby allowing radiation oncologists to quickly estimate radiation toxicities when prescribing treatment.

Methods: Retrospective review of 153 patients at the London Regional Cancer Program from January 2014 to April 2021 was performed. Patients were included if they received SBRT treatment to the lung (either one ore more lesions) and were prescribed regimens with 8 or less fractions. Patients were excluded if they received previous radiation to the lung or mediastinum. For each patient, the CT scan, radiotherapy plan dose distribution and segmented structures were exported. 3DSlicer with the SlicerRT extension was used for analysis. A sum of exponentials model was used to model radiation fall off for treatment delivered to single lesions. The dose distribution of patients who received SBRT with only one lesion were used to fit and evaluate the coefficients of the model. The radiation distribution of SBRT to multiple lesions was estimated as a summation of doses to the individual lesions. The percentage of healthy lung receiving radiation above 20, 13.5, 11 and 8 Gray (V20, V13.5, V11 and V8) was compared between the ground truth and estimated doses.

Results: The values of the coefficients in the exponential values determined by regression are different than published literature values. The difference in V20, V13.5, V11, V8 (units are percentage of healthy lung) between the ground truth and estimated values in the single lesion training set (N=15) used to calculate the regression model coefficients are (mean ± SD): -0.60 ± 0.53, -1.20 ± 0.86, -1.41 ± 0.99, -1.42 ± 1.62. The same metrics evaluated in the testing set (N=34) are: -0.34 ± 0.87, -0.52 ± 1.29, -0.45 ± 1.53, 0.05 ± 1.94. The difference in V20, V13.5, V11 and V8 between the metrics in the multi-lesion patients (N=14) are: 3.59 ± 6.50, 4.44 ± 7.77, 5.29 ± 8.50, 7.33 ± 9.29.

Conclusion: A sum of exponentials model can model V20, V13.5, V11 and V8 metrics to within 2 absolute percentage points with no overfitting, even when fit on a small sample size. The accuracy of multi-lesion cases is less accurate, and indicates that simple summation of doses of individual lesions is inadequate. For the multi-lesion cases, the calculated metrics are more accurate at higher thresholds. Future work is needed to improve accuracy and will involve using more complex aggregation methods. This work builds the foundation for the creation of a clinical tool that radiation oncologists can use in clinic to quickly determine the feasibility of SBRT for the treatment for patients, and to compare different treatment regimens.

Visualization of the zonal anatomy for transrectal ultrasound guided prostate biopsy

Catherine O. Wu[1], B. Diao[2], L. Groves[1], T. Ungi[1], A. Sedghi[1], R. Kikinis[3], P. Mousavi[1], G. Fichtinger[1]
[1]Queen's University, Kingston, Canada, [2]Cheikh Anta Diop University, Dakar, Senegal, [3]Harvard Brigham and Women's Hospital, Boston, USA

INTRODUCTION: The diagnosis and treatment of prostate cancer are reliant on accurate biopsy of the prostate (PBx), the systematic sampling of the anatomical zones of the prostate under transrectal ultrasound (TRUS) guidance. Unfortunately, TRUS offers poor appreciation of the prostate anatomy zones, in addition to low sensitivity in showing early-stage cancerous foci growing in the zones. In North America and Europe, "fusion biopsy" (i.e., spatial navigation that registers TRUS with multi-parametric MRI) has been emerging as a new standard for PBx [1]. In fusion biopsy, the anatomical zones and suspected cancer foci are localized in pre-biopsy MRI and visually superimposed on real-time TRUS to guide the biopsy. In Senegal, in all patients referred for PBx, cancer is found in only 30%, even though over 60% have advanced disease [2], indicating the failure of systematic zonal sampling. Unfortunately, fusion biopsy is utterly infeasible in Senegal and generally in West Africa, where fewer than 40 MRI units serve a population larger than North America, with Senegal having just two suitable units [3].

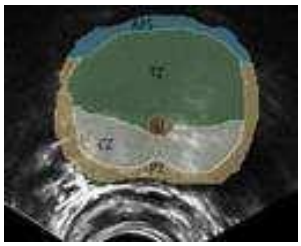

Fig. 1: Zonal overlay on TRUS

METHODS: We base our approach on the practical observation that for accurately acquiring a 20mm long biopsy core, it is sufficient to produce an approximate outline of the targeted anatomical zone. To generate approximate zonal overlays, we imported prostate zone segmentations in 4 MRI volumes from a generic prostate cancer patient population, deformably registered with 8 patient specific TRUS volumes. The registration was performed in 3D Slicer, an open-source platform [4], yielding a zonal map (Fig. 1). Seven expert urologists assessed the quality of the zonal overlays on a 5-point Likert scale and labeled the zones in the TRUS, allowing comparison of their interpretation to our overlay.

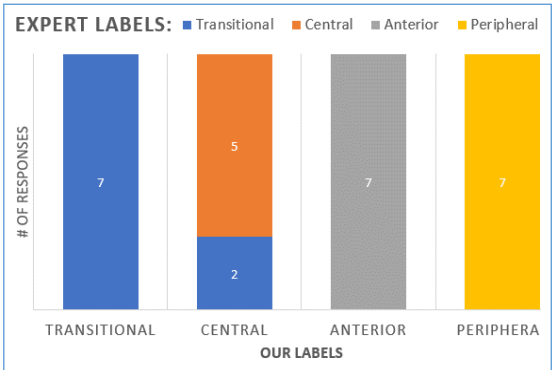

Fig. 2: Results from TRUS labelling questionnaire

RESULTS: When assessing the quality of the overlay, the experts, on average, rated the accuracy at 4 on a 5-point scale. When viewing the TRUS, 7 out of 7 experts labelled the peripheral, anterior, and transitional zones in the regions we overlaid them, and 5 out of 7 did so for the central zone (CZ) (Fig. 2), possibly due to difficulties in identifying CZ borders in TRUS.

CONCLUSION: The seven expert urologists found the approximate zonal overlays on the TRUS to be qualitatively sufficient for orienting PBx.

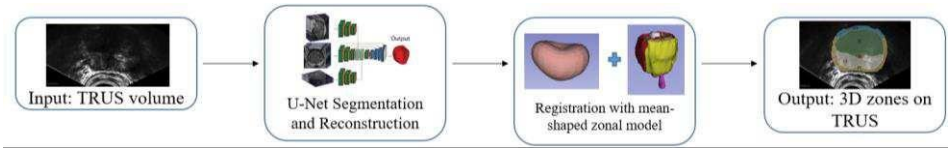

Fig. 3: Workflow for automated generation of the zonal overlay on TRUS

In ongoing work, we apply a deep learning network [5] to segment the prostate gland in TRUS, then deformably register it with a mean-shaped zone model, automating the workflow to produce the overlay of the corresponding anatomical zones on the TRUS (Fig. 3).

REFERENCES: [1] Das CJ et al. Prostate MRI-TRUS fusion biopsy: a review of the state of the art procedure. Abdom Radiol 546(NY). 2020 Jul;45(7):2176-2183; **[2]** Niang et al. Screening for Prostate Cancer by Digital Rectal Examination and PSA Determination in Senegal. ISRN Oncol. 2011; 2011:943704. **[3]** Ogbole GI et al. Survey of magnetic resonance imaging availability in West Africa, Pan Afr Med J. 2018; 30: 240. **[4]** Fedorov A et al. 3D Slicer as an Image Computing Platform for the Quantitative Imaging Network. Magn. Reason. Imaging 30(9), 1323-1341 (2012); **[5]** Orlando N et al. Automatic prostate segmentation using deep learning on clinically diverse 3D transrectal ultrasound images. Med Phys, 2020; 47(6): 2413-2426 (2020).

Cell phenotyping using unsupervised clustering on multiplexed fluorescence images of breast cancer tissue specimens

Wenchao Han[1,2], Alison M. Cheung[1], Dan Wang[1], Kela Liu[1], Martin J. Yaffe[1,2], and Anne L. Martel[1,2]
[1]Biomarker Imaging Research Laboratory, Sunnybrook Research Institute, Toronto, Ontario, Canada
[2]Department of Medical Biophysics, University of Toronto, Toronto, Ontario, Canada

Introduction: Cytometry plays essential roles in immunology and oncology. Recent advancements in cellular imaging allow more detailed characterization of cells by labeling each cell with multiple protein markers. The increase of dimensionality makes manual analysis challenging. Clustering algorithms provide a means for phenotyping high-dimensional cell populations in an unsupervised manner for downstream analysis. The choice and usability of the methods are critical in practice. Literature provided comprehensive studies on those topics using publicly available flow cytometry data, which validated cell phenotypes by those methods against manual gated cell populations.
Methods: In order to extend the knowledge for identification of cell phenotypes including unknown cell populations in our dataset, we conducted an exploratory study using clinically relevant tissue types as reference standard. In this study, we used in-house database of multiplexed immunofluorescence images of breast cancer tissue microarrays. It includes a total of 101 cores from 59 cases (42 cases with duplicates (1.1 mm diameter) cores) of invasive breast cancer. We experimented with two commonly used algorithms (PhenoGraph[1] and FlowSOM[2]). Our pipeline includes: 1) cell phenotyping using Phenograph/FlowSOM; 2) clustering TMA cores into four groups using the percentage of each cell phenotypes with the algorithms (PhenoGraph/Spectral/K-means); 3) comparing the tissue groups to clinically relevant subtypes that were manually assigned based on the immunohistochemistry scores of serial sections. We experimented with different hyperparameter settings and input markers.
Results: Experiment results are shown in Fig. 1. Cell phenotypes using Phenograph with 10 markers and tissue clustering using Spectral yielded the highest mean F-measure (average over four tissue subtypes) of 0.71. Also, Phenograph demonstrated better performance for the downstream tissue type classification in most of the experiments with larger variability than the FlowSOM (see the higher values and longer tails indicated by the blue boxplots than the orange boxplots).
Conclusion: In general, our results showed that cell phenotypes by Phenograph yielded better performance with larger variations than FlowSOM, which gives very consistent results when using 4 markers.

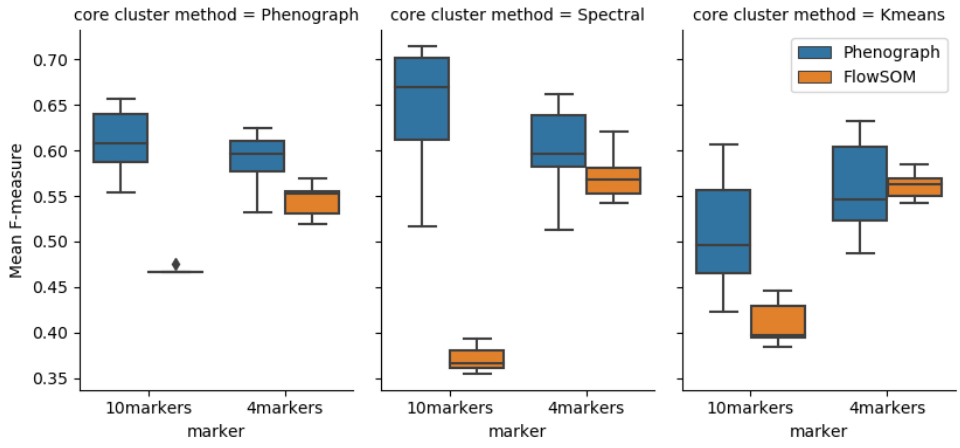

Fig. 1. Boxplots for our experiment results (mean F-measure vs. number of markers). Three subplots used PhenoGraph, Spectral, and K-means as second-stage tissue clustering respectively. The blue and orange are the results using PhenoGraph and FlowSOM for cell phenotyping respectively.

Reference:

1 Levine, J. H. *et al.* Data-driven phenotypic dissection of AML reveals progenitor-like cells that correlate with prognosis. *Cell* **162**, 184-197 (2015).
2 Van Gassen, S. *et al.* FlowSOM: Using self-organizing maps for visualization and interpretation of cytometry data. *Cytometry Part A* **87**, 636-645 (2015).

Impact of the Location of Tumor in Prostate Cancer Detection on 3-T Multiparametric MRI Based on the Prostate Sector Map

Fatemeh Zabihollahy[1], Steven S. Raman[1], Robert Reiter[2], Holden Wu[1], Kyunghyun Sung[1]
[1]*Department of Radiology, David Geffen School of Medicine at UCLA, Los Angeles, CA, United States*
[2]*Department of Urology, David Geffen School of Medicine at UCLA, Los Angeles, CA, United States*

Introduction: Multiparametric MRI (mpMRI) has been shown to be accurate for the diagnosis of clinically significant prostate cancer (csPCa) that requires treatment [1]. Previously, several studies determined the performance of mpMRI based on the tumor size, Gleason score (GS), index, etc. [2-3], compared with whole-mount histopathology (WMHP) as an ideal reference standard for correlating individual prostate lesions to mpMRI. Sector map is a canonical model of the prostate, consisting of forty-one sectors, to enable clinicians to easily localize MRI findings, described by the Prostate Imaging Reporting and Data System (PI-RADS) version 2.1 [4]. The purpose of this study is to illustrate the sector-based performance of mpMRI for PCa detection as a form of spatially localized probabilities to provide a useful roadmap for mpMRI-based PCa diagnosis and prognosis.

Method: This HIPAA compliant study was approved by the review board of our local institute. A total of 776 consecutive men underwent 3T mpMRI prior to radical prostatectomy at a single institution between 2010 and 2020. 3T mpMRI was compared with thin-section WMHP prepared by experienced genitourinary (GU) pathologists. A lesion that appeared on mpMRI was labeled as a true positive (TP) if it presents on the WMHP, and its sectors were recorded based on the appearance on mpMRI. If PCa lesions shown on WMHP were not detected on mpMRI, they were classified as FN lesions, and their sectors were assigned based on their appearance on WMHP. The mpMRI lesions were categorized as false positives (FP) if there is no corresponding lesion on WMHP. Clinically significant PCa was defined as a lesion with a GS of 7 or greater. The index lesion was defined as the PCa lesion with the highest GS or the largest size or both. To calculate spatial probability, the number of TP, FP, and FN lesions in each region of the sector map was counted and divided by the total number of PCa lesions at the corresponding level. To illustrate the probability on the sector map, three different colors, including red, orange, and yellow, were used to display probability values of larger than 10%, less than 10% and larger than 5%, and less than 5% at different anatomic zones, respectively.

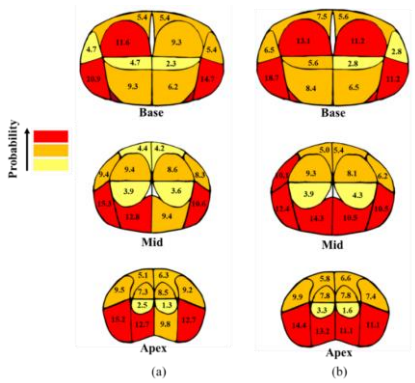

Figure 1. Spatial probability map of FN a) csPCa and b) index lesions at the basal, mid, and apex levels, corresponding to prostate sector map, using mpMRI compared to WMHP as a reference.

Results: In 776 patients, there existed 1,465 PCa lesions at WMHP including TP and FN lesions, and of 1,465 PCa lesions, the detection rate of overall PCa lesions was 52% including 72% of the csPCa tumors and 78% of the index lesions. 76% of FN tumors were small (tumor diameter of < 1.5 cm). At all anatomical levels, most FN csPCa and index lesions were located at the left posterior of peripheral zone (PZ). **Figure 1** shows the spatial probability map for FN csPCa and index lesions. On multivariate analysis, the majority of FN large (tumor diameter of > 1 cm), clinically significant, index lesions with PSA>4 was in the posterior of PZ.

Conclusion and Discussion: We characterized the spatial localization of the detection of PCa on mpMRI in terms of spatial probability corresponding to the sector map. Also, the results may reduce the need for systematic prostate biopsy as it helps obtain samples from areas with the highest probability of PCa lesion existence instead of removing samples from random areas of the prostate gland. The outcomes facilitate the characterization of disease appearance relative to anatomic levels and zones, which in turn may obviate the necessity of MR-based prostate atlas. Moreover, incorporating our results into the computer-aided diagnosis tools designed for automated detection of PCa lesions is important, may lead to better performance as prior information and hints given to the learner is a substantial ingredient to obtain a good generalization error [5]. Overall, mpMRI performance for sectoral localization of PCa within the prostate was moderate in the posterior of PZ and more attention needs to be paid to this region, where most of the csPCa and index tumors are undiagnosed.

References

[1] Futterer JJ, Briganti A, De Visschere P, et al. Can Clinically Significant Prostate Cancer Be Detected with Multiparametric Magnetic Resonance Imaging? A Systematic Review of the Literature. Eur Urol. 2015;68:1045–1053.
[2] Johnson D, Raman SS, Afshari Mirak S, et al. Detection of Individual Prostate Cancer Foci via Multiparametric Magnetic Resonance Imaging. Eur Urol. 2019;75:712– 720.
[3] Wibulpolprasert P., Raman SS, Hsu W et al. Detection and Localization of Prostate Cancer at 3-T Multiparametric MRI Using PI-RADS Segmentation. AJR. 2019;212(6): W1-W10.
[4] PI-RADS, Prostate Imaging – Reporting and Data System 2019, Version 2.1. https://www.acr.org/Clinical-Resources/Reporting-and-Data-Systems/PI-RADS. Accessed November 8,2021.
[5] Gulcehre C. and Bengio Y. Knowledge Matters: Importance of Prior Information for Optimization. Journal of Machine Learning Research. 2016; 17:1-32.

Pitch Session 8:

Ultrasound and Optical Imaging

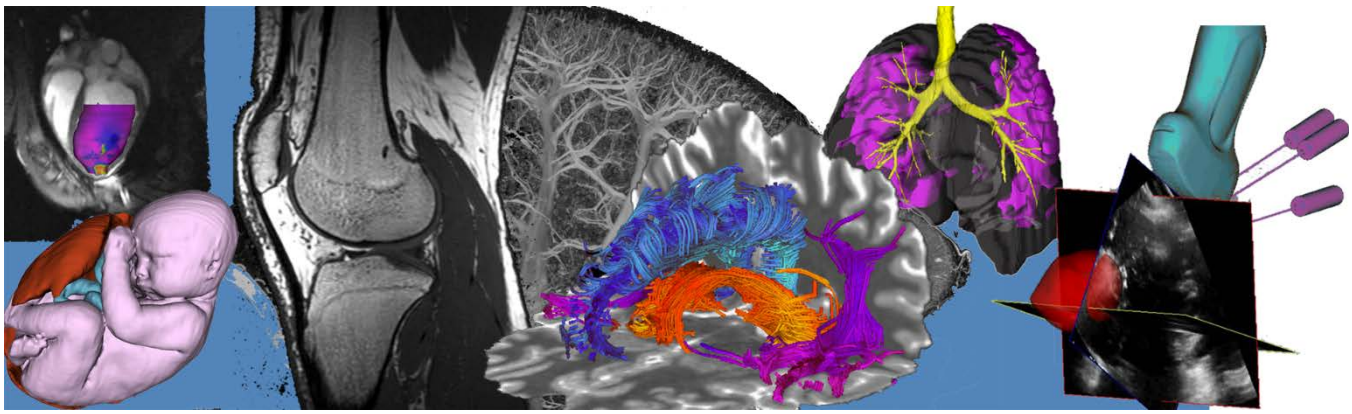

Development of a simulation training curriculum for ultrasound-guided vascular access for sustainable translation to West Africa

Sarah GF Ryan[1], Tamas Ungi[2], Sarah Maxwell[3], Melanie Jagger[3], Lindsay Patterson[3], Parvin Mousavi[2], Gabor Fichtinger[2].
Department of Medicine[1], School of Computing[2], and Department of Anesthesiology[3], Queen's University, Kingston ON.

Introduction: As simulation training in medical education becomes more prevalent, it is imperative we share knowledge in resource-limited settings. PerkTutor (www.PerkTutor.org) is a free open-source training platform, which allows 3D visualization of ultrasound images and procedural instruments in real-time using electromagnetic tracking[1]. The position of small sensors in an electromagnetic field can be identified without line of sight. The platform has been used in multiple procedures including vascular access[2,3]. We are creating a training curriculum using PerkTutor for vascular access, to be implemented in a newly constructed simulation centre in Mauritania.

Methods: As commercial phantoms are overly expensive and not available in West Africa, we developed a low-cost and easily reproducible vascular phantom. We used Alumisol plastic with 0.1% cellulose poured into a glass container with a wooden dowel that is later removed to create an open vascular tract [Figure 1]. An ultrasound training curriculum was developed, based on the input of expert anesthesiology staff. The training curriculum includes pre-reading with a PowerPoint presentation on ultrasound imaging basics, followed by sections on the steps for both in-plane and out-of-plane needle insertion under ultrasound guidance. Afterwards, trainees are given time to practice in the simulation centre using the PerkTutor platform to augment their learning. These practice sessions will occur at 0, 1 and 3 months. During these training sessions, metrics of skill proficiency are collected through PerkTutor, to evaluate the effectiveness of the simulation program.

Results: Realism and image quality of the phantom under ultrasound guidance is comparable to commercially available phantoms [Figure 2]. Including the one-time cost for the container the phantom costs ~$10, whereas the commercial Blue Phantom costs over $500. We hope to implement testing of the curriculum as described in the methods with local medical students over the next few months.

Conclusions: Simulation curricula in resource-rich settings, such as Canada, tend to require high-cost materials and expert physician time to lead the practice sessions. We aim to study how we can mitigate these costs by leveraging educational technologies. This will serve as a proof of concept, to guide sustainable implementation of vascular access training in West Africa, as well as inform the development of future curricula to come.

Figure 1. Vascular phantom after alumisol plastic is allowed to harden.

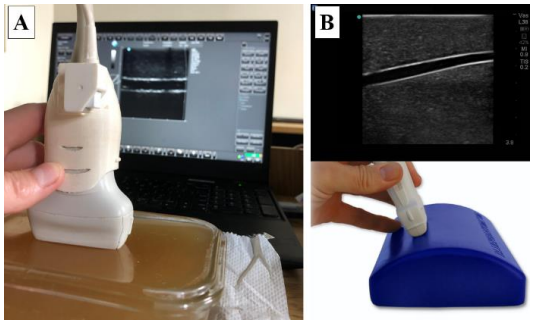

Figure 2. Appearance of the (A) home made versus (B) commercial phantom under ultrasound

References:

[1] Ungi, T., Sargent D., Moult E., Lasso A., Pinter C., McGraw R. C., et al. (2012). Perk Tutor: An open-source training platform for ultrasound-guided needle insertions. IEEE Trans Biomed Eng. 59, 3475-3481.

[2] Lia, H., Keri Z., Holden M. S., Harish V., Mitchell C. H., Ungi T., et al. (2017). Training with Perk Tutor improves ultrasound-guided in-plane needle insertion skill. SPIE Medical Imaging. 10135,

[3] McGraw, R. C., Chaplin T., McKaigney C., Rang L., Jaeger M., Redfearn D., et al. (2016). Development and evaluation of a simulation-based curriculum for ultrasound guided central venous catheterization. Canadian Journal of Emergency Medicine. 18, 405-413.

In vitro and *in vivo* assessment of focused ultrasound-triggered docetaxel-loaded nanobubbles for locally advanced breast cancer therapy

Patrick Dong Min Chang[1], Yiran Zou[2], Yun Xiang[2,3], Sharshi Bulner[5], Alex Wright[5], David E. Goertz[4,5], and Naomi Matsuura[1,2,3]
[1]Institute of Biomedical Engineering, [2]Department of Materials Science & Engineering, [3]Department of Medical Imaging, and [4]Department of Medical Biophysics, University of Toronto, Ontario, Canada; [5]Sunnybrook Research Institute, Toronto, Ontario, Canada

Introduction: Docetaxel (DTX; clinical formulation Taxotere®) is an anticancer drug used to treat locally advanced breast cancer (LABC)[1,2]. To overcome the characteristic systemic toxicity of DTX, non-invasive focused ultrasound (FUS) can be used to locally release DTX from drug-loaded microbubble contrast agents (diameter~1-8 μm)[3]. However, the administered gas dosage, a key safety metric for cavitation-mediated applications, needs to be considered for translation to human patients[4,5]. To enhance the drug loading capacities per unit gas volume of micron-scale bubbles, higher surface-area-to-volume ratio nanobubble (NB) drug carriers can be used[5]. In this study, we combine advances in contrast-enhanced ultrasound (CEUS) imaging of NBs at diagnostic ultrasound frequencies[6,7] and drug-loaded NBs for localized tumour therapy *in vivo*[8,9] to assess whether (1) DTX-NBs can achieve clinical DTX dosages in comparison to the FDA-approved Taxotere® for LABC; (2) FUS stimulation of DTX-NBs can enhance *in vitro* cytotoxicity compared to Taxotere®; (3) FUS can release DTX from the DTX-NBs *in vivo*; and (4) bubble destruction can be visualized by CEUS imaging.

Methods: Decafluorobutane-filled, phospholipid (DPPA, DPPC, DPPE-mPEG5k)-stabilized, DTX-NBs were assessed for *in vitro* size and stability (Multisizer 4e) at 37°C. *In vitro* cytotoxicity was examined on murine breast cancer EMT-6 cells using an MTT assay (*Fig. 1i*). Samples were cavitated under peak negative pressures (0.25-1.36 MPa) using a 1-MHz FUS transducer. *In vivo* circulation lifetimes of DTX-NBs were assessed by CEUS using a clinical ultrasound scanner on subcutaneous EMT-6 tumour-bearing BALB/c mice models (*Fig. 1ii)*. DTX loading and degradation was assessed using a liquid chromatography system.

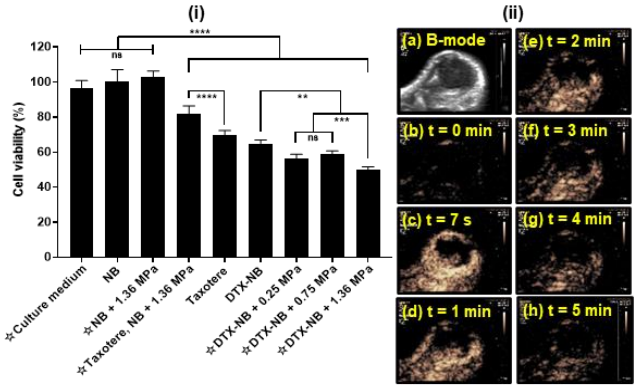

Figure 1. *(i)* Column chart presenting the *in vitro* normalized EMT-6 cell viability post-treatment of experimental groups: DTX-NBs, NBs, and Taxotere® subject to FUS from 0.25 to 1.36 MPa (n≥6) (mean±SD). Statistical analysis was conducted using a one-way ANOVA and Tukey's post-hoc Honesty Significant Difference test where ****p<0.0001, ***p<0.001, **p<0.01, *p<0.05, ns means non-significant; *(ii)* ultrasound images depicting the *(a)* brightness mode image of the subcutaneous EMT-6 tumour; *(b)* to *(h)* minute intervals of CEUS images of DTX-NBs *in vivo* circulation (mechanical index of 0.06) (n≥3).

Results: A total of 106±16 μg of DTX (n≥6) was loaded onto ~10^{10} bubbles (d_{mode}~230 nm) per ~0.4 μL of gas (n≥9). *In vitro*, DTX-NBs were more cytotoxic than Taxotere® with no FUS exposure. DTX-NBs demonstrated FUS pressure-dependent cytotoxicity with the most cytotoxic effects exerted upon exposure to a FUS pressure of 1.36 MPa. *In vivo*, DTX-NBs can be monitored via CEUS with circulation lifetimes of ~5 min.

Conclusions: Using a safe-for-injection gas dosage of 9 μL/kg[10], DTX-NBs offer DTX doses of ~2.5 mg/kg, comparable to the highest FDA-approved dosages of Taxotere®[11]. FUS-stimulated cavitation of DTX-NBs can enhance *in vitro* cytotoxicity compared to DTX-NBs with no FUS stimulation and Taxotere®. FUS can trigger DTX release from DTX-NBs and be coupled with CEUS imaging to monitor bubble destruction in real-time using a clinical ultrasound system *in vivo*. Future work will assess the *in vivo* biodistribution of DTX-NBs with FUS pulsing parameters for drug delivery and vascular disruption regimes and conduct longitudinal survival studies examining DTX delivery for tumour regression in preclinical breast cancer mice models.

References: [1] Tryfonidis et al., *Nat. Rev. Clin. Onco.*, 2015. [2] Simos et al., *Curr. Opn. Supp. Pall. Care.*, 2014. [3] Ting et al., *Biomaterials*, 2012. [4] Stride et al., *Ultrasound in Med. & Biol.*, 2020. [5] Helfield et al., *Frontiers in Physics*, 2021. [6] Zhang et al., *Frontiers in Pharmacology*, 2019. [7] de Leon et al., *RSC Nanoscale*, 2019. [8] Zhou et al., *Nanoscale Research Letters*, 2019. [9] Zhong et al., *Pharm. Dev. and Tech.*, 2020. [10] Goertz et al., *IEEE Int. Ultrason. Symp. Proc.*, 2008. [11] United States Food & Drug Administration, *TAXOTERE® Injection Label*, 1999.

Label Noise Compensation in Prostate Cancer Classification

Mahdi Gilany[1], Amoon Jamzad[1], Minh Nguyen Nhat To[2], Brian Wodlinger[3], Purang Abolmaesumi[2], Parvin Mousavi[1]
[1]Queen's University, CA, [2]The University of British Columbia, CA, [3]Exact Imaging, CA

INTRODUCTION: According to recent statistics, prostate cancer (PCa) is the second most frequently diagnosed and the fifth most deadly cancer among men. As the standard of care, PCa is diagnosed by histopathology analysis of tissue samples obtained from transrectal-ultrasound (TRUS) guided biopsy where ultrasound (US) is used for anatomical navigation rather than for targeting PCa. In the past, many studies have shown the possibility of tissue characterization and targeted biopsy using US imaging. Recently, a novel high resolution micro-ultrasound imaging system called ExactVu (Exact Imaging, ON, Canada) with a higher transmitting pulse frequency of 29 MHz has shown superior performance compared to conventional US systems [1]. There are some models proposed for PCa classification on ExactVu data [2, 3]. Although they were successful, they assign coarse pathology reported labels for biopsy cores to **all** extracted patches from the biopsy cores, or from the needle region of interests (NROI) in Figure 1 (a). This assignment of labels to all extracted patches is problematic since the given labels to patches may not necessarily match with the ground truth, i.e., the assigned labels may not match with the tissues present in the patches (label noise issue). The performance of deep learning models are shown to be largely affected when a portion of data is wrongly labeled. In this paper, we try to build up on the proposed models for PCa detection by studying novel deep learning techniques that are robust in learning with label noise. We specifically investigate the effect of a promising method named Co-teaching proposed for learning from label noise [4] along with leveraging the Resnet architecture for detection of patch classes.

METHODS: For training, 400 biopsy cores, followed by 100 for each test and validation were acquired via ExactVu machine from a single center. Totally, 194 patients participated in the study and underwent systematic TRUS guided biopsy (as part of protocol NCT02079025). Each core has a single radio-frequency (RF) ultrasound frame with the size of 20 mm depth and 46mm width. The NROI is manually selected from B-mode ultrasound images and used to extract corresponding RF data frames as shown in Figure 1 (a). Each NROI is then split to 43 patches of size 5mm by 5mm with the overlap of 4.5mm with adjacent patches in both dimensions. We evaluate our hypothesis by comparing the method with and without the presence of Co-teaching. Co-teaching employs a co-training strategy to discard noisy labeled data. In this strategy, two deep neural networks are trained simultaneously on all data. In each mini batch, some data with possibly clean labels are selected by each network. Then, these clean data are later used to train the other network, Figure 1 (b).

RESULTS: Core level balanced accuracies of 74.5±2.2 with Co-teaching and 62.0±5.5 without it are achieved. In addition to reporting the accuracy, we utilized extra pathology information called *involvement* or percentage of cancerous tissue in cores. Figure 1 (c) shows how our model is able to capture label noise by increasing the correlation between cores' true *involvement* and predicted *involvement*, i.e., the predicted percentage of cancerous patches which estimates the cancer involvement in cores (right figure includes Co-teaching).

CONCLUSIONS: Results show the promise of deep learning in PCa classification of micro-ultrasound data. Specially, they show the importance of addressing label noise in PCa detection which is widely ignored in this domain and can adversely affect the performance by a large margin.

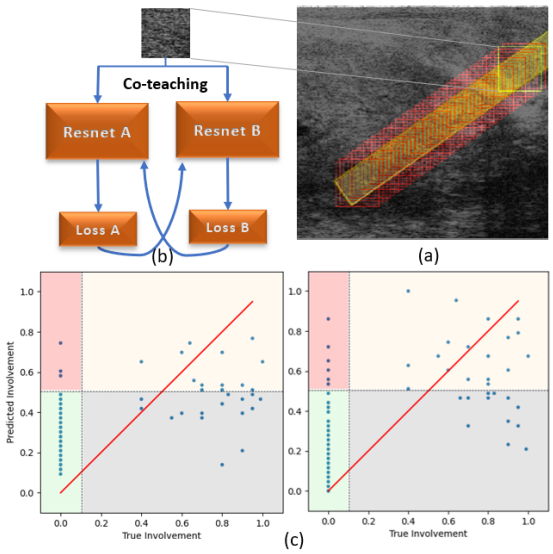

Figure 1: (a) Patch extraction from NROI (b) Co-teaching methodology (c) Scatter plots of true vs. predicted *involvement*.

REFERENCES: [1] Abouassaly R. et al., World journal of urology, 2019, 38 [2] Rohrbach D. et al., Ultrasound in medicine biology, 2018, 44 [3] Shao Y., IEEE T-MI, 2020, 39 [4] Han B. et al., Neurips, 2018

Automated catheter segmentation in 3D ultrasound images from high-dose-rate prostate brachytherapy

N. Kitner[1], J.R. Rodgers[1], T. Ungi[1], M. Korzeniowski[2], T. Olding[2], C.P. Joshi[2], P. Mousavi,[1] G. Fichtinger[1]
School of Computing, Queen's University[1]; Kingston General Hospital[2]. Kingston, Ontario

Introduction: High-dose-rate brachytherapy (HDR-BT) is an internal radiotherapy technique in which catheters are guided through the perineum and into the prostate with the help of three-dimensional (3D) transrectal ultrasound (TRUS) images. Once placed, medical physicists manually track the catheters before administering radiation. This process is time-consuming and subject to human variability, which can affect radiation dosimetry and clinical outcomes[1]. Some approaches for catheter tracking have been proposed that utilize deep learning architectures,[2] and others that use Hough transforms[3]. None use the combination of deep learning and the Hough transform, which can rectify the poor results for partially shadowed catheters, as was a problem when using the Hough transform alone. We propose a two-step pipeline involving a deep learning approach to automatically segment catheters in prostate HDR-BT using a U-Net architecture, followed by Hough transform algorithms for feature extraction.

Methods: The 3D TRUS images and the corresponding manual catheter segmentations were obtained for 97 prostate HDR-BT patients from Kingston General Hospital. The 3D TRUS images were cropped and resized to 128 × 128 × 128. The manual contours were converted to binary segmentations and resized to the same dimensionality as their corresponding TRUS images. These segmentations were then used as the ground truth for training the deep learning model. Once pre-processed, the data was exported for training on the 3D U-Net model. Training made use of 77 images and their corresponding ground truths, while 20 were used for testing. The network was trained for 50 epochs, and an Adam optimizer was used with a minimum learning rate of 0.00001 and a maximum rate of 0.01. Binary cross entropy was the chosen loss function for the model. The resulting predictions from the deep learning model were then transformed using the Hough transform algorithm for both circle and line detection. Circles were detected in the axial view of the 3D TRUS images, and then connected coronally using the line detection algorithm. This was followed by post-processing to decrease the width of the segmented catheters using a binary erosion operation with a 3 × 3 kernel as the structuring element.

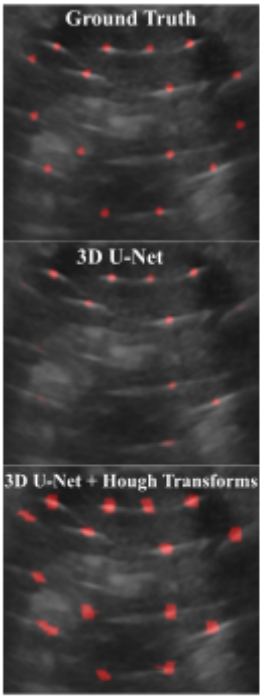

Fig 1: Example of catheter segmentations of U-Net and U-Net + Hough Transform methods compared to ground truth labels

Results: The deep learning model produced true positive segmentations on 317 of the 324 catheters in the test dataset, while falsely labelling 18 noisy regions as catheters. The same deep learning model followed by the Hough transform produced true positive segmentations on 319 catheters, while labelling 21 false positives. Table 1 shows the pixel-level evaluation metrics used to assess both methods of segmentation, while Fig. 1 depicts a visual comparison of the methods relative to the ground truth segmentation. Hough transforms following the deep learning model increased the recall metric while reducing the precision. The decreased precision is likely due to discrepancies in catheter diameter between ground truth segmentations and the larger diameters predicted by the proposed pipeline. This may be mitigated by resizing the segmentations to have the same diameter as the catheters used during the procedu.

Conclusions: The deep learning model in combination with the Hough transform can lead to the development of a practical application to be used by medical physicists in the operating room, providing a tool that allows for secondary checks by comparing manual tracks with automatic segmentations. The proposed method delivers a potential way of decreasing time spent verifying the initial manual catheter tracking, and equips clinicians with an aid to improve the clinical workflow.

Table 1: Pixel-level evaluation metrics of U-Net and U-Net + Hough Transforms

	Dice	Precision	Recall	F1 Score
3D U-Net	0.58	0.78	0.61	0.65
3D U-Net + Hough Transforms	0.58	0.61	0.82	0.66

References: [1] Chicas-Sett et al. *Brachytherapy* 2018. [2] Zhang et al. *Physics in Medicine & Biology* 2020. [3] Hrinivich et al. *Medical Physics* 2017

3D Spatial-Frequency Domain Imaging for Oral Cancer Surgery: Initial Simulations using Deep Learning

Arjun Jagota,[1] Yasmeen El-Rayyes,[1] Stefanie Markevich,[1] Scott Holthouser,[1] Leonardo Franz,[2] Sharon Tzelnick,[2] Brian C. Wilson,[1,3,4] Jonathan C. Irish[1-3] and Michael J. Daly[1]

[1]TECHNA Institute, University Health Network, Toronto ON
[2]Department of Otolaryngology – Head & Neck Surgery, University of Toronto
[3]Ontario Cancer Institute, Princess Margaret Cancer Centre, Toronto ON
[4]Department of Medical Biophysics, University of Toronto

Introduction: Promising clinical trials are driving new applications for fluorescence-guided oral cancer surgery. Existing 2D fluorescence systems lack subsurface imaging capabilities, and thus provide limited information on tumour depth. We are developing a 3D fluorescence system to help guide surgical resection.[1] A prototype spatial frequency domain imaging (SFDI) device has been constructed for pre-clinical evaluation (Fig. a). Our previous approaches to 3D fluorescence used analytical or iterative numerical methods; here, we investigate deep learning (DL) methods as an alternative for fast 3D reconstruction.

Methods: A deep convolutional neural network (CNN) architecture was adapted from prior work for fluorescence lifetime imaging of sub-surface inclusions.[2] In our case, we used fluorescence images across spatial frequency (f_x) to estimate the depth and concentration of infiltrative fluorescent inclusions ("iceberg model"). Absorption (μ_a) and scattering (μ_s') properties were estimated using SFDI reflectance images.[3] A Siamese DL architecture combined optical properties and fluorescence (Fig. b). For initial DL network validation, synthetic training data was simulated using a numerical light propagation model based on diffusion theory for cylindrical tumours over depths 1-5 mm. Two simulated cases were used to test DL predictions : Case 1, fixed optical properties (μ_a=0.0045 & μ_s'=1 mm^{-1}) and PpIX concentration (5 µg/mL); Case 2, variable parameters (μ_a=0.0015 – 0.015, μ_s'=0.75 – 2 mm^{-1}, concentration 1-10 µg/mL).

Results: (Fig. c) In Case 1, the mean structural similarity index measure (SSIM) for depth and concentration were 0.95±0.04 and 0.99±0.01, respectively, with depth errors < 1mm. In Case 2, the mean SSIM were both 0.91±0.06; however, Case 2 demonstrated a systematic underprediction of depth and concentration.

Conclusions: Initial DL simulations show promise under simplified assumptions (Case 1), but not when considering wider optical property variations (Case 2). We hypothesize that fluorescence variations across spatial frequency may be lost in the 3D CNN, and future work will explore changes to the convolution kernel and stride lengths. Future experimental studies in pre-clinical models displaying complex heterogeneity are an essential next step to assess system resolution and depth limits.

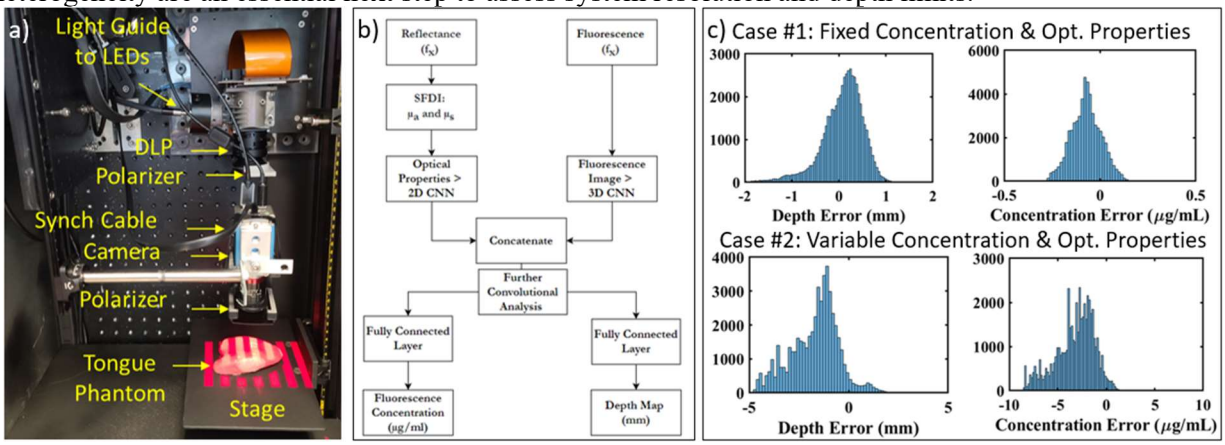

Figure. (a) Structured illumination system. (b) Deep learning architecture. (c) Initial simulation results.

References:

1. Daly MJ et. al., SPIE Photonics West 2021, Vol 11625.
2. Smith JT et. al., Opt Lett. 2020 45(15):4232-4235.
3. Cuccia DJ et. al., J Biomed Opt. 2009; 14(2):024012.

Development & Evaluation of a Bone-Targeted Photoacoustic Imaging Agent

Rowan Swann[1], Samantha Slikboer[2], Afaf R. Genady [1], Luis Rafael Silva[1], Nancy Janzen[1], Amber Faraday[2], John F. Valliant[1,2], & Saman Sadeghi[1]

[1] *Department of Chemistry & Chemical Biology, McMaster University, Hamilton, ON, Canada*
[2] *Fusion Pharmaceuticals, McMaster University, Hamilton, ON, Canada*
E-mail: swannr@mcmaster.ca

Molecularly targeted organic dyes present an opportunity to expand photoacoustic imaging (PAI) applications by allowing for the detection of biological entities that do not possess intrinsic photoacoustic (PA) properties. [1] Thus far, PAI of bone has predominantly consisted of the use of endogenous contrast or passive targeting strategies. [2-4] Therefore, this work focuses on the development and evaluation of a PA dye targeted to bone using alendronate, a bisphosphonate (BP) with a high affinity to the calcium-containing mineral present on bone; hydroxyapatite (HA). [5] Here, we demonstrate that a BP-derived *trans*-cyclooctene employed with a novel 1,2,4,5-tetrazine bound IR-783 dye, binds specifically to bone, enabling *in vivo* PAI in a healthy murine model, using three different delivery strategies.

In vitro analysis was first used to verify the specificity of the probe to bone through incubation with powdered HA. In comparison to the non-targeted dye, which exhibited a low percent binding to HA (1 ± 1.2%), the targeted dye demonstrated significant binding using both active (62 ± 5.7 %, where $P = 0.005$) and pre-targeting (55 ± 2.7%, where $P < 0.001$) strategies. *In vivo* PAI, using the Vevo LAZR-X, was then performed to demonstrate the ability of the probe to localize and be retained at bone. Local, intrafemoral, injection of the targeted and non-targeted dyes was used to demonstrate the ability of the targeted dye to bind to bone in a complex biological environment. As early as 4 hours post-injection (h P.I.) complete wash-out of the non-targeted dye was observed (0.04 ± 0.01 a.u.), with respect to the pre-injection signal (0.02 ± 0.003 a.u.). Significant signal of the targeted dye was retained out to 24 h P.I. (0.27 ± 0.09 a.u., where $P \leq 0.006$) when compared with the pre-injection signal. Assessment of the probe's ability to localize to bone through systemic circulation was then tested through intravenous injection of the targeted and non-targeted dyes. Quantification of the PA signal demonstrated that BP-specific accumulation of dye occurred at bone 4 h P.I. (0.18 ± 0.02 a.u [targeted] and 0.05 ± 0.01 a.u. [non-targeted], where $P < 0.001$). Finally, pre-targeting was assessed as a strategy to deliver the dye to bone. Quantification of the PA signal demonstrated that, by 4 h P.I., significant concentrations of the pre-targeted dye were obtained compared to the non-targeted dye (0.11 ± 0.03 a.u. and 0.07 ± 0.01 a.u., respectively, where $P < 0.04$), thus confirming the *in vivo* biorthogonal reaction between tetrazine and trans-cyclooctene occurred.

When compared to both background signal and a non-targeted control group, distinct, spectrally verified PA signal was achieved at the bone of healthy mice using the BP-targeted dye through local intrafemoral injection, actively targeted intravenous injection, and pre-targeted intravenous injection. Future work will focus on assessing the efficacy of this bone-targeting PAI probe for distinguishing disease states from healthy bone tissue.

References:

1. Weber, J.; Beard, P. C.; Bohndiek, S. E. Contrast Agents for Molecular Photoacoustic Imaging. *Nat. Methods* **2016**, 13 (8), 639-650.
2. Park, E.-Y.; Lee, D.; Lee, C.; Kim, C. Non-Ionizing Label-Free Photoacoustic Imaging of Bones. *IEEE Access* **2020**, 8, 160915-160920.
3. Shubert, J.; Lediju Bell, M. A. Photoacoustic Imaging of a Human Vertebra: Implications for Guiding Spinal Fusion Surgeries. *Phys. Med. Biol.* **2018**, 63(14), 144001.
4. Hu, J.; Yu, M.; Ye, F.; Xing, D.; *In Vivo* Photoacoustic Imaging of Osteosarcoma in a Rat Model. *J. Biomed. Opt.* **2011**, 16(2), 020503.
5. Cole, L. E.; Vargo-Gogola, T.; Roeder, R. K. Targeted Delivery to Bone and Mineral Deposits Using Bisphosphonate Ligands. *Adv. Drug. Deliv. Rev.* **2016**, 99, 12-27.

Methotrexate-loaded microbubbles for imaging and treatment of inflammatory bowel disease

Yara Ensminger[1], Haochen Zhang[1], Una Goncin[2], Steven Machtaler[2] and Naomi Matsuura[1,3,4]
[1]Department of Materials Science & Engineering, University of Toronto, Ontario, Canada, [2]Department of Medical Imaging, University of Saskatchewan, Saskatchewan, Canada, [3]Institute of Biomedical Engineering, [4]Department of Medical Imaging, University of Toronto, Ontario, Canada

Introduction: Inflammatory bowel disease (IBD) is a prevalent autoimmune disease lacking advanced treatment options. Routinely treated with methotrexate (MTX), adverse side effects and a small therapeutic window limit administered dosages [1, 2]. Thus, an approach to release a high, localized dose of MTX in the diseased region of bowel is required, without side effects caused by a high systemic dose. Here we propose a lipid-based microcarrier for improved drug delivery. Spatially restricting release to the diseased site by targeting microcarriers could further reduce side effects. As ultrasound (US) assessments for IBD become more routine due to accessibility and patient compatibility [3], it is advantageous to load MTX into targeted US-detectable drug carriers for efficient release into the diseased site. In this study, we synthesized and characterized MTX-loaded US detectable microbubbles (MTX-MB), to enhance drug delivery for treatment of IBD. Requirements for these MTX-MBs include drug loading exceeding 2 μg per μg gas dose to ensure therapeutic effects compare to routine 15 mg MTX doses; stability >1 hour to allow for MB preparation and *in vivo* circulation at 37˚C; retained imaging signal intensity in comparison to control MBs, to assess when the drug carrier has reached the target site; as well as US detectability at frequencies used for treatment (~3 MHz) [4]. Limitations of this method are comparable to limitations of other US contrast agents, such as restricted imaging depth through thick tissue.
Methods: For MTX-MBs, a MTX and lipid complex was formed by dissolving MTX and lipid in tetrahydrofuran, followed by evaporation of the solvent to create dried MTX-loaded lipid films, which was used to create lipid-shelled MTX-MBs [5]. Control MBs (without MTX) were synthesized following the same procedure. MB size distribution using number concentration and stability was determined using a Beckman Coulter Multisizer 4e, measuring samples using a 20 μm aperture at 10 min intervals after bubble hydration. MTX loading was assessed using a Molecular Devices SpectraMax M2 Spectrophotometer (using a Quartz cuvette at peak absorbance of 298 nm) and ultrahigh performance liquid chromatography on a UPLC-MS/MS-PDA system. Preliminary imaging ability of control and MTX-MBs flowing through an agarose flow phantom at concentrations of 3 x 10^9 MBs/mL was assessed using B-mode and contrast-enhanced mode using a 6 MHz Aplio US transducer. Imaging signal intensity in region of interest were quantified using MATLAB.
Results: MTX-loaded MBs with 33 μg MTX loading into ~10^9 MBs and an encapsulation efficiency of 17% were synthesized. The mean size of control MBs and MTX-MBs were approximately 0.8 μm. Stability of control and MTX-MBs both decreased from 20˚C to 37˚C (Fig. 1). MTX-MBs were stable for 120 min at 20˚C and 90 min at 37˚C, while control MBs were stable for 90 min at 20˚C and 60 min at 37˚C, respectively. Both MTX-MBs and control MBs were visible using US imaging (Fig. 1).
Conclusion: Lipid MTX-MBs were synthesized with 0.0167 mg MTX loaded per mL MBs. MTX-MBs showed improved stability over the control MBs and were visible on US showing promise as an US-detectable drug carrier. Future work will assess cytotoxicity of free and encapsulated MTX by exposing MBs to cavitating US pressures and incubating with Caco-2 and THP-1 cells to mimick inflammation, as well as bioavailability in *in vivo* murine inflammatory bowel disease models. Successful synthesis and clinical translation would improve treatment methods for inflammatory diseases, particularly IBD.

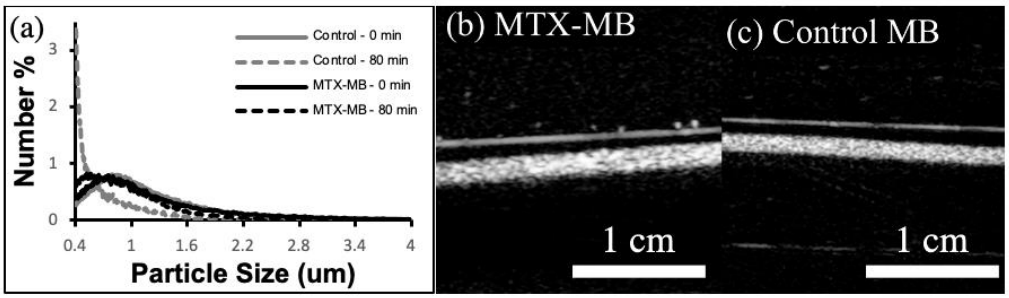

Figure 1: (a) Normalized Number Concentration of control and MTX-MBs at 37˚C for 60 min; (b) MTX-MBs and (c) Control MBs flowing through agarose flow phantom under contrast-enhanced ultrasound mode

References: [1] Lahad et al., World J Gastrointest Pathophysiol, (2015); [2] Swaminath et al., World J Gastrointest Pharmacol Ther, (2014); [3] Bettinger et al., Investig. Radiol, (2012); [4] Ferrara et al., Annu. Rev. Biomed. Eng., (2007); [5] Matsuura et al., Proc. IEEE Int. Ultrason. Symp. (IUS), (2015)

Ideal Chromophore for Intralipid-Based Tissue-Mimicking Phantom

Rasa Eskandari[1] and Mamadou Diop[1-3]

[1]*Department of Medical Biophysics, Western University, London, ON, Canada*
[2]*School of Biomedical Engineering, Western University, London, ON, Canada*
[3]*Imaging Program, Lawson Health Research Institute, London, ON, Canada*

Introduction: Near-infrared photons (i.e., wavelength range of 650 to 900 nm) can harmlessly penetrate deep into biological tissues to probe thick structures such as the adult brain.[1] Near-infrared spectroscopy (NIRS) is now commonly used to non-invasively measure the wavelength-dependent attenuation of light by tissues to estimate the concentrations of biomarkers of cerebral health such as cerebral blood content and oxygenation.[2] Furthermore, the reliability of NIRS devices and algorithms is typically assessed using phantoms, which are media prepared with accessible resources to mimic the optical properties of biological tissues. Tissue-mimicking phantoms are typically made of a light scatterer, which is commonly a lipid emulsion (e.g., Intralipid), and one or multiple chromophores (i.e., light-absorbing dyes). Current evidence, however, suggests that the optical properties of dyes can change as a function of the phantom composition—two different concentrations of the same dye in a consistent concentration of the same light scatterer may present different absorption spectra.[3] This is important because in an ideal phantom, there would be minimal interaction between the scatterer and the chromophores, thereby preserving the absorption spectrum of the phantom for any combination of scatterer and chromophore concentration. The objective of this study is to identify the ideal chromophore among the commonly used dyes for Intralipid-based tissue mimicking phantoms.

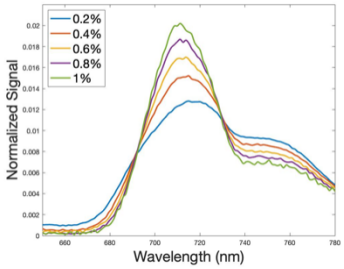

Figure 1 *Transmitted intensity signal (normalized with the area under the curve) for a constant methylene blue concentration of 0.9 μM as Intralipid was increased from 0.2 to 1% in steps of 0.2%.*

Methods: A custom-made spectrometer (Sciencetech, ON, Canada) was used to measure light intensities from a 20-W halogen lamp (Ocean Optics HL-2000-HP), transmitted through Intralipid-based phantoms with methylene blue as the chromophore. Two sets of data were acquired for the wavelength range of 650 to 780 nm: (1) for a constant chromophore concentration, transmitted spectra were acquired stepwise for a linearly increasing Intralipid concentration; (2) for a constant Intralipid concentration, transmitted spectra were acquired stepwise for a linearly increasing chromophore concentration. Spectra were plotted collectively for each set of measurements using MATLAB R2021b.

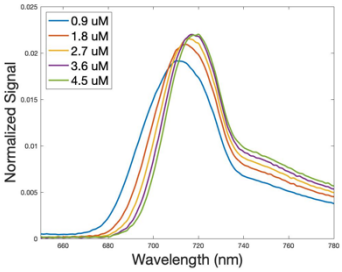

Figure 2 *Transmitted intensity signal (normalized with the area under the curve) for a constant Intralipid concentration of 0.8% as methylene blue concentration was increased from 0.9 to 4.5 μM in steps of 0.9 μM.*

Results: Fig. 1 and 2 show the variations in the absorption properties of methylene blue as a response to the phantom composition. For a fixed amount of methylene blue, the spectra were shifted to the right and peaks were narrowed as Intralipid concentration was increased from 0.2 to 1 %. When a fixed Intralipid concentration of 0.8 % was used, the spectra were shifted to the longer wavelength and peaks were narrowed as the dye concentration was increased from 0.9 to 4.5 μ.

Conclusions: The results suggest that methylene blue is not an ideal chromophore for Intralipid-based phantoms since its absorption properties are not preserved when the concentration of either Intralipid or dye changes. The shifts observed in fig. 2 suggest that there is interaction between Intralipid and methylene blue. When scattering is constant, the change in light attenuation is equal to the product of the absorption coefficient and optical pathlength; however, the pathlength can be assumed to be constant because of the unchanging light scattering. Therefore, the shifts in fig. 2 are likely due to changes in the molar extinction coefficients of methylene blue as it interacts with Intralipid. Future work will investigate how the interaction of Intralipid with methylene blue compares to other commonly used dyes, including indocyanine green and India ink. Further, we will test alternative light scatterers such as glass microspheres and titanium oxide[4] with the goal of finding the best combination of light absorbers and scatterers for NIRS tissue-mimicking phantoms.

References: [1] Owen-Reece H., et al. *British Journal of Anaesthesia* **82**(3), 418-444 (1999). [2] Lange F., et al. *IEEE Journal of Selected Topics in Quantum Electronics* **25**(1), 7100312 (2019). [3] Yuan B., et al. *Journal of Biomedical Optics* **9**(3), 497-503 (2004). [4] Pogue B. W., et al. *Journal of Biomedical Optics* **11**(4), 041102 (2006).

Oral Session 9:
Imaging for Musculoskeletal Analysis

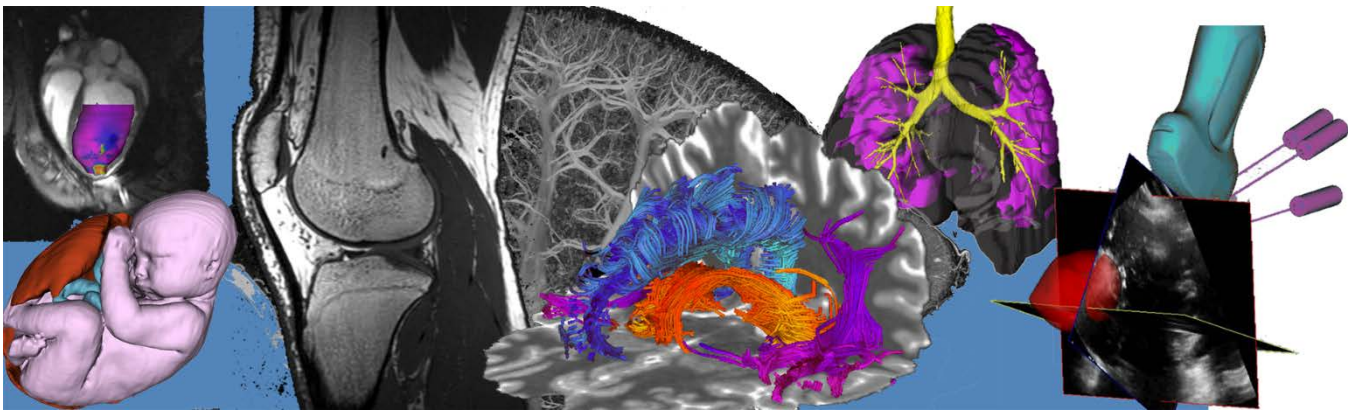

In-Vitro Characteristics of Embolic Agents for Osteoarthritis

Kierdra I. Dowling[1], Robert Koucheki[2,3], Kakit Cheung[4], Camilo Barragan[2,5], Edmond Young[4], Sebastian Mafeld[2,5] Naomi Matsuura[1,3,5]

[1] Department of Materials Science and Engineering University of Toronto, Toronto, Canada. [2] Faculty of Medicine University of Toronto, Toronto, Canada. [3] Institute of Biomedical Engineering University of Toronto, Toronto, Canada. [4] Department of Mechanical and Industrial Engineering University of Toronto, Toronto, Canada. [5] Department of Medical Imaging, Toronto General Hospital, Toronto, Canada

Introduction: Osteoarthritis (OA) is a chronic and painful condition that affects ~303 million people globally. This condition creates a significant burden on the health care system and has economic consequences of around $5 billion annually in Canada.[1] Interventional radiology offers a new and innovative solution to treat OA pain with embolization, a minimally invasive procedure in which target blood vessels are blocked via injected particulate agents. Histopathological studies of knee OA have demonstrated the existence of abnormal neovessels that contribute to the genesis and maintenance of low-grade inflammation and associated pain. A crystalline antibiotic, Imipenem/Cilastatin (IPM/CS), mixed in iodinated contrast media to enable visualization via fluoroscopy has been shown to occlude neovessels for ~48 hours.[2-3] However, the mechanisms behind their embolic properties have not yet been established, which is required to advance this procedure for more complex applications (i.e., OA of the spine and hip). The hip and spine are located closer to vital organs (e.g., liver, kidney, etc.) and off-target embolization at these sites can result in severe complications. The ideal embolic agent for OA should be degradable, able to completely block neovessels and able to decrease the occurrence of a chronic inflammatory response. In this study, we investigated the mechanical blockage, surface characteristics and blood contacting properties of IPM/CS and compared it to clinical agents to gain an improved understanding of how this antibiotic reduces OA pain in patients and how it can be improved for embolotherapy.

Methods: Clinical embolic agents Embosphere (a permanent microsphere), Polyvinyl Alcohol (irregular flakes of PVA), and Ekobi (a poly(lactic-co-glycolic acid) (PGLA) microsphere coated in collagen) were characterized and compared to IPM/CS. Flow channels designed to mimic the geometry of neovessels were used to characterize how the agents mechanically block vessels. Surface characterization of agents was done using Environmental Scanning Electron Microscopy (SEM) with a FEI Quanta FEG 250. A thrombin time assay was also performed with bovine plasma in the presence of these agents to determine the bloods' coagulation response to different embolic agents.

Results: IPM/CS blocked the channels similar to PVA by adhering to the wall followed by aggregation. The round microspheres (Embosphere and Ekobi) had more predictable blockage as they would become wedged into the flow channels due to size matching with the channel diameter. Unlike Ekobi, Embosphere could be compressed in the catheter and then return to the original shape upon injection, reducing the risk of catheter clogging, a limitation of many clinical embolic agents. SEM images of the embolic agents showed that IPM/CS tended to clump together and had particles down to around 1 micron in size. The thrombin time assay showed that after activating coagulation, blood clots formed in the plasma samples containing Embosphere, Ekobi and PVA at ~6 minutes. The IPM/CS containing sample showed no sign of blood clotting.

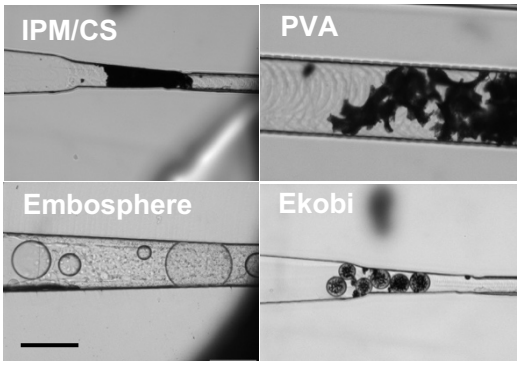

Figure 1: Embolic agents blocking the flow channels. Scale bar 400 µm.

Conclusion: In conclusion, IPM/CS's ability to decrease clotting and degrade in ~48 hours contributes to its success as an embolic for OA. However, its wide size range, unpredictable blockage and risk for catheter clogging are limitations. Future work will focus on incorporating IPM/CS into a degradable and compressible microsphere that results in predictable blockage and decreased blood coagulation to prevent a chronic inflammatory response. A more tailored agent could allow for safer embolization of the knee and be adapted into embolization in OA of more complex areas, such as the hip and spine.

References: [1] B. Sharif, *Osteoarthritis Cartilage*., 2015; [2] Y. Okuno, *JVIR.,* 2013; [3] K. Yamada, *JVIR*., 2021.

Four-Dimensional Computed Tomography Scanning Allows for the Visualization and Measurement of Glenohumeral Joint Arthrokinematics

Baraa Daher[1,2,3], George S. Athwal[4,5], Emily Lalone[1,2,3,4]
[1]School of Biomedical Engineering, [2]Department of Mechanical and Materials Engineering, [3]Bone and Joint Institute, Western University, [4]Lawson Health Research Institute, [5]Roth|McFarlane Hand and Upper Limb Center, London, Ontario, Canada

Introduction: The glenohumeral joint (GH) is the most mobile joint in the human body, making it more susceptible to injury and pathology. The main goal of treating any shoulder injury or pathology is to restore normal GH biomechanics and arthrokinematics. However, quantifying GH biomechanics remains challenging due to associated limitations with current techniques. Recently, four-dimensional computed tomography (4DCT) technology has emerged and may be a useful alternative to three-dimensional computed tomography (3DCT), as it overcomes the challenges associated with previous techniques. This new technique produces 3DCT images that demonstrate movement in real-time. No study has evaluated the contact patterns and arthrokinematics of the GH joint during active internal rotation to the back using this technique yet. This motion is important in activities of daily living, and is usually limited following reverse shoulder arthroplasty (RSA). Therefore, the objectives of this study are 1) to describe a technique which employs 4DCT to quantify in vivo GH contact patterns during dynamic shoulder motion, and 2) to quantify normal GH joint contact mechanics and translation in the healthy adult during internal rotation to the back.

Methods: Seven participants underwent static (120 kV, 211 mA, 1.0 s rotation time, 512x512 matrix, axial) and dynamic (80 kV, 130 mA, 0.35 s rotation time, 512x512 matrix, axial) 4DCT scanning of their dominant shoulder. Dynamic 4DCT started with elbow fixed at 90° and palm flat on stomach. Participates then actively elevated and internally rotated the shoulder to position the back of the hand behind their back. The static CT frame and dynamic frames obtained were reconstructed into 3D models of the glenoid and humerus using 3D Slicer software version 4.11.0. The static models were registered to the position of the dynamic frames using surface-based registration (iterative closest point (ICP)) algorithm. Then, GH joint congruency was measured using a previously developed algorithm which calculates minimum inter-bone distances between opposing bone surfaces. To display inter-bone distances, a color scale from 0 to 6.0 mm (0 mm, red; 6 mm, blue) was selected. Glenohumeral arthrokinematics were determined by tracking the centroid of contact of the joint surface area. The centroid was determined by finding the geometric average of the x, y, and z coordinates of the points on the surface of the glenoid that were within 4 mm of the humeral head. The y-axis was defined as the line connecting the inferior (I) and superior (S) landmarks, pointing superiorly. The x-axis was defined as the line perpendicular to the plane formed by the three landmarks, pointing laterally. The z-axis was the common line perpendicular to both the x- and y-axes, connecting the anterior (A) and posterior (P) landmarks, pointing posteriorly.

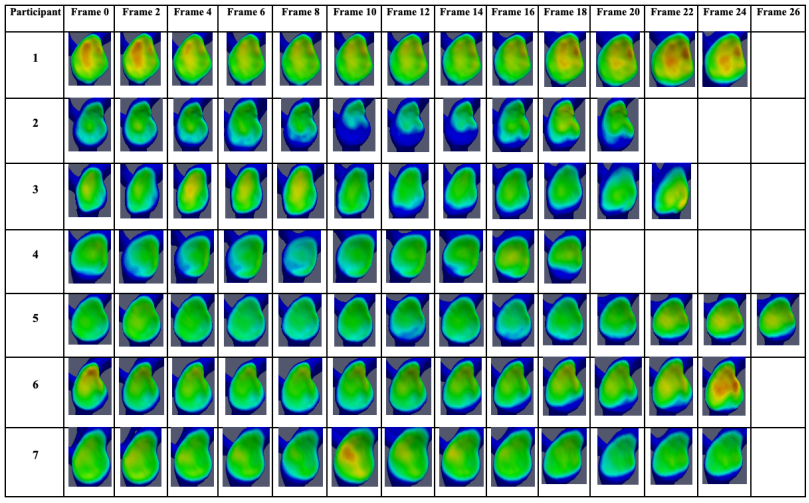

Table 1: Proximity maps n=7 during internal rotation to the back. Inter-bone distances from 0 to 6.0 mm (0 mm. red: 6 mm. blue).

Results: Proximity maps of the GH for seven healthy participants throughout the motion are shown in Table 1. The joint congruency maps show that the contact patterns of the joint change as the shoulder moves throughout the motion. The translation of the humerus relative to the glenoid was calculated in the y- and z-axis. The average humerus translated a total of 4.9 ± 2.8 mm (S/I) and 3.1 ± 1.3 mm (A/P).

Conclusion: The internal rotation to the back motion is significant in activities of daily living, such as washing the back and opposite shoulder, using a back pocket, managing toileting and clasping a brassiere. This motion is limited after a RSA surgery as a consequence of inverting the anatomic concavities of the glenoid and humerus that creates a fixed structure in which is limited to only rotate/spin. Therefore, quantifying dynamic joint congruency and arthrokinematics of the healthy adult can explain the importance of translation to achieve a healthy range of motion and eventually improve implant designs.

Estimating Muscle Fiber Composition Via Resting-State Muscle BOLD Signal Complexity

Joshua E. McGillivray[1,2], Dinesh Kumbhare[1,2,3], Michael D. Noseworthy[1,2,4,5]

[1]School of Biomedical Engineering, McMaster University. [2]Imaging Research Centre, St. Joseph's Healthcare. [3]Department of Medicine and Biomedical Engineering, University of Toronto. [4]Electrical and Computer Engineering, McMaster University. [5]Department of Radiology, McMaster University.

Introduction:

The blood oxygen dependent level (BOLD) effect uses hemoglobin oxygenation variation to infer changes in blood flow/volume and metabolic need, and aids in characterizing healthy and diseased skeletal muscle.[1,2] However, for diagnosis of some muscular and neuromuscular disorders, muscle biopsy is the gold-standard, as it identifies slow-twitch (ST) to fast-twitch (FT) fiber ratio.[3] Differing fiber perfusion demands suggest the muscle BOLD signal could non-invasively characterize muscle fiber profiles, which would be clinically valuable.[3,4] The temporal fractal dimension (FD), a measure of signal complexity, is proposed to provide this insight.

Methods:

Preliminarily 8 male subjects (4 endurance (ST) : 4 power (FT) athletes), were grouped based on their physical activity habits. Prior to scanning subjects lay supine for 30min to normalize leg muscle blood-flow, shown to affect the skeletal muscle BOLD signal.[5] Using a GE MR750 3T scanner, resting-state muscle BOLD images were collected (TE/TR/flip=35/109ms/70^0, 2slices, 10mm thick, 64x64, 16cm FOV, 2424 temporal phases). Using the FMRIB Software Library, BOLD images (truncated to middle 2048 time points) were motion corrected, and soleus [ST dense], gastrocnemius [ST/FT dense], and anterior muscles (Ant.Muscles) (tibialis anterior, peroneus and extensor longus groups) [FT dense] were manually segmented, using a high-resolution anatomical reference.[6] Time-series were normalized to the first time point and then segmented into four 512 temporal-point sections. Voxel-wise segmented BOLD timeseries bi-FD was computed using the scaled windowed variance approach, with linear detrending.[7] The bi-FD was computed by estimating the slope by fitting two lines to the non-saturated portion of the log-log plot for a given voxel and segment, then averaging across segments. Averaging improved FD reliability, which is impacted by linear fitting slope estimates. Bi-FD voxel distributions for component 1 (C_1) and 2 (C_2) were negatively skewed; thus, Wilcoxon rank sum and Kruskal-Wallis tests were used to examine within and across subject differences, respectively.

Results:

The median bi-FD regardless of activity grouping or component, followed the trend soleus > gastrocnemius > Ant.Muscles and regardless of muscle, ST > FT group (**figure 1**). Across subjects the bi-FD for each muscle was significantly different with p-values of 1.925e-16 for C_1 and 2.901e-9 for C_2. This suggests a larger median FD corresponds to a higher ST fiber density and variable component discriminability. To identify fiber type sensitivity, we leveraged gastrocnemius homogeneity increases, to respective fiber type grouping, and expected decreased discriminability between similar muscle profiles. Activity group averaged, subject-wise, ranked-sum muscle comparison tests (**table 2**) show the discriminability of the power (FT) group's similar gastrocnemius vs. Ant.Muscles was $C_2 > C_1$ and of the endurance (ST) group's similar gastrocnemius vs. soleus was $C_1 > C_2$, suggesting C_1 is influenced by FT and C_2 by ST fibres.

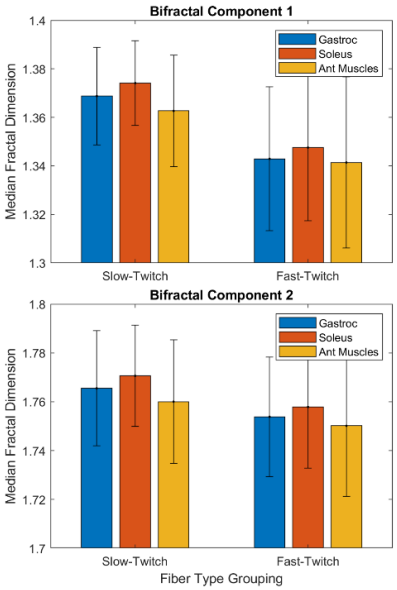

Figure 1. Group averaged median muscle BOLD FD (median absolute deviation) for components C_1 and C_2.

Twitch Group	Gas. Vs Sol.		Gas. Vs Ant. Grp	
	C_1	C_2	C_1	C_2
Slow	0.03	0.47	0.23	0.07
Fast	0.08	0.01	0.12	0.08

Table 1. P-values for muscle group comparisons for each bi-FD component C_1 and C_2. Green indicates significant ($p<0.05$), yellow indicates possible trend ($p<0.1$) and red is not significant.

Conclusion:

Median voxel bi-FD differentiated soleus, gastrocnemius, and Ant.Muscles within subjects and based on ST/FT activity groupings, with C_1 being influenced by FT and C_2 by ST fibers. This indicates that muscle BOLD FD characterization could non-invasively provide information on muscle fiber type ratios, possibly replacing the need for muscle biopsy. Female athlete recruitment is required to validate our promising technique. Clinical outlook will be explored via correlation of muscle function to fiber profiles.

References:

[1]Ogawa S, et al. *Proc Natl Acad Sci.* 1990;87(24):9868–9872. **[2]**Jacobi B, et al. *J Magn Reson Imaging*. 2012;35:1253-1265. **[3]**Joyce NC, et al. *Phys Med Rehabil Clin N Am*. 2012;23(3):609-631. **[4]**Behnke BJ, et al. *Am J Physiol Regul Integr Comp Physiol.* 2011;301(3):R783-R790. **[5]**Elzibak AH, Noseworthy MD. *Magn Reson Mater Phys. Biol Med.* 2014;27: 387–395. **[6]**Jenkinson M, et al. *Neuroimage*. 2012;62(2):782-790. **[7]**Cannon MJ, et al. *Physica A.* 1997;241(3-4):606-626.

3D Ultrasound to Characterize Synovial Volume in First Carpometacarpal Osteoarthritis Patients

Carla du Toit[1,2], Robert Dima[1], Melanie Jonnalagadda[3], Aaron Fenster[2,3], Emily Lalone[4,1]

[1]Faculty of Health Sciences, Collaborative Specialization in Musculoskeletal Health Research, and Bone and Joint Institute, Western University, London, Ontario N6A 3K7, Canada[2]Robarts Research Institute, Western University, London, Ontario N6A 3K7, Canada[3] Department of Medical Biophysics, Western University, London, Ontario N6A 3K7, Canada,[4]Faculty of Engineering Western University, London, Ontario N6A 3K7, Canada

Introduction: Synovitis is one of the defining characteristics of osteoarthritis (OA) in small joints, such as the carpometacarpal (CMC1) joint of the thumb. It has been strongly correlated to measures of worsening OA such as joint space narrowing as well as adverse patient outcomes (i.e. pain). Quantitative characterization of synovial volume is important for treatment and monitoring of CMC1 OA and to further our understanding of how it affects disease progression. In previous studies, three-dimensional ultrasound (3-D US) has demonstrated the feasibility of being a point of care system for monitoring knee OA. However, 3-D US has not been tested on the smaller joints of the hand, which present unique challenges from a physiological and imaging standpoint. The purpose of this research project is to validate the use of 3-D US using CMC OA patients to assess the measurement capabilities of the device in a clinically diverse population in comparison to MRI.

Methods: Four CMC OA patients were referred to the study by an experienced hand surgeon. A motorized submerged transducer moving assembly was designed for this device specifically for imaging the hands and wrist. For this study a Canon Aplio i700 US machine with a 14L5 linear transducer was used. The device used a linear scanning approach, where a 2D US transducer was translated linearly over an 8.12 cm region of interest in 16 seconds. To acquire the complementary MR images, a 3.0 T MRI system was used. Boundaries were established for each image and consisted of the most lateral and medial edges of the first metacarpal and trapezium bones. The raters proceeded to manually segment every second slice (0.33 mm between slices) of the MRI and 3-D US images to find the volume percent differences between the two modalities and between raters (Fig. 1). Interclass Correlation Coefficients were used to determine inter- and intra-rater reliability.

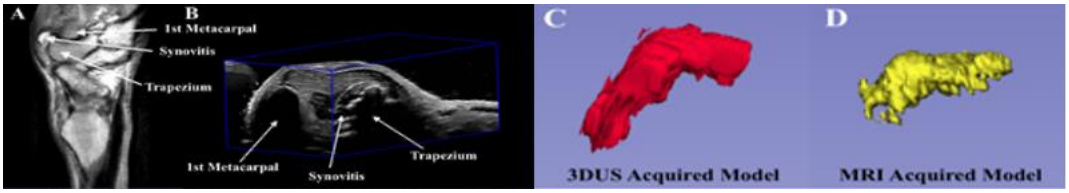

Figure 1. (A) MRI image of a CMC1 OA patient with matched (B) 3-D US image. 3-D tissue models produced from the manual segmentation of the synovitis present in the CMC1 joint were compared between 3-D US (C) and MRI (D).

Results: The mean volume percent difference observed between the two raters for the 3-D US and MRI acquired synovial volumes was 1.77 ± 4.35% and 4.76 ± 4.44%, respectively. The smallest percent difference in volume found between raters was 0.91% and was from an MR image. The average difference found between MRI and 3-D US for this sample was 8.25± 10.03mm^3. ICC values of 0.99 and 0.98 for 3-D US and MRI, respectively, indicate that there was excellent inter-rater reliability between the two raters.

Conclusion: A novel application of a 3-D US acquisition device was evaluated using a CMC OA patient population to determine its clinical feasibility and measurement capabilities in comparison to MRI. It was observed that the two raters exhibited excellent inter-rater reliability and that there was no statistically significant difference found between the volumetric measurement found using 3-D US and MRI. This device significantly increases its accessibility and ease of use, while proving a method for overcoming some of the limitations associated with radiography, MRI and 2-D US. 3-D US has the potential to provide clinicians with a tool to quantitively measure and monitor OA progression at the patient's bedside.

Oral Session 10:
MR Imaging II

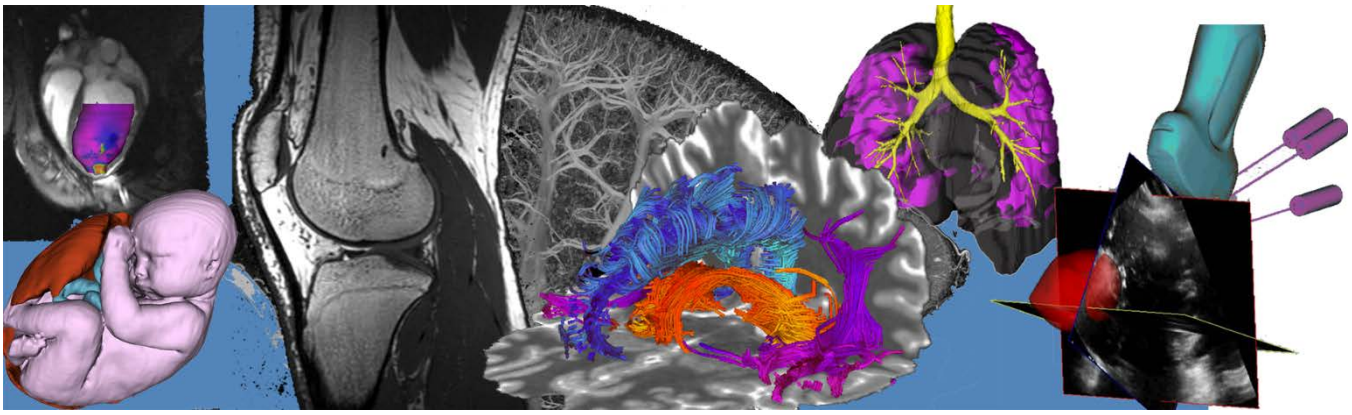

Advanced diffusion MRI metrics reveal acute sensitivity to mild traumatic brain injury in a mouse model

Naila Rahman, Kathy Xu, Arthur Brown, Corey A. Baron
Robarts Research Institute, Western University, London, ON, Canada

Introduction: Current neuroimaging techniques lack the specificity required to reliably detect signs of mild traumatic brain injury (mTBI).[1] Microstructure imaging with advanced diffusion MRI (dMRI) techniques have shown increased sensitivity and specificity to microstructural changes in various disease and injury models. Oscillating gradient spin echo (OGSE) dMRI[2] and microscopic anisotropy (μA) dMRI[3] may provide additional insight by increasing sensitivity to smaller spatial scales and disentangling fiber orientation dispersion from true microstructural changes, respectively. Here, we evaluate mean diffusivity difference (ΔMD: difference in MD between the highest (190 Hz) and lowest (0 Hz) OGSE frequencies), microscopic fractional anisotropy (μFA), and traditional dMRI metrics (such as MD and FA) longitudinally in sham and concussed mice.

Methods: The sham and concussed cohort each consisted of six female C57Bl/6 mice, aged 10-12 weeks at the start of the study. Longitudinal imaging was performed on the sham and concussed cohort at baseline, 2 days post-mTBI, 1-week post-mTBI, and 4 weeks post-mTBI. Imaging was performed at 9.4T with a 1 T/m gradient insert using single-shot EPI with an in-plane resolution of 0.175x0.2mm^2, 0.5mm slice thickness, and a total scan time of 2 hours. The OGSE and μA sequence were implemented as outlined by Rahman et al.[4] Post processing included PCA denoising[5] and eddy current correction with FSL.[6]

Results: Parameter maps at baseline and 4 weeks post-mTBI, in one concussed mouse, are shown in Fig. 1. In the prefrontal cortex, a 7.1 % increase in μFA and a 16.7 % increase in ΔMD was found 2 days post-mTBI, compared to baseline (Fig. 2). In the corpus callosum, a 5.1 % decrease in ΔMD was found 2 days post-mTBI. No significant changes were found in the traditional dMRI metrics, except an increase in FA in the corpus callosum for both sham and concussed cohorts.

Conclusion: Changes in ΔMD can be related to neurite beading.[7] Elevated μFA may reflect increased trapped water in swollen axons.[9] In conclusion, we demonstrate that both μFA and ΔMD show acute sensitivity to concussion, while traditional dMRI markers (FA and MD) do not.

References: [1]Eierud C et al. *Neuroimage Clin* (2014). [2]Baron CA et al. *MRM* (2014). [3]Lasič S et al. *Front Phys* (2014). [4]Rahman N et al. *PLoS One* (2021). [5]Veraart J et al. *Neuroimage* (2016). [6]Andersson JLR et al. *Neuroimage* (2016). [7]Baron CA et al. *Stroke* (2015). [8]Skinner NP et al. *NMR Biomed* (2015). [9]Zhou M et al. *ISMRM* (2021).

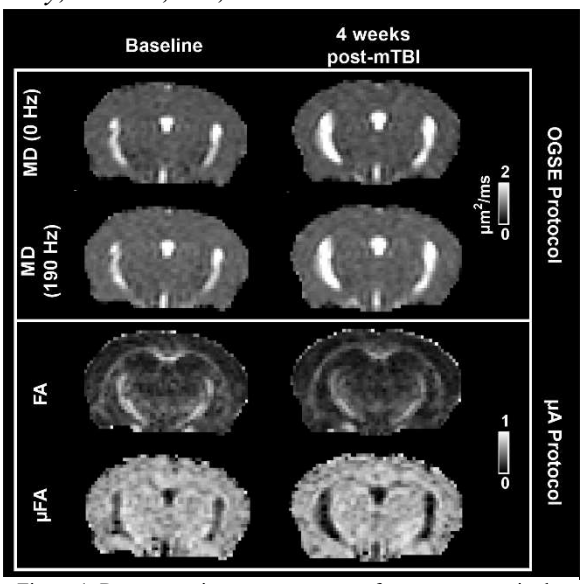

Figure 1. Representative parameter maps from one mouse in the concussed cohort taken at baseline and 4 weeks post-mTBI. From the OGSE protocol, mean diffusivity (MD) maps are shown at 0 Hz and 190 Hz. Fractional anisotropy (FA) and microscopic fractional anisotropy (μFA) maps were estimated from the μA protocol.

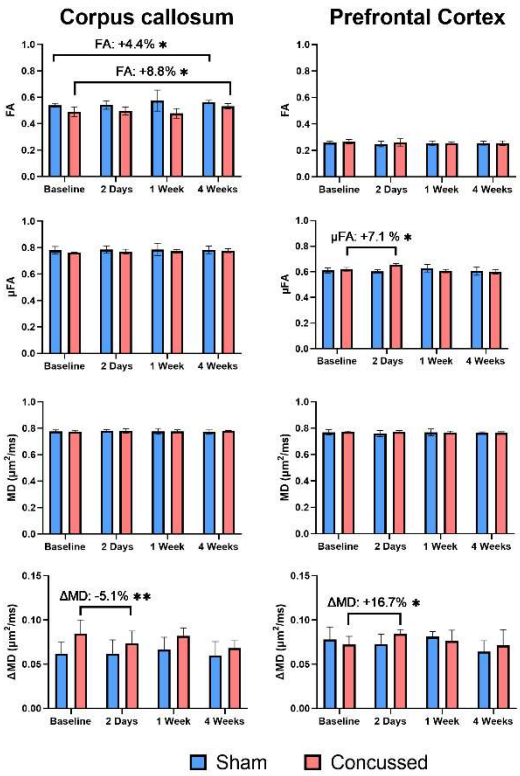

Figure 2. Comparison of dMRI metrics in the corpus callosum (left column) and the prefrontal cortex (right column). Paired t-tests in each cohort between each timepoint and the baseline show a 7.1 % increase in μFA at 2 days post-mTBI in the prefrontal cortex, as well as significant changes in ΔMD (the difference between MD at 190 Hz and MD at 0 Hz) at 2 days post-mTBI.

Human brain multi-slice imaging using hyperpolarized ^{129}Xe

Vira Grynko[1,2], Yurii Shepelytskyi[2,3], Tao Li[3], Ayman Hassan[4,5], Karl Granberg[4], Mitchell S. Albert[2,3,5]

[1]Chemistry and Materials Science Program, Lakehead University, Thunder Bay, ON, Canada. [2]Thunder Bay Regional Health Research Institute, Thunder Bay, ON, Canada [3]Chemistry Department, Lakehead University, Thunder Bay, ON, Canada [4]Thunder Bay Regional Health Sciences Centre, Thunder Bay, ON, Canada [5]Northern Ontario School of Medicine, Thunder Bay, ON, Canada

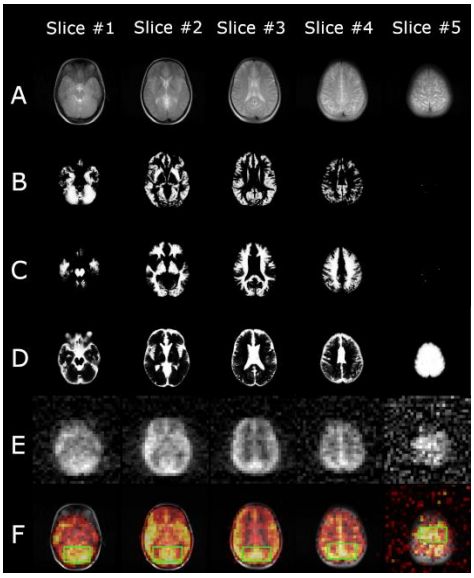

Figure 1. ^{1}H T_2W anatomical axial TSE images (A) segmented on gray matter (B), white matter (C), CSF (D). HP ^{129}Xe axial images (E). (F) HP ^{129}Xe axial brain slice images superimposed on top of the corresponding ^{1}H anatomical images[5].

Introduction: Currently, the most promising applications of hyperpolarized (HP) ^{129}Xe brain imaging are the visualization of cerebral blood perfusion[1,2], stroke[3] and Alzheimer's disease[4] detection, and hemodynamic response visualization[2]. The main limitation for further development is the single slice acquisition or the whole brain projection currently utilized due to low concentration of HP ^{129}Xe in the human brain. In the present work, we performed multi-slice human brain imaging for the first time using 3D gradient echo imaging (GRE) with a Cartesian readout.

Methods: Two healthy female volunteer participants were scanned using a Philips Achieva 3T clinical MR scanner (^{1}H/^{129}Xe head coil (Clinical MR Solution LLC, WI, USA)). Enriched (83%)^{129}Xe was used for the study and was polarized up to 50% with a commercial polarizer (Xemed LLC, NH, USA) and dispensed into 1L Tedlar bags. Brain localization was done with high-resolution ^{1}H T_2-weighted (T_2W) fast spin echo anatomical scans with the following parameters: TR/TE=3000/80 ms, FOV = 250x250mm^2, acq. matrix = 256x256, FA = 90°, slice = 20mm, nr of slices =5, gap = 0mm.

HP ^{129}Xe 3D GRE MRI was performed after the 1L HP ^{129}Xe gas inhalation by the participants. The breathold period was 20s, the acquisition started on the 10th second. The imaging parameters for the axial orientation were: TR = 6.2ms, TE = 1.45ms, flip angle (FA) = 12.5°, BW = 150 Hz/pixel, FOV = 250x250mm^2, acquisition matrix = 32x32x5, the reconstruction matrix was the same, slice thickness = 20mm, number of slices =5. Anatomical ^{1}H images had the same orientation as the HP ^{129}Xe images. Custom-written MATLAB scripts (MATLAB R2016b, MathWorks, Inc, Natick, MA) were used for data reconstruction.

	Correlation coefficients				
	slice 1	slice 2	slice 3	slice 4	slice 5 (top)
Gray matter	0.6420	0.6238	0.6576	0.5630	0.0215
White matter	0.3535	0.4945	0.4575	0.5760	0.0346
Cerebrospinal fluid	0.5507	0.5070	0.4776	0.6025	0.6857

Table 1. Pearson's correlation coefficients for gray matter, white matter, and cerebrospinal fluid (CSF)

Results :*In vivo* axial multi-slice HP ^{129}Xe MR images of the human brain are shown in Figure 1E. Figure 1F shows HP ^{129}Xe images superimposed on top of ^{1}H anatomical T_2W images[5]. A high correlation was observed between the gray matter tissue distribution and the HP ^{129}Xe signal on the first four slices in the axial orientation (Figure 1B and F, Table 1). The correlation between the white matter distribution and the HP ^{129}Xe signal was smaller, most likely because of the greater perfusion of HP ^{129}Xe in the gray matter than in the white matter and different solubility values[5]. The correlation between the CSF and the ^{129}Xe distribution was higher on the top-most slices (Table 1). Overall, five slices of the human brain were imaged with a slice thickness of 20 mm and a voxel volume of 1.22 cm^3, which is the smallest voxel volume of HP ^{129}Xe human brain imaging currently achieved so far.

Conclusions: Multi-slice 3D MRI acquisition of the human brain with HP ^{129}Xe was achieved for the first time.

Acknowledgements: This research was funded by the Ontario Research Fund (ORF-RE-09-029), Northern Ontario Academic Medical Association (A-18-05), and Mitacs Elevate (IT25574).

References: [1] Rao M et al, *Radiology*. 2018; [2] Shepelytskyi Y *Diagnostics*. 2020; [3] Rao M *J Magn Reson Imaging*. 2019; [4] Hane F *Diagnostics*. 2018; [5] Grynko V et al, *Magn Reson Med*. 2021;

Tracking disease progression in Parkinson's Disease using striato-cortical gradients

Dimuthu Hemachandra[1 2], Roy Haast[1,3], Penny MacDonald[5*], Ali R. Khan[1 2 4*]

[1] School of Biomedical Engineering, University of Western Ontario, London, ON, N6A5C1, Canada [2]Robarts Research Institute, University of Western Ontario, London, ON, N6A5B7, Canada
[3]Aix-Marseille University, CNRS, CRMBM, UMR 7339, Marseille, France
[3]Department of Medical Biophysics, University of Western Ontario, London, ON, N6A5C1, Canada
[4]Brain and Mind Institute, University of Western Ontario, London, ON, N6A5B7, Canada

Introduction: It has been shown that pathogens called Lewy bodies propagate from the brain stem, through the cortex to the striatum, eventually causing dopamine depletion in Parkinson's Disease (PD)[1]. In parallel, cortical abnormalities have been associated with PD disease stage[2]. Together, these findings suggest that cortico-striatal connectivity could potentially highlight early symptoms of PD. Recent work has demonstrated the value of studying the brain's macroscopic functional hierarchy to unravel the brain's (dys)functioning. Here, we employ these same methodologies to analyze the structural and functional connectivity between the cortex and the striatum to track down brain abnormalities in PD subjects.

Methods: In order to achieve this goal, a longitudinal dataset of 40 PD patients was obtained from the Parkinson's Progression marker Initiative. These data consist of 3 Tesla T1-weighted, diffusion and resting-state functional MRI scans, acquired at two time points: 12 months and 24 months into the disease. Functional connectivity and structural connectivity matrices were obtained between striatal voxels and cortical regions of interest (ROIs, N=1000) after automatic segmentation of the T1w image using FreeSurfer. Diffusion embedding[3] was applied to reduce this high dimensional data to lower dimensional embeddings called 'gradients'. The three striatal gradients (G1-3) explaining most of the variance were then studied further and projected back to image space to visualise the gradient profiles and for comparison across time points. To perform voxel-wise statistical analysis, FSL's randomize with 5000 permutations was used.

Results: Gradients based on both structural and functional connectivity show significant changes ($p<0.05$ with randomize) between month 12 and 24, with most prominent changes observed for the structural gradients. Striatal voxels corresponding to higher changes in G1-3 were selected to observe their corresponding connectivity to known, large-scale brain networks[4]. Structural connectivity with the somato-motor and control networks showed changes between the two time points for all the gradients. We observed significant negative correlations of the structural connectivity (G3) and the UPDRS score based on those networks (e.g. limbic network with $r=-0.5$, $p=0.008$). Moreover, G3 based on functional connectivity showed significant differences between the two time points, specifically in the right putamen area.

Conclusions: Current work highlights the promise of the gradient-based method to identify connectivity changes with disease progression. This is supported by the negative correlation found between the structural connectivity and the UPRS scores. Moreover, the changes found in the right putamen confirm recent work that has shown a higher correlation to dopamine transportation measured using DAT-SPECT[5]. Somato-motor and control networks are corresponding to motor and cognitive (e.g., executive) functions of the brain and these detected abnormalities can be related to the motor and non-motor symptoms of PD.

References

1. Braak H, Tredici K Del, Rüb U, de Vos RAI, Jansen Steur ENH, Braak E. Staging of brain pathology related to sporadic Parkinson's disease. *Neurobiol Aging*. 2003;24(2):197-211.
2. Zarei M, Ibarretxe-Bilbao N, Compta Y, et al. Cortical thinning is associated with disease stages and dementia in Parkinson{\textquoteright}s disease. *J Neurol Neurosurg Psychiatry*. 2013;84(8):875-882.
3. Coifman RR, Lafon S. Diffusion maps. *Appl Comput Harmon Anal*. 2006;21(1):5-30.
4. Yeo BT, Krienen FM, Sepulcre J, Sabuncu MR, Lashkari D, Hollinshead M, Roffman JL, Smoller JW, Zöllei L, Polimeni JR, Fischl B, Liu H, Buckner RL. The organization of the human cerebral cortex estimated by intrinsic functional connectivity. J Neurophysiol. 2011 Sep;106(3):1125-65. Epub 2011 Jun 8. PMID: 21653723; PMCID: PMC3174820.
5. Oldehinkel M, Llera A, Faber M, et al. Mapping dopaminergic projections in the human brain with resting-state fMRI. *medRxiv*. 2021

The Impact of Western Diet Consumption upon Guinea Pig Placental Metabolism at Two Time Points in Pregnancy using [1-^{13}C]pyruvate MRI

Lindsay E. Morris[1], Lanette J. Friesen-Waldner[1], Trevor P. Wade[1], Lauren M. Smith[4], Mary-Ellen ET. Empey[1], Timothy RH. Regnault[2,3,5], Charles A. McKenzie[1,5]

[1]Medical Biophysics, [2]Physiology and Pharmacology, [3]Obstetrics and Gynaecology, Western University, London, ON, Canada, [4]Radiation Oncology, University of California Los Angeles Health, Los Angeles, California, USA, [5]Division of Maternal, Fetal and Newborn Health, Children's Health Research Institute, London, ON, Canada

Introduction: Maternal consumption of an unbalanced diet (e.g. Western Diet (WD): high saturated fat and refined sugar[1]) during pregnancy can negatively affect the fetoplacental environment during critical periods of development. Moreover, this suboptimal *in utero* environment alters the formation of tissues and organs, which can have long-lasting metabolic effects for an individual in later life. This project focuses on the placenta as its main function is nutrient transport. Observation of placental metabolism throughout fetal development will increase understanding of the physiology in a healthy state and the metabolic changes in a compromised state.

When a cell is under stress, it may utilize most of the pyruvate to generate lactate even in the presence of sufficient oxygen.[2] This effect is a hallmark of cellular metabolic dysfunction, where the cell switches from oxidative metabolism to glycolysis for energy metabolism. We hypothesize that we will observe aerobic glycolysis as an increase in lactate production in WD exposed placentae relative to Control Diet (CD) exposed placentae.

Methods: Twenty in-house-bred Dunkin-Hartley guinea pig sows were weaned onto either a WD (n=10) or a CD (n=10). The pregnant sows were randomly allocated to imaging at two different gestational ages: mid-gestation (33 ± 0.6 days, WD: n=5, CD: n=5) or late-gestation (60 ± 0.8 days, WD: n=5, CD: n=5). Mid- and late-gestation timepoints enable the observation of different placental metabolism as it changes during pregnancy. Each sow underwent HP ^{13}C MRI to generate images of [1-^{13}C]pyruvate and its downstream metabolic products using previously described methods [3–5]. T1-weighted anatomical images were manually segmented in 3D Slicer to obtain volumes for each fetus and placenta. The mean signal intensities of [1-^{13}C]pyruvate and its metabolites were measured in the placental volumes as a function of time. The metabolic conversion rates from pyruvate to each of lactate (LAC), alanine (ALA) and bicarbonate (BIC) were estimated using the area under the curve (AUC) method.[6] The fetal and placental data were compared between diets using a linear mixed model (LMM) controlled by the individual sow and including gestational age as a covariate.

Results: At mid-gestation, there were no significant differences ($p>0.05$) between the WD and CD groups for fetal and placental volumes and AUC ratios. At late-gestation, there was no significant difference between the diets in fetal volumes; however, the WD placental volumes were significantly higher ($p<0.02$). The mean AUC ratios for LAC and BIC were 39% and 50% higher respectively ($p<0.01$ and $p<0.002$, respectively) in the WD group. The AUC ratio for ALA was not significantly ($p>0.05$) different between diets.

The AUC ratios are proportional to the metabolic conversion rates and an indirect measurement of the enzyme concentrations.[7] The increased AUC ratios for LAC and BIC at late-gestation suggest increased enzyme activity for lactate dehydrogenase and pyruvate dehydrogenase, respectively, indicating altered pyruvate metabolism in WD-exposed placentae.

Conclusions: This study of guinea pigs investigated how life-long maternal WD consumption affects placental metabolism and fetal volume at two gestational ages. We conclude that the WD was associated with increased lactate and bicarbonate production in late gestation. We observed indications of dysfunctional metabolism in WD-exposed placentae, aligning with our hypothesis that pyruvate metabolism may switch to aerobic glycolysis.

[1] Cordain, et al., *Am. J. Clin. Nutr*. 2005, [2] Heiden, et al., *Science*. 2009, [3]. Smith, et al., *Magn. Reson. Med*. 2020, [4] Friesen-Waldner, et al., *J. Magn. Reson. Imaging*. 2016, [5] Wiens, et al., *Magn. Reson. Med*. 2015, [6] Larson, et al., *NMR Biomed*. 2018, [7] Daniels, et al., *NMR Biomed*. 2016.

Pitch Session 9:

Imaging for Musculoskeletal Analysis

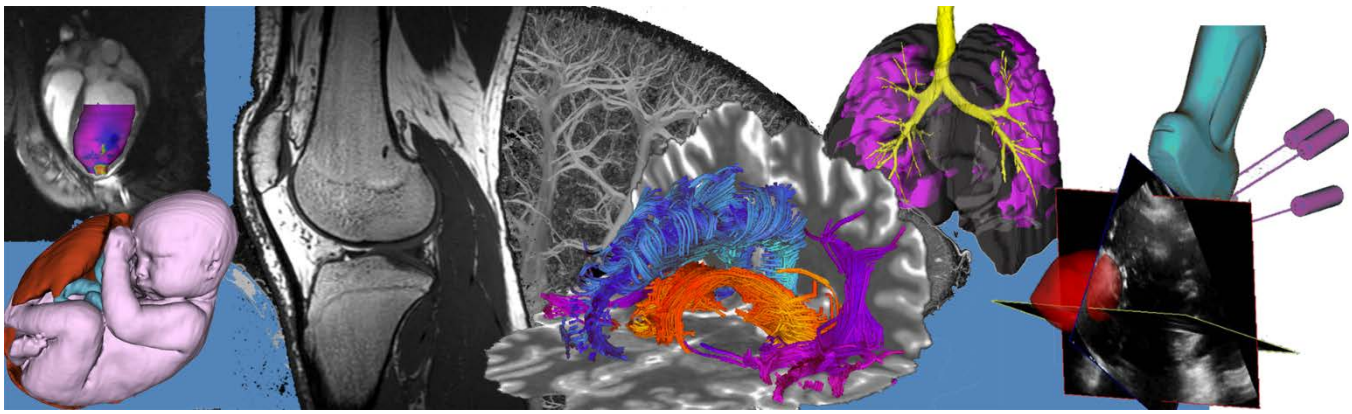

The Exploration of the Relationship between Kinematic Joint Contact and Subchondral Volumetric Bone Mineral Density in People With and Without Wrist Trauma

Lauren N. Straatman[1,2,3,6], Nikolas Knowles[4], Nina Suh[3], David M. Walton [2,5], Emily A. Lalone[2,3,6]
[1]Department of Health and Rehabilitation Science, Western University, [2]Bone and Joint Institute, Western University, [3]Hand and Upper Limb Center, St. Joseph's Hospital, [4]Cumming School of Medicine, University of Calgary, [5]Department of Physical Therapy, Western University, [6]Department of Mechanical and Materials Engineering, Western University
lstraatm@uwo.ca

INTRODUCTION: Pain and disability following wrist trauma are highly prevalent, however the mechanisms underlying them are highly unknown. Repetitive joint loading leads to adaptive changes to the underlying bone that enable it to cope with these loads (Wolff's law). Wrist trauma often results in altered joint loading (joint contact) within the joint, otherwise considered malalignment. As some degree of malalignment within a joint can be tolerated, in isolation anatomical malalignment is not indicative of poor prognosis. Recently, studies have been turning to the subchondral bone as a potential mechanism underlying pain due to its vascularity, using a depth-specific imaging technique, quantitative CT (QCT). We've demonstrated the utility of QCT in measuring depth-specific changes in the subchondral bone of the distal radius when compared to static, neutral joint contact of the radiocarpal joint. However, analyzing a static joint in a neutral position is not necessarily related to changes in volumetric bone mineral density (vBMD). Therefore, the purpose of this study is to explore the relationship between subchondral vBMD and kinematic joint contact using the same imaging technique, in a cohort of healthy adults.

METHODS: To demonstrate the relationship between kinematic joint contact and subchondral vBMD, we analyzed the wrists of n = 5 healthy participants. Participants underwent 4DCT scans while performing maximum flexion to maximum extension to estimate radiocarpal (specifically the radiolunate (RL) and radioscaphoid (RS)) joint contact area (JCa) between the articulating surfaces. The participants also underwent a static CT scan accompanied by a calibration phantom with known material densities that was used to estimate subchondral vBMD of the distal radius. Joint contact is measured by calculating inter-bone distances (mm^2) using a previously validated algorithm. Subchondral vBMD is presented using mean vBMD (mg/K_2HPO_4) at three normalized depths from the subchondral surface (0 to 2.5, 2.5 to 5 and 5 to 7.5 mm) of the distal radius. Pearson's correlation coefficients will be used to demonstrate the strength of the relationship between vBMD and JCa for all layers and both the RL and RS articular surfaces.

RESULTS: Our results demonstrated a strong, positive relationship between JCa and subchondral vBMD during extension in the RS joint in the middle (2.5 to 5mm) and deep (5 to 7.5mm) layers of vBMD, $r = 0.89$, $p = 0.04$, and $r = 0.91$, $p = 0.04$, respectively. This indicates that in the RS joint during extension specifically, as JCa increased, vBMD also increased. The relationship between JCa and vBMD in the RL during flexion and extension, as well as the RS during flexion, was not significantly correlated.

CONCLUSION: Within our study sample, subchondral vBMD is most impacted in the RS joint during extension. Historically, anatomical malalignment does not indicate poor prognosis. Therefore, when coupled with changes to depth-specific layers of subchondral bone, the relationship between altered joint contact or joint loading and vBMD may demonstrate a more robust explanation for lasting pain and disability following wrist trauma. These results will be used as comparative, normative data for future analysis on clinical populations that are studied longitudinally, to better understand when these changes are occurring.

Optical imaging for rheumatoid arthritis disease activity monitoring: an *in silico* and disease-mimicking phantom study

Seva Ioussoufovitch[a] and Mamadou Diop[a,b,c]

[a]*Western University, Faculty of Engineering, School of Biomedical Engineering, Collaborative Training Program in Musculoskeletal Health Research, Bone & Joint Institute, London, Canada*

[b]*Western University, Schulich School of Medicine & Dentistry, Medical Biophysics, London, Canada*

[c]*Lawson Health Research Institute, Imaging Program, London, Canada*

Introduction: Rheumatoid arthritis (RA) affects about 1% of the population and is one of the most common types of inflammatory arthritis. While this disease can lead to significant reductions in patient quality of life, early treatment within 3 to 6 months of disease onset substantially improves patient prognosis. Yet, even if a diagnosis can be quickly established, treatment failure—which is typically identified after a 3 – 6 month delay—still occurs in 30% of RA patients[1] and puts them at risk of irreversible joint damage. Near-infrared diffuse optical imaging (DOI) is an objective and non-invasive approach that can differentiate between healthy and inflamed joints;[2] however, little investigation has been done into using DOI to track gradual changes in disease activity. Thus, the objective of this study was to investigate whether parameters extracted from time-resolved (TR) DOI data of virtual disease models and disease-mimicking phantoms can distinguish between a gradient of rheumatic disease states.

Methods: Simulations were conducted using a realistic tissue geometry derived from a segmented MRI image of a healthy human finger and 4 sets of tissue optical properties corresponding to different states of RA disease activity (None, Light, Moderate, Severe).[3] Monte Carlo simulations of TR light propagation through the 4 virtual disease models' proximal interphalangeal joints were conducted using MCXLAB at 800 nm.[4] Further, four semi-cylindrical solid phantoms containing central rectangular inclusions, to simulate a joint cavity, were fabricated. Phantoms were made using a transparent silicone rubber (PlatSil® SiliGlass) mixed with various amounts of black silicone pigment and glass microspheres. Optical properties of the bulk phantom and inclusions were tuned to match the properties of the subcutaneous tissue and synovial fluid, respectively, used in the four virtual disease models. Phantom measurements were acquired with an in-house TR-DOI system and each phantom was imaged 5 times. Datasets obtained from both simulations and the phantoms were processed using statistical moments, temporal binning, and temporal Fourier decomposition to extract a series of parameter images, which underwent spatial Fourier decomposition. Based on previous work where changes in image spatial frequency were correlated with changes in RA disease activity[2], spatial Fourier components of parameter images were then ranked based on their ability to accurately identify which models had worse disease activity in a series of two-model comparisons.

Results: On average, DC and 0.06 mm^{-1} spatial frequency components correctly identified worse disease activity with the highest accuracy (Fig. 1). Images of the sum of photons (0^{th} statistical moment) parameter performed the most consistently across spatial frequencies, while the phase at 0.06 mm^{-1} performed most consistently across all parameters.

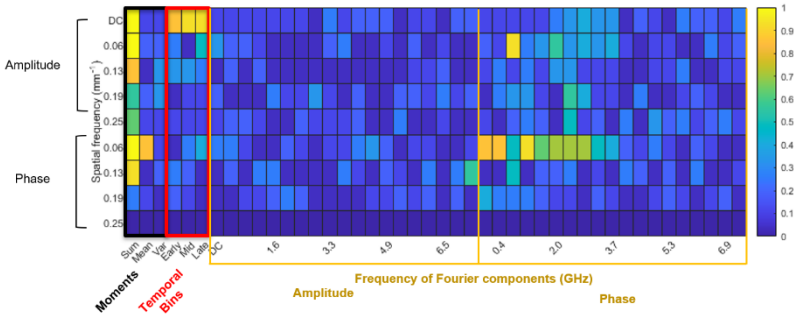

Fig. 1: Normalized accuracy of spatial components of various parameters images at identifying increased disease activity.

Conclusions: Differences in spatial frequency content at 0.06 mm^{-1} were most often linked with correct identification of disease activity. This frequency corresponds to a spatial disturbance of ~16.7 mm which is approximately twice the size of the joint used in both simulations and phantoms (8 mm). Many components displaying high (>90%) identification accuracy were derived from one parameter image or at one spatial frequency; suggesting that they could be combined in the future into a single disease index to improve robustness. Future work will focus on using our non-invasive TR-DOI system to acquire data from healthy volunteers and patients with rheumatoid arthritis, and determine whether the parameters highlighted in this work will show sensitivity to *in vivo* disease activity.

References:

[1] Moreland, L. W., et al. *Arthritis and Rheumatology* **64**(9), 2824–2835 (2012).
[2] Lighter, D., et al. *Journal of Biomedical Optics* **24**(06), 1 (2019).
[3] Ioussoufovitch, S., et al. Proc. SPIE 11639, 116390J (2021).
[4] Fang, Q., et al. *Optics Express* **17**(22), 20178 (2009).

Provocative Scapholunate Instability Wrist Positioning

Elizabeth Norman[1,2], Nina Suh [2,3], Emily Lalone[1,2]
[1]School of Biomedical Engineering, Western University, [2]Roth McFarlane Hand and Upper Limb Centre [3]Schulich School of Medicine and Dentistry

Disclosures: No disclosure

INTRODUCTION: Scapholunate (SL) instability is the most frequent type of carpal instability [1] and is common in young working age males. Injuries to the SL ligament result in a widening of the space between scaphoid and lunate (diastasis) that is measured clinically using radiographs. Early SL tears are often missed and leads to the development of SLAC (scapholunate advanced collapse), a leading cause of wrist arthritis [2]. Stress x-rays can be used to image the joint in a provocative position or under load. However, stress x-rays are still 2D projection images and the full 3D consequence of the increased gap on 3D mechanics of the joint is unknown. Having a comprehensive understanding of how the 3D gapping effects joint mechanics and further development of SLAC arthritis would assist identification of pathomechanics of SLAC. The objective of this study is to employ stressCT to image patients who have suffered an SL ligament tear to examine pathomechanics.

METHODS: In this parametric study, three SL patients were recruited through our tertiary hand and upper limb clinic with approval from our institutional ethics board and underwent stressCT (four-dimensional computed tomography (4DCT)) scanning at our facility. Through the motion of radial/ ulnar deviation we obtained CT images of the wrist in extreme radial, extreme ulnar and kinematic neutral positions. In addition, static scans were taken with the wrist neutral position and neutral clenched fist position. 3D models of the scaphoid, lunate, capitate, and radius were created using 3D Slicer. Next, contact maps were created from these models, this allows identification of regions of contact or close contact between the scaphoid and lunate (scapholunate gap) and the capitate and radius (radiocapitate gap). This application identifies the minimum distance within the gap.

RESULTS SECTION: Preliminary results have been analyzed and show interesting findings. First, when examining the minimum distance between the scaphoid and lunate the distances vary with wrist position indicating that this injury is dynamic and for proper injury detection alignment is very important. In addition, the minimum distance between the radius and capitate decreases when n a clenched fist position when compared to the neutral positions.

DISCUSSION: These preliminary results show how the minimum distance is affected based on positioning of the wrist and how this could ultimately be detrimental to the patient as the distance may fall below the mark of minimum distance for detection of an injury (deemed as a 3mm distance between the scaphoid and lunate and is detected using plain radiographs). As stated above, SL instabilities are sometimes diagnosed as false negatives and as a result, identification of the ideal positioning to increase the gap would allow for a decrease in false negative results. Ensuring proper diagnosis is important to ensure that the patient receives appropriate intervention to avoid the advancement to SLAC arthritis. In addition, the results show that the capitate becomes closer to the radius when in the clenched fist position as compared to neutral, this indicates that as the wrist is clenched the capitate becomes closer to the scaphoid and lunate and ultimately could shift these bones outside of their normal location. This results in degradation of the surrounding bones and could lead to SLAC arthritis. Future work will include imaging individuals pre injury detection to determine if this pipeline can detect injury pre static instability and examine a healthy population to examine the pathomechanics.

REFERENCES:

[1] Sikora S, Tham S, Harvey J, et al. The Twist X-Ray: A Novel Test for Dynamic Scapholunate Instability. *J Wrist Surg*. 2019. doi:10.1055/s-0038-1673344
[2] Kuo CE, Wolfe SW. Scapholunate Instability: Current Concepts in Diagnosis and Management. *J Hand Surg Am*. 2008. doi:10.1016/j.jhsa.2008.04.027
[3] Capo JT, Accousti K, Jacob G, Tan V. The effect of rotational malalignment on X-rays of the wrist. *J Hand Surg Eur Vol*. 2009. doi:10.1177/1753193408090393

ACKNOWLEDGEMENTS: Department/School of Biomedical Engineering University of Western Ontario, Faculty of Engineering, Collaborative Specialization in Musculoskeletal Health Research, and Bone and Joint Institute, Western University, Canada

A deep learning algorithm for automatic cartilage segmentation in knee 3D ultrasound images

Nathan Orlando[1,3] and Carla Du Toit[2,3], Sam Papernick[1,3], Robert Dima[2,3], Igor Gyacskov[3], Aaron Fenster[1,3]
[1]Department of Medical Biophysics, [2]Faculty of Health Sciences and Bone and Joint Institute, [3]Robarts Research Institute, Western University, London, Ontario, Canada

Introduction: Cartilage degradation is one of the defining characteristics of knee osteoarthritis (KOA). Quantitative measurement and characterization of cartilage thickness is important for disease monitoring and treatment, with average cartilage loss of 0.2 mm every three months in KOA patients. In recent studies, 3D ultrasound (US) has been shown to be a potential point of care system for monitoring KOA; however, variability and time efficiency are two challenges faced when using 3D US for manual segmentation of the femoral articular cartilage (FAC). The purpose of our study was to develop a deep learning-based approach to automatically segment the FAC in 3D US images of the knee to increase time efficiency and decrease rater variability.

Methods: Our method involved deep learning predictions on 2D US slices sampled in the transverse plane to view the cartilage of the femoral trochlea, followed by reconstruction into a 3D surface. A 2D U-Net was modified and trained using a dataset of 200 2D US images resliced from 20 3D US images of the knee in healthy participants, with ground truth manual segmentations completed by rater 1. Segmentation accuracy was evaluated using a holdout dataset of 50 2D US images resliced from 5 3D US images, with manual segmentations completed by rater 1 and a second rater. Absolute and signed error metrics were computed, including Dice similarity coefficient (DSC), volume percent difference (VPD), mean surface distance (MSD), and Hausdorff distance (HD). FAC segmentation performance was compared between rater 1 and 2 manual segmentations.

Results: Our U-Net-based algorithm performed with mean 3D DSC, VPD, MSD, and HD of 73.1± 3.9%, 10.4 ± 6.0%, 0.3 ± 0.1mm, and 1.6 ± 0.7mm compared to rater 1 manual segmentations, and 72.3 ± 2.8%, 14.2 ± 11.0%, 0.3 ± 0.2mm, and 2.7 ± 2.9mm compared to rater 2 manual segmentations, respectively. Paired sample t-tests showed no statistically significant difference. The percent difference between the manually segmented volumes of the 2 raters was 3.4%, aligning with differences in VPD shown above. Compared to the individual 2D predictions, our algorithm demonstrated a decrease in performance after 3D reconstruction due to a portion of the cartilage being cut off as shown in Fig. 2, but these differences were found to be not statistically significant.

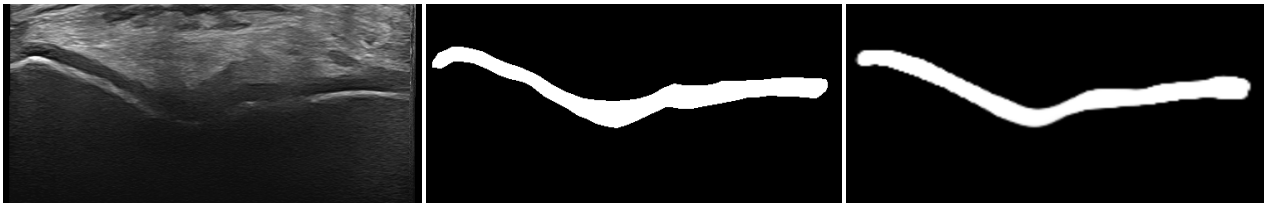

Fig 1: Example 2D cartilage segmentation resliced from a knee 3D US image of a healthy participant. The original 2D US image, manual segmentation, and algorithm output are shown from left to right.

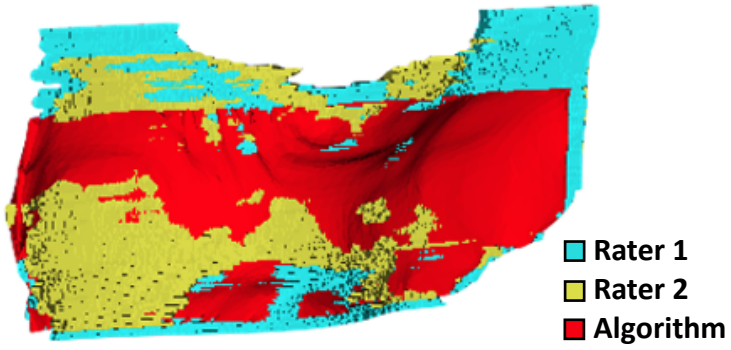

Fig 2: Example 3D FAC segmentation results comparing manual segmentations from rater 1 (teal) and rater 2 (yellow) to the reconstructed 3D surface generated by our algorithm (red). Our 3D reconstruction method produced a rectangular surface, preventing coverage of the whole condyle. Future work includes development of an improved reconstruction method to overcome this limitation.

Conclusions: We present a modified U-Net algorithm to automatically segment the FAC in 3D US knee images of healthy volunteers. DSC and MSD metrics were similar whether comparing to rater 1, who provided ground truth segmentations for the training dataset, and rater 2, whose segmentations were not seen by the network during training, demonstrating our methods robustness to rater. Future work will look to increase dataset size to improve performance, specifically utilizing knee images from patients with KOA to assess the clinical utility of our method. This method has the potential to increase the efficiency of cartilage volume estimation, allowing for efficient longitudinal monitoring of KOA.

A comparative study of bone plug movement in rectangular versus cylindrical bone tunnel using bone-patellar tendon-bone grafts.

Michele Matsubara[1], David W. Holdsworth[2], Alan Getgood[3], Timothy Burkhart[1],
[1]Kinesiology and Physical Education, University of Toronto; [2]Robarts Research Institute, Western University;
[3]Fowler Kennedy Sports Medicine Clinic, Western University

Introduction

Anterior cruciate ligament reconstruction (ACLR) using a bone-patellar tendon-bone (BPTB) graft is a common treatment for ACL ruptures. Complications associated with the BPTB graft include poor post-operative bone-block integration and residual post-ACLR laxity; partially owing to excessive motion between the bone-block and tunnel. To mitigate these issues, Shino et al. (2005) proposed a rectangular bone-block and tunnel BPTB reconstruction technique as an alternative to the traditional cylindrical technique. While this technique has shown good clinical outcomes, bone-block micromotion within the tunnels, which could have implications on post-operative bone-block integration and graft failure, has not been investigated. The purpose of this in vitro cadaveric study is to use 3D computed tomography (CT) scans to compare bone-block movement within the femoral tunnels between rectangular and cylindrical bone tunnels when using a BPTB graft. It is hypothesized that while some micromotion will be present in both groups, there will be less motion attributed to the rectangular bone-block group compared to the cylindrical.

Methods

16 fresh-frozen, cadaveric knee specimens were subjected to various loading conditions (internal rotation, anterior translation and combined loading [internal rotation, valgus rotation and anterior translation]) at 0°, 30°, 60°, and 90° of knee flexion, applied by a CT compatible knee joint simulator. The ACL was sectioned and the specimens were randomly assigned to either a rectangular or cylindrical bone-block and tunnel group for the ACL reconstruction. For each knee angle-load combination, a baseline scan was taken in an unloaded-state, and a subsequent scan in the loaded-state. The images were imported into 3D Slicer (version 4.11.20210226) where initial registration between the unloaded and loaded-state scans was performed using the femoral diaphysis as the reference. Segmentations (i.e. solid geometries) of the bone-blocks were then created, and an "Oriented Bounding Box" (OBB), a 3D box that is sized and rotated to best fit the segmentation, was created for the unloaded-state bone-block. A by-product of creating an OBB is a transform that can be inverted and applied to the bone-blocks, to re-center and reorient them at the origin of the GCS. After re-aligning the bone-blocks within the GCS, the bone-blocks were registered, and the three translations and three rotations were obtained.

Results

The study is currently at the stage of verifying the reliability of its methods. We present the data of four specimens from the rectangular bone-block group, loaded in the 0˚-anterior translation condition. The data suggests that the largest translations occurred axially within the bone tunnel with a mean (SD) translation of 0.27 (0.12) mm in the direction of the applied load from the patella tendon acting on the bone block. This appears to be consistent across specimens. The largest mean [SD] rotation occurred about the x-axis (0.48 [0.58] °); the magnitudes of rotations were less consistent across specimens.

Table 1: Translational and rotational motions of the three rectangular bone-blocks relative to the non-loaded position.

Specimen	Translation			Rotation		
	x	y	z	x	y	z
1	-0.20	0.36	-0.40	-1.31	0.50	1.25
2	0.02	0.02	-0.24	-0.26	0.94	0.16
3	-0.03	0.06	-0.31	-0.48	-0.46	-0.70
4	0.04	0.06	-0.11	-2.77	-0.58	1.51
Mean (SD)	-0.04 0.11	0.13 0.16	-0.27 0.12	-1.21 1.13	0.10 0.74	0.55 1.02

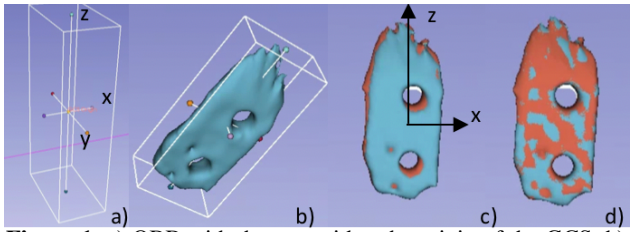

Figure 1: a) OBB with the centroid at the origin of the GCS; b) OBB encompassing the non-loaded state bone-block after transformation; c) re-oriented and re-entered bone-block segmentations (non-loaded state in blue, loaded state in orange); d) bone-block segmentations after model registration.

Discussion

As previously mentioned, bone-block micromotion has potential implications on post-operative bone-block integration and graft failure. Comparison of bone-block movements between the rectangular and cylindrical bone-block and tunnel could further the research of the potential benefits or demerits when using rectangular bone-blocks and tunnels for ACLR using a BPTB graft.

A convolutional neural network for detection of corrosion on retrieved hip arthroplasty systems

Anastasia M. Codirenzi[1], Brent A. Lanting[1], Matthew G. Teeter[1],
[1]Western University, London, Canada
acodiren@uwo.ca

INTRODUCTION: Corrosion at the modular head-neck junction of total hip arthroplasty implants (trunnionosis) has become recognized as a cause of early implant failure requiring revision. Visual evaluation of femoral stem taper junctions in implant retrieval studies has resulted in a greater understanding of the factors that cause trunnionosis. Unfortunately, the study of retrieved implants through damage scoring is time consuming and labor-intensive, requiring multiple expert scorers to ensure measurement repeatability and potential logistical hurdles from shipping implants. We propose an automated scoring approach to evaluate the presence of corrosion on retrieved implant trunnions using high-quality images assessed by a convolutional neural network with a test accuracy of 85%.

METHODS: Femoral stems with an intact trunnion (n = 467) were selected across multiple implant designs from our implant retrieval laboratory. Images of each stem trunnion were acquired using a standardized imaging protocol for optical microscopy (Olympus DSX1000 digital microscope) with the stems positioned for imaging of the anterior, posterior, medial, and lateral anatomical aspects of the trunnion. Images were assessed by a trained observer and assigned a corrosion score using the common Goldberg scale. Images in the anterior and posterior positions (n = 934) were deemed to have a more uniform appearance than images in the medial and lateral positions and were therefore selected for the initial trial of the classifier. Images from the posterior and anterior that were judged to be of insufficient quality (e.g., due to improper focus or presence of glare) were excluded (n = 9). Two classes were created for the classifier: corrosion and no corrosion. The no corrosion class (n = 348 images) was comprised of implants with a Goldberg corrosion score of 1 (no visible corrosion present) and the corrosion class (n = 116 images) was comprised of implants with a Goldberg corrosion score of 3 or 4 (discoloration of >30% of the surface or any sized region with black debris, pits, or etch marks). Class 2 (discoloration of <30% of the surface) was excluded as this class has the greatest variation in appearance due to its definition of up to 30% discolouration. The images were separated into groups for classifier training, validation, and testing: 75% (n = 397) for training, 10% (n = 53) for validation, and 15% (n = 79) for testing. Care was taken to ensure equal amounts of each class were included in the validation and testing sets, which required the training set corrosion class to be augmented to be balanced to the no corrosion class. The validation set was used during training while the test set was held-out until after training to evaluate the final network. No image preprocessing steps were performed. A multilayer perception was trained from scratch using an ADAM optimizer and consisting of an input layer, a hidden layer, and a classification layer. The hidden layer consisted of a single convolution with 32 filters, batch normalization, a rectified linear unit function, and max pooling, and the classification layer comprised of a flatten layer, fully connected layer and SoftMax.

RESULTS: The validation accuracy of the corrosion classifier was 77.36% and the testing accuracy was 87.34%. The area under the curve, AUC, was 0.81, indicating that is excellent at discriminating between the two classes. Within the test set, 2.53% (n = 2) of testing images were a false positive (classified as having corrosion when corrosion was not present) and 10.13% (n = 8) of test images were a false negative (classified as lacking corrosion when corrosion was present). Of the 10 images misclassified, all but one could be explained by the presence of irregular geometry, prominent machining lines, presence of gouging during implant removal, or corrosion patterns near the base of the trunnion.

CONCLUSIONS: The corrosion classifier was found to demonstrate excellent accuracy in discriminating the presence of moderate to severe corrosion from the lack of corrosion and the test accuracy was achieved. The validation accuracy was lower than the testing accuracy, but within 10%, which may speak to the test set being of higher quality than the validation set (more image uniformity, distinct corrosion). The misclassified images show that the classifier is sensitive to the presence of prominent machining lines when gouging from implant extraction is also present and is less accurate for images of geometries that were less represented in the training set. The benefits of this classifier include accuracy across multiple implant designs, simplified image acquisition, and no need for image preprocessing. Limitations with this preliminary classifier were the inclusion of only the anterior and posterior aspects of the trunnion and the exclusion of Goldberg class 2 damage. Ongoing work includes the incorporation of additional implants, all perspectives of the implant trunnion, and of Goldberg class 2.

[18F]FEPPA Autoradiography as a Measure of Macrophage Content in Knee Synovial Tissue

Zachary J. Koudys,[1-3] Garth Blackler,[1] Holly Philpott,[1] Matthew Fox,[3] Brent A. Lanting,[1] C. Thomas Appleton,[1] Matthew G. Teeter,[1-3] Jonathan D. Thiessen[1,3]

[1]Schulich School of Medicine & Dentistry, Western University, London, Canada;
[2]Robarts Research Institute, London Canada;
[3]Lawson Health Research Institute, London, Canada;

INTRODUCTION: The progression of osteoarthritis (OA) involves an inflammatory component marked by symptoms of joint pain, swelling, and stiffness. Resident macrophages in the synovial lining play a critical role in maintaining synovial homeostasis and inflammation. Non-invasive positron emission tomography (PET) provides sensitive imaging of biological processes. Through the high expression of the translocator protein (TSPO) on activated macrophages, TSPO-PET has been widely reported as an effective method to image macrophages in vivo. [18F]FEPPA is a novel PET radiotracer for targeting TSPO and has been shown to have higher affinity for TSPO and less off target binding than previous generations of TSPO-PET ligands. This study aimed to investigate the relationship between in vitro [18F]FEPPA tracer uptake and the activated macrophage content of knee synovial tissue of patients with osteoarthritis. We hypothesize that signal gathered from inflamed knee synovial tissue incubated in [18F]FEPPA will correlate to immunofluorescence staining for TSPO.

METHODS: Knee synovial tissue of 4 patients with late-stage osteoarthritis were sectioned to 5μm using a cryostat. The tissue sections were fixed, and paraffin embedded on cold resistant glass slides. Slides were Hematoxylin and Eosin, TSPO, and CD68 stained and imaged with a confocal microscope. Tissue samples were graded on a histopathological scale for 6 standard inflammatory markers by a rheumatologist. Knee synovial tissue was taken from the same 4 patients but from different synovial regions. The knee synovial tissue was sectioned, fixed, and embedded in the same way and incubated in [18F]FEPPA aliquots for 1 hour. After incubation the tissue slides were thoroughly washed in buffer and then distilled water. The samples were then imaged using a digital autoradiograph with a scan duration of 3 hours. The TSPO immunofluorescence data was segmented using the synovial intima as the region of interest (ROI) and autoradiography images were segmented with the entire tissue section as the ROI. The mean signal intensity over the ROI was calculated for both immunofluorescence and autoradiography. Mean signal intensity from autoradiography and TSPO staining were compared statistically to calculate the t, p, and R^2 values. H&E staining was analyzed qualitatively by a rheumatologist to look at relative cell infiltration into the intima.

RESULTS: [18F]FEPPA tracer uptake calculated from autoradiography was significantly correlated to the signal from TSPO immunofluorescence with $p=0.002642$ and $R^2=0.8$. The TSPO and CD68 staining showed high co-localization when the images were overlayed.

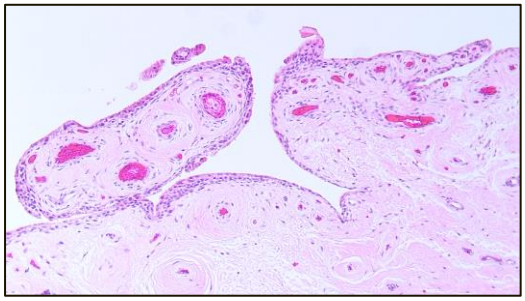

FIGURE 1. Histopathology image of knee synovial tissue sections. Tissue was formalin fixed, paraffin embedded, sectioned to 5 μm, stained with hematoxylin and eosin and imaged under a confocal microscope.

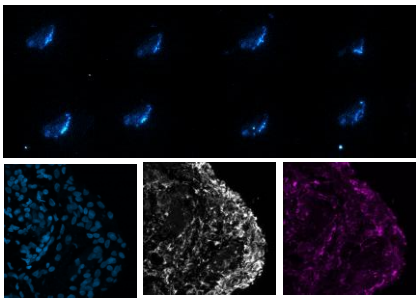

FIGURE 2. Knee synovial tissue samples were identically prepared and imaged with autoradiography (top) and immunofluorescence staining for nuclei (left), TSPO (center), and CD68 (right).

CONCLUSIONS: [18F]FEPPA uptake corresponds to the presence of macrophages in the intima of knee synovial tissue taken from patients with end-stage OA. This result suggests that [18F]FEPPA PET may be an effective tool for evaluating the role of synovial inflammation in the progression of OA. Future clinical work will examine how chronic knee synovial inflammation relates to pain and stiffness in late-stage knee OA.

Pitch Session 10: Neuro Imaging II

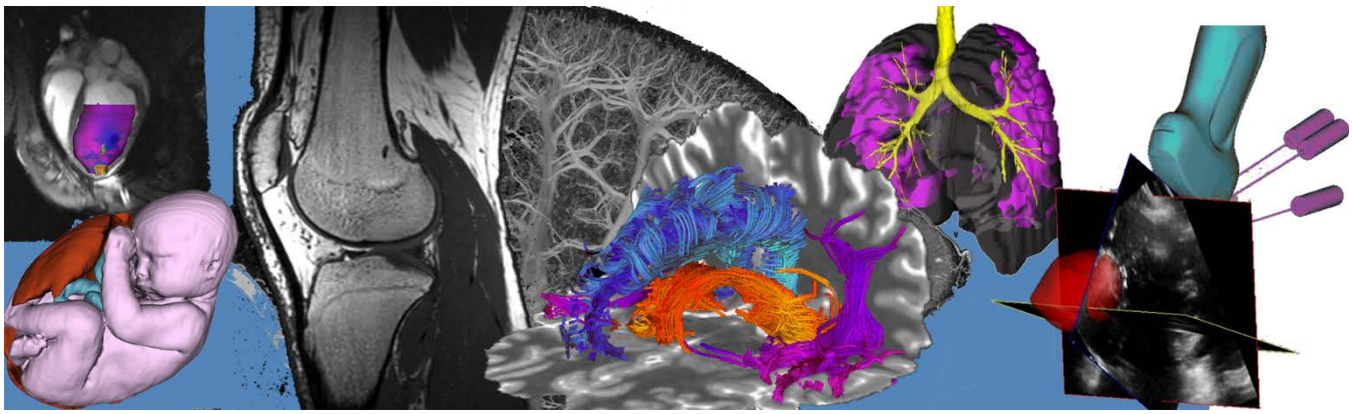

Neuroimaging VMAT2 in Parkinson's Disease with Rapid Eye Movement Sleep Behaviour Disorder

Mikaeel Valli [1, 2], Sang Soo Cho [3], Carme Uribe [1], Mario Masellis [4], Robert Chen [5], Alexander Mihaescu[1,2], & Antonio P. Strafella [1, 2, 5]

1. Brain Health Imaging Centre, Campbell Family Mental Health Research Institute, Centre for Addiction and Mental Health, University of Toronto, Ontario, Canada.
2. Institute of Medical Science, University of Toronto, Ontario, Canada.
3. Department of Brain and Cognitive Science, Seoul National University, South Korea
4. Hurvitz Brain Sciences Program, Sunnybrook Health Sciences Centre, Toronto, Ontario, Canada
5. Morton and Gloria Shulman Movement Disorder Unit & E.J. Safra Parkinson Disease Program, Neurology Division, Dept. of Medicine, Toronto Western Hospital, UHN, University of Toronto, Ontario, Canada.

Disclosures: All authors declare none.

Introduction:
Rapid Eye Movement (REM) Sleep Behaviour Disorder (RBD) is a condition marked by the lack of normal skeletal muscle atonia during REM sleep, resulting in dream enacting behaviours. RBD is one of the strong prodromal clinical predictors of PD. Molecular imaging evidence shows that PD with RBD (PD-RBD+) show lower dopamine transporter activity within the caudate and putamen compared to PD without RBD (PD-RBD–). However, the characterization of the vesicular monoamine transporter 2 (VMAT2), an index of nigrostriatal dopamine innervation, has been rarely explored in PD patients with RBD.

Methods:
We enrolled 15 PD-RBD+, 15 PD-RBD– and 15 age matched healthy controls (HC) for the [^{11}C]DTBZ PET imaging study.[1] This technique measures VMAT2 availability within striatal regions of interest (ROI). The radioligand binding potential was calculated in each ROI using the simplified reference tissue model with occipital lobe as a reference region. A mixed effect model was used to compare the radioligand binding of VMAT2 between the three groups for each striatal ROI, while co-varying for sex, cognitive and depression scores. The fixed factors in this model were group and ROI hemisphere (i.e., left vs. right ROI), while participants were kept as a random factor. Significant level was set at $p<0.05$ (Bonferroni corrected). Multiple regressions were also computed to predict clinical measures from group condition and VMAT2 binding within all ROIs explored.

Results:
Significant main effect was observed within the caudate, putamen, ventral striatum, external globus pallidus, internal globus pallidus, and substantia nigra. Specifically, we observed that both PD-RBD+ and PD-RBD– group generally had lower VMAT2 availability compared to HC in all these regions. Only PD-RBD– patients showed a negative relationship between motor severity and VMAT2 availability within the left caudate.

Conclusions:
Our findings reveal that both PD patient subgroups had similar denervation within the nigrostriatal pathway. This study was unable to detect interactions between clinical scores and radioligand binding in PD-RBD+ patients. Taken together, VMAT2 and striatal dopamine denervation in general may not be a significant contributor to the underlying mechanisms driving RBD in PD patients. Future studies are encouraged to examine other possible pathophysiological mechanisms that are at stronger play contributing to RBD in PD patients.

References:
[1.] Valli, M., Cho, S.S., Uribe, C. et al. VMAT2 availability in Parkinson's disease with probable REM sleep behaviour disorder. Mol Brain 14, 165 (2021). https://doi.org/10.1186/s13041-021-00875-7

Quantifying lasting regional microstructural and functional abnormalities in aging retired professional football players

Ethan Danielli,[1,2] Nicholas Simard,[2,3] Mitchell Doughty,[1,2] Michael D. Noseworthy[1,2,3,4]

1. School of Biomedical Engineering, McMaster University, Hamilton, ON, Canada;
2. Imaging Research Centre, St. Joseph's Healthcare Hamilton, Hamilton, ON, Canada;
3. Department of Electrical and Computer Engineering, McMaster University, Hamilton, ON, Canada;
4. Department of Radiology, McMaster University, Hamilton, ON, Canada

Introduction: Concussions and sub-concussive impacts can cause lasting diffuse axonal injuries **[1]** and decreased functional activation, leading to dementia **[2]**. The purpose of this study was to identify and quantify the severity of abnormal structural and functional brain regions in a retired athlete sample. It was hypothesized that longer fibre tracts, more susceptible to tearing, and cortical regions would be more seriously damaged.
Methods: Retired Canadian Football League (rCFL) players (n=17, 100% male, aged 58.3±6.2) were scanned using a 3T MRI system and 32-channel head and neck coil. High-resolution T1-weighted, 60-direction diffusion tensor imaging (DTI), and resting state functional MRI (rsfMRI) scans were acquired for each subject. Age and sex matched control data (n=88) was downloaded from the Alzheimer's Disease Neuroimaging Initiative (ADNI)**[3]**. MRI data was processed using TBIFinder software to produce personalized regional Z-scores **[4,5]**. Forty-eight grey and 19 white matter brain regions-of-interest (ROIs) were segmented **[6]**. The ROI masks were individually multiplied over all rCFL and control subjects to calculate regional DTI (FA, MD, AD and RD) and rsfMRI temporal complexity values (Hurst index, ***H***). A subject-specific total injury burden (IB) was calculated for each metric as mild (1), moderate (2), or severe (3) based on Z-scores that fell 2, 3 or 4 standard deviations from the control means, respectively. Correlations were performed in RStudio for the IB of each metric, with age, head impact (based on position), and career length as covariates.
Results: From the DTI data, the left cingulum had the most outliers: 4 subjects had an FA IB of 1 and one subject had an FA IB of 3. The rsfMRI global complexity data was highly variable between subjects. Four subjects had high ***H*** IB scores (9,11,15,28) and four had moderate ***H*** IB (1,1,2,6). The highest ***H*** IB ROI were the right premotor cortex BA6 (n=4), visual cortex V1 BA17 (n=3), visual cortex V2 BA18 (n=3), and hippocampus dentate gyrus (n=3). Neither FA nor global ***H*** were correlated with age, position or career length.
Conclusions: Although there are normal age-related decreases in grey and white matter **[7]**, our study identified decreases in rCFL subjects surpassing that found in normal aging brains. Only one subject expressed a high FA and ***H*** IB (FA IB=3, ***H*** IB=15). Continued research is being conducted to explore relationships between MRI IB and neuropsychological testing.

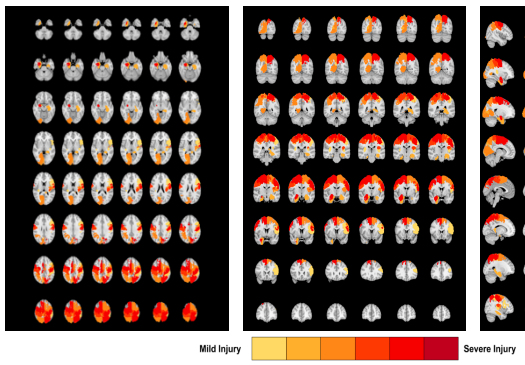

Figure 1. A colour coded visualization of the personalized rsfMRI-based resting state complexity analysis (**H**) from one subject who sustained a global injury burden ($\mathbf{H}_{IB}$) of 28, with a left $\mathbf{H}_{IB}$ = 11 and right $\mathbf{H}_{IB}$ = 17. This figure is separated into three to show the injured ROI from the axial (left), coronal (middle) and sagittal (right) perspectives.

References: **[1]** Multani N. et al. J Neurol 2016: 263: 1332; **[2]** Churchill N. et al. Brain Injury 2017: 31: 39; **[3]** Alzheimer's Disease Neuroimaging Initiative (ADNI). http://adni.loni.usc.edu/wp-content/uploads/how_to_apply/ADNI_Acknowledgement_List.pdf; **[4]** Cox RW Comput Biomed Res 1996: 29: 162; **[5]** Jenkinson M. et al. NeuroImage 2012: 62: 782; **[6]** Eickhoff SB. et al. NeuroImage 2005: 25: 1325; **[7]** Farokhian F. et al. Aging Dis 2017: 8: 899.

Quantifying Myelin Water Fraction in the Fetal Guinea Pig Brain

Simran Sethi[1], Lanette J. Friesen-Waldner[1], Trevor P. Wade[1,2], Ousseynou Sarr[3], Brian Sutherland[3], Timothy R.H. Regnault[3,4,5], Charles A. McKenzie[1,2,5]

[1]Medical Biophysics, [2]Robarts Research Institute, [3]Physiology & Pharmacology, [4]Obstetrics & Gynaecology, Western University, [5]Maternal, Fetal & Newborn Health, Children's Health Research Institute, London, ON, Canada

Introduction: Myelin, a lipid-rich substance that insulates nerve cells' axons, is essential for healthy brain development[1]. In the human fetus, the myelin sheath is first seen at 18 weeks gestation, followed by an increasing rate of brain myelination that continues postnatally[2]. Assessment of fetal myelin content is necessary to understand the impact of pathologies on myelination[3], but we have yet to quantify fetal myelin content *in vivo.* Myelin water imaging (MWI) separates signals from myelin water and intra-/extra-cellular water, with signal amplitudes proportional to the relative amounts of water in each environment[1]. The primary measurement of MWI is myelin water fraction (MWF), the ratio of signal from protons in myelin water to total signal from all protons in water[1]. MWF has been validated as a strong marker for myelin lipid[4]. Therefore, this study aims to quantify MWF in the fetal environment, specifically the fetal guinea pig brain.

Methods: 11 pregnant chow-fed guinea pigs (~60 days gestation), with 38 fetuses, were anesthetized and imaged in a 3 T MRI. Eight SPGR volumes (TR/TE: 4.6 – 5.9 ms/1.9 – 2.0 ms, FA: 2° – 16°) and 16 bSSFP volumes (TR: 6.4 – 7.4 ms, TE: 3.2 – 3.7 ms, FA: 8° – 64°) of the entire maternal guinea pig were acquired for DESPOT1/2, respectively[5] (FOV: 23-24 cm, voxel size: 0.7mm^3 – 0.9mm^3, acceleration: 2x). mcDESPOT[6] was used to reconstruct each maternal and fetal brain's MWF map, with the maternal brain used as an internal control. Using 3D Slicer[7], regions of interest (ROIs) were placed in the following areas: maternal corpus callosum (CC), fetal CC, and fetal fornix (FOR), which are all regions typically associated with pathologies[8,9]. The mean MWF value of the fetal CC and FOR were compared using a paired t-test (α=0.05).

Results: MWF maps were successfully generated for each fetal guinea pig brain (Figure 1). The mean MWF in the maternal CC, fetal CC, and fetal FOR are (mean ± standard deviation) 30.1 ± 2.40%, 16.3 ± 3.01%, and 22.5 ± 1.5%, respectively (Figure 2). The mean MWF of the fetal FOR was significantly greater than the fetal CC ($p < 0.05$); all results are consistent with previously publish literature[8,9].

Conclusion: We have successfully produced MWF maps in the fetal guinea pig brain, demonstrating the feasibility of MWI to assess fetal brain myelin content.

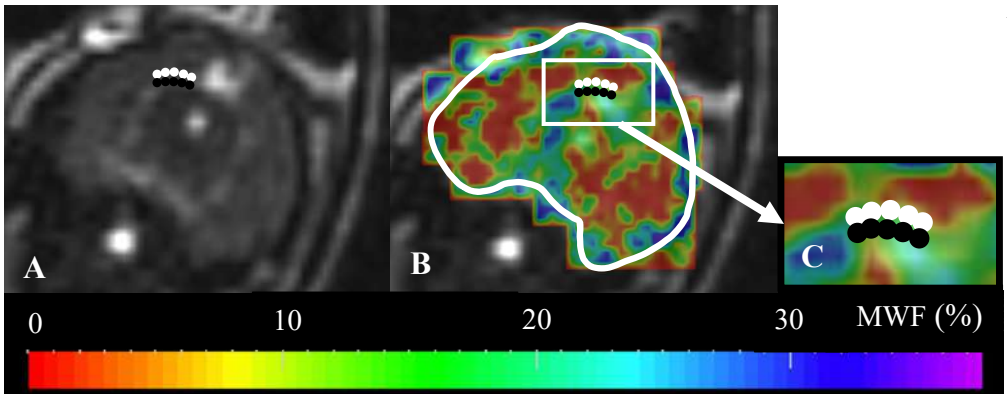

Figure 1. **A)** Coronal T2-weighted image slice of a fetal guinea pig brain at 60 days gestation. **(B)** A MWF map of the same guinea pig brain slice overlaid on the anatomical image shown in A. **(C)** A zoomed-in view of the section highlighted by the white rectangle seen in B. ROIs placed within the CC (white) and FOR (black).

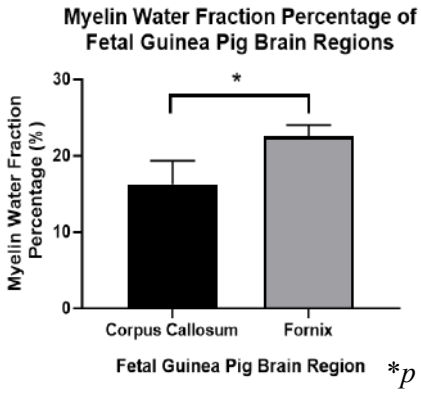

Figure 2. Histogram comparing the MWF of the fetal guinea pig CC and FOR 60 days gestation. The mean MWF percentage of the FOR was significantly greater than that of the CC ($p < 0.05$).

References: (1) MacKay A, *et al.* Magn Reson Med 1994. (2) Jakovcevski I, *et al.* Glia 2005. (3) Chase HP, *et al.* Pediatrics 1972. (4) Laule C, *et al.* Brain Pathol 2018. (5) Deoni SCL, *et al.* Magn Reson Med 2005. (6) Deoni SCL, *et al.* Magn Reson Med 2008. (7) Fedorov A, *et al.* Magn Reson Imaging 2012. (8) Gareau PJ, *et al.* Magn Reson Imaging 2000. (9) Piorkowska K. Electronic Thesis 2012.

Resting-state brain activity in pediatric concussion: A sex-based analysis

Bhanu Sharma[1,2,4] PhD, Carol DeMatteo[3] MSc, DipP&OT, Michael D. Noseworthy[1,4,5,6] PhD, Brian W. Timmons[2,4*] PhD

[1] Department of Electrical & Computer Engineering, McMaster University, [2] Child Health and Exercise Medicine Program, Department of Pediatrics, McMaster University. [3] School of Rehabilitation Science, McMaster University. [4] Imaging Research Centre, St. Joseph's Healthcare, Hamilton, ON, Canada. [5] McMaster School of Biomedical Engineering, McMaster University. [6] Department of Radiology, McMaster University.

Introduction: Pediatric concussion is among the most common childhood injuries, and recent research has identified marked sex-differences in the clinical presentation of this injury. Namely, girls with concussion report more symptoms and symptoms with greater severity than boys, and are also at risk of protracted recovery. To date, however, no studies have examined whether resting state brain activity (rs-fMRI) differs by sex in pediatric concussion. The objective of this study was to perform the first investigation of rs-fMRI differences, by sex, in pediatric concussion. We hypothesized, based on research on adults with concussion, that there would be greater impairments observed in girls with concussion than boys with concussion.

Methods: Children with concussion (n=27; mean 11.2 ± 6.2 years old, 55.6% female) were recruited from the emergency department at a large, teaching hospital, and were imaged, on average, at 28.8 ± 14.5 days. Imaging was performed on a 3-Tesla GE Discovery MR750 scanner with a 32-channel phased array head coil. The following data were collected, with acquisition parameters briefly outlined: *Anatomical:* 3D IR-prepped fast SPGR T1-weighted sequence (TE/TR/TI=4.25/11.36/450ms, flip angle=12°, 512x256 matrix interpolated to 512x512, 22cm axial FOV, 0.43mm in-plane, 1mm thick). *rs-fMRI:* Single shot gradient echo EPI sequence (TE/TR=35/2000ms, flip angle=90°, 64x64 matrix, 180 time points, 22cm FOV, 3.44mm in-plane 3mm thick), with participants asked to keep their eyes open not think of anything in particular. *B_0 maps:* Acquired using the same geometric prescription as rs-fMRI. Seed-based analyses was used for groupwise comparison of the default mode network (DMN), salience network (SN), and fronto-parietal network (FPN). Asides from unwarping (performed using the *epiunwarp* script), all data were pre-processed and analysed using CONN19c (run on MATLAB R202a and SPM12). Control data were acquired from the open-source neuroimaging database (ABIDE-II), matched 1:1 to cases on sex and age; scan parameters were similar between groups, but were not controlled for, and harmonization of MR parameters was not performed. Between-group, same-sex comparisons were performed to directly assess, for example, how healthy and concussed females differed on rs-fMRI.

Results: No differences were observed between boys with concussion and healthy boys. Females with concussion, vs. healthy females, showed both hypo-connectivity (between the DMN and SN and anatomical regions, including the precuneus, cingulate gyrus, and cingulate cortex) and hyper-connectivity (between the lateral pre-frontal cortex and inferior frontal gyrus and lateral occipital cortex, and between the PCC and cerebellum (all family-wise error p-values <0.05); ***Figure 1.***

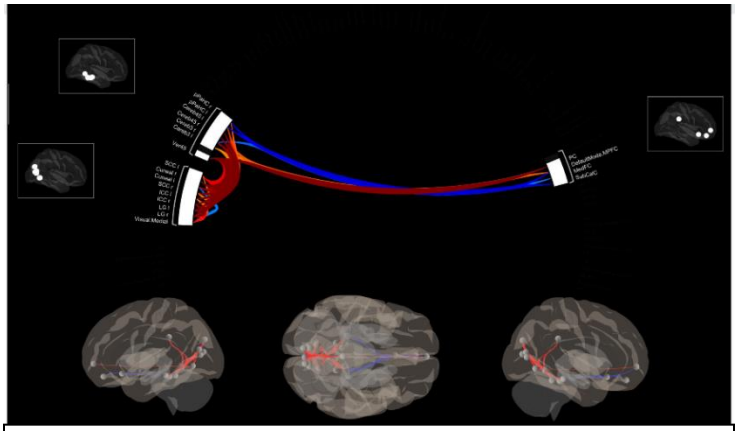

Figure 1: rs-fMRI differences in girls with concussion vs. healthy girls.

Conclusion: This is the first study to report on rs-fMRI sex-differences in children with concussion. Consistent with clinical findings suggesting a disproportionate injury burden in females, our study shows greater rs-fMRI disturbance in females vs. males with concussion. This may suggest a neurological underpinning to the clinical findings previously reported on.

Neural Correlates of Connected Speech in Cerebrovascular Disease

Dana N. Broberg[1,2], Seyyed M.H. Haddad[2], Katharine Aveni[3], Alexander Havens[4], ONDRI Investigators, J.B. Orange[5], Paula McLaughlin[6], Malcolm Binns[7], Angela Roberts[3], Robert Bartha[1,2]

[1]Dept. of Medical Biophysics, Western University; [2]Center for Functional & Metabolic Mapping, Robarts Research Institute; [3]Roxelyn & Richard Pepper Dept. of Communication Sciences & Disorders, Northwestern University; [4]School of Medicine, Case Western Reserve University; [5]School of Communication Sciences and Disorders, Western University; [6]Nova Scotia Health; [7]Rotman Research Institute, Baycrest

Introduction: Individuals with cerebrovascular disease (CVD) leading to cognitive impairment often experience altered communication ability, particularly with respect to spoken language. Deficits in connected speech, defined as speech that involves whole phrases rather individual words, can indicate cognitive impairment in this disease. Recently, a combination of 10 connected speech measures related to syntax (3), productivity (2), information content (2), fluency (2), and lexical diversity (1) detected cognitive impairment in CVD with a sensitivity of 77% and specificity of 80% [1]. However, the neurological basis for altered connected speech performance in CVD is poorly defined. Therefore, the objective of this study was to correlate these connected speech measures with indicators of white matter microstructural integrity provided by diffusion tensor imaging (DTI) to establish the link between CVD-related neurodegeneration and altered connected speech. We hypothesized that DTI and connected speech would be significantly associated in white matter tracts known to be involved in language – the inferior longitudinal, superior longitudinal, and uncinate fasciculi (ILF, SLF, and UNC, respectively).

Methods: Baseline connected speech and 3T DTI data (30-32 directions, b=1000) was obtained from the CVD cohort of the Ontario Neurodegenerative Disease Research Initiative (ONDRI) [2] (n=133). Connected speech analyses were completed previously [1]. A DTI analysis pipeline developed by our laboratory [3] was used to generate brain maps of two diffusion metrics: fractional anisotropy (FA) and mean diffusivity (MD). A white matter tract template was incorporated in the DTI analysis pipeline to extract diffusion information from specific white matter tracts. Therefore, this pipeline produced mean FA and MD values for each of the following tracts in the left and right hemisphere of the brain: ILF, SLF – parietal endings (SLFp), SLF – temporal endings (SLFt), and UNC. Four canonical correlation analyses examined the association of the DTI data from all four tracts with the 10 connected speech measures as follows: FA in the left hemisphere, FA in the right hemisphere, MD in the left hemisphere, MD in the right hemisphere.

Results: Canonical correlations were significant in the left hemisphere of the brain (FA: r_c=0.47, p<0.05; MD: r_c=0.51, p<0.01) but not the right hemisphere (FA: r_c=0.34, p=0.90; MD: r_c=0.40, p=0.15). Among the white matter tracts, the strongest canonical loadings were seen for the SLFp (FA: 0.81; MD: -0.59) and SLFt (FA: 0.71; MD: -0.40) compared to the ILF (FA: 0.44; MD: 0.03) and UNC (FA: -0.34; MD: 0.10). Among the connected speech measures, the strongest canonical loadings were seen in measures of syntax, fluency, and information content; productivity and lexical diversity were less important. Higher FA (indicative of healthier white matter microstructure) in the SLFp and SLFt was associated with higher performance on measures of fluency and information content, and – interestingly – lower performance on measures of syntax. Lower MD (indicative of healthier white matter microstructure) in these two tracts was associated with higher performance on measures of fluency, information content, and syntax.

Conclusion: Connected speech performance was only associated with measures of white matter microstructural integrity in the left hemisphere of the brain. This result is consistent with the typical lateralization of language function on the left side of the brain. Of the four white matter tracts investigated in this study, the SLFp and SLFt were most strongly associated with connected speech performance – particularly fluency, information content, and syntax – while the ILF and UNC had moderate associations with connected speech for FA alone. We conclude that, of the white matter tracts investigated in this study, worsened connected speech performance in CVD is most strongly linked to neurodegeneration in the parietal and temporal endings of the superior longitudinal fasciculus.

References: [1] Roberts A, et al. (2021). *Topics in Language Disorders* 41(1):73-98; [2] Farhan SMK, et al. (2017). *Can J Neurol Sci* 44(2):196-202; [3] Haddad SMH, et al. (2019). *PLoS One* 14(12): e0226715

Hyperpolarized ^{129}Xe Time-of-Flight pulse sequence for substantial brain signal stability improvement

Yurii Shepelytskyi[1,2], Vira Grynko[2,3], Tao Li[1], Ayman Hassan[4,5], Karl Granberg[4], Mitchell S. Albert[1,2,5]

[1]Department of Chemistry, Lakehead University, Thunder Bay, Ontario, Canada; [2]Thunder Bay Regional Health Research Institute, Thunder Bay, Ontario, Canada; [3]Chemistry and Materials Science Program, Lakehead University, Thunder Bay, Ontario, Canada; [4]Thunder Bay Regional Health Sciences Centre, Thunder Bay, Ontario, Canada; [5]Northern Ontario School of Medicine, Thunder Bay, Ontario, Canada

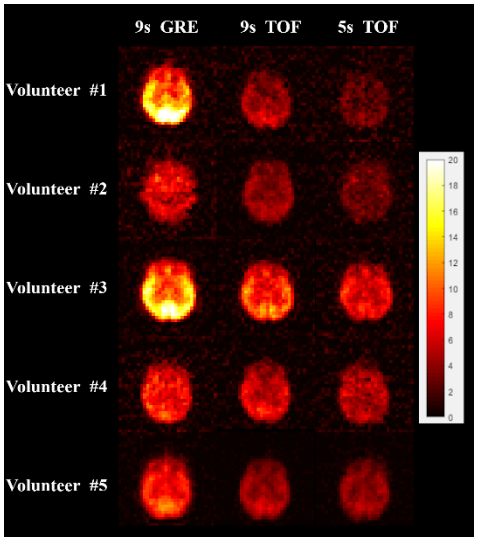

Figure 1. HP ^{129}Xe SNR SD maps calculated for conventional GRE pulse sequence (first column) and TOF pulse sequence (second and third column).

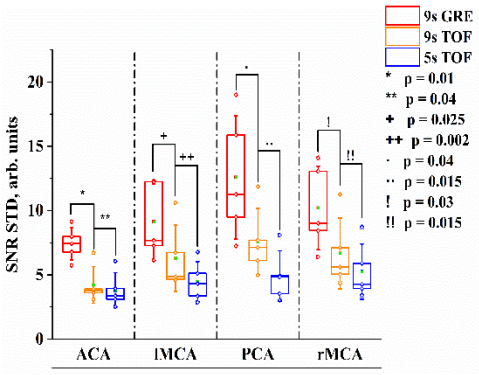

Figure 2. Comparative box-chart of the localized HP ^{129}Xe image SNR SD showing signal variabilities from the regions supplied by ACA, PCA, lMCA, and rMCA. The HP ^{129}Xe TOF pulse sequence significantly reduces ^{129}Xe SNR variability.

Introduction: Hyperpolarized (HP) ^{129}Xe MRI of the human brain is currently under extensive development[1–4]. Despite numerous advances in the field, there is still noticeable image SNR variability (up to ± 28% withing the same subject) which complicates quantitative applications of HP ^{129}Xe brain imaging[5]. Recently, a novel HP ^{129}Xe time-of-flight (TOF) pulse sequence has been developed[6,7]. This technique relies on the time-selective depolarization of ^{129}Xe with subsequent imaging following the TOF delay time. HP ^{129}Xe TOF renders the signal to depend mainly on the blood flow and, therefore, was hypothesized to reduce the HP ^{129}Xe signal variability.

Methods: 5 healthy volunteers (1 male; 4 females) were recruited. Imaging was conducted using a Philips Achieva 3.0T scanner with a dual-tuned ^{1}H/^{129}Xe head coil (CMRS LLC, USA). Enriched ^{129}Xe (83%) was polarized up to 50% using a XeBox-10E polarizer (Xemed LLC, USA). A proton localizer was acquired initially using the following parameters: FOV=250x250mm^2; matrix=256x256; TR/TE=3s/80ms; flip angle (FA)=90^o.

Following the initial brain localization, participants inhaled 1L of HP ^{129}Xe gas and held their breath for 20s. Each participant performed six breath-holds. During three breath-holds, a conventional single-slice gradient echo (GRE) image was acquired 9s into the breath-holds. During the other breath-holds, two dynamic TOF images were acquired with either a TOF delay time of 5s or 9s. The imaging parameters for both GRE and TOF imaging were: FOV=250x250mm^2; matrix=32x32; TR/TE= 6.1ms/1.37ms; FA=12.5^o. HP ^{129}Xe images were reconstructed and analyzed using custom-built Matlab scripts in Matlab R2020b (MathWorks, US). All images were recalculated into SNR maps, registered, and recalculated into HP ^{129}Xe SNR standard deviation (SD) maps (3 images/map) to assess the signal variability.

Results: Fig. 1 shows HP ^{129}Xe SNR SD maps calculated for HP ^{129}Xe images acquired using conventional GRE acquisition methods and the HP ^{129}Xe TOF pulse sequence[7]. Due to the presence of the initial depolarization pulse, HP ^{129}Xe demonstrated up to 2.26 times less signal variability compared to the conventional GRE image acquisition approach. The lowest ^{129}Xe variations were observed from the area supplied by the anterior cerebral artery (ACA), whereas the highest variability in ^{129}Xe signal was observed from the posterior region of the brain (Fig. 2). The area supplied by the right middle cerebral artery (rMCA) demonstrated slightly higher Xe signal variability compared to the left MCA (lMCA) region.

Conclusions: The HP ^{129}Xe TOF perfusion imaging technique substantially improves the stability of the HP ^{129}Xe signal from brain tissues.

References: [1]Rao, M.,et al. *Radiology* (2017);[2]Hane, F. *et al. Diagnostics*(2018);[3]Rao, M.*et al. J. Magn. Reson. Imaging* (2019);[4]Grynko,V.*et al. Magn. Reson. Med.* (2021); [5]Rao, M.,et. al. in *Proc. Intl. Soc. Mag. Reson. Med* (2019); [6]Shepelytskyi,Y.*et al. Diagnostics* (2020); [7]Shepelytskyi,Y.*et al. Magn. Reson. Med.* (2021).

7 Tesla Diffusion MRI in Subcortical Structures following COVID-19 Infection

Helma Heidari*, BSc[1,2], Tales Santini[1,2], Stephanie Handsor[3], Koula Pantazopoulos[4], Lauryn Richardson[4], Kristy Coleman[4], Michael Silverman[5], Erin Spicer[3], Stephen Pasternak[4,6], Luciano Sposato[6], Doug Fraser[7], Anthony Tang[8], Ravi Menon[1,2], Corey Baron[1,2], Michael Jurkiewicz[9], Elizabeth Finger[4,6], Marko Mrkobrada[3], Megan Devlin[3], and Robert Bartha, PhD[1,2]

[1]Robarts Research Institute, [2]Departments of Medical Biophysics; [3]Internal Medicine, [5]Infectious Diseases, [6]Clinical Neurological Sciences, [7]Paediatric Critical Care, [8]Medicine, [9]Medical Imaging, The University of Western Ontario, and [4]Parkwood Institute.

Introduction: The novel coronavirus SARS-CoV-2 causes unusual viral pneumonia with a wide range of symptoms including fever, cough and chest discomfort with dyspnea and bilateral infiltration in severe cases [1]. The receptor for the SARS-CoV-2 virus (ACE-2 receptor) is also present in the brain and brain stem suggesting the possibility of direct viral invasion of the CNS [2]. Diffusion weighted magnetic resonance imaging (dMRI) provides non-invasive robust assessment of cerebral tissue microstructure sensitive to pathological changes. Specifically, diffusion tensor imaging (DTI) can quantify the water mean diffusivity (MD) and degree of directionality known as fractional anisotropy (FA) [3]. Moreover, microscopic FA (μFA) is an advanced diffusion technique that is potentially more sensitive to pathologies [4]. The purpose of this study was to demonstrate the feasibility of estimating brain tissue microstructural changes by ultra-high field MRI after SARS-CoV-2 infection using both conventional and advanced diffusion metrics.

Methods: Imaging was successfully performed in 46 study participants on a Siemens 7T Plus head-only MRI scanner. Participants had neurological symptoms documented during their illness and were recovered for at least one month from their COVID-19 respiratory symptoms. Participants with acute psychosis, pre-existing dementia, or claustrophobia were excluded. The imaging protocol included T_1-weighted MP2RAGE, FLAIR, 3D time of flight imaging, susceptibility weighted imaging, b-tensor encoded diffusion MRI, and chemical exchange saturation transfer (CEST) imaging. For the current study, brain extraction and segmentation were performed using FSL (Figure 1) on the T_1-weighted MP2RAGE (700 μm isotropic) images. The subcortical structure masks were eroded to reduce potential partial volume artifacts in the analysis (Figure 2). Diffusion weighted images (including μFA, FA, and MD, 2 mm isotropic) were registered to the anatomical MP2RAGE images using affine registration. In this preliminary feasibility study, we demonstrate the successful measurement of diffusion metrics in one subject (Figure 3).

Results: Diffusion scans in all 46 participants were successfully preprocessed. Preliminary results demonstrate the feasibility of segmenting subcortical structures in all participants and aligning diffusion maps with anatomical MP2RAGE images. The average μFA, FA, and MD values (mean ± s.d.) for left hippocampus of this cohort are 0.37±0.15, 0.27±0.09, and 0.001±0.0003 respectively.

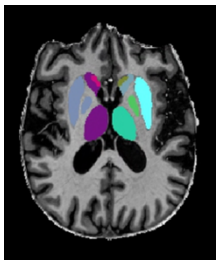

Figure 1: subcortical segmentation masks

Figure 2: Left hippocampus mask after 2 voxel erosion (green)

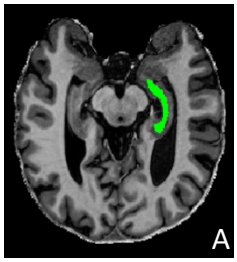

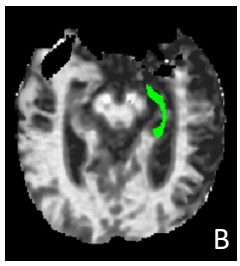

Figure 3: Left hippocampus segment in anatomical (A) and dMRI-μFA (B) image

Conclusions: This preliminary work demonstrates the feasibility of assessing sub-cortical microstructural integrity including μFA by ultra-high field diffusion MRI following SARS-CoV-2 infection. Measured values using this pipeline are consistent with previous measurements [4]. In the next phase, diffusion measurements from all 46 participants will be used to examine associations with functional deficits including memory.

References:[1] Gralinski et al. https://doi.org/10.3390/v12020135;[2] U. Jain, 10.7759/cureus.9540;[3] McCunn et al. 10.1371/journal.pone.0215974;[4] Arezza et al. https://doi.org/10.1016/j.mri.2021.04.015

Evaluating regional correlations between glutamate+glutamine and GABA+ in the resting human brain

Claire Shyu[1,2], Sonja Elsaid[1,3], Peter Truong[1], Bernard Le Foll[1,2,3], and Sofia Chavez[1,3]
[1]Brain Health Imaging Centre, Centre for Addiction and Mental Health (CAMH), Toronto, ON, Canada
[2]Department of Pharmacology and Toxicology, University of Toronto, Toronto, ON, M5S 1A8, Canada
[3]Institute of Medical Science, Faculty of Medicine, University of Toronto, Toronto, ON, Canada

Introduction: Excitation-inhibition balance is a key principle of healthy neuronal circuitry function. In many neuropsychiatric disorders, imbalances between levels of inhibitory (γ-aminobutyric acid, GABA) and excitatory (glutamate + glutamine, Glx) neurotransmitters have been observed[1,2]. Magnetic Resonance Spectroscopy (MRS) is a non-invasive way to study region specific E/I metabolite relationships in-vivo. By establishing E/I regional relationships in healthy subjects, alterations in disease conditions can be uncovered. To date, only one multi-site study has investigated the correlations between regional Glx and GABA levels in healthy human brains[3]. GABA appears in the brain at low concentrations and thus requires MEGA-PRESS (MEscher- GArwood Point RESolved Spectroscopy), a sequence utilizing the J-difference editing technique to uncover GABA peaks[4,5]. J-difference editing involves an interleaved acquisition of 2 spectra: edit-ON (RF editing pulses placed at 1.9 ppm) and edit-OFF (RF editing pulses placed at 7.5 ppm)[4]. Because Glx resonances are also located near 1.9 ppm, they are co-edited. The subtraction of the edit-ON and edit-OFF spectra results in a difference spectrum (diffS), where Glx and GABA+ (GABA + macromolecules) appear at 3.75ppm and 3 ppm, respectively. Glx can thus be measured in both diffS and edit-OFF spectra. Recent investigations suggest that the edit-OFF Glx measurement may be more stable and less biased[6]. Here we examine whether the regional concentrations of GABA and Glx are correlated in the resting human brain, using Glx from both diffS and the edited-OFF spectra. Our regions of interest (ROIs) include the right insula, anterior cingulate cortex (ACC), and left dorsal lateral prefrontal cortex (DLPFC).

Methods: 40 healthy volunteers (24.5 ± 3.3yrs., 16 males) were scanned on a 3T scanner (General Electric Healthcare) with a 32-channel head coil (Nova Medical) as per institutional REB. Subjects underwent two consecutive MEGA-PRESS scans per ROI (6:45 min/scan for insula, 5:12 min/scan for ACC and DLPFC) and resulting values were averaged to yield reproducible data[7]. MEGA-PRESS parameters were: TE/TR = 68 ms/1500 ms, 192 averages for ACC/DLPFC, 256 averages for insula, editing RF pulse width = 14.4ms. The diffS GABA+ and Glx peaks are fit and quantified using Gannet 3.1[8]. Glx values from the edited-OFF spectrum were first processed using FID-A[9] then analyzed using LCModel[10]. Gannet and SPM12 (www.fil.ion.ucl.ac.uk/spm) were used for voxel-to-T1-weighted image registration. $GABA_+$ and Glx values are reported in institutional units (I.U.) where the unsuppressed water signal is used as internal water reference and values are corrected for partial volumes of CSF/GM/WM using tissue segmentation with FSL (FMRIB Software Library).

Results: In the insula, there was significant correlation between GABA+ and Glx from the edit-OFF spectra (p = 0.01). In the ACC and DLPFC, correlations were significant between GABA+ and diffS Glx (p = 0.03; p = <0.001).

GABA+ vs.	Insula	ACC	DLPFC
diffS Glx	n = 28; r = 0.31; p = 0.05	n = 28; r = 0.37*; p = 0.03	n = 25; r = 0.69**; p = <0.001
edit-OFF Glx	n = 29; r = 0.43**; p = 0.01	n = 27; r = 0.04; p = 0.41	n = 25; r = 0.22; p = 0.15

* Correlation is significant at the 0.05 level (2-tailed).** Correlation is significant at the 0.01 level (2-tailed).

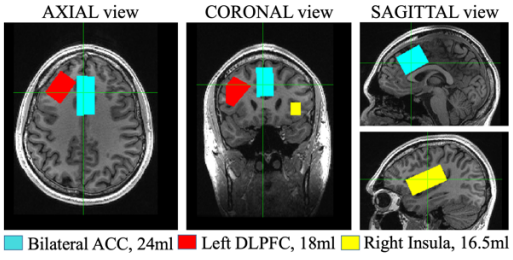

Fig 1. Voxel Placements

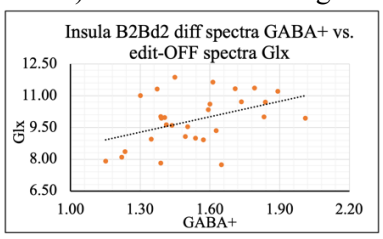

Fig 2. Pearson Correlation plot for Insula GABA+ vs. edit-OFF Glx

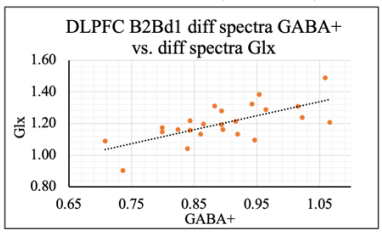

Fig 3. Pearson Correlation plot for DLPFC GABA+ vs. diffS Glx

Conclusion: We found significant correlations between GABA+ and Glx in all regions for either the edit-OFF-Glx measurement (insula) or the diffS-Glx (ACC and DLPFC) but not both. The correlations differ regionally, likely due to regionally dependent spectral quality, metabolite concentrations and macromolecular contamination of the peaks. The stability of these results and sex/age effects are currently being investigated.

References: 1) Barron et al. *PNAS*. 2017.; 2) Chiu et al. *Schizophr Res.* 2018. ; 3) Steel et al. *NeuroImage.* 2020.; 4) Mullins et al. *NeuroImage*. 2014. ; 5) Mescher M et al. *NMR Biomed.* 1998.; 6) Van Veenendaal et al. *JMRI*. 2017.; 7) Shyu et al. *Brain Sci*. 2021.; 8) Edden et al. *JMRI.* 2014.; 9) Simpson et al. *MR in Med*. 2017.; 10) Provencher, S.W. *NMR Biomed*. 2001.

Oral Session 11: Lung Imaging

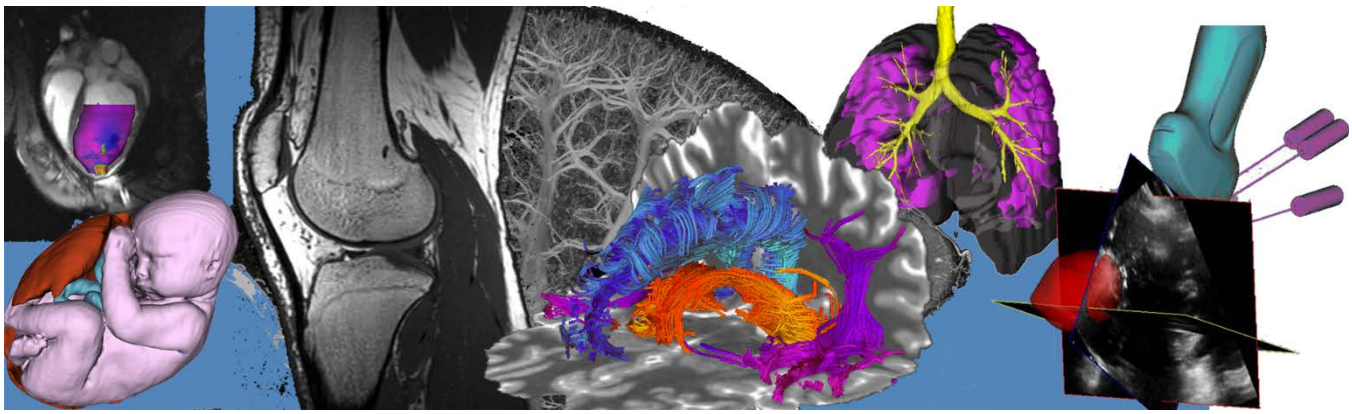

Investigating the Relationship between Quantitative UTE MRI Measurements and Pulmonary Function of Healthy Pediatric Subjects

Daniel Genkin BEng[1], Brandon Zanette PhD[2], Patrick Grzela BA[2], Elizabeth Tullis MD[3,4], Felix Ratjen MD[2,5], Giles Santyr PhD[2,6] and Miranda Kirby PhD[7]

Introduction: Computed tomography (CT) imaging is the current clinical standard for obtaining structural information about the airways, such as airway remodeling. However, a critical limitation of CT imaging is that it exposes patients to ionizing radiation. Children are approximately 10 times more radiosensitive than adults, and the effective dose of acquiring 2-3 thoracic CT images for longitudinal monitoring (30-90 mSv) may result in a statistically significant risk of developing cancer.[1] Therefore, for airway analysis to be used as a routine clinical monitoring tool for pediatric patients with respiratory disease, radiation-free approaches must be developed. Ultra-short echo time (UTE) is a recent-advent pulse sequence technique for magnetic resonance imaging (MRI).[2] By decreasing echo times to 8-100μs, high-resolution, radiation-free images of the lungs can be obtained. Our objective was to develop a UTE MRI airway segmentation pipeline in healthy pediatric subjects, and determine if quantitative UTE MRI measurements are correlated with subject demographics (e.g. age and height) and pulmonary function measurements.

Methods: Healthy pediatric subjects were retrospectively assessed (SickKids Hospital, Toronto, Canada). Subject demographics, pulmonary function tests, and UTE MRI lung images (TR=2.81ms, TE=0.05ms, flip angle=5°, FOV=480x480mm^2, resolution=1.25x1.25x1.25mm^3) were collected. Previous work by *Baldacci et al*[3] was used as a framework for the development of a semi-automated airway segmentation and analysis pipeline in MATLAB. To increase the inter-tissue contrast, a Gaussian filter was applied (σ=25, size=25x25x25) and the result was subtracted from the original volume. Next, 10% of the gradient of the volume (Sobel filter) was added to the Gaussian output to increase edge content. An optimal 5x5x5 median filter oriented in one of 9 possible 3-dimensional directions was applied to minimize intra-tissue contrast. Airway segmentation was performed using region growing with a manually selected threshold, followed by manual edits. To extract the airway curve-skeletons, a thinning algorithm was used. The optimal cross-section orientation for each segment's skeleton points was calculated using the Voronoi Covariance Measure. Finally, for each segment, the lumen area, diameter, perimeter, volume, and surface area were extracted and averaged across each airway generation. Spearman correlations were used to determine the association of UTE MRI measurements to subject demographics, and pulmonary function measurements.

Figure 1. Thoracic UTE MRI Image with Overlaid Segmented Airway Tree

Results: A total of 8 healthy subjects were evaluated (age=11.3±2.7 years, n=6 females). There were significant correlations for age with UTE MRI lumen area (ρ=0.88; $p<0.01$) and segment volume (ρ=0.81; $p<0.05$), as well as height with lumen perimeter (ρ=0.74; $p<0.05$). There were also significant correlations for Forced Expiratory Volume in 1 second (FEV_1) with lumen area (ρ=0.81; $p<0.05$) and surface area (ρ=0.86; $p<0.05$), and Total Lung Capacity (TLC) with lumen area (ρ=0.88; $p<0.01$).

Conclusion: In this proof-of-principle study, we showed that airway measurements extracted from UTE MRI in healthy pediatric subjects are significantly associated with age and height, and pulmonary function test measurements. These findings motivate further development and validation of UTE MRI using larger sample sizes and in pediatric patients with respiratory diseases, such as cystic fibrosis.

Author Affiliations
[1]Department of Electrical, Computer, and Biomedical Engineering, Ryerson University, Canada; [2]Department of Translational Medicine, The Hospital for Sick Children, Canada; [3]Division of Respirology, St. Michael's Hospital, Canada; [4]Department of Medicine, University of Toronto, Canada; [5]Institute of Medical Science, University of Toronto, Canada; [6]Department of Medical Biophysics, University of Toronto, Canada; [7]Department of Physics, Ryerson University, Canada.

References

[1] Pierce DA, Preston DL. Radiation-related cancer risks at low doses among atomic bomb survivors. Radiat Res. 2000.
[2] Chassagnon G, et al. High-resolution lung MRI with Ultrashort-TE: 1.5 or 3 Tesla? Magn Reson Imaging. 2019.
[3] F. Baldacci, et al. 3D human airway segmentation from high Resolution MR Imaging. Eleventh International Conference on Machine Vision. 2019.

Abnormal ^{129}Xe Ventilation MRI and Inhaled Corticosteroid Deposition in Severe Asthma

Ashutosh Thakar[1], Hosein Sadafi[2], Hana Serajeddini[1,3], Carmen Venegas[1,3], Melanie Kjarsgaard[3], Norman B Konyer[4], Ben Lavon[2], Myrna Dolovich[1,3,4], Parameswaran Nair[1,3], and Sarah Svenningsen[1,3,4]

[1]Department of Medicine, McMaster University, Hamilton, Canada; [2]FLUIDDA, Inc., New York, United States of America; [3]Firestone Institute for Respiratory Health, [4]Imaging Research Center, St. Joseph's Healthcare Hamilton, Hamilton, Canada.

INTRODUCTION: Patients with severe asthma have persistent symptoms and exacerbations despite adherence to high-dose inhaled corticosteroids (ICS). A consequence of airway obstruction in patients with severe asthma is regionally heterogeneous airflow distribution, directly quantifiable with hyperpolarized gas magnetic resonance imaging (MRI). Because optimal therapeutic effect depends, in part, on the deposition of inhaled drugs conveyed by airflow to the site of inflammation, we hypothesized that abnormal ventilation may contribute to suboptimal ICS response by altering deposition patterns. In this proof-of-concept study, our objective was to ascertain the relationship between abnormal ventilation (quantified by ^{129}Xe MRI) and simulated ICS deposition (quantified by Functional Respiratory Imaging[1]) in severe asthmatics with a type-2 immune signature.

METHODS: Ten severe asthmatics (7 female; age=49±16 years; forced expiratory volume in one second=63±24%$_{pred}$; asthma-control-questionnaire=2.4±1.2) with a type-2 immune signature (FeNO≥25 ppb, sputum eosinophils≥3%, and/or blood eosinophils≥300/μL) performed same-day post-bronchodilator hyperpolarized ^{129}Xe MRI and inspiratory and expiratory CT. Abnormal ventilation was quantified using the ^{129}Xe MRI ventilation-defect-percent (VDP).[2] CT-derived subject-specific internal airflow distribution and airway models were coupled to simulated inhalers to quantify total, peripheral and central lung deposition of fluticasone propionate HFA (*Flovent*) and beclomethasone dipropionate HFA (*Qvar*) using computational fluid dynamics, with a prescribed inhalation maneuver. Between-group differences were evaluated using unpaired t-tests. Univariate relationships were evaluated using Pearson correlations.

RESULTS: The median post-bronchodilator ^{129}Xe MRI VDP was 6% (minimum=1%, maximum=35%) and seven of the ten asthmatics had an abnormal ^{129}Xe MRI VDP (≥2%[3]). Total (Flovent: 45±2%, Qvar: 67±3%, p<0.0001), central (Flovent: 18±3%, Qvar: 24±4%, p<0.0001) and peripheral (Flovent: 27±4%, Qvar: 43±5%, p<0.0001) deposition of Qvar was greater than Flovent. Asthmatics stratified by median ^{129}Xe MRI VDP (<6% vs. ≥6%) had similar total, central and peripheral deposition of Flovent and Qvar. As shown in Figure 1A, in the subgroup of seven asthmatics with abnormal ventilation (^{129}Xe MRI VDP≥2%[3]), greater VDP was correlated with lower central (Flovent: r=-0.82, p=0.02; Qvar: r=-0.85, p=0.01) and higher peripheral deposition (Flovent: r=0.94, p=0.002; Qvar: r=0.96, p=0.0006), but not total deposition (Flovent: r=0.36, p=0.30; Qvar: r=0.36, p=0.31). Figure 1B details two representative asthmatics with abnormal ventilation.

CONCLUSIONS: It is unknown why some asthmatics respond sub-optimally to ICS and require more aggressive parenteral or oral treatment strategies to maintain asthma control. In this small, proof-of-concept study, severe asthmatics with greater ventilation abnormalities observed by MRI (i.e., higher ^{129}Xe MRI VDP) had higher peripheral and lower central ICS deposition, irrespective of particle size.

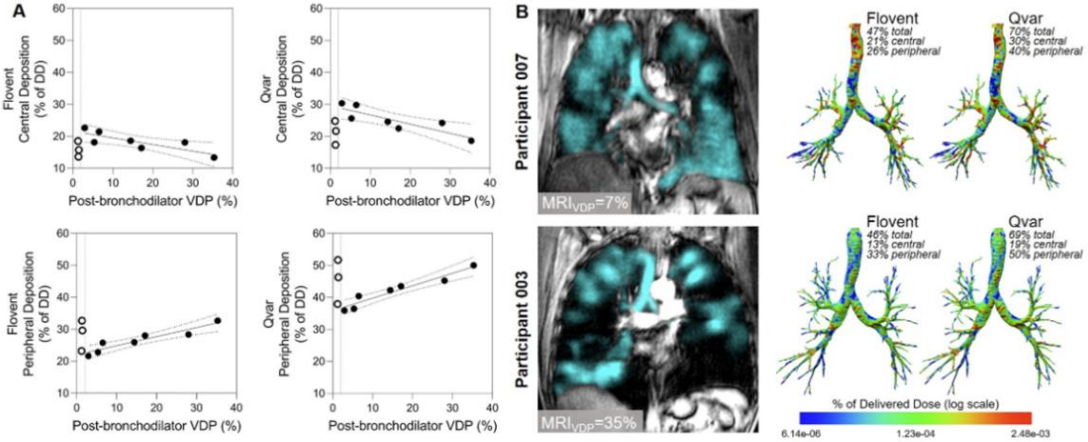

Figure 1. Relationship of ^{129}Xe Ventilation MRI with simulated inhaled corticosteroid deposition in severe asthma. **(A)** Closed and open circles represent asthmatics with abnormal (VDP≥2%) and normal (VDP<2%) ventilation. In asthmatics with abnormal ventilation, greater VDP was correlated with lower central (Flovent: r=-0.82, p=0.02; Qvar: r=-0.85, p=0.01) and higher peripheral deposition (Flovent: r=0.94, p=0.002; Qvar: r=0.96, p=0.0006). Correlations show best-fit line with 95% confidence bands for seven asthmatics with abnormal VDP. **(B)** ^{129}Xe ventilation MRI and CT-derived 3D models of central Flovent and Qvar deposition for two representative asthmatics. Participant 007 is a 63-year-old female with a 7% VDP, high central and low peripheral ICS deposition. Participant 003 is a 62-year-old male with a 35% VDP, low central and high peripheral ICS deposition.

[1]J.W DeBacker et al. Radiol 2010; [2]M Kirby et al. Acad Radial 2012; [3]R Eddy et al. Eur Respir J 2018.

Feasibility of Simultaneous Whole-Lung Ventilation-Perfusion Imaging with Volumetric CT in Non-Small Cell Lung Cancer

Heather M Young[1,2,3], Feng Su[3], Ting-Yim Lee[2,3] and Stewart Gaede[1,2]

[1]Department of Physics and Engineering, London Regional Cancer Program, [2]Department of Medical Biophysics, [3]Robarts Research Institute, University of Western Ontario

Introduction: There are several clinical trials currently underway investigating the effectiveness of functional lung avoidance in radiation therapy for lung cancer, a technique that shows great promise for improving patient outcomes. However, there remain many obstacles to implementing these techniques in a clinical setting. Lung function depends on both ventilation and perfusion, but many of these studies rely on ventilation or perfusion alone. Studies which include both ventilation and perfusion rely on nuclear imaging or MRI methods, which may be more difficult to integrate into routine clinical practice. The purpose of this study was to generate a comprehensive map of regional lung function including both ventilation and perfusion in a single dynamic contrast-enhanced CT scan using a volumetric CT scanner.

Methods: Two patients with stage III non-small cell lung cancer were imaged on a GE Revolution volumetric CT scanner before and 6 weeks after radiotherapy. Images were acquired at a single couch position using the following parameters: cine mode, 0.28 s/revolution, 100 kV, 100 mA, and 160 mm axial field-of-view for 45-50 s. Iodine-based contrast was injected 6 s after the start of the acquisition. All images in the series were non-rigidly registered in Elastix. Blood flow maps were generated using GE's prototype CT Perfusion software. End-inhale and end-exhale images were identified from the pre-contrast images and were used to calculate specific ventilation maps using an existing density-based method. Ventilation (V) and perfusion (Q) maps were normalized to the 99th percentile of the distribution to facilitate direct comparison, and V/Q maps were calculated as a ratio of the normalized maps.

Results: After radiotherapy, ventilation in the treated lung decreased for both patients and blood flow decreased in Patient 1 but increased in Patient 2. Tumour blood flow was heterogeneous in Patient 1, and uniformly low in Patient 2. In both patients, regions of the lung that appear to have normal function based on ventilation or perfusion imaging alone are shown to have V/Q mismatch.

Conclusions: These results demonstrate the feasibility of generating both ventilation and perfusion imaging using volumetric CT in a single imaging protocol performed in under 1 minute. Further investigation is needed to determine the potential of method to facilitate the clinical translation of functional lung imaging in radiation treatment planning.

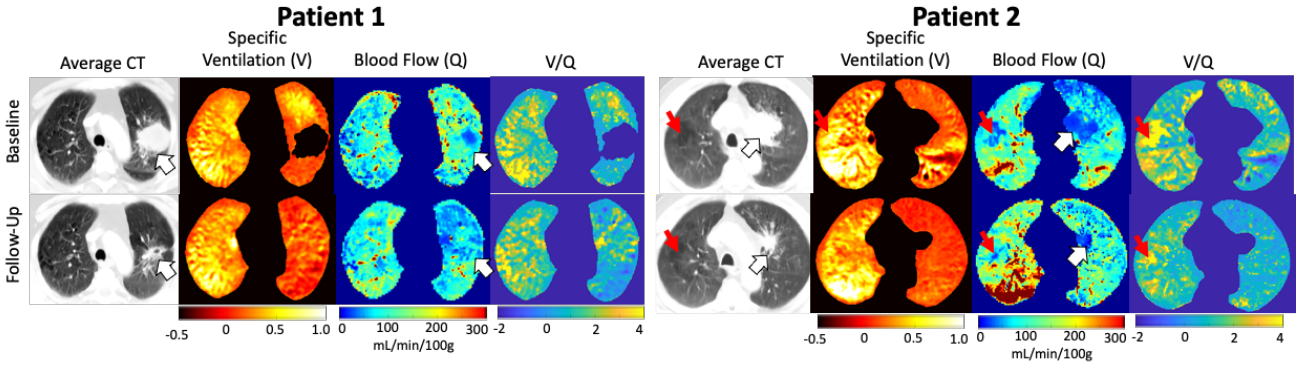

Figure 1. Representative image slices at baseline (top row) and after radiotherapy (bottom row) for Patient 1 (left) and Patient 2 (right). The registered average CT image (first column) provides anatomical reference. Specific ventilation maps (second column) indicate decreased ventilation in the left lung after treatment. Blood flow maps (third column) indicate tumour perfusion at baseline (white arrows) and changes to blood flow in the left lung after treatment. V/Q maps (last column) indicate regions of V/Q mismatch (yellow) or reversed mismatch (blue).

Evaluating CT Imaging Structural Changes in Cystic Fibrosis Responders and Non-responders Following CFTR Modulator Therapy

Gaurav Veer Singh[1], Elizabeth Tullis MD[2,3], and Miranda Kirby PhD[1]

[1]Department of Physics, Ryerson University, Canada; [2]Division of Respirology, St. Michael's Hospital, Canada; [3]Department of Medicine, University of Toronto, Canada.

Introduction: Cystic Fibrosis is an inherited disorder that affects approximately 5,000 Canadians [1]. CF is caused by mutations in the cystic fibrosis transmembrane conductance regulator protein (CFTR), and the dysfunction results in progressive multi-organ disease which affects the pancreas, gastrointestinal tract, the sweat glands, and the airways [1]. Recurring airway infection leads to scarring, decreased lung function over time and, eventually, to respiratory failure [2]. CFTR-modulator therapies have shown promise in modifying the course of CF disease by reducing the number of pulmonary exacerbations [2] and increasing forced expiratory volume in 1 second (FEV_1) [2], but very limited studies have examined the structural changes which leads to improved lung function in CF patients that respond to treatment [3]. Computed tomography (CT) imaging is a sensitive tool for providing information and regional quantification of structural abnormality in the lungs. However, it is unclear if CT imaging can quantify the structural changes that occur in the airways in CFTR treatment responders. In this pilot study, our objective was to determine if CT airway measurements are significantly different between CF patients classified as responders and non-responders 1-year following modulator therapy treatment. We hypothesize that significant structural differences in the airway tree measurements will be detected in CF responders.

Methods: CT images were retrospectively acquired from patients in the Adult CF Program at St. Michael's Hospital at baseline and 1-year follow-up that had undergone modulator therapy treatment. These modulators were Symdeko (n=14), Orkambi (n=6) and Kalydeco (n=1), which were selected based on the type of gene mutation. Responders were defined as the change in percentage predicted FEV_1 was greater than zero [4] between baseline and 1-year follow up. CT images were analyzed using VIDA diagnostic software. CT total airway count (TAC) was generated for all the sub-lobes left upper lobe (LUL), left lower lobe (LLL), right upper lobe (RUL), right middle lobe (RML) and right lower lobe (RLL). A two-sided unpaired t-test with Welch's correction was used to determine significance between change in post- and pre-treatment CT airway measurements between the responders and non-responders.

Results: A total of n=21 CF patients were evaluated pre- and 1-year post-Modulator therapy. Of these, n=15 were classified as responders, and n=6 were non-responders. As shown in Figure 1, the difference between post- and pre-treatment CT TAC was significantly different in the responder compared to the non-responder group for the LLL (p=0.01), and there was a trend for significance for post-pre difference in TAC measurements between the responders and non-responders in other lobes, but no significant difference (p=0.11) was found in the whole lung between responders and non-responders.

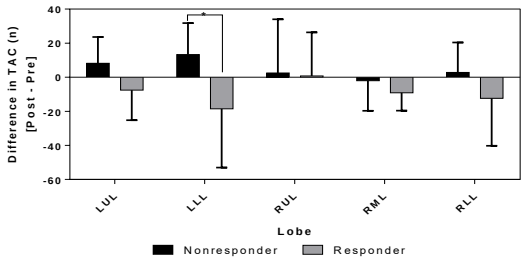

Figure 1. Comparison between Responders and Non-responders

Conclusion: The results in this pilot study supported the hypothesis that CT imaging can detect structural differences in airway tree measurements between responders and non-responders following Modulator therapy treatment. The CT TAC measurement decreased 1-year following Modulator therapy in the responder group compared to the non-responder group, which may reflect a decrease in airway dilation associated with bronchiectasis. Future studies will focus on investigating a larger number of CF patients pre- and 1-year post-Modulator therapy treatment to confirm these preliminary findings.

References:

1) Burgener EB, Moss RB. Cystic fibrosis transmembrane conductance regulator modulators: precision medicine in cystic fibrosis. Curr Opin Pediatr [Internet] 2018 [cited 2019 Oct 9];30(3):372–377. Available from: http://www.ncbi.nlm.nih.gov/pubmed/29538046; **2)** Loeve M, Rosenow T, Gorbunova V, Hop WCJ, Tiddens HAWM, Bruijne M de. Reversibility of trapped air on chest computed tomography in cystic fibrosis patients. Eur J Radiol 2015 [cited 2020 Feb 19];84(6):1184–1190. Available from https://linkinghub.elsevier.com/retrieve/pii/S0720048X15000790 ; **3)** Wijker, N. E., Vidmar, S., Grimwood, K., Sly, P. D., Byrnes, C. A., Carlin, J. B., Cooper, P. J., Robertson, C. F., Massie, R. J., Kemner van de Corput, M. P. C., Cheney, J., Tiddens, H. A. W. M., & Wainwright, C. E. (2020). Early markers of cystic fibrosis structural lung disease: Follow-up of the ACFBAL cohort. *European Respiratory Journal*, *55*(4), 1901694. https://doi.org/10.1183/13993003.01694-2019; **4)** Heltshe, S. L., Rowe, S. M., Skalland, M., Baines, A., & Jain, M. (2018). Ivacaftor-treated patients with cystic fibrosis derive long-term benefit despite no short-termclinical improvement. *American Journal of Respiratory and Critical Care Medicine*, *197*(11), 1483–1486. https://doi.org/10.1164/rccm.201710-2046le;

Oral Session 12:
Image-Guided Intervention and Surgery

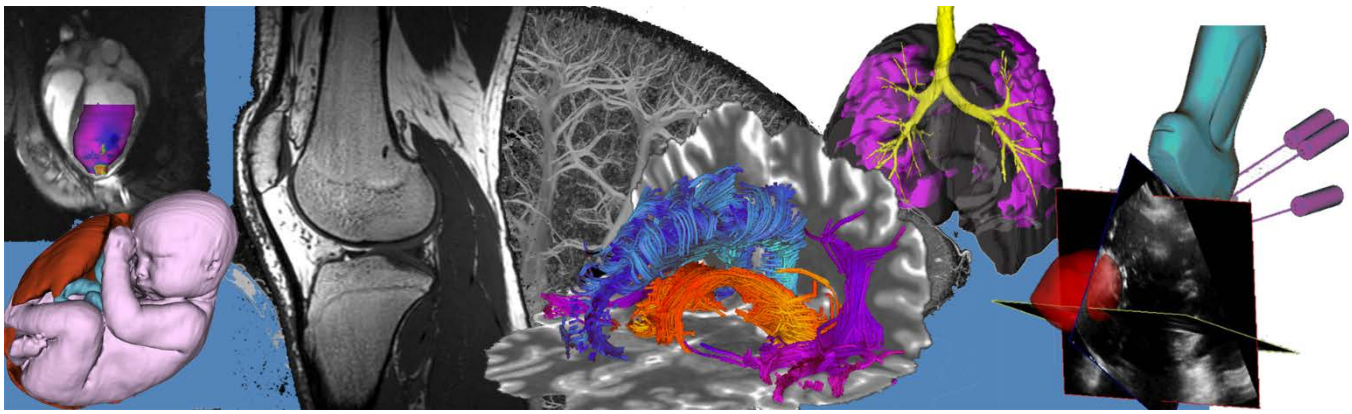

Impact of Real-Time Magnetic Resonance Thermometry Motion Compensation on Focused Ultrasound Controlled Hyperthermia in a Small Animal Model

Suzanne Wong[1,2], Claire Wunker[2,3], Ben Keunen[1], Maryam Siddiqui[4], Karolina Piorkowska[1], Yael Babichev[3], Warren Foltz[2,5], Rebecca Gladdy[2,3], Samuel Pichardo[4], Adam C. Waspe[1,2], James Drake[1,2]
[1]Hospital for Sick Children, [2]University of Toronto, [3]Mount Sinai Hospital, [4]University of Calgary, [5]University Health Network

Introduction. Magnetic resonance guided high intensity focused ultrasound (MRgHIFU) can administer localized hyperthermia at a temperature of 40°C for targeted drug release from thermosensitive liposomes. Image guidance and monitoring is performed with real-time, high resolution thermal maps, which provide a method to control thermal delivery and evaluate therapy accuracy at the treatment point. Our custom hyperthermia software, Proteus, controls tumor temperature to ±1°C based off real-time thermometry using a proportional integral derivative (PID) controller. One of the main challenges with MR thermometry is that it is highly susceptible to motion artifacts which confounds temperature measurements and can skew temperature readings. Real-time motion compensation algorithms can reduce temperature uncertainty to allow Proteus to deliver more accurate levels of sonication. The motion compensation algorithm used is a hybrid method of principal component analysis and projection onto dipole fields (PCA-PDF). The objective of this work is to demonstrate the ability of a real-time PCA-PDF motion compensation algorithm to negate motion artifacts from MR thermometry obtained from controlled hyperthermia treatments in a murine model.

Methods. Healthy immunocompetent mice (n=6) received 5 minutes of controlled hyperthermia in the hindlimb without PCA-PDF, followed by a 5-minute cooling period before a sequential 5-minute hyperthermia with real-time PCA-PDF. The hyperthermia was administered using a small-animal MRgHIFU system consisting of a 7T Bruker MRI (70/30 BioSpec, Bruker, Ettlingen, Germany) and Image Guided Therapy (IGT) HIFU device (LabFUS, IGT, Pessac, France). Experimental set-up is shown in Figure 1. Proteus monitored the temperature in a region of interest (ROI) set in the hindlimb with a target temperature set at 40.5°C. A drift tube measured any MR bore temperature shift over time. Retrospective PCA-PDF analysis was completed on the hyperthermia sessions without motion compensation. The sonication power was analyzed by calculating the spatial average temporal average intensity (I_{SATA}). A paired t-test was performed between I_{SATA} values for the hyperthermia with and without the PCA-PDF algorithm, where a p-value < 0.05 is deemed statistically significant.

Results. Figure 2 shows the average I_{SATA} values for the controlled hyperthermia with no motion compensation and real-time PCA-PDF, which were statistically different at 424 W/cm^2 and 683 W/cm^2 respectively. Over the 5-minute hyperthermia treatment without motion compensation, the average temperature was 39.6°C ± 1.3°C for the mice. Retrospective PCA-PDF motion artifact removal completed on these hyperthermia treatments decreased the average temperature significantly to 37.4°C ± 1.1°C. The hyperthermia treatments with the real-time PCA-PDF motion compensation algorithm had an average temperature of 39.6°C ± 1.0°C.

Conclusions. Ideal hyperthermic temperatures can be maintained with more confidence that motion isn't overestimating the temperature when using the PCA-PDF algorithm in real-time. By removing any motion artifacts present, the PID controller required significantly higher levels of sonication power to reach the same target temperature. Future work includes investigating whether implementing the real-time PCA-PDF algorithm leads to increased drug release in vivo.

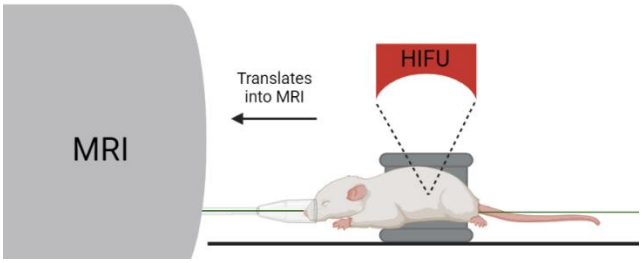

Figure 1: Experimental set-up for controlled hyperthermia administered by a small-animal MRgHIFU on anesthetized mice. Rectal and esophageal probes were used to monitor body core temperatures.

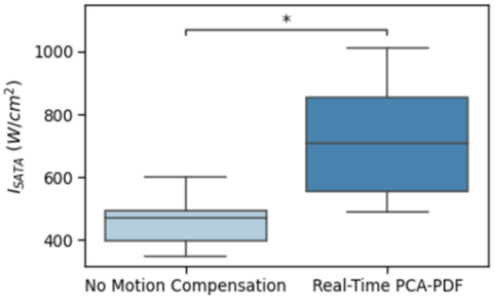

Figure 2: I_{SATA} for all 6 mice for the hyperthermia sessions with and without real-time PCA-PDF applied. There was a statistically significant difference between the two groups ($p<0.05$).

Combining colour and ultrasound video for central venous catheterization workflow recognition

Rebecca Hisey, Colton Barr, Gabor Fichtinger, Tamas Ungi

Laboratory for Percutaneous Surgery, School of Computing, Queen's University, Kingston, Canada

Introduction: Computer-assisted skill assessment has made substantial progress in the improvement of simulated medical skills training. Unfortunately, even current state-of-the-art systems still rely on sensor-based tracking systems to monitor workflow progress and assess motion quality. This reliance on additional sensors is not only expensive and cumbersome, but it also reduces the face and predictive validity of any training system as sensors add weight to the surgical tools and tracking is not readily available in a real patient setting. Central Line Tutor is a training system that has been designed to provide trainees with automated instruction and feedback during independent, simulated practice of central venous catheterization (CVC). Central Line Tutor has previously relied on electromagnetic (EM) tracking to recognize tasks that require knowledge of where the tools are relative to the internal anatomy of the phantom. In this study, we investigate the feasibility of combining video streams from a webcam and ultrasound (US) machine to recognize these tasks that were previously recognized by tracking.

Methods: We propose three different network architectures to combine the US and webcam video to perform workflow recognition. Each of these networks is composed of a different combination of 3 distinct network blocks. We will refer to these blocks as: CNN block, U-Net block and LSTM block. The three architectures can be distinguished from one another based on when they merge the data from the US and webcam video frames and so we will refer to them as Early-merge, Mid-merge and Late-merge models. The general structure of each architecture is shown in Figure 1. We compare the performance of each network to Central Line Tutor's current approach to workflow recognition using the webcam video and EM tracking.

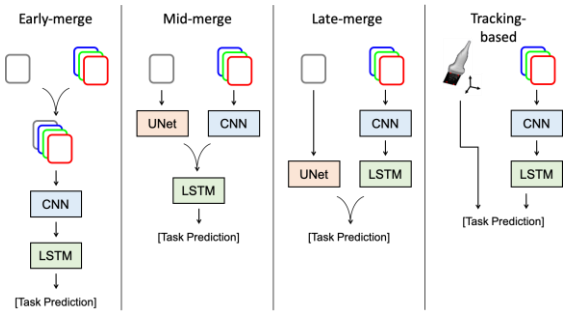

Figure 1. General structure of network architectures

To evaluate our networks, participants recorded 40 trials of CVC being performed on the Central Line Tutor setup. The participants included 4 attending anesthesiologists and 4 medical students. The recordings contained synchronized US and webcam video streams, as well as the tracking information from EM sensors placed on the needle, US probe and phantom. After the trials were recorded the videos were divided into individual frames. The webcam video frames were labelled with the workflow task being performed. The possible task labels included: cross-section US scan, long-axis US scan, insert needle, or other. The US video frames were labelled with the segmented location of the simulated blood vessels. Each network was trained on the labelled images using a leave-two user out cross validation scheme. In each fold, all videos from one novice and one expert were reserved for testing, one video from each of the remaining 6 participants was randomly selected for validation and all remaining videos were used for training. To measure the performance of each of the three architectures and the previous tracking-based approach, we computed the average accuracy, precision and recall for each fold.

Results: The overall accuracy for the new architectures were 84.4%, 87.0% and 87.8% for the Early, Mid and Late-merging models respectively. The original tracking-based method achieved an average accuracy of 86.7%. The Mid-merge model had the highest average precision of the new architectures at 79.5%, whereas the Late-merge model had the highest recall at 76.5%. The tracking-based approach had an average precision and recall of 80.6% and 76.8% respectively. There was no significant difference in precision or recall between any of the new architectures and the tracking-based method ($p < 0.05$).

Conclusions: Both the Late and Mid-merging models obtained higher overall accuracy compared to the tracking-based method. Given that there was no significant difference between any of the combined video-based approaches and Central Line Tutor's current tracking-based method, we conclude that tracking can feasibly be replaced by combining webcam and US video for task recognition in CVC.

Acknowledgements: This work was funded, in part, by NIH/NIBIB and NIH/NIGMS (via grant 1R01EB021396-01A1), by CANARIE's Research Software Program, and is supported as a Collaborative Health Research Project (CHRP #127797) by the Natural Sciences and Engineering Research Council of Canada (NSERC) and the Canadian Institutes of Health Research (CIHR). R. Hisey is supported by the Canada Graduate Scholarship from NSERC. G. Fichtinger is supported as a Canada Research Chair.

Identifying tissues for task recognition in training of open inguinal hernia repairs

Elizabeth Klosa[a], Rebecca Hisey[a], Tahmina Nazari[b], Theo Wiggers[c], Boris Zevin[d], Tamas Ungi[a], Gabor Fichtinger[a]

[a]Laboratory for Percutaneous Surgery, School of Computing, Queen's University, Kingston, Canada
[b]Department of Surgery, Erasmus University Medical Center, Rotterdam, The Netherlands
[c]Incision Academy, Amsterdam, The Netherlands
[d]Department of Surgery, Queen's University, Kingston, Ontario, Canada

Introduction: Competency-based medical training requires experts to continually instruct and assess surgical residents. The extra time spent by experts in doing this can be mitigated by introducing a computer-guided training platform to guide residents through procedures and provide them with feedback. In order to provide instruction, we first need to recognize the surgical workflow. In this study, we work towards recognizing workflow tasks of an open inguinal hernia repair. The tasks in this procedure are recognizable based on the interactions of various surgical tools with different tissues. This study thus aims to train a neural network to identify tissues of an IHR phantom as we work towards identifying the tool-tissue interactions needed for task recognition.

Methods: Five surgeons performed an open IHR on a synthetic phantom previously developed by Nazari *et al*[1]. They wore head-mounted cameras to record the procedure. The phantom represented the male groin region, including the skin, subcutaneous tissue, superficial epigastric vessels, Scarpa's fascia, external oblique aponeurosis, spermatic cord, hernia sac, and nerves. The tissues were segmented throughout 1708 frames from the five videos and each pixel was assigned a class label for a tissue or nothing. The percentage of frames each tissue appeared in can be seen in Figure 1. A U-Net was trained using leave-one-user-out cross validation. The F-scores, false positive rates and false negative rates were computed for each tissue to evaluate the U-Net's performance.

Figure 1: Percentage of frames each tissue appeared in

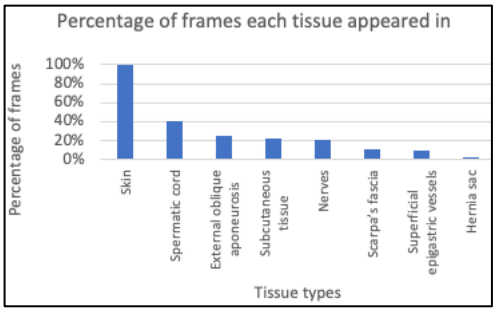

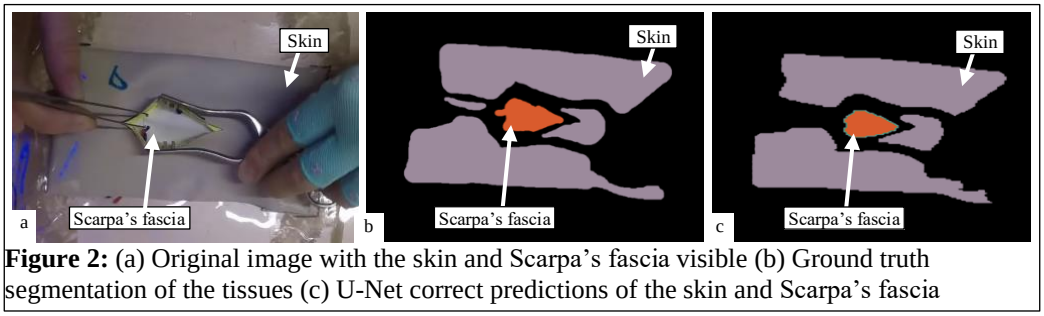

Figure 2: (a) Original image with the skin and Scarpa's fascia visible (b) Ground truth segmentation of the tissues (c) U-Net correct predictions of the skin and Scarpa's fascia

Results: The U-Net produced higher F-score values for the spermatic cord, skin, and nothing with F-scores of 0.61, 0.69, and 0.97. The U-Net produced slightly lower F-scores for the subcutaneous tissue, Scarpa's fascia, and external oblique aponeurosis, with values of 0.39, 0.37 and 0.43. The superficial epigastric vessels, hernia sac, and nerves were often not recognized. Figure 2 shows a U-Net prediction in which the skin and Scarpa's fascia were correctly classified.

Conclusions: The U-Net performed better in recognizing nothing, the skin, and the spermatic cord, as these classes were more prevalent in the videos and represented larger portions of the dataset. The U-Net struggled to recognize the hernia sac, vessels and nerves, as they were present in less frames and took up smaller portions of the frames. The Scarpa's fascia and external oblique aponeurosis were often misclassified with each other as they were made of similar materials on the IHR phantom. However, since the videos were recorded at 20 frames/second, the tool-tissue interactions last for multiple frames. Thus, misclassifications in individual frames will not be important in task recognition as long as the majority of the classifications for a given interaction are correct. As well, since some tissues are only visible after previous steps, we can mitigate misclassifications by incorporating procedural knowledge. We thus believe our U-Net can sufficiently recognize tissues for workflow recognition. Future studies will look to recognize tool-tissue interactions as we develop a computer-guided IHR training platform.

References:

[1] Nazari, T., Simons, M.P., Zeb, M.H., et al., "Validity of a low-cost Lichtenstein open inguinal hernia repair simulation model for surgical training," Hernia 24, 895–901 (2020).

Development of a mini stereotactic guidance system for percutaneous liver tumour ablation

Joeana Cambranis Romero[a], Terry M. Peters[a,b,c], and Elvis C. S. Chen[a,b,c]
[a]School of Biomedical Engineering, [b]Robarts Research Institute, [c]Department of Medical Biophysics, Western University, London, Ontario, Canada

Introduction: Percutaneous ablation is a viable treatment option for patients with early-stage hepatocellular carcinoma (HCC) who are not candidates for surgical resection or liver transplantation[1,2]. Focal heating is achieved through the placement of the applicator in the center of the target, around which heating occurs[3]. The efficacy of the ablation depends heavily on the surgeon's ability to place the ablation probe accurately into the target tumor. We hypothesize that the combination of electromagnetic tracking and mechanical stabilization provided by the needle guider will improve the targeting accuracy for the focal treatment of HCC.

Methods: A patient-attached "mini" aiming device (CuraWay Medical Technology, China) with stereotactic characteristics was used as the main component. The guidance device is attached to the patient skin at the, previously planned, "point of entry" of the applicator. The range of angle movement of the guider is ~180 degrees. An Electromagnetic (EM) Tracking System (Aurora Tracking System, NDI, Canada) was used to track the needle guider turntable position. An EM pose sensor (Aurora 5DOF FlexTube, NDI, Canada) was placed and secured to the guider using a specific design clamp. Using the platform 3D Slicer, a guidance module was created. A guider calibration was performed by acquiring points of a pre-calibrated needle () while being inserted into the guider and then acquiring the least square fitting of the obtained points. The resultant curve parameters were then applied to the transform matrix of the sensor attached to the guider and a virtual line was projected according to the position of the sensor. For displaying the estimated ablation zone, a model of an ellipsoid was generated using 3D slicer, with parameters added before the procedure by the user depending on the parameters used in the ablation procedure. The estimated zone usually is provided by the clinical systems, which are based on the design of the ablation applicator and treatment parameters. Testing will be performed using an ultrasound-compatible anthropomorphic liver phantom with vasculature and simulated tumors. A simulated ablation procedure will be performed inserting an ablation needle to the phantom using the aiming device and guidance module.

Results: The guidance system projects a virtual line that follows the needle guider movements and shows the applicator path before needle insertion (Fig 1.a). The estimated ablation zone is displayed at the tip of the virtual line to help the user ensure total tumor coverage before needle insertion. The ablation zone is displayed in a 3D environment and a 2D Ultrasound view to guarantee complete tumor volume coverage (Fig 1.a and b).

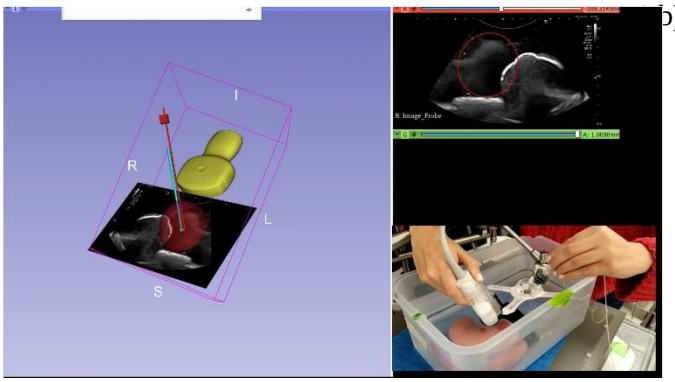

Figure 1 a) Surgical navigation system in a 3D environment (virtual path, ablation zone, and needle) b) 2D display of the ablation zone in real-time. c) Real-life aiming device and needle

Conclusion: We developed a guidance system using a mini stereotactic aiming device that projects a virtual line and estimation ablation zone before needle insertion. We believe that the ablation zone estimation and the virtual line projection in real-time will help the physician to reach the target, ensure tumor coverage and reduce needle reposition.

References: [1] Lencioni, R., Cioni, D., Crocetti, L., and Bartolozzi, C., \Percutaneous ablation of hepatocellular carcinoma: State-of-the-art," Liver Transplantation 10, 91{97 (2004)
[2] Marrero, J. A., Kulik, L. M., Sirlin, C. B., Zhu, A. X., Finn, R. S., Abecassis, M. M., Roberts, L. R., & Heimbach, J. K. (2018). Diagnosis, Staging, and Management of Hepatocellular Carcinoma: 2018 Practice Guidance by the American Association for the Study of Liver Diseases. Hepatology (Baltimore, Md.), 68(2), 723–750. [3] Van Sonnenberg, E., McMullen, W. N., and Solbiati, L., eds., [], Springer, New York, NY (2005)

Pitch Session 11: Lung Imaging

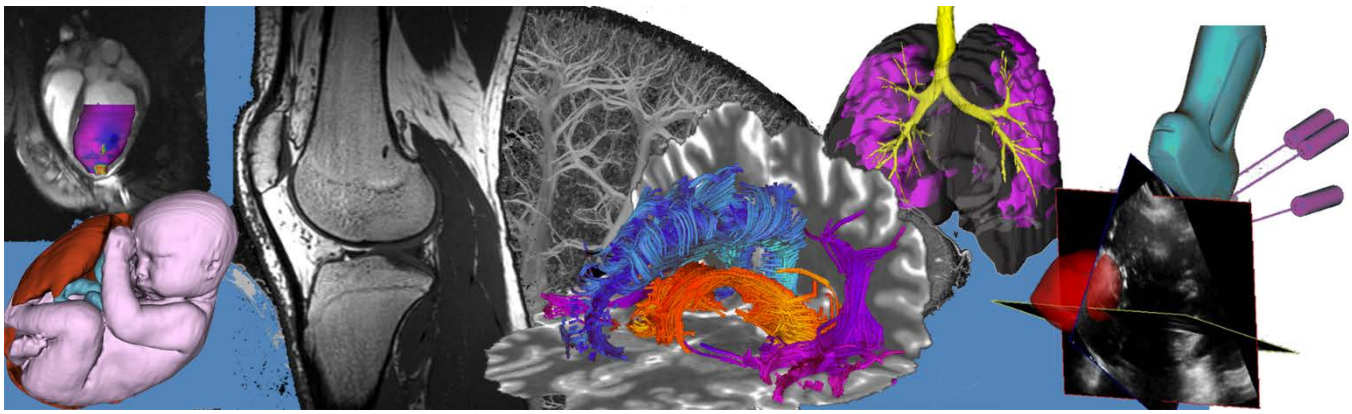

Comparison of Computed Tomography Texture-based Radiomic Features with Machine Learning for Predicting Chronic Obstructive Pulmonary Disease

Authors and Institutions: Kalysta Makimoto BSc[1], Ryan Au MSc[2], Amir Moslemi MSc[1], James C. Hogg MD, PhD[3], Jean Bourbeau MD[4,5], Wan C. Tan MD[3] and Miranda Kirby PhD[1]

[1]Ryerson University, Ontario, Canada; [2]Western University, Ontario, Canada; [3]Center for Heart, Lung Innovation, University of British Columbia, Vancouver, Canada; [4]Montreal Chest Institute of the Royal Victoria Hospital, McGill University Health Centre, Montreal, QC, Canada; [5]Respiratory Epidemiology and Clinical Research Unit, Research Institute of McGill University Health Centre, Montreal, QC, Canada.

Introduction: Radiomics is an emerging area in image analysis that involves converting medical images, most commonly from either computed tomography (CT) or magnetic resonance imaging (MRI), into numerical features that can be investigated with machine learning methods. Texture-based radiomic features include 6 different feature sets that are calculated based on different voxel distributions of the various grey-level intensity values, including: grey level co-occurrence matrix (GLCM), grey level distance zone matrix (GLDZM), grey level run length matrix (GLRLM), grey level size zone matrix (GLSZM), neighbouring grey level dependence matrix (NGLDM), and neighbourhood grey tone difference matrix (NGTDM). CT radiomics-based analysis has shown potential for diagnosis and monitoring in chronic obstructive pulmonary disease (COPD). However, with a variety of different texture-based radiomic sets used between studies, it is unknown if the use of different feature sets impact COPD prediction performance. The objective of this study was to compare the different feature sets and determine the optimal texture-based radiomic features extracted from CT images for COPD prediction with the use of the machine learning.

Methods: CT images from the multi-center (9 sites) Canadian Cohort Obstructive Lung Disease (CanCOLD) study were pre-processed by resampling the image to a 1mm isotropic voxel volume, segmenting the lung and removing the airways (VIDA Diagnostics Inc.), and applying a threshold of -1000HU to 0HU. A total of 95 unique texture-based radiomics features were then extracted from each CT image: n=25 GLCM, n=16 GLDZM, n=16 GLRLM, n=16 GLSZM, n=17 NGLDM, n=5 NGTDM. Z-normalization was applied to all extracted features. Separate models containing each of the six feature sets, as well as all features from all feature sets, resulting in 7 different models were evaluated. The cohort was split into a training dataset (8 sites) and a testing dataset (1 site), to train and test the machine learning model. The L-based support vector machine (SVM) feature selection method was applied to select the top 5 features for each model. These selected features were then implemented with the logistic regression classification method to determine the prediction accuracy for each model. The area under the curve (AUC) from the receiver operating characteristic curve was used to evaluate the model prediction performance with the testing dataset. The most important features were identified by determining the feature importance scores with the training dataset, using the built-in functions in the sci-kit learn python package.

Results: A total of 1204 participants were evaluated (n=570 no COPD, n=634 COPD). There were no significant differences between the groups for female sex (no COPD=48.6%; COPD=36.9%; p=0.11), or BMI (no COPD=27.4kg/m^2; COPD=26.9kg/m^2; p=0.07). Among all models, the highest accuracy was obtained when the GLDZM feature set was evaluated (AUC=0.718). The lowest accuracy was obtained when the GLRLM feature set was evaluated (AUC=0.575). For the model including all 6 feature sets, an accuracy was obtained when the top 5 features were selected (AUC=0.715). From all the features combined, the top 5 features that were identified as the most important included 4 features from the GLDZM feature set and 1 feature from the GLSZM feature set.

Conclusion: Different texture-based radiomic feature sets have different prediction performance for COPD. We showed that the optimal feature set for the prediction of COPD was the GLDZM feature set when the top 5 features were selected. We also showed that when the top 5 features from all feature sets were evaluated, 4/5 of the selected features were GLDZM features. Overall, the GLDZM feature set has the most optimal performance in terms of accuracy, and those features were selected even in the model with all the features included. Due to increased computation time when more features are inputted into a machine learning model, the optimal features to include for the prediction of COPD is the GLDZM feature set.

Intra-Visit and Inter-Visit Repeatability of ^{129}Xe Multiple-Breath Washout MRI in Children with Stable Cystic Fibrosis Lung Disease.

Faiyza Alam[1,2], Brandon Zanette[2], Sharon Braganza[2], Daniel Li[2], Felix Ratjen[2,3] and Giles Santyr[1,2].
[1]Department of Medical Biophysics, University of Toronto, Toronto, ON, Canada,[2]Translational Medicine Program, The Hospital for Sick Children, Toronto ON, Canada, [3]Division of Respirology, The Hospital for Sick Children, Toronto, ON, Canada

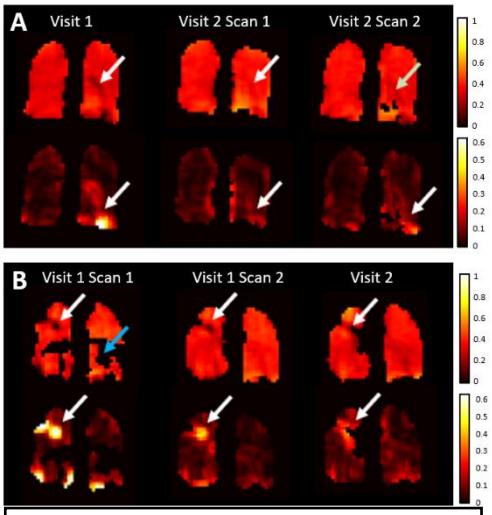

Figure 1: FV (top) and CoV (bottom) maps for A: healthy subject and B: stable CF subject.

Introduction: Conventional pulmonary function tests (PFTs), such as spirometry, are insensitive to early lung function changes in pediatric CF[1]. This is particularly important for monitoring the effects of new CFTR modulator treatments. The lung clearance index (LCI) derived from the multiple breath washout (MBW) test is more sensitive[2] but limited to whole-lung averages of the temporal heterogeneity of washout[3]. Hyperpolarized ^{129}Xe MRI (Xe-MRI), conducted in a MBW fashion, yields maps of fractional ventilation (FV), a measure of percent gas clearance per breath[3,4,5,6]. This approach provides insight into regional temporal dynamics of gas washout, making it potentially more sensitive to paediatric CF. Before Xe-MRI is used to assess treatment response, its repeatability in stable CF must be established. This work shows the intra- and inter-visit repeatability of Xe-MRI from baseline to one-month in paediatric stable CF.

Methods: 23 subjects were recruited (5 healthy, 18 stable CF, median age 15 [range=11-18]), 2 visits each (baseline, one-month). Intra-visit repeatability was assessed with repeat scans during a given visit (6 CF, 3 healthy). Each visit involved spirometry (FEV1), N_2 MBW (LCI), and Xe-MRI (FV). The coefficient of variation (CoV) defined as the standard deviation over mean of FV in one pixel compared to neighbouring pixels was used as a measure of ventilation heterogeneity. Xe-MRI was performed as described by Couch et al[3], with the exception that the ^{129}Xe bag was topped up with N_2 to a volume of 1/6th TLC and inhaled from FRC[7]. Data analysis was performed using the variable T_1 method[3]. For statistical analysis, inter-class coefficient (ICC), coefficients of variation (CV%) and reproducibility (CR), and Pearson correlation (R) were calculated on the FV and CoV map means. Results from healthy and CF subjects were compared via t-test. The correlation of FV and CoV with PFT's was also tested using the Pearson correlation.

INTRA-VISIT REPRODUCIBILITY					
	n	ICC	CV (%)	CR (+/-)	R
FV CF	6	0.766	8.03	0.057	0.601
FV H	3	0.930	7.92	0.043	0.954
CoV CF	6	0.723	18.60	0.040	0.717
CoV H	3	0.741	14.96	0.022	0.796
INTER-VISIT REPRODUCIBILITY					
	n	ICC	CV (%)	CR (+/-)	R
FV CF	11	0.870	11.53	0.060	0.805
FV H	6	0.949	8.09	0.035	0.921
CoV CF	11	0.838	29.86	0.045	0.787
CoV H	6	0.720	27.86	0.032	0.681

Table 1: Summary of statistics. n represents number of samples.

Results: Figure 1 shows representative FV and CoV maps (white arrow points to a consistency, blue arrow is an artifact of the processing pipeline). ICC, CV%, CR, and R are listed in Table 1. Intra-visit ICC was excellent for FV_H (0.930), good for FV_{CF} (0.766), and moderate for CoV_{CF} (0.723), CoV_H (0.741). Inter-visit ICC was excellent for FV_H (0.949), good for FV_{CF} (0.870), CoV_{CF} (0.838), and moderate for CoV_H (0.720). R showed strong linear correlations for all metrics. Intra-visit CR and CV% was smaller than inter-visit. Inter-visit is more repeatable than intra-visit for all metrics except CoV_H. The strongest correlation found was CoV_{CF} with LCI_{CF} (R=0.55). CoV distinguished health from disease at 5% significance while FV did not.

Conclusions: In summary, Xe-MRI has good inter- and intra-visit repeatability for both $FV_{H,CF}$ and $CoV_{H,CF}$. CoV distinguished health from disease and correlated significantly with LCI. Inter-visit repeatability was higher in CoV_{CF} than CoV_H. This unexpected result may be due to ventilation defects in stable CF serving as anchors to improve repeatability, with such anchors non-existent in healthy subjects. The ability of CoV to distinguish health from disease and correlate with LCI in CF is note-worthy, especially with FV more repeatable than CoV (intra/inter-visit). This may point to the importance of spatial heterogeneity of FV in CF compared to the average value of FV, a finding consistent with previous work[6,8]. With repeatability established, Xe-MRI may provide a novel approach for following pediatric CF lung disease progression and treatment response.

REFERENCES: [1] Marshall et al., CF Foun Pat Reg 2019. (2020), 43. [2] Stanojevic et al., AJRCCM. (2017) 195(9), 1216-1225. [3] Couch et al., MRM. (2019) 84(1), 304-311. [4] Horn et al., J Appl Physiol. (2014) 116, 129-139. [5] Horn et al., MRM. (2017) 77, 2288-2295. [6] Horn et al., Proc Intl Soc MRM. (2015), 23. [7] Thomen et al., J of CF. (2017) 16(2), 275-282. [8] Safavi et al., Resp Med. (2021) 180, 106368.

The Use of the ^{129}Xe MRI *v*ADC Approach for the Emphysema Progression Evaluation

Elnaz Parniyany[1], Elise Woodward[1], Tingting Wu[1], Matthew S Fox[1,2], and Alexei Ouriadov[1-3].
[1]Department of Physics and Astronomy, The University of Western Ontario, London, Canada [2]Lawson Health Research Institute, London, ON, Canada [3]School of Biomedical Engineering, Faculty of Engineering, The University of Western Ontario, London, Ontario, Canada

INTRODUCTION: Hyperpolarized (HP) ^{129}Xe lung MRI[1,2] is an efficient technique used to investigate and assess pulmonary diseases. The longitudinal observation of the emphysema progression using HP gas MRI-based ADC (apparent diffusion coefficient) can be problematic, as the disease progression can lead to increasing unventilated lung areas, which likely excludes the largest ADC estimates.[4] One solution to this problem is to combine static-ventilation (SV) and ADC measurements following the idea of ventilatory ADC (*v*ADC).[4] Clearly, the SV measurements providing the gas-distribution should still show an increase in the ventilation defects reflecting emphysema-progression. We hypothesize that this method adapted for ^{129}Xe MRI should help to overcome the above-mentioned shortcomings and provide an accurate assessment of the emphysema-progression. For this work, we used the SV and ADC data acquired using ^{129}Xe MRI to demonstrate the feasibility of the xenon *v*ADC approach and evaluation of emphysema-progression.

METHODS: 5 patients, underwent spirometry and ^{1}H/^{129}Xe (SV and ADC) MRI scans. ^{129}Xe imaging [3]was performed at 3.0T (MR750, GEHC, WI) using whole-body gradients (5G/cm max) and a commercial ^{129}Xe quadrature-flex RF coil.[5] HP ^{129}Xe gas (polarization=35%) was obtained from a turn-key, spin-exchange polarizer system (Polarean-9820 ^{129}Xe polarizer).[6] The DW data were reconstructed using the key-hole- method[7,8] to get matching resolution with SV. Calculated ADC values[5] were normalized on the corresponding ventilation defect percent (VDP, calculated as previously described[9]) estimates to obtain *v*ADC (=**ADC/(1 – VDP/100)**,[4] Table 1).

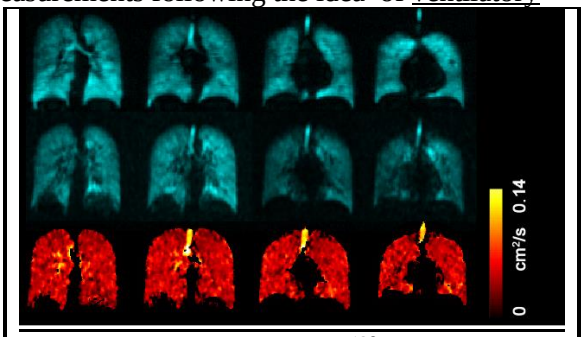

Figure 1: Representative ^{129}Xe MRI static-ventilation images (top-panel), matched voxel-size unweighted (b=0) images (middle-panel), and correspondening ADC maps (bottom-panel) in coronal view obtained for P2.

Table 1: Patient demographics and ^{129}Xe MRI results

	P 1	P2	P3	P4	P5
Age	74F	76M	29F	61F	36M
BMI (kg/m²)	33.6	36.6	19.2	38.4	32.0
FEV_1 %	71	78	67	117	76
FVC %	91	73	92	111	73
RV %				73	116
DL_{CO}%				83	91
VDP %	18	7.4	5.0	12.7	5.9
ADC (SD) s/cm²	0.034 (0.016)	0.041 (0.015)	0.037 (0.013)	0.04 (0.015)	0.048 (0.016)
***v*ADC, s/cm²**	0.042	0.043	0.038	0.047	0.048
SV SNR	15.0	14.0	24.0	29.0	40.0
UW SNR	13.0	16.0	20.0	18.0	21.5

P=Patient; BMI=body mass index; FEV_1=forced expiratory volume in 1 second; FVC=forced vital capacity; RV=residual volume; DL_{CO}=diffusing capacity for carbon monoxide; ^{129}Xe MRI-based VDP=ventilation defect percent; ADC=apparent diffusion coefficient; *v*ADC= ventilatory ADC; SNR=signal to noise ratio; SV=static-ventilation image; UW=un weighted image.

RESULTS: Figure 1 show the acquired SV images (top-panel), matched voxel-size unweighted (b=0) images (middle-panel) and corresponding ADC maps (bottom-panel) in coronal view for Parcipant-2. Table 1 summarizes demographic and PFT-information, as well as imaging results including SNR (central slice) for SV and matched voxel-size unweighted images, global mean VDP**,** and global mean ADC/*v*ADC.

DISCUSSION & CONCLUSION: The diffusion data reconstructed with the key-hole-technique had sufficient SNR to generate reliable ADC maps and reasonable matching (visual image similarity) with the SV data. For the first time the feasibility of the *v*ADC ^{129}Xe MRI-based approach was demonstrated and shown that this method can be potentially used to evaluate the emphysema progression. To proof this concept, we plan to rescan the study participants in 12 months, so we have two sets of the SV and ADC data to generate *v*ADC and demonstrate the emphysema progression over the year using the *v*ADC approach.

We acknowledge the support of NSERC, R5942A04, and a UWO Research Catalyst Grant, R5942A03.

References:

1.Mugler, J.P., et al. *JMRI*, 2013. 37(2): p. 313-31
2. Driehuys, et al., Radiol, 2012. 262(1): p. 279-89.
3. Young, H. M., Clinbiomech, 2017.p. 09.016
4. Westcott, A. *JMRI*,2019. 49(2):p. 311-13
5. Svenningsen*et al.* J.ACRA.2021. 28(2):p. 817-26.
6. Kaushik, *et al.* MRM.2016.75(2) :p. 1434-1443
7. Kirby, M. *et al. Radiol.2012.19(2)* :p. 141-152
8. Ranota, T. K., *Isotropic* Voxel 129Xe MRI.*2021*
9. Niedbalski, P. J. *et al. Mrm.2019.82(2):p.367-76*

Fractal Dimensions of airway Surfaces from Computed Tomography in Chronic Obstructive Pulmonary Disease

Jason Bartlett (MSc Candidate)[6], James C. Hogg (MD, PhD)[7], Jean Bourbeau[8,9], Wan C. Tan (MD)[7] and Miranda Kirby (PhD)[6]

Introduction: Histology and CT studies have shown that as the severity of Chronic Obstructive Pulmonary Disease (COPD) increases, the surfaces of the peripheral and central airway tree exhibits increased surface roughness due to tissue inflammation[1;2]. Current *in vivo* CT airway measurements such as Wall Area Percent and Lumen Diameter do not fully capture such changes in roughness, and to do so requires new methods. One such method is Fractal analysis, which has been used to characterize the roughness of natural rock surfaces, and has shown that an increase in a surfaces fractal dimension (FD) can be associated with an increase in its overall surface roughness[3]. We hypothesize that the airway tree surfaces of patients with COPD will have increased FD compared to those without COPD and that increased FD values will be significantly correlated with spirometry lung function measurements.

Methods: From CanCOLD[4] 1324 subjects were selected for segment surface analysis and grouped according to disease severity using GOLD[5] guidelines according to spirometry lung function measurements Forced Expiratory Volume in one second (FEV_1) and the ratio of FEV_1 over Forced Vital Capacity (FEV_1/FVC). Full-inspiration CT images were segmented and labelled. An airway segment was defined as the segment between branch points. Segment surfaces were mapped using multiple slices composed of 72 radial points. Surface meshes were then generated by finding the deviation (δ) between all radial points and their equivalent arc location (q_2) on an ideal cylinder of equivalent diameter aligned to the central axis of the segment (q_1)[6]. FD values were generated using a 3d box counting method, where a surface meshes FD is equivalent to the slope of $log(n(r))/log(1/r)$; where $n(r)$ is the number of boxes of size $r=2^k$; $k=:\{0,1,\ldots,7,8\}$ required to cover the surface[3]. Comparison between no-COPD and COPD groups was performed using a one-way analysis of variance (ANOVA).

Results: Of 1324 subjects evaluated, the no-COPD group contained n=684 and the COPD group contained n=640 subjects. The outer Trachea surfaces demonstrated a significant increase in segment FD values between the no-COPD and COPD groups ($|\Delta FD|=0.01$, $p<.001$) *(figure 1)*. Furthermore, Pearson correlations identified that FD values are positively correlated with FEV_1 [$r=.312$, $p<.001$], and negatively correlated with FEV_1/FVC [$r=-.141$, $p<.001$].

Conclusion: We demonstrated fractal measurements reflect changes to airway tree surface roughness in COPD and are related to airflow limitation. These results indicate that FD airway roughness is a novel imaging biomarker and may be useful for quantifying the extent of longitudinal changes in airway tree surface inflammation/remodeling.

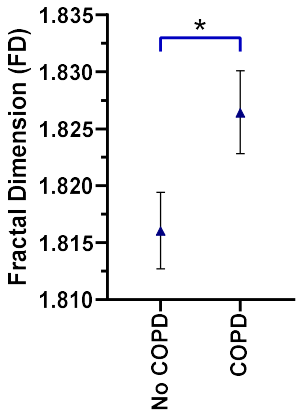

Figure 1: Outer Surface FD (95% confidence), *=significance

[1] Baraldo, Turato, and Saetta, "Pathophysiology of the Small Airways in Chronic Obstructive Pulmonary Disease."
[2] Pini et al., "Central Airways Remodeling in COPD Patients."
[3] Ai et al., "Box-Counting Methods to Directly Estimate the Fractal Dimension of a Rock Surface."
[4] Bourbeau et al., "Canadian Cohort Obstructive Lung Disease (CanCOLD)…"
[5] Global Initiative for Chronic Obstructive Lung Disease, "GOLD Report 2020."
[6] Qiao et al., "Approach to the Deviation Representation of Non-Ideal Cylindrical Surfaces..."

Author Affiliations:
[6] Department of Physics, Ryerson University, Toronto, ON, Canada; [7] UBC Centre for Heart Lung Innovation, St. Paul's Hospital, Vancouver, BC, Canada; [8] Montreal Chest Institute of the Royal Victoria Hospital, McGill University Health Centre, Montreal, QC, Canada; [9] Respiratory Epidemiology and Clinical Research Unit, Research Institute of McGill University Health Centre, Montreal, QC, Canada.

The Use of Two De-Noising Methods in Healthy Rats for ^{129}Xe Diffusion-Weighted and ^{19}F/^{129}Xe Dynamic-Ventilation MRI Imaging

Elise Noelle Woodward[1], Gregory Lemberskiy[2], Matthew S Fox[1,3], and Alexei Ouriadov[1,3]
[1]Physics and Astronomy, Western University, London, ON, Canada, [2]New York University Grossman School of Medicine, New York, NY, United States, [3]Lawson Health Research Institute, London, ON, Canada

Introduction: Hyperpolarized gas, specifically diffusion-weighted (DW) and dynamic-ventilation (DV) lung imaging has provided relevant biomarkers such as specific diffusion length scale estimates ($L\mathrm{m}_D$) and mean-linear-intercept-estimate (L_m), which have proven important in the characterisation of lung disease progression.[1-3] Another useful metric is the regional-fractional-ventilation (r).[4-6] An issue with most DW/DV data is a noisy decay-tail accelerating the decays and leading to the over-estimation of the diffusion/ventilation decay rate constants.[7] We hypothesize that one can extract the accurate regional biomarkers by applying the MP-PCA based de-noising methods to DW/DV data.

Methods: Four normal-rats (Sprague Dawley rats) were studied (ethics board approved protocol). ^{129}Xe MR was performed at 3.0T (MR750, GEHC, WI). A single breath-hold, interleaved (eight interleaves) centric 2D FGRE DW sequence was acquired for a coronal slice (TE/TR=10.3ms/14.5ms, BW=8kHz, matrix size=64x64, and FOV=50x50mm^2, variable flip angle, 10sec breath-hold).[8] ^{19}F MRI ventilation measurements were performed using a 3.0T Philips Achieva Scanner. Pulse sequence details and the breathing protocol were previously described.[9] Two de-noising methods (Method-1: MP-PCA[18] & Method-2: MP-PCA preceded by hard-thresholding over a nuclear norm in k-space, in order to suppress noise-correlations from the reconstruction) were applied to the ^{129}Xe DW data, ^{19}F DV data, and ^{129}Xe dynamic-ventilation data. (*MP-PCA is a de-noising scheme focused on noise removal by decomposing images, reducing the size of noisy components and reconstructing the signal.*[10]) To improve this method, similar images are grouped before deconstruction. $L\mathrm{m}_D$ & L_m were generated using the stretched-exponential-model[11] as previously described.[12] Signal to noise ratio (SNR) was calculated as previously described.[13]

Results: Mean L_m & $L\mathrm{m}_D$ estimates (Fig.1, top-panel) for the original data were significantly larger compared to corresponding mean estimates obtained from the denoising-1 data ($p<.03$, Table). Original mean r estimates (Fig.1, bottom-panel) were significantly larger compared to corresponding mean r estimates for the denoising-2 data ($p<.08$, Table) and not significantly different from corresponding mean r estimates for the denoising-1 data ($p>.05$, Table).

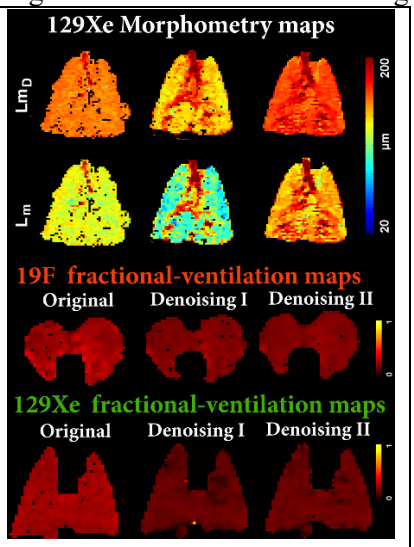

***Figure 1**. Representative ^{129}Xe MRI Lm_D/L_m maps obtained from original and de-noised data for normal rat (**top panel**). ^{19}F/^{129}Xe MRI-based r maps obtained from original and de-noised data for two rats (**bottom panels**).*

^{129}Xe MRI-based Morphometry Measurements

	Lm$_D$±SD (Org)	Lm$_D$±SD (Den-I)	Lm$_D$±SD (Den-II)
Mean±SD	145±20.0	125±55.0	150±25.0
p-value		0.013	0.091
	Lm±SD (Org)	Lm±SD (Den-I)	Lm±SD (Den-II)
Mean±SD	120±15.0	100±55.0	130±20.0
p-value		0.050	0.097

^{19}F (top) & ^{129}Xe MRI-based Fractional-Ventilation Measurements

	r±SD (Org)	r±SD (Den-I)	r±SD (Den-II)
Mean±SD	0.22±0.026	0.21±0.015	0.20±0.010
p-value		0.32	0.081
Mean±SD	0.23±0.010	0.17±0.020	0.17±0.020

***Table** showing overall pixel means for ^{129}Xe based Lm_D/L_m & ^{19}F/^{129}Xe based r.*

Discussion and Conclusion: The denoising method-2 led to significant over-estimation of $L\mathrm{m}_D$ & L_m and cannot be recommended for improving the DW ^{129}Xe MRI data. In turn, the ^{129}Xe/^{19}F DV data de-noised using the method-2 permitted to extract the reasonable mean r estimates, while the de-noising method-1 did not change the mean r estimate compared to r-estimates extracted from the original data. In this study, we demonstrated that the denoising-1 method improves SNR of DW data and therefore $L\mathrm{m}_D$ & L_m matched with the previously reported values. For the first-time we have demonstrated that the ^{129}Xe/^{19}F MRI images can be de-noised using two different methods and it does not lead to compromising the accuracy of the regional-biomarkers such as regional $L\mathrm{m}_D$, L_m, and r estimates.

References: Couch, M. J. et al. *NMR Biomed* 29, 545-552 (2016). 2. Couch, M. J., Ouriadov, A. V. & Albert, M. S. Hyperpolarized and Inert Gas MRI (2017) 3. Ouriadov, A. et al. *MRM* (2013). 4. Mugler, J. P., 3rd& Altes, T. A. *JMRI* (2013) 5. Driehuys, B. et al. *Radiology* (2012) 6. Santyr, G. E., Lam,W. W. & Ouriadov, A. *MRM* (2008) 7. Couch, M. J., Ouriadov, A. & Santyr, *MRM* (2012) 8. Ouriadov, A. et al. *MRM* (2016) 9. Ouriadov, A. V. et al. *MRM* 74 (2015) 10. Manjon, Jose V., et al. *PLoS ONE (2013)* 11. Parra-Robles, J., Marshall, H. & Wild, J. M. *ISMRM 21st Annual Meeting*, 0820 (2013) 12. Ouriadov, A. V. et al. *MAGMA* 34 (2021) 13. Santyr, G. E at al. *MRM* (2011)

We acknowledge the support of the Natural Sciences and Engineering Research Council of Canada, R5942A04

Optimization of Tube Voltage for Xenon-enhanced Dual-energy Radiography for Imaging Lung Function

Fateen Basharat[1] and Jesse Tanguay[1]

[1]Department of Physics, Ryerson University, Toronto, Ontario, Canada

Introduction: Chronic obstructive pulmonary disease (COPD) is one of the leading causes of adult morbidity and mortality in Canada. COPD is characterized by persistent airflow limitation due to emphysema and small airway disease. Functional imaging of COPD allows the possibility of earlier disease detection. Using mathematical models, we recently showed that xenon-enhanced dual-energy (XeDE) radiography may enable detection of functional abnormalities associated with early-stage COPD. (Med Phys.,47(12),2020.) The purpose of this work is to investigate the optimal tube voltage combination for XeDE imaging of lung function by theory and experiment.

Methods: We quantified the image quality of XeDE radiography in terms of the contrast-to-noise-ratio (CNR) of ventilation defects normalized by the square root of total patient entrance exposure (X_{tot}). Experiments were performed using a custom-built X-ray imaging cabinet and a custom-built chest phantom. The chest phantom consisted of a rectangular vacuum chamber and a PMMA slab. The vacuum chamber represented the thoracic volume and the PMMA slab simulated X-ray attenuation through soft tissue. Inside the vacuum chamber, a sealed air-filled cylinder with an inner length of 2 cm and radius of 1 cm was positioned. The vacuum chamber was ventilated with xenon and xenon could not diffuse inside the sealed cylinder. Therefore, the sealed air-filled cylinder simulated a 2-cm-thick ventilation defect. The fractional molar concentration of xenon was set to 0.5. Dual-energy imaging of the phantom was performed using a Rad-92 X-ray tube from Varex60 Imaging (Salt Lake City, UT) and a CsI/CMOS energy integrating X-ray detector (XINEOS-3030HS, Teledyne DALSA - Professional Imaging, Ontario, Canada) with 151.8 μm pixel width. We also theoretically modeled the CNR accounting for the contrast of ventilation defects, quantum noise, detector gain and noise and X-ray scatter. Image signal and noise were modelled using cascaded system analysis and accounted for the quantum efficiency, K fluorescence, optical collection efficiency, optical blur, and noise aliasing. The CNR of ventilation defects was optimized with respect to the tube voltage combination. We considered low-energy (LE) tube voltages ranging from 50 kV to 70 kV with 1.2 mm Al filtration and high-energy (HE) tube voltages ranging from 130 kV to 140 kV. The total entrance exposure was fixed at ~60 mR and ~1/3 of the total exposure was allocated to HE image.

Results: Our theoretical models of defect contrast, image noise and CNR agreed well with experimental results. The $\mathrm{CNR}/\sqrt{X_{\mathrm{tot}}}$ maximized at a LE tube voltage of 60 kV and has a weak dependence on the HE tube voltage. The optimal LE tube voltage was independent of HE tube voltage. Reasonable agreement between theory and experiment was observed.

Conclusion: Our analysis indicates that in XeDE radiography for imaging of lung function, the LE tube voltage has a stronger effect on defect CNR than the HE tube voltage. The results presented here can be used as a guide to optimization of X-ray-based xenon-enhanced imaging of lung function. Future work will focus on investigation of xenon-enhanced tomosynthesis for functional imaging of respiratory disease.

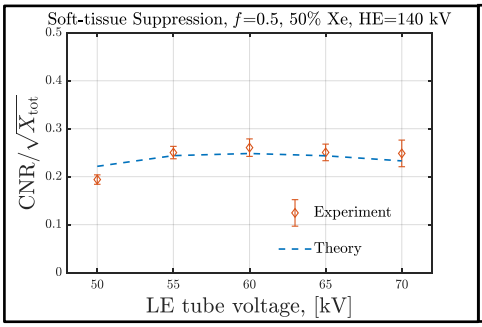

Figure 1: Modeled and measured $\mathrm{CNR}/\sqrt{X_{\mathrm{tot}}}$ as a function of LE tube voltage. Results are shown for HE tube voltage of 140 kV and exposure allocation (f) of 0.5

Inter- & Intra-visit Reproducibility of Free-Breathing Magnetic Resonance Imaging in Stable Pediatric Cystic Fibrosis Lung Disease

Samal Munidasa[1,2], Brandon Zanette[1], Marcus Couch[3], Robert Grimm[4], Ravi Seethamraju[5], Marie-Pier Dumas[6], Wallace Wee[6], Jacky Au[6], Sharon Braganza[1], Daniel Li[1], Felix Ratjen[1,6], Giles Santyr[1,2]
[1]Translational Medicine Program, The Hospital for Sick Children, Toronto, ON, Canada.
[2]Department of Medical Biophysics, University of Toronto, Toronto, ON, Canada.
[3]Siemens Healthcare Limited, Montreal, QC, Canada.
[4]MR Application Predevelopment, Siemens Healthcare GmbH, Erlangen, Germany.
[5]MR Collaborations North East, Siemens Healthineers, USA
[6]Division of Respiratory Medicine, The Hospital for Sick Children, Toronto, ON, Canada.

Introduction. Hyperpolarized ^{129}Xenon-MRI (Xe-MRI) has been shown to reveal abnormal pulmonary ventilation distributions in lung disease but requires a breath-hold, which can be challenging in very sick and/or young children[1]. Free-breathing proton lung MRI[2] does not require breath-holds and therefore may be an attractive alternative for the evaluation of Cystic Fibrosis (CF) lung disease. Free-breathing lung MRI has been shown to correlate with Xe-MRI and be a responsive measure to CF pulmonary exacerbation treatments[3,4] but has not been used to track stable disease progression over multiple visits. In this study we assessed the inter- and intra-visit reproducibility of free-breathing lung MRI in children with stable CF lung disease.

Methods. The work was carried out using an REB-approved protocol at The Hospital for Sick Children (clinicaltrials.gov: NCT04259970). 16 stable CF patients and 5 age-matched healthy subjects (15±2 years old) were recruited. N_2 multiple breath washout, conducted to obtain lung clearance index (LCI), and MRI were performed on all participants on 2 separate visits. Visit 2 occurred one month after visit 1. Free-breathing lung MRI and Xe-MRI was conducted on a 3T MRI scanner as previously described[4,5]. When time permitted, free-breathing MRI and Xe-MRI acquisitions were repeated in 7 CF patients within their same visit. Free-breathing lung MRI fractional ventilation (FV) maps were calculated using the PREFUL method[2] and ventilation defect percentage (VDP) was determined using k-means clustering[6]. VDP was calculated from xenon ventilation distributions using a threshold of 60% of the mean[7]. The absolute difference, coefficient of variance (% CV), coefficient of reproducibility (CR), intra-class coefficient (ICC), and percentage change were used to calculate inter- and intra-visit reproducibility. FV VDP, Xe-MRI VDP, and LCI were correlated using linear regression.

Results. Table 1 summarizes the inter-visit reproducibility of FV VDP, Xe-MRI VDP, and LCI, respectively. FV VDP had a higher %CV, CR, and percentage change as compared to both Xe-MRI VDP and LCI. All 3 parameters showed high intra-scan reproducibility. The within-subject standard deviation of the VDP found from FV VDP across the two visits was found to be proportional to the magnitude of the VDP, while Xe-MRI was not. FV VDP moderately correlated to Xe-MRI VDP (R^2=0.46; p<0.0001) and LCI (R^2=0.37; p=0.0001).

	% CV	CR	ICC	Absolute Change (95% CI)	% Change (95% Limits)
FV VDP (%)	30.1	17.9	0.73	0.5 (-18;19)	26.3 (-98;151)
Xe-MRI VDP (%)	13.5	8.5	0.73	-1.5 (-10;7)	-8.8 (-51;33)
LCI	5.5	1.6	0.90	-0.1 (-1.7;1.5)	-0.2 (-18;17)

Table 1. Inter-visit reproducibility of FV VDP, Xe-MRI VDP, and LCI in 16 stable pediatric CF patients across 2 visits on month apart.

Discussion and Conclusion. Overall, FV VDP and Xe-MRI VDP showed high intra-scan reproducibility. VDP from both free-breathing lung MRI and Xe-MRI of the pediatric CF patients showed high inter-scan variability between the 2 visits as indicated by the CR values. There was a moderate and significant correlation between FV VDP and Xe-MRI VDP. Additionally, the inter-scan reproducibility of VDP derived from Xe-MRI and PREFUL MRI of the 5 healthy participants (CR = 3.4 and 5.9, respectively) was higher than the CF group (CR = 8.5 and 17.9 respectively) during the first two visits, suggesting the higher variability in the CF group may be due to disease instability. The higher variability of PREFUL MRI compared to Xe-MRI may be due to fact that free-breathing MRI acquires only a 2D slice of the lung, the placement of which may have varied between visits. The sensitivity and reproducibility of a 3D implementation of PREFUL MRI will be explored in the future. Overall, PREFUL MRI may serve as a reproducible measure for assessing lung disease longitudinally in CF.

References. 1. Santyr G et al. Acad Radiol. 2019;26(3):344-354. 2. Voskrebenzev A et al. Magn Reson Med. 2018;79(4):2306-2314. 3. Couch MJ et al. Acad Radiol. 2021;28(8): e209-e218. 4. Rayment J. et al. Eur Respir J. (2019) 53: 1802188. 5. Munidasa S et al. Eur. Respir. J. 2021;57(4):2003104 6. Kirby M et al. Acad. Radiol. 2012;19(2):141-52 7. Thomen RP et al. J. Cyst. Fibros. 2017;16(2):275-282

The Use of 3D Hyperpolarized ^{129}Xe Lung MRI for Deep-Learning-Based Automated Quantification of Ventilation Defects and Heterogeneity

Tuneesh K Ranota[1], Fumin Guo[2], Tingting Wu[3], Matthew S Fox[3,4] and Alexei Ouriadov[1,3,4]
[1]School of Biomedical Engineering, Faculty of Engineering; [2]Sunnybrook Research Institute, University of Toronto, Toronto, Canada, [3]Department of Physics and Astronomy;[4]Lawson Health Research Institute, London, Canada, The University of Western Ontario, London, ON, Canada

RATIONALE: Hyperpolarized ^{129}Xe MRI allows for the visualization of lung structure and function, paving way to investigate pulmonary diseases.[1-3] Two VDP calculations using high-resolution 3D imaging from FGRE, combined with a key-hole method, was demonstrated in participants with ventilation abnormalities. Currently, the gold standard of semi-automated (SA) segmentation[4] can be used to quantify 3D isotropic ^{129}Xe lung images to generate ventilation-defect-percent (VDP), however, this method is not suitable for analysis due to the large number of slices (~45min per 80 slices). We hypothesize that fully automated deep learning-based (DL) lung segmentation algorithm can be used for accurate calculation of VDP from high-resolution images.

METHODS: Ten participants with established ventilation heterogeneity provided written informed consent and underwent spirometry and ^{1}H/^{129}Xe MRI scanning. ^{129}Xe imaging was performed at 3.0T using whole-body-gradients and a ^{129}Xe RF coil.[5] Traditional resolution xenon images (voxel size=3x3x15mm^3) and high-resolution images (3x3x3mm^3) were acquired using techniques previously described.[6,7] SNR was calculated for three central slices, as previously described.[8] A U-net++ network[9] was used to segment the lung in the isotropic proton-lung images. The ^{1}H MR image was registered to the ^{129}Xe volumes using a registration method provided by the NiftyReg package. The lungs were automatically segmented into 5-clusters using a 3D k-means-clustering-approach. VDP was calculated by normalizing ^{129}Xe ventilation-defects represented by the 1st cluster to the warped lung-masks.[10] The DL-based VDP was compared with a SA method using Pearson correlation coefficient.[11]

RESULTS: Table 1 summarizes demographic-information, SNR & Dice Coefficients (DC) for three slices (lowest SNR>5), and two VDP calculations. The largest disagreement between two VDP estimates was found for P7, showing the smallest SNR values. The SA-based VDP values with the DL-based fully automated VDP values obtained from nine participants showed a strong linear correlation (intercept=-0.06±0.18, slope=0.88±0.09, R=0.92). Bland Altman (BA) analysis was conducted for the SA and DL-based VDP estimates (Figure 1).

CONCLUSIONS: The mean VDP values from both methods are comparable to the values reported in the literature obtained with asthma[11] patients. BA analysis indicated there was negligible bias between SA and DL based VDP. DCs from SA and DL based VDP suggested a good match between the ground truth (SA) and DL segmentations. This proof-of-concept study suggests that ^{129}Xe MRI (with SNR>>5) coupled with the DL-based lung-segmentation can be used to rapidly evaluate ventilation heterogeneity across a wide range of disease.

Table 1: Demographics and ^{129}Xe MRI results

	P1	P2	P3	P4	P5	P6	P7	P8	P9	P10
Age	74F	76M	69M	29F	47F	61F	63F	52F	36M	55M
BMI (kg/m^2)	33.6	36.6	41.1	19.2	20.8	38.4	33.4	28.4	32.0	29.0
FEV_1 %	71	78	70	67	75	117	89	61	76	82
FVC %	91	73	66	92	60	111	88	66	73	94
RV %						73	95	95	116	115
DL_{CO}%						83	66	90	91	63
SA VDP %	2.3	2.9	1.9	0.5	0.3	3.9	2.5	0.6	0.8	0.9
DL VDP %	2.6	2.3	1.1	0.3	0.3	3.4	3.9	0.4	0.7	0.8
SNR-1	12.5	14.8	14	40	24.2	28.6	6.8	19.3	24.6	26.3
SNR-2	11.9	16	13.3	42.1	28.4	30.1	5.7	21.8	22.7	24.6
SNR-3	12.7	13.2	16	35.4	34.8	33.2	6.1	21.3	26.2	19.7
DC-1 %	91	95	92	94	93	95	92	96	94	95
DC-2 %	91	92	92	92	92	94	93	96	92	95
DC-3 %	96	89	93	93	94	96	95	94	94	93

P=participant; BMI=body mass index; FEV_1=forced expiratory volume in 1 second; FVC=forced vital capacity; RV=residual volume; DL_{CO}=diffusing capacity for carbon monoxide; ^{129}Xe MRI-based VDP=ventilation defect percent, SNR=signal to noise ratio, SA= Semi-Automated, DL=Deep Learning, DC=Dice Coefficient.

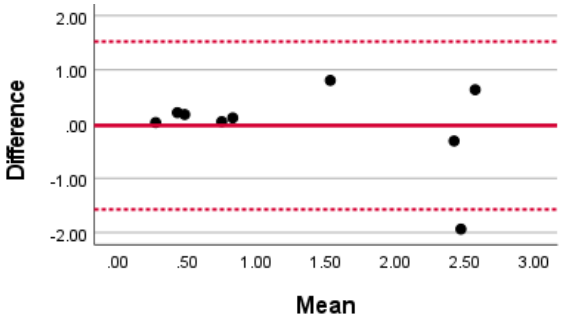

Figure 1. *Bland Altman analysis was conducted for the SA and DL based VDP estimates.*

References: 1. Kirby M et al Radiol (2014). **2**. Svenningsen S et al AJRCCM (2018). **3.** Hoover D et al BMC Cancer (2014). **4**. Kirby M et al Radiol (2012). **5**. Litjens G et al Med Image Anal (2017). **6**. Svenningsen S et al JMRI (2013). **7**. Ouriadov A et al MAGMA (2009). **8**. Niedbalski P et al MRM (2019). **9**. Zhou Z et al IEEE (2020). **10**. Guo F et al. Med Phys (2017). **11**. Barker A et al ISMRM (2019).

We acknowledge the support of NSERC, R5942A04 and a UWO Research Catalyst Grant, R5942A03.

Pitch Session 12: Image-Guided Intervention and Surgery

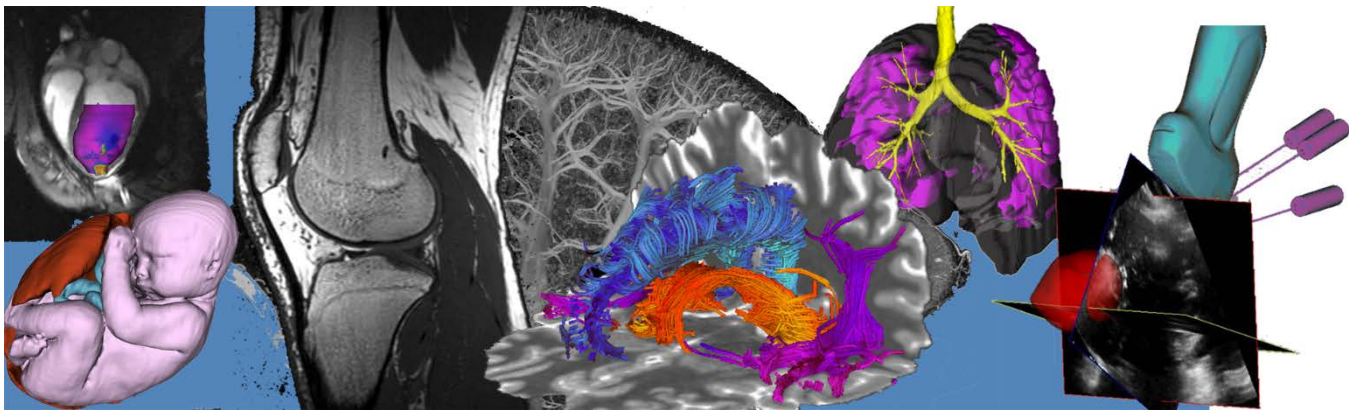

Recognizing needle insertion attempts in webcam video for skill assessment in central venous catheterization training

Catherine Austin[a], Rebecca Hisey[a], Olivia O'Driscoll[a], Daenis Camire[b], Jason Erb[c], Daniel Howes[c], Tamas Ungi[a], Gabor Fichtinger[a]
[a]Laboratory for Percutaneous Surgery, School of Computing, Queen's University, Kingston, Canada
[b]Department of Anesthesiology, Queen's University
[c]Department of Critical Care Medicine, Queen's University

Introduction: Central venous catheterization (CVC) is a common procedure used to create an intravenous drug delivery port. One of the critical elements of the procedure is the accurate insertion of a cannulated needle into the vein. A critical error made during CVC is multiple needle insertion attempts; the chance of experiencing complication is more than eight times greater when cannulation is attempted more than once [1]. The objective of this work was to develop a method for recognizing this critical error through object detection by counting the number of needle insertions attempts in webcam video during a CVC procedure. We implemented and tested this method in the Central Line Tutor computer-assisted training system [2].

Methods: To recognize a needle insertion attempt, we first trained an object detection network, Faster region-based convolutional neural network (Faster R-CNN) to locate the syringe and the phantom in video recordings of CVC. Next, we determined the regions in the video where a needle insertion attempt was most likely occurring. To identify this region, we constructed a confidence heat map based on the number of ground truth bounding box locations of the syringe that overlapped each pixel. To ensure this method can accommodate slight adjustments in camera position, the images were registered based on the location of the phantom in the image (Fig. 1). We computed upper and lower confidence thresholds to define the start and end of an insertion attempt. A needle insertion attempt began when the confidence value at the center pixel of the syringe bounding box was above an upper confidence threshold. The attempt ended when the confidence fell below a lower threshold. To test the effectiveness of our method, we obtained 30 video recordings of five experts and one novice participant performing CVC. Each of the frames was annotated with a bounding box location for the syringe and the phantom, the time that the needle initially intersects the phantom and the time the needle is fully removed from the phantom for each needle insertion attempt. We trained Faster R-CNN using 16 of these videos for the training set, 4 for validation and 10 for the test set. To evaluate Faster R-CNN's ability to recognize the syringe and phantom, we computed the mean average precision (mAP) for the network. We then compared the number of needle insertion attempts computed from the test set to the number of attempts counted by human reviewers.

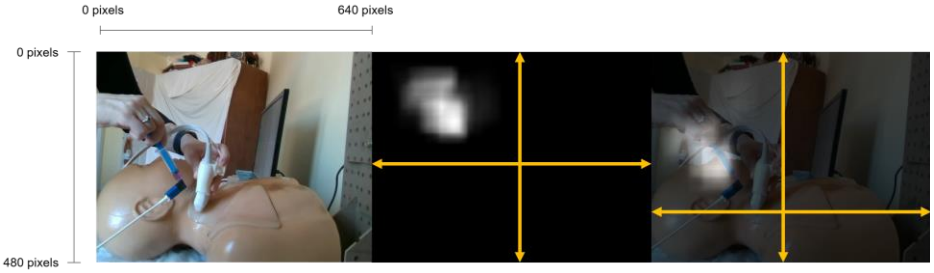

Fig 1: Left: original image. Center: confidence heat map for the universal coordinate system (axes shown in yellow). Right: image overlayed with the heat map transformed to the coordinate system for the frame (axes shown in yellow).

Results: The overall mAP of the network was 0.83. The computed upper threshold was 0.65, and the lower threshold was 0.33. The average number of computer-counted insertion attempts for each performance of the procedure used in the test set was 1.90 ± 2.23 compared to an average of 1.87 ± 1.87 counted by 3 reviewers.

Conclusions: The average number of attempts computed for both the video-based method and the count by human reviewers were close in value. The primary limitation of our experiments was the small size of our dataset. In future work we will expand upon our dataset, allowing us to test this method using a greater number of both expert and novice participants and evaluate its statistical significance. Additionally, we will adjust the skill assessment metrics in Central Line Tutor to account for multiple needle insertions as a critical procedural error.

References: [1] Schummer, W., Schummer, C., Rose, N., Niesen, W.-D., Sakka, S. G., "Mechanical complications and malpositions of central venous cannulations by experienced operators," Intensive Care Medicine **33**(6), 1055–1059 (2007).

[2] Hisey R, Camire D, Erb J, Howes, Fichtinger G, Ungi T. System for central venous catheterization training using computer vision-based workflow feedback. IEEE Transactions on Biomedical Eng. 2021 Nov. 2 (online ahead of print)

Toward automated three-dimensional ultrasound image guidance of gynecological brachytherapy treatments

Tiana Trumpour[1,2], Jessica R. Rodgers[3], Lucas C. Mendez[4], Kathleen Surry[1,4,5], Aaron Fenster[1,2,4]

[1] *Department of Medical Biophysics, Western University, London, Canada* [2] *Robarts Research Institute, Western University, London, Canada* [3] *School of Computing, Queen's University, Kingston, Canada* [4] *London Regional Cancer Program, London, Canada* [5] *Department of Oncology, Western University, London, Canada*

Introduction: High dose rate brachytherapy is a common treatment method for gynecological cancer which places radioactive sources locally to the tumour, providing the required dose to the malignant region while sparing surrounding healthy tissue. Typically, radiation is delivered through internal applicators, interstitial needles, or a hybrid combination of both methods. Accurate placement of the applicator and needle tips is vital for a successful treatment. Three-dimensional (3D) transrectal ultrasound (TRUS) and transabdominal ultrasound (TAUS) imaging have been previously investigated for the visualization of applicators and needles [1]. However, due to image artifacts from the applicator, needle tip identification is severely restricted when using a single 3D US view [2]. We aim to develop an automated TRUS-TAUS fusion technique for complete visualization of the applicator, needle tips, and surrounding anatomy.

Methods: An agar female pelvic phantom and relevant structures were embedded. Images were acquired from both 3D TRUS (7 MHz, end-fire endocavity) and 3D TAUS (3.5 MHz, curved array) views using automated systems developed in our lab. The 3D TRUS images were acquired at 2 positions within the rectum to ensure a full field-of-view. The images were combined using a voxel overlap technique to create a complete 3D TRUS image. A physical model of the applicator was then rigidly registered to the 3D TRUS and 3D TAUS images, individually. Using a custom software developed in C++, the 3D US images were fused based on the rigid geometry of the applicator, resulting in a 3D visualization of the entire pelvic region. The final 3D US image was then rigidly aligned with computed tomography (CT) images to assess needle tip positions and fusion accuracy. Tip positions were quantified by target registration error (TRE) and fusion accuracy by fiducial registration error (FRE).

Results: Figure 1 shows an overview of the phantom and 3D US images. The needle tips are anticipated to have a TRE of less than 5 mm when compared with CT images, based on initial proof-of-concept experiments. We aim to have FRE of less than 1 mm for accurate visualization of the region.

Conclusions: Using 3D US, the proposed fusion technique will ensure precise placement of radioactive sources, leading to more accurate gynecological brachytherapy treatments. This method will also be accessible to overburdened and cost-constrained healthcare systems.

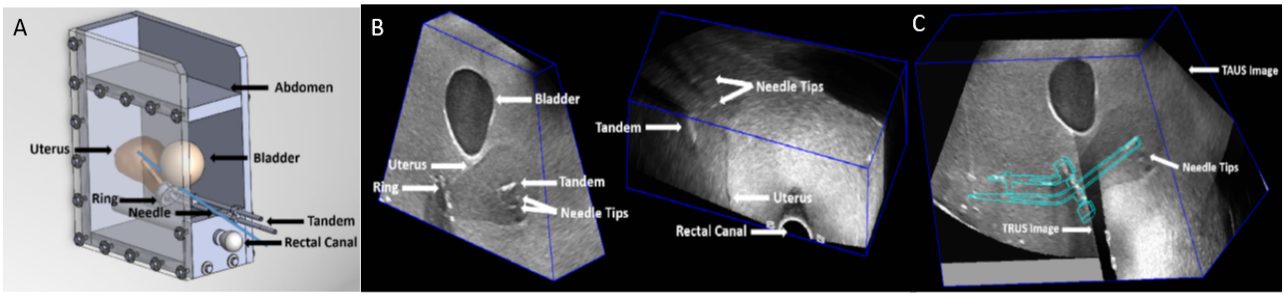

Figure 1: (A) The female pelvic phantom box with revelant structures; (B) Individual 3D TAUS and TRUS images; (C) Merged 3D TAUS and 3D TRUS images with applicator model overlay

Acknowledgements: Financial support provided by the Ontario Institute of Cancer Research, the Canadian Institutes of Health Research, and the Natural Sciences and Engineering Research Council.

References: [1] Rodgers et al. *Med. Phys.* 2017. 44(5); [2] Mendez et al. *Rad. Oncol.* 2020. 15(1)

Feasibility of a video-based skill assessment method for central venous catheterization

Olivia O'Driscoll[1], Rebecca Hisey[1], Matthew Holden[2,] Daenis Camire[3], Jason Erb[3], Daniel Howes[3], Gabor Fichtinger[1], Tamas Ungi[1]

[1]Laboratory for Percutaneous Surgery, School of Computing, Queen's University, Kingston, Canada

[2]School of Computing, Carleton University, Ottawa, Ontario

[3]Department of Critical Care Medicine, Queen's University, Kingston, Canada

Introduction: Computer-assisted surgical skill assessment methods have traditionally relied on tracking tool motion with physical sensors that measure skill assessment with six degrees of freedom (DOF). For instance, Clinkard et al. used EM tracking to compute metrics for central venous catheterization (CVC), including the path lengths and usage times of the needle and ultrasound probe[1]. These tracking systems can be expensive and impede tool function. We focus in on a low-cost, video-based alternative to current physical tracking systems for surgical skill assessment. We assess the feasibility of this method by comparing video-based metrics to the current gold standard of computer-assisted skill assessment.

Methods: We recorded tracking and video of four novices and four experts performing 13 CVC trials on a phantom. We compute both using the video-based object detection method and the EM tracking-based method presented by Clinkard et al. The EM tracking-based method serves as a ground truth to assess the feasibility of our video-based method.

We computed the ultrasound probe's and syringe's path lengths and usage time using two different methods. EM tracking-based metrics were computed using the Perk Tutor extension of 3D Slicer. For the video-based method, an object detection network was trained on the ultrasound probe and syringe. The video-based metrics were computed from the network's bounding box predictions. A Spearman rank correlation was performed between the metrics computed by both methods and between the opposite metrics for both tracking methods. The latter tested how well the video-based metrics captured the corresponding EM-tracked metrics.

Results: Figure 1 shows the decrease in metrics over 13 trials for both the experts and novices, as computed by both methods. The path lengths had a rank correlation coefficient of 0.22 for the syringe ($p<0.03$) and 0.35 ($p<0.001$) for the ultrasound probe. For the usage times, the correlation coefficient was 0.37 ($p<0.001$) for the syringe and 0.34 ($p<0.001$) for the ultrasound probe. The alternately paired metrics had insignificant correlations.

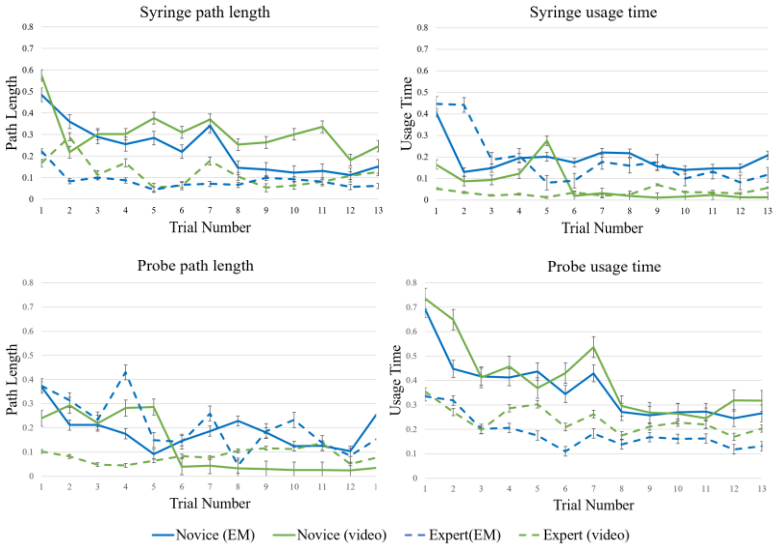

Figure 1. Performance metrics for the syringe (top) and the probe (bottom), as computed by tracking and video-based methods. These metrics were normalized for comparison on the same axes.

Conclusions: The three DOF, in-plane metrics from video correlated significantly with the six DOF metrics from EM tracking. EM tracking has previously been validated against trainee skill, so results reveal that object detection is promising as a skill assessment method. Further, the correlation was stronger between the matching metrics versus the alternately paired metrics, suggesting that the video-based metrics are indeed measuring the same attributes of skill as are measured with the EM-tracked metrics. These results are encouraging and show promise that an inexpensive camera can provide a similar assessment of skill comparable to current expensive, bulky, six DOF tracking systems

[1] Clinkard, D., Holden, M., Ungi, T., Messenger, D., Davison, C., Fichtinger, G., McGraw, R., "The development and validation of hand motion analysis to Evaluate competency in Central LINE CATHETERIZATION," Academic Emergency Medicine 22(2), 212–218 (2015).

Machine Learning the Assessment of Surgeon Technical Skill for One Handed Surgical Knot Tying

K. Kasa[1]; D. Burns[1,2,3]; M. G. Goldenberg[4], O. Selim[5]; C. Whyne[1,2,3], O. Safir[6]; M. Hardisty[1,2]

[1]Holland Bone and Joint Program, Sunnybrook Research Institute, [2]Institute of Biomedical Engineering, [3]Division of Orthopaedics, Department of Surgery, [4]Division of Urology, Department of Surgery, University of Toronto, [5]Department of Surgery, Royal Victoria Regional Health Center, [6]Division of Orthopaedic Surgery, Mount Sinai Hospital

Introduction: There has been an evolution in surgical education towards objective competency assessment as a requirement for trainee advancement. Competency-based medical education (CBME) can increase the burden on surgical faculty, and assessments have not been well validated by the surgical community [1]. Advances in motion sensors and machine learning present the opportunity to automate surgical skill assessments, potentially improving their objectivity and reducing assessment burden. The purpose of this investigation was to develop a deep learning approach for domain specific and global assessment of one-handed surgical knot tying.

Methods: Seventy-two surgical trainees and surgeons were recruited for participation in this study during the 2018 University of Toronto Department of Surgery Prep Camp and Orthopaedics Bootcamp suturing modules.

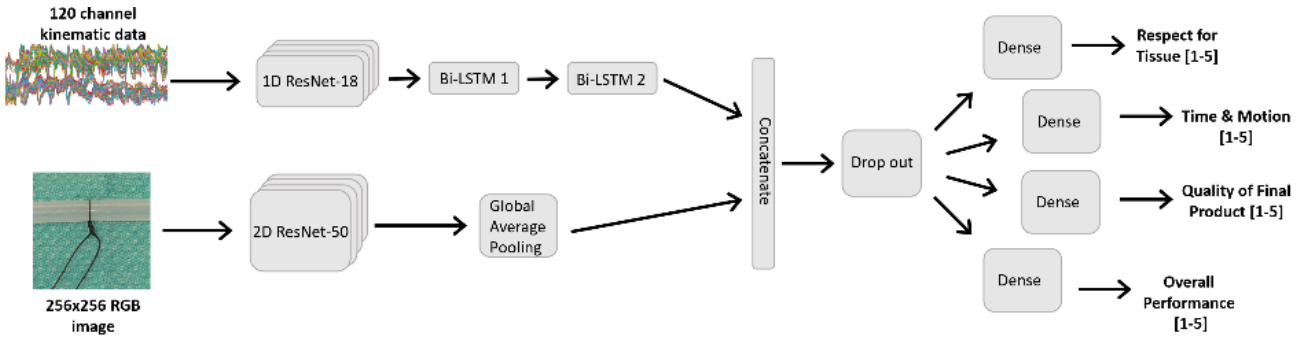

Figure 1: Multi-modal modal with time-series and image data as input, and score predictions for the 4 GRS domain outputs. Images were analyzed using an ImageNet pretrained ResNet-50, and the kinematic data was analyzed using a Res-LSTM network – a 1D ResNet-18 as a 'feature extractor', followed by 2 bidirectional LSTM layers.

Participant technical skill were assessed for performing a one-handed knot-tying task simulating vessel ligature using 0 silk ties and polypropylene tubing. Each participant performed 5 tasks (360 total) which were recorded using video of the operative field, a high-resolution photograph of the final product, and 3D kinematic hand motion tracking using a Leap Motion Sensor (120 channel timeseries data). Three blinded independent raters from the divisions of orthopaedic, urology, and vascular surgery performed the assessments from the recorded video and photograph, using the Objective Structured Assessment of Technical Skill Global Rating Scale (GRS) [2] on 4 domains: 1) Respect for Tissue, 2) Time and Motion, 3) Quality of Final Product, 4) Overall Performance, scored on a 5-point scale (1-5). Three deep learning models were developed: The first used the images of the simulated vessel and ligature as input and the Quality rating as output. The second model used the hand kinematic data as input and predicted the 3 other domains (Respect for Tissue, Time and Motion, Overall Performance). The final composite model with ResNet and LSTM components used both RGB and kinematic data and output all 4 domains. The models were trained using supervised learning; data was randomly split into training / validation / test sets, with a test-set of 7 (10%) participants (35 tasks).

Results: The human raters showed good to moderate agreement on the test set (intraclass correlation (ICC (2,3): 1) 0.782, 2) 0.808, 3) 0.932, 4) 0.864). The multi-modal model showed the best overall performance with moderate to good agreement in the test set (ICC >0.7), and low point errors (MSE <0.5). The AI performance was comparable to the human raters – the AI has a lower point error, and the humans show slightly better agreement (0.024 higher ICC).

Model	Metric	Respect for Tissue	Time and Motion	Quality of Final Product	Overall Performance
Image	ICC (2,4)	-	-	0.899	-
	MSE	-	-	0.146	-
Kinematic	ICC (2,4)	0.762	0.789	-	0.845
	MSE	0.336	0.420	-	0.373
Multi-modal	ICC (2,4)	0.739	0.781	0.923	0.852
	MSE	0.480	0.356	0.186	0.194
Rater 1	MSE	0.464	0.348	0.531	0.505
Rater 2	MSE	0.546	0.553	0.545	0.466
Rater 3	MSE	0.288	0.363	0.193	0.290

Table 1: Mean Square Error (MSE) and Interclass Correlation (ICC) of human Raters and machine learning models

Conclusion: Our multi-modal deep learning approach successfully rated all four surgical skill domains with performance comparable to expert human raters – an important step towards automated objective assessment and reducing surgical faculty burden.

References: [1] Sonnadara et al., J. Surg. Educ., 71(1) 151, 2014. [2] Martin *et al.*, *Br. J. Surg.*, 84(2) 273, 1997

Deep learning based vessel segmentation from ICE imaging: Towards an ultrasound-based vascular navigation image guidance system

Hareem Nisar, Patrick K Carnahan, Terry M. Peters, and Elvis C.S. Chen

Robarts Research Institute, Western University
Department of Biomedical Engineering, Western University

Introduction:

Vascular navigation, including traversing the inferior vena cava (IVC), is a prerequisite to many transcatheter cardiac interventions. By current clinical standards, the vessels are navigated by the guidewires and catheters under fluoroscopy which places the interventionalists at the risk of eye cataracts and cancer. It also famously causes spinal issues and neck and back pain which has led towards the coining of the term "interventionalist's disc disease". A suitable alternative is to have an ultrasound-guided vascular navigation system where an intracardiac (ICE) probe scans the IVC, reconstructs the vascular roadmap which can then be traveled by tracked guidewire or catheter. For such a vessel reconstruction, one of the biggest challenges is to segment the vessel lumen from the ICE images.

Methods:

In this study, we address this challenge using a deep learning based approach. We acquired IVC images from an animal study performed using a radial, forward-looking Foresight™ ICE probe. The training data included 90 ICE images of the vena cava of two swine. The ground truth was established using manual segmentations and validated by an expert clinician. We use the MONAI platform to train a U-net architecture on our dataset. The images are cropped to retain only the central 300 pixels as the traversed vessel will always appear central to the radial ICE image. Data augmentation, including 90° rotation and 2D elastic deformation, was performed to enhance the number of images available for training. Post-processing includes keeping the largest connected island and hole filling.

Results:

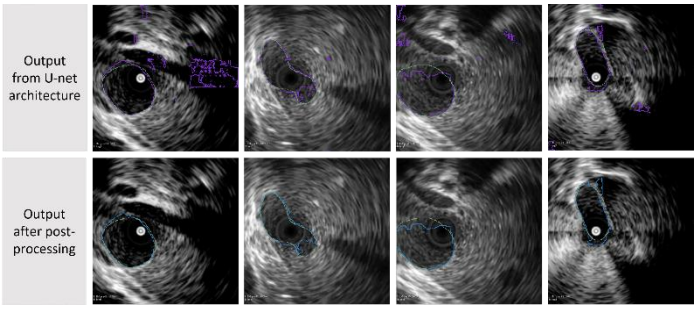

The preliminary results show that the Dice coefficient was 0.86 for the output of the U-net model on test data. Figure (top row) shows the performance of the DL-based output only. The green outline represents the contours of the ground truth labels, whereas the purple outline represents the segmentation output by the U-net model. Figure (bottom row) compares the ground truth to the algorithm output after the post-processing steps are applied which resulted in a Dice score of 0.90.

Conclusion:

The results show that U-net architecture has sufficient potential to perform vessel segmentation from ICE images, however, the output can benefit from a larger training dataset. This technique, combined with tracking technology, can create a fluoro-free image-guided system to guide tools and catheters through the vessels during transcatheter cardiac interventions. Without fluoroscopy, there will be no need for wearing heavy shielding equipment to protect the interventionalists from radiation and will thus help reduce the interventionalists' disc disease.

Determining the location of tumor classifications in breast cancer surgery

Joshua Ehrlich, Amoon Jamzad, Martin Kaufmann, Jessica R. Rodgers, John Rudan, Tamas Ungi, Parvin Mousavi, Gabor Fichtinger.

Queen's University, Kingston ON, Canada

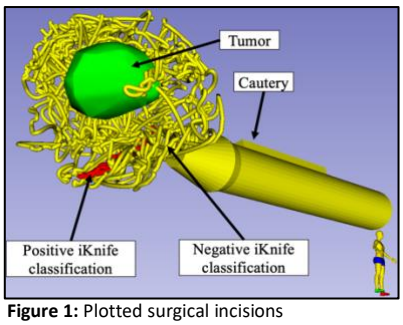

Figure 1: Plotted surgical incisions

Introduction: Lumpectomies are performed in early-stage breast cancer to remove tumors. To ensure no cancer is left behind following the procedure, a healthy tissue margin (i.e., negative margin) surrounds the resected tumor. Mass spectrometry (iKnife) has been used to differentiate tumor from healthy tissue in various surgical procedures [1]. In comparison to other mass spectrometry techniques, a NaviKnife system with real-time spatial tracking and tissue classification would address critical problems surrounding breast-conserving surgery [2]; however, fusing the position tracking and iKnife classification data streams is computationally challenging. The iKnife has a variable time-delay, dependent on factors related to the surgical set-up (e.g., length of cautery vapour tube and suction of fume hood). In contrast, position tracking has a high temporal resolution and minimal temporal delay. Our objective is to calculate the time-delay and use position tracking to locate where the cautery was when we received a cancerous (positive) iKnife signal.

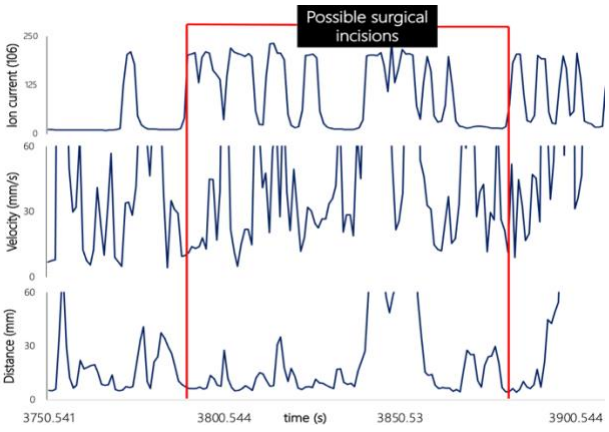

Figure 2: Red = low cautery velocity, short distance-to-tumor, and iKnife vapour

Methods: The iKnife's time delay was measured by video recording tissue incisions and corresponding iKnife classifications and replaying the sequence. Lumpectomy surgeries were replayed using the LumpNavReplay module in 3D-Slicer. A surgical incision was estimated to be in progress when the cautery tip was within 25 mm of the tumor's center because a positive margin is most likely near the tumor boundary. A custom python script was used to calculate the distance travelled (mm), length of time (s), and speed (mm/s) of each incision. By multiplying the average cautery speed of an incision by the variance in the iKnife's temporal delay, we calculated the average distance the cautery travels during the error in the iKnife classification time delay. The magnitude of the variance in distance represents the uncertainty in locating where the iKnife classification most likely originated. Positive classifications, extracted from the chromatogram of iKnife, were adjusted to surgical incision time using the calculated time delay. A visualization was completed by mapping the set of points to a string model (Figure 1).

Results: The average time delay was 2.84 s with a standard deviation of 0.42 s. The standard normal variance was found to be 1.68 s, such that 97.5% of our samples fell in a delay between 2 s and 3.68 s. The average incision velocity was 21 mm/s. A time variance of 1.68 s translates to an iKnife classification region of 36 mm.

Conclusions: Our study spatially locates iKnife classifications in breast cancer surgery enabling analysis of potential positive margins following the surgical procedure. A source of error resulting in a large spatial region for an iKnife classification is due to calculating the velocity of cautery movements outside of a surgical incision. This occurred because we used a single parameter to identify a surgical incision, which is not accurate (Figure 2). In the future, we will use four inputs to isolate a surgical incision: cautery energy state [3], low cautery velocity, short cautery distance-to-tumor, and a chromatogram signal. It will be important to investigate if some inputs correlate with one another. To ensure minimal redundancy, we will combine inputs with machine learning to isolate a surgical incision. Using these methods, we may be able to localize positive iKnife classifications to a region of less than 36 mm. This is likely a clinically sufficient indicator for the need to adjust excision boundaries intraoperatively and will be explored in future studies.

1. Santagata, S., et al. *Proc. Natl. Acad. Sci.*, vol. 111, p. 11121–11126, 2014.
2. Ungi T., et al. *IEEE Trans Biomed Eng*, vol. 63, no. 3, pp. 600-606, March 2016.
3. Ehrlich, J., et al. Imaging Network of Ontario 2022 (submitted).

Catheter Tracking Error Characterization for MRI-Guided Interventions

Arjun Gupta[1], Labonny Biswas[2], Jay Soni[2], Brandon Coles[1], Sebastian Ferguson[2],
Graham A. Wright[1,2,3], Nilesh R. Ghugre[1,2,3]

[1]Department of Medical Biophysics, University of Toronto, [2]Physical Science Platform, Sunnybrook Research Institute, [3]Schulich Heart Program, Sunnybrook Research Institute, Toronto, ON, Canada

Introduction. MRI is a promising image guidance modality for minimally invasive cardiac interventions. Some examples of such catheter-based interventions include radiofrequency (RF) ablation treatment for ventricular tachycardia, and therapy delivery involving biologics (cells, genes, biomaterials) for the treatment of myocardial infarction [1]. Studies in the past have had success with MRI-guided RF ablations in left ventricular myocardium [2] and have also shown feasibility with transendocardial cell delivery [3] but have not characterized the errors associated with MRI-guided catheter positioning within the heart. Recent work has shown that a targeting accuracy of <5mm is desired for RF ablations [4], as well as for optimal transplantation of stem cell-derived cardiomyocytes [5]. Given these results, a target of constraining tracking error to <5mm is warranted. Hence, the aim of our study was to characterize the errors associated with MRI-guided catheter tracking under static conditions, using a phantom setup and two different types of pulse sequences.

Methods. The catheter has two micro-coils embedded at its distal end, which allows for active tracking under MRI. Using both conventional 3-projection [6] (Flip angle = 5°; FOV = 30 x 30 x 30cm; acquisition size = 512; TR = 9ms) and Hadamard multiplexed (HM) [6] (Flip angle = 5°; FOV = 17.3 x 17.3 x 17.3cm; acquisition size = 256; TR = 2ms) active tracking sequences in a 1.5-T MRI scanner, we tracked the catheter tip (extrapolated from the coil positions – see Fig 1) at 16 positions within a polyacrylic acid gel. The 16 positions were mainly constrained to the (+X, +Z) octant of the bore, within the boundaries of X<100mm and Z<80mm. These were chosen to encompass the likely location of the heart during a scan. A fixture was used to maintain tip alignment with the Z-axis at each position. We acquired both ground truth imaging data (Fig 1) and 15 seconds of real-time tracking data at each position. Error was calculated as the absolute difference between the ground truth coordinate and the mean tracked coordinate.

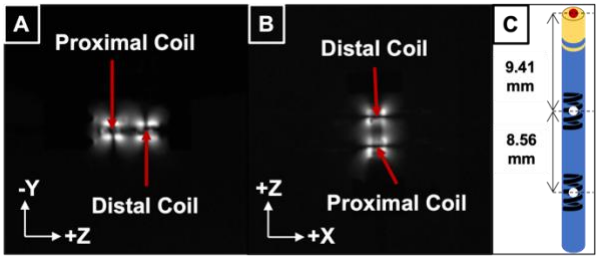

Figure 1. (A) Ground truth sagittal and (B) coronal slices of proximal and distal coils embedded at the catheter tip, with (C) catheter tip graphic to scale.

Results. Two heat maps of catheter tip tracking error are presented (Fig 2). With the conventional sequence, the mean error was 3.33±0.02mm, while the min and max errors were 0.91±0.003mm and 11.67±0.08mm, respectively. With HM, the mean error was 1.64±0. 08mm, while the min and max errors were 0.60±0.04mm and 3.37±0.12mm, respectively. The error observed with HM was kept below our target constraint of 5mm.

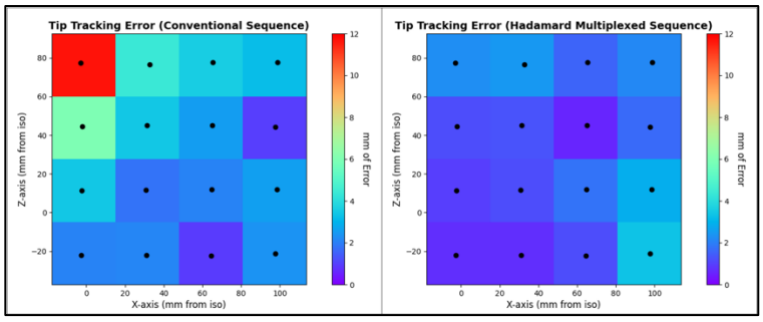

Figure 2. Tracking error heat maps generated from manipulating X- & Z-positions of the catheter tip within the gel phantom. The Y-position was held constant at -45mm. The black markers indicate the 16 tracked positions within the gel phantom. The error exceeded our 5mm target at (X, Z) = (-3mm, 77mm) & (-2mm, 45mm) positions while using the conventional sequence.

Conclusions. For active catheter tracking under static conditions, employing HM was preferable to using the conventional sequence as the former is, by design, insensitive to off-resonance errors due to static magnetic field inhomogeneities. Our next step is to characterize the tip tracking error under dynamic conditions (using a motion phantom) to simulate cardiac and respiratory motion. In vivo conditions will introduce additional error sources, notably relative tissue motion; however, our study confirms that static tracking errors should not be limiting for the 5mm target accuracy, encouraging next steps toward in vivo translation for applications including MRI-guided cardiac EP and delivery of biologics.

[1] Wang, W. *Magn. Reson. Imaging Clin. N. Am.* (2015). [2] Chubb, H., et al. *Arrhythmia Electrophysiol. Rev.* (2017). [3] Dick, A. J., et al. *Circulation.* (2003). [4] Piers, S. R. D., et al. *JACC Cardiovasc. Imaging.* (2014). [5] Chong, J. J. H., et al. *Nature.* (2014). [6] Dumoulin, C. L., Souza, S. P. & Darrow, R. D. *Magn. Reson. Med.* (1993).

Semi-supervised cautery detection with preprocessing in basal cell carcinoma surgical videos

L March[1], JR Rodgers[1], A Jamzad[1], AML Santilli[1], R Hisey[1], D McKay[2], JF Rudan[2], M Kaufmann[3], KYM Ren[3], G Fichtinger[1], P Mousavi[1]

[1]School of Computing, [2]Department of Surgery, [3]School of Medicine; Queen's University, Kingston, Ontario

Introduction: Treatment of basal cell carcinoma (BCC) may include a surgery using an electrocautery tool to remove cancerous tissue. By collecting and analyzing vapors extracted from the cautery tool, iKnife technology can detect cancerous cells but it lacks spatial information, making it difficult for the surgeon to return to potential sites of remaining cancerous cells (i.e., positive margins). Intraoperative videos from BCC surgeries may serve as an aid in connecting chemical signal data of the iKnife with spatial information, providing a visual indicator that can show where the cautery was located when burns along the resection margin were made. We propose the use of a deep learning pipeline to analyze intraoperative videos from BCC surgeries to first establish frames in the video showing the surgical scene then to localize the cautery. The goal of this study is to incorporate intraoperative videos in BCC surgery, serving as a link to enhance iKnife feedback to surgeons by providing spatial information that can aid in identifying positive margins.

Methods: The dataset contains 14 GoPro recordings of intraoperative BCC surgeries. To perform phase recognition as a preprocessing step, video frames were annotated as belonging to one of three phases: (1) iKnife display, (2) Surgery, and (3) Transition. The dataset was stratified by patient, resulting in a 70/15/15 percent-wise split between training, validation, and testing and was used to train the MobileNetv2 model, chosen for its success in previous studies.[2] Following phase recognition, tool localization was performed using the End-to-End Semi-Supervised Object Detection (SSOD) with Soft Teacher model[1] trained with Surgery phase frames and partitioned as a 60 (30/30) /20/20 split between training (labeled, unlabeled), validation, and testing sets. Data augmentation, including colour and geometric transformations, was used to overcome video quality issues, such as variable lighting conditions and positional environments.[1] The network runtime on the testing set was measured with and without using the phase recognition step to demonstrate the effectiveness of this preprocessing step to reduce video analysis time.

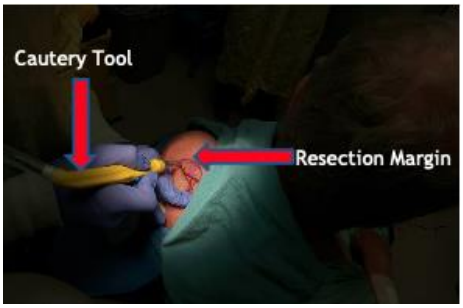

Figure 1. Example "Surgery" frame

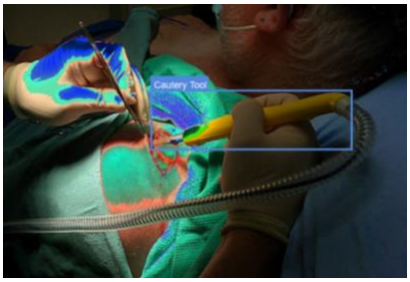

Figure 2. Example cautery tool prediction on augmented data

Results: In the phase recognition preprocessing task, Surgery frames were identified with a precision of 0.76 and recall of 0.88. Some Transition frames were misclassified as Surgery, meaning that unintended frames were passed into the sequential object detection network; however, in this application it is most important that Surgery frames are not missed. Results of the SSOD algorithm show that this approach can detect the cautery location and exploit a relatively small and unlabeled dataset with a mean average precision at 0.50 intersection over union threshold of 0.956. Comparing the mean runtime of cautery localization with and without phase recognition as a preprocessing step showed a decrease of 66.5% with preprocessing, from a 929s to a 311s analysis time on the testing set.

Conclusions: The work presented in this study shows the potential utility of intraoperative videos to connect iKnife data with spatial information. The proposed implementation can quickly analyze and target important frames by using a sequential two-model approach, adding a minimal amount of time to the surgical workflow. Future work will investigate the synchronization of the burn location information from intraoperative video analysis with the iKnife chemical signal data and a technique that is under development to detect whether the cautery is being actively used to make a burn at a given time.

References: [1] Xu et al. arXiv preprint arXiv:2106.09018 (2021), [2] Hisey et al. *IJCARS.* 94-95 (2020).

Author Index

Name	Presentation	Page
Abdelrazek, Mohamed	O1-1	23
Abolmaesumi, Purang	P1-4	36
	P7-1	117
	P7-3	119
	P8-3	128
Adamo, Sabrina	O2-1	28
Adams, John	P3-5	65
Ahmed, Moeiz	O6-3	86
Alam, Faiyza S	P11-2	173
Alawneh, Yara M	P4-3	72
	P4-4	73
Albert, Mitchell	O10-2	141
	P10-6	158
Al-Hayali, Abdullah	P1-2	34
	P5-7	95
Allam, Nader M	O1-3	25
	O7-1	107
Allen, Abbigail	P3-7	67
Amla, Zaiba	P4-8	77
Andersen, Michael	P4-6	75
Appleton, Tom	P1-8	40
	P9-7	151
Aragaki, Masato	O7-2	108
Asselin, Mark	O4-1	56
Athwal, George	O9-2	136
Au, Jacky	P11-7	178
Au, Ryan	P11-1	172
Austin, Catherine	P12-1	181
Aveni, Katharine	P10-5	157
Azad, Azar	P1-2	34
	P5-3	91
Babichev, Yael	O12-1	167
Bainbridge, Daniel	P6-7	104
Barker, Kevin	O4-3	58
Baron, Corey	O3-1	51
	O10-1	140
	P10-7	159
Barr, Colton A	P1-7	39
	O12-2	168
Barragan, Camilo	O9-1	135
Barry, Jennifer	O8-2	113
	O8-4	115
Barszczyk, Mark	P1-5	37
Bartha, Robert	P2-4	45
	P3-1	61
	P10-5	157
	P10-7	159
Bartlett, Jason Todd	P11-4	175
Basharat, Fateen	P11-6	177
Begum, Housne	O7-3	109
Bellyou, Miranda	P3-1	61
Berih, Maryam A	P6-6	103
Bernards, Nicholas	O7-2	108
Bhan, Aparna	O2-1	28
Bhat, Mamatha	O5-2	80
Biernaski, Heather	O8-1	112
Binns, Malcolm	P10-5	157
Biswas, Labonny	P12-7	187
Black, Sandra	O2-1	28
	O2-4	31
Blackler, Garth	P9-7	151
Blazquez-Garcia, Raul	O5-2	80
Bocti, Christian	O2-1	28
Boileau, Isabelle	O2-2	29
Borrie, Michael	O2-1	28
Bourbeau, Jean	P11-1	172
	P11-4	175
Boyle, Amanda	P6-5	102
Brackstone, Muriel	O8-1	112
Braganza, Sharon	P11-2	173
	P11-7	178
Broberg, Dana N	P10-5	157
Brown, Arthur	O10-1	140
Brown, Danny	P4-7	76
Bulnar, Sharshi	P8-2	127
Burkhart, Timothy A	P9-5	149
Burns, David	P12-4	184
Butler, John	O8-1	112
Cambranis Romero, Joeana N	O12-4	170
Camire, Daenis	P12-1	181
	P12-3	183
Campbell, Catherine	O7-4	110
Carnahan, Patrick	P6-7	104
	P12-5	185
Chad, Jordan	O2-1	28
Chafey, Chris	P4-7	76
Chan, Rachel	O1-2	24
Chang, Patrick Dong Min	P8-2	127
Chao, Thomas	O2-2	29
Chau, Oi Wai	O8-1	112
Chavez, Sofia	P10-8	160
Chen, Elvis CS	P6-7	104
	O12-4	170
	P12-5	185

Name	Presentation	Page
Chen, Jean	O2-4	31
Chen, Matthew	O2-7	108
	O7-4	110
Chen, Robert	P10-1	153
Chen, Yuanxin	P6-1	98
Cheng, Ivy	O2-4	31
Cherin, Emmanuel	O4-2	57
Chertkow, Howard	O2-1	28
Cheung, Alison	P7-7	123
Cheung, Kakit	O9-1	135
Chinnery, Tricia	P5-1	89
Cho, Eunyoung	O3-2	52
Cho, Sang Soo	P10-1	153
Chong, Jaron	P5-4	92
Christie, Jaryd R	O1-1	23
Chronik, Blaine	P3-5	65
Chung, Kevin J	O2-3	30
Codirenzi, Anastasia M	P9-6	150
Coleman, Kristy	P10-7	159
Coles, Brandon J	P12-7	187
Connolly, Laura P	P4-2	71
Couch, Marcus	P11-7	178
Cronin, Alicia	P2-4	45
Cunningham, Ian	P6-8	105
Curpen, Belind	P1-5	37
Cusimano, Michael	O2-2	29
Daher, Baraa	O9-2	136
Daher, Omar	O1-1	23
Daly, Michael J	P8-5	130
Danielli, Ethan	P10-2	154
de Ribaupuerre, Sandrine	P5-7	95
DeMatteo, Carol	P2-3	44
Demidov, Valentin	O1-3	25
	O1-4	26
Demidova, Natalia V	O1-4	26
Demore, Christine	O4-2	57
Desmond, Kim	P2-7	48
Detombe, Sarah	P2-4	45
Detsky, Jay	O1-2	24
Devlin, Megan	P10-7	159
DeVries, David A	P1-3	35
Diao, Babacar	P1-7	39
	P7-6	122
Diez-Cirarda, Maria	P2-2	43
Dima, Robert	O9-4	138
	P9-4	148
Dinniwell, Robert	O8-1	112
Diop, Mamadou	P2-8	49
	P8-8	133
	P9-2	146
Dobrota, Elena	P2-7	48
Dolovich, Myrna	O11-2	163
Doughty, Mitchell	P10-2	154
Dowling, Kierdra I	O9-1	135
Drake, James	O7-4	110
	O12-1	167
Drangova, Maria	P1-8	40
	O3-3	53
Driscoll, Brandon	P4-6	75
Du Toit, Carla	O9-4	138
	P9-4	148
Duarte, Kaue	P2-5	46
Dubovan, Paul I	O3-1	51
Dueck, Andrew	P4-3	72
	P4-4	73
Duggal, Neil	P2-4	45
Dumas, Marie-Pier	P11-7	178
Ebrahimi, Mehran	P3-3	63
	P5-2	90
Ehrlich, Josh H	O4-1	56
	P12-6	186
El Kaffas, Ahmed	O5-2	80
El-Rayyes, Yasmeen	P8-5	130
Elsaid, Sonja	P10-8	160
Empey, Mary-Ellen	O10-4	143
Ensminger, Yara	P8-7	132
Erb, Jason	P12-1	181
	P12-3	183
Escartin, Terenz R	O8-2	113
Eskandari, Rasa	P8-8	133
Faraday, Amber	P8-6	131
Farncombe, Troy	O7-3	109
Fenster, Aaron	O4-3	58
	P5-4	92
	P5-7	95
	O9-4	138
	P9-4	148
	P12-2	182
Ferguson, Sebastian	P12-7	187

Name	Presentation	Page
Fichtinger, Gabor	P1-7	39
	O4-1	56
	P4-2	71
	O5-3	81
	P5-6	94
	P7-6	122
	P8-1	126
	P8-4	129
	O12-2	168
	O12-3	169
	P12-1	181
	P12-3	183
	P12-6	186
	P12-8	188
Finger, Elizabeth	P10-7	159
Flueraru, Costel	O1-3	25
	O1-4	26
	O7-1	107
Foltz, Warren	O1-3	25
	O7-1	107
	O12-1	167
Fooladgar, Fahimeh	P1-4	36
Foster, Paula	P6-2	99
	P6-4	101
	P6-6	103
Fowler, Rob	O2-4	31
Fox, Matthew S	P5-8	96
	P6-2	99
	P9-7	151
	P11-3	174
	P11-5	176
	P11-8	179
Franz, Leonardo	P8-5	130
Fraser, Douglas	P10-7	159
Frayne, Richard	O2-1	28
	P2-5	46
Friesen-Waldner, Lanette	O10-4	143
	P10-3	155
Gaede, Stewart	O8-1	112
	O11-3	164
Gaikar, Rohini P	P5-3	91
Gale, Eric	O6-1	84
Gao, Fuqiang	O2-4	31
Garcia, Armando	P2-7	48
Garland, Lisa M	P6-8	105
Gelman, Neil	O6-3	86
Genady, Afaf	P8-6	131
Genkin, Daniel	O11-1	162
Getgood, Alan	P9-5	149
Gevaert, Julia	P6-2	99
	P6-4	101
Ghugre, Nilesh	O8-4	115
	P12-7	187
Gilany, Mahdi	P7-1	117
	P7-3	119
	P8-3	128
Gilbert, Kyle	O3-1	51
Gilboa, Asaf	O2-4	31
Gilliland-Rocque, Rene	O4-2	57
	P4-3	72
Gladdy, Rebecca	O12-1	167
Goertz, David	P8-2	127
Goldenberg, Mitchell	P12-4	184
Goldhawk, Donna	O6-3	86
Goncin, Una	P8-7	132
Gou, Shuiping	P5-4	92
Goubran, Maged	O2-1	28
	O2-4	31
Graf, Chantelle	O8-1	112
Graff-Guerrero, Ariel	P2-2	43
Graham, Simon	O2-4	31
Granberg, Karl	O10-2	141
	P10-6	158
Gregor, Alexander	O7-2	108
Grimm, Robert	P11-7	178
Grol, Matthew	O8-3	114
Groves, Leah A	P1-7	39
	P7-6	122
Grynko, Vira	O10-2	141
	P10-6	158
Grzela, Patrick	O11-1	162
Guo, Fumin	P11-8	179
Gupta, Arjun	P12-7	187
Gyackov, Igor	P9-4	148
Haast, Roy AM	P3-7	67
	O10-3	142
Habach, Fayez	O8-4	115
Haddad, Seyyed MH	P10-5	157
Hajdok, George	P1-3	35
Han, Wenchao	P7-7	123
Handler, William	P3-5	65
Handsor, Stephanie	P10-7	159
Hanks, James	P4-7	76
Hannan, Fahad	P2-6	47

Name	Presentation	Page
Hardisty, Michael	P10-4	156
	P12-4	184
Harris, Gordon	P4-7	76
Hassan, Ayman	O10-2	141
	P10-6	158
Hassan, Salvan	O6-3	86
Hassan, Saqeeb	P3-6	66
Havens, Alexander	P10-5	157
Heidari, Helma	P10-7	159
Hemachandra, Dimuthu	O10-3	142
Hewlett, Miriam	O3-3	53
Heyn, Chinthaka (Chris)	O2-4	31
Hicks, Justin	P2-1	42
	O6-4	87
	P6-2	99
Hisey, Rebecca	O5-3	81
	O12-2	168
	O12-3	169
	P12-1	181
	P12-3	183
	P12-8	188
Holden, Matthew	O5-3	81
	P12-3	183
Holdsworth, David W	P1-8	40
	O4-3	58
	O8-3	114
	P9-5	149
Holtshousen, Scott	P8-5	130
Houle, Sylvain	O2-2	29
	P2-7	48
Howes, Daniel	P12-1	181
	P12-3	183
Hsiung, Robin	O2-1	28
Hu, Zoe	P5-6	94
Huang, Chynna	O7-3	109
Huang, Henry	P2-7	48
Huang, Susan	P2-6	47
Husain, Ishrat	O2-2	29
Ioussoufovitch, Seva	P9-2	146
Irish, Jonathan	P8-5	130
Islam, Ali	O8-1	112
Izard, Jason	P1-1	33
Jaeger, Melanie	P8-1	126
Jagota, Arjun	P8-5	130
Jamal, Mobin	O7-3	109
James, James	P11-1	172
	P11-4	175
Jamieson, Marne	O8-4	115
Jamzad, Amoon	P1-1	33
	P1-4	36
	O4-1	56
	P4-2	71
	P4-5	74
	P7-1	117
	P7-3	119
	P8-3	128
	P12-6	186
	P12-8	188
Janzen, Nancy	P8-6	131
Jegatheesan, Aravinthan	O2-4	31
Ji, Xiang	O2-4	31
Jones, Blake	O1-3	25
Jonnalagadda, Melanie	O9-4	138
Joshi, Chandra	P8-4	129
Jurkiewicz, Michael	P2-6	47
	P10-7	159
Kadota, Brenden T	O3-4	54
	P3-4	64
Kalia, Vishal	P3-7	67
Kanagasabai, Kesavi	P3-8	68
Kang, Min Su	O2-1	28
Kasa, Kevin	P12-4	184
Kaufmann, Martin	O4-1	56
	P12-6	186
	P12-8	188
Kelly, John	P6-2	99
Kelly, John J	O6-4	87
Keunen, Ben	O12-1	167
Khan, Ali R	P3-7	67
	O10-3	142
Kikinis, Ron	P1-7	39
	P7-6	122
Kim, Janny	P6-3	100
Kim, William SH	O2-4	31
Kirby, Miranda	O11-1	162
	O11-4	165
	P11-1	172
	P11-4	175
Kish, Stephen	O2-2	29
Kiss, Alex	O2-1	28
Kitner, Nicole	P8-4	129
Kjarsgaard, Melanie	O11-2	163
Klosa, Elizabeth H	O12-3	169
Knight, Ashley	O6-2	85

Name	Presentation	Page
Knowles Nikolas	P9-1	145
Komeili, Amin	P1-2	34
Konyer, Norm	O7-3	109
	O11-2	163
Korzeniowski, Martin	P8-4	129
Koshimori, Yuko	O2-2	29
Kosik, Ivan	O4-4	59
Koucheki, Robert	O9-1	135
Koudys, Zachary J	P9-7	151
Kovacs, Michael	P2-1	42
Kuling, Grey	P1-5	37
Kumbhare, Dinesh	O9-3	137
Kuo, Philliph	O2-1	28
Laflamme, Michael	O8-4	115
Laforce, Robert	O2-1	28
Lagerwaard, Frank	P1-3	35
Lalone, Emily	O9-2	136
	O9-4	138
	P9-1	145
	P9-3	147
Lam, Ben	O2-1	28
	O2-4	31
Lang, Pencilla	P5-1	89
	P7-5	121
Lanting, Brent	P3-7	67
	P9-6	150
	P9-7	151
Larsen, Melissa	O8-2	113
	O8-4	115
Lasso, Andras	P4-2	71
Lau, Angus	O1-2	24
LaVigne, Nicola	O7-3	109
Lavon, Benjamin	O11-2	163
Law, Christine	O5-3	81
Lawrence, Liam SP	O1-2	24
Le Foll, Bernard	P10-8	160
Lee, Hung-Yu	O5-3	81
	P7-3	119
Lee, Jenny	P4-6	75
Lee, Junghoon	O5-1	79
Lee, Ting	O2-3	30
	O11-3	164
Lemberskiy, Gregory	P11-5	176
Lewis, Rob	P4-7	76
	P5-5	93
Li, Alex	P3-1	61
Li, Daniel	P6-3	100
	P11-2	173
	P11-7	178
Li, Melody	O8-2	113
Li, Natalie	P2-8	49
Li, Tao	O10-2	141
	P10-6	158
Liebig, Patrick	P2-4	45
Lightstone, Adi	O5-2	80
Lin, Peter	O8-2	113
Lin, Xun	P4-6	75
Lin, Zhongmin	O2-4	31
Lindberg, Anton	P2-7	48
Liontos, Larissa	P7-2	118
Litvack, Michael	P6-3	100
Liu, Ever	P4-6	75
Liu, John	O5-3	81
Liu, Junmin	O3-3	53
Liu, Kela	P7-7	123
Liu, Ningtao	P5-4	92
Liu, Shirley	P6-1	98
Lock, Michael	O8-1	112
Luciw, Nicholas	O2-4	31
Lugez, Elodie	P4-8	77
MacDonald, Penny	O10-3	142
MacDonald, Steven	P3-7	67
Machtaler, Steven	P8-7	132
MacIntosh, Bradley	O2-4	31
Mafeld, Sebastian	O9-1	135
Magnin, Christopher	P4-3	72
Makimoto, Kalysta M	P11-1	172
Malthaner, Richard	O1-1	23
Maralani, Pejman	O1-2	24
March, Lucas D	P12-8	188
Markevich, Stefanie	P8-5	130
Marriott, Christopher	O7-3	109
Martel, Anne	P1-5	37
	P7-2	118
	P7-7	123
Martinez, Paco	O6-1	84
	O6-4	87
Masellis, Mario	O2-4	31
	P2-2	43
	P10-1	153
Matsubara, Michele T	P9-5	149

Name	Presentation	Page
Matsuura, Naomi	P1-5	37
	O7-2	108
	O7-4	110
	P8-2	127
	P8-7	132
	O9-1	135
Mattonen, Sarah	O1-1	23
	P5-1	89
	P7-5	121
Maxwell, Sarah	P8-1	126
McCreary, Cheryl	P2-5	46
McGillivray, Joshua E	O9-3	137
McGrath, Sean F	O7-2	108
McKay, Doug	P12-8	188
McKenzie, Charles A	O10-4	143
	P10-3	155
McLachlin, Stewart	P10-4	156
McLaughlin, Paula	P10-5	157
McQuade, Paul	O6-2	85
McRae, Sean	O6-1	84
Menard, Alexandre	P1-1	33
Mendez, Lucas	P12-2	182
Menon, Ravi	P3-7	67
	P10-7	159
Meyer, Jeffrey	O2-2	29
	P2-7	48
Mihaescu, Alexander	P2-2	43
	P10-1	153
Mojiri Forooshani, Parisa	O2-1	28
Moore, Kevin RJ	O8-3	114
Moriguchi, Sho	O2-2	29
Morris, Lindsay E	O10-4	143
Moslemi, Amir	P11-1	172
Motooka, Yamato	O7-2	108
Mousavi, Parvin	P1-1	33
	P1-4	36
	P1-7	39
	O4-1	56
	P4-2	71
	P4-5	74
	P5-5	93
	P7-1	117
	P7-3	119
	P7-6	122
	P8-1	126
	P8-3	128
	P8-4	129
	P12-6	186
	P12-8	188
Mozaffari, Maryam	P3-1	61
Mrkobrada, Marko	P10-7	159
Munidasa, Samal	P11-7	178
Murrell, Emily	P6-5	102
Myrehaug, Sten	O1-2	24
Naim Ibrahim, Miriam	O5-2	80
Nair, Chaithanya	P3-7	67
Nair, Parameswaran	O7-3	109
	O11-2	163
Nair, Viswam	O1-1	23
Napel, Sandy	O1-1	23
Narang, Abhijeet	P5-2	90
Narvaez, Andrea	P6-5	102
Nasser, Zahra	O2-2	29
Nayak, Rahul	O1-1	23
Nazari, Tahmina	O12-3	169
Near, Jamie	O3-4	54
	P3-2	62
	P3-4	64
Ng, Matthew	O8-2	113
Nichols, Anthony	P5-1	89
Nikniazi, Arash	P4-2	71
Nikolov, Hristo N	O4-3	58
Nisar, Hareem	P12-5	185
Norman, Elizabeth	P9-3	147
Noseworthly, Michael	O2-1	28
	P2-3	44
	O7-3	109
	O9-3	137
	P10-2	154
Nunzi, Jean Michel	P4-2	71

Name	Presentation	Page
Nyström, Nivin N	P3-1	61
	P6-1	98
Oakden, Wendy	O3-4	54
O'Driscoll, Olivia	P12-1	181
	P12-3	183
Olding, Tim	P8-4	129
Orange, JB	P10-5	157
Orlando, Nathan	P9-4	148
Ottoy, Julie	O2-1	28
Ouriadov, Alexei V	P5-8	96
	P11-3	174
	P11-5	176
	P11-8	179
Oyeniran, Stephen	P2-1	42
Ozzoude, Miracle	O2-1	28
Palaniyappan, Lena	P3-8	68
Pantazopoulos, Koula	P10-7	159
Papernick, Sam	P9-4	148
Parasram, Tristhal	O5-4	82
Park, Claire K	O4-3	58
Parniyany, Elnaz	P11-3	174
Pasternak, Ofer	O2-1	28
Pasternak, Stephen	P10-7	159
Patel, Dhruv	P5-5	93
Patel, Jaykumar	P3-6	66
Patterson, Lindsey	P8-1	126
Pavlosky, William	O8-1	112
Peerani, Raheem	P7-2	118
Perera-Ortega, Andrea	P1-4	36
Perron, Samuel	P5-8	96
Peters, Terence M	P6-7	104
	O12-4	170
	P12-5	185
Petts, James	P4-7	76
Philpott, Holly	P9-7	151
Pichardo, Samuel	O12-1	167
Pickering, Geoffrey	O8-3	114
Pieper, Steve	P4-7	76
Piorkowska, Karolina	O12-1	167
Poepping, Tamie	O8-3	114
Pop, Mihaela	P5-2	90
	O8-2	113
Post, Martin	P6-3	100
Poushimin, Rana	P4-2	71
Prato, Frank	O2-1	28
	O6-3	86
	O8-1	112
Priel, Eldar	O7-3	109
Publicover, Julia	P4-6	75
Qi, Qi	P6-2	99
Qiabi, Mehdi	O1-1	23
Quadri, Amaar	O4-2	57
	P4-3	72
Rabin, Jennifer	O2-4	31
Radadia, Nisarg Y	O7-3	109
Radford, Katherine	O7-3	109
Rahman, Naila M	O10-1	140
Raj, Abhigyan	P5-2	90
Raman, Steven S	P7-8	124
Ramirez, Joel	O2-1	28
Ranota, Tuneesh K	P11-8	179
Rashid, Shawkh Ibne	P3-3	63
Ratjen, Felix	O11-1	162
	P11-2	173
	P11-7	178
Regnault, Timothy	O10-4	143
	P10-3	155
Reiter, Robert	P7-8	124
Ren, Kevin Yi Mi	P12-8	188
Richardson, Lauryn	P10-7	159
Roa, Felipe	O4-2	57
Roberts, Angela	P10-5	157
Rodgers, Jessica R	O4-1	56
	P8-4	129
	P12-2	182
	P12-6	186
	P12-8	188
Rodrigues, George	P1-3	35
Roifman, Idan	O8-2	113
Romine, Perrin	O1-1	23
Ronald, John	O6-1	84
	O6-4	87
	P6-1	98
	P6-2	99
Roudaia, Eugenie	O2-4	31
Rudan, John	O4-1	56
	P4-2	71
	P12-6	186
	P12-8	188
Rukas, Dan	P4-7	76
Ruschin, Mark	O1-2	24
Rusjan, Pablo	O2-2	29
Ryan, Sarah	P8-1	126
Sadafi, Hosein	O11-2	163

Name	Presentation	Page
Sadeghi, Saman	P8-6	131
Safir, Oleg	P12-4	184
Sahgal, Arjun	O1-2	24
Sahlas, Demetrios	O2-1	28
Santilli, Alice	P12-8	188
Santini, Tales	P10-7	159
Santyr, Giles	P6-3	100
	O11-1	162
	P11-2	173
	P11-7	178
Sare, Daniel	O3-2	52
Sarr, Ousseynou	P10-3	155
Schieda, Nicola	P1-2	34
	P5-3	91
Schifani, Christin	P6-5	102
Schmidt, Ehud	O5-1	79
Scholl, Timothy J	P3-1	61
	O6-1	84
	O6-4	87
	P6-2	99
Scott, Christopher	O2-1	28
Sedghi, Alireza	P4-7	76
	P5-5	93
	P7-6	122
Seethamraju, Ravi	P11-7	178
Sehl, Olivia C	P6-2	99
	P6-4	101
	P6-6	103
Sekuler, Allison	O2-4	31
Selim, Omar	P12-4	184
Senthil, Sneha Vaishali	P3-4	64
Serajeddini, Hana	O11-2	163
Sethi, Simran	P10-3	155
Sewani, Alykhan	O4-2	57
	P4-3	72
Shakibapour, Elham	P3-3	63
Shalaby, Nourhan	O6-4	87
	P6-2	99
Shargall, Yaron	O7-3	109
Sharma, Bhanu	P2-3	44
Sharp, Mackenzie	P4-5	74
Shen, Yu-Jack	O7-2	108
Shepelytskyi, Yurii	O10-2	141
	P10-6	158
Shyu, Claire	P10-8	160
Siddiqui, Maryam	O12-1	167
Sidhu, Abhijot S	P2-5	46
Siemens, Robert	P1-1	33
Silva, Luis Rafael	P8-6	131
Silverman, Michael	P10-7	159
Simard, Nicholas	P10-2	154
Singh, Gaurav V	O11-4	165
Singh, Michael D	P7-4	120
Singh, Navneet	P1-5	37
Singnurkar, Amit	O8-4	115
Sivan, Vignesh	P10-4	156
Slikboer, Samantha	P8-6	131
Smart, Kelly	P2-7	48
Smith, Eric	O2-1	28
Smith, Lauren	O10-4	143
Sojoudi, Samira	P7-3	119
Soni, Jay	P12-7	187
Sossi, Vesna	O2-1	28
Soucy, Jean-Paul	O2-1	28
Spicer, Erin	P10-7	159
Sposato, Luciano	P10-7	159
Stanisz, Greg	O1-2	24
	O3-2	52
Stewart, James	O1-2	24
Straatman, Lauren	P9-1	145
Strafella, Antonio	P2-2	43
	P2-7	48
	P10-1	153
Strasser, Bernhard	O3-4	54
Strother, Stephen	O2-1	28
Su, Feng	O11-3	164
Suh, Nina	P9-1	145
	P9-3	147
Sun, Qin	O6-3	86
Sunderland, Kyle	P4-2	71
Sung, Kyung Hyun	P7-8	124
Surry, Kathleen	P12-2	182
Sussman, Dafna	O3-2	52
Sutherland, Brian	P10-3	155
Svenningsen, Sarah	O7-3	109
	O11-2	163
Swann, Rowan E	P8-6	131
Swardfager, Walter	O2-1	28
Szentimrey, Zachary	P5-7	95
Taleb, Shahnaz	P3-7	67
Tan, Wan-Cheng	P11-1	172
	P11-4	175
Tang, Anthony	P10-7	159
Tanguay, Jesse	P11-6	177

Name	Presentation	Page
Tardif, Jean-Claude	O2-1	28
Tavallaei, Ali	O4-2	57
	P4-3	72
	P4-4	73
Taylor, Edward	O1-3	25
	O7-1	107
Teeter, Matthew	P3-7	67
	P9-6	150
	P9-7	151
Thakar, Ashutosh	O11-2	163
Théberge, Jean	P3-8	68
Theriault, Aimee	O1-2	24
Thiel, Alexander	O2-1	28
Thiessen, Jonathan	P2-6	47
	P6-2	99
	P9-7	151
Thompson, R Terry	O6-3	86
Thomson, Emma	O2-2	29
Timmons, Brian	P2-3	44
To, Minh Nguyen Nhat	P1-4	36
	P7-1	117
	P8-3	128
Tong, Junchao	P2-7	48
	P6-5	102
Trumpour, Tiana	P12-2	182
Truong, Peter	P3-2	62
	P10-8	160
Tseng, Chia-Lin	O1-2	24
Tullis, Elizabeth	O11-1	162
	O11-4	165
Turley, Eva	P1-8	40
Tzelnick, Sharon	P8-5	130
Ukwatta, Eranga	P1-2	34
	O5-2	80
	P5-3	91
	P5-7	95
Umoh, Joseph U	P1-8	40
Ungi, Tamas	P1-7	39
	O4-1	56
	P4-2	71
	O5-3	81
	P5-6	94
	P7-6	122
	P8-1	126
	P8-4	129
	O12-2	168
	O12-3	169
	P12-1	181
	P12-3	183
	P12-6	186
Urban, Trinity	P4-7	76
Uribe, Carme	P2-2	43
	P2-7	48
	P10-1	153
Uribe-Munoz, Carlos	P4-6	75
Valli, Mikaeel	P2-2	43
	P10-1	153
Valliant, John	P8-6	131
Van Beek, Kyle JT	P6-4	101
van der Pol, Luuk	O1-3	25
Van Oirschot, Matthew AN	P1-5	37
Varela-Mattatall, Gabriel	P3-7	67
Varlow, Cassis	O6-2	85
Vasdev, Neil	O2-2	29
	P2-7	48
	O6-2	85
	P6-5	102
Venegas, Carmen	O11-2	163
Vidarsson, Logi	O3-2	52
Viswanathan, Akila	O5-1	79
Vitkin, I Alex	O1-3	25
	O1-4	26
	O7-1	107
	P7-4	120
Vivekanantha, Prushoth	O6-3	86
Wade, Trevor	O10-4	143
	P10-3	155
Walton, Dave	P9-1	145
Wang, Dan	P7-7	123
Wang, Edward	P7-5	121
Wang, TianDuo	P6-1	98
Ward, Aaron	P1-3	35
Waspe, Adam	O7-4	110
	O12-1	167

Name	Presentation	Page
Wee, Wallace	P11-7	178
Weersink, Robert	O4-4	59
West, Frederick	P6-5	102
Whyne, Cari	P12-4	184
Wiggers, Theo	O12-3	169
Wilson, Brian C	O4-4	59
	P8-5	130
Wilson, Paul F R	P7-1	117
Wilson, Sydney	O4-3	58
Wisenberg, Gerald	O8-1	112
Wodlinger, Brian	P7-1	117
	P7-3	119
	P8-3	128
Wong, Alexander	P10-4	156
Wong, Suzanne	O12-1	167
Woodward, Elise	P11-3	174
	P11-5	176
Wouters, Bradley	P4-6	75
Wright, Alex	P8-2	127
Wright, Graham	O4-2	57
	P3-6	66
	P4-3	72
	P4-4	73
	P12-7	187
Wu, Catherine O	P7-6	122
Wu, Holden	P7-8	124
Wu, Tingting	P11-3	174
	P11-8	179
Wuest, Frank	P6-5	102
Wuest, Melinda	P6-5	102
Wunker, Claire	O12-1	167
Xia, Ying	O6-4	87
Xiang, Yun	P8-2	127
Xiao, Dan	O5-4	82
Xiao, Ting	P7-2	118
Xu, Kathy	O10-1	140
Yaffe, Martin	P7-7	123
Yaremko, Brian	O8-1	112
Yasufuku, Kazuhiro	O7-2	108
Yeung, Chris	P5-6	94
Yeung, Timothy	P1-3	35
Yohans, Jonathan	O6-3	86
Young, Edmond	O9-1	135
Young, Heather M	O11-3	164
Yu, Edward	O8-1	112
Zabel, William	O1-3	25
	O7-1	107
Zabihollahy, Fatemeh	O5-1	79
	P7-8	124
Zanette, Brandon	P6-3	100
	O11-1	162
	P11-2	173
	P11-7	178
Zevin, Boris	O12-3	169
Zhang, Haochen	P8-7	132
Zhou, James J	O4-2	57
	P4-3	72
Zhou, Meng	P1-1	33
Ziegler, Erik	P4-7	76
	P5-5	93
Zindler, Jaap	P1-3	35
Zou, Yiran	O7-4	110
	P8-2	127
Zukotynski, Katherine	O2-1	28

The Organizing Committees for the ImNO 2022 Annual Symposium would like to thank you for attending and acknowledge our supporting consortia and sponsors.

We invite you to attend the 21st ImNO Annual Symposium in March 2023 in Toronto, Ontario.

OICR
Ontario Institute for Cancer Research

Ontario
Research Fund

Scintica:
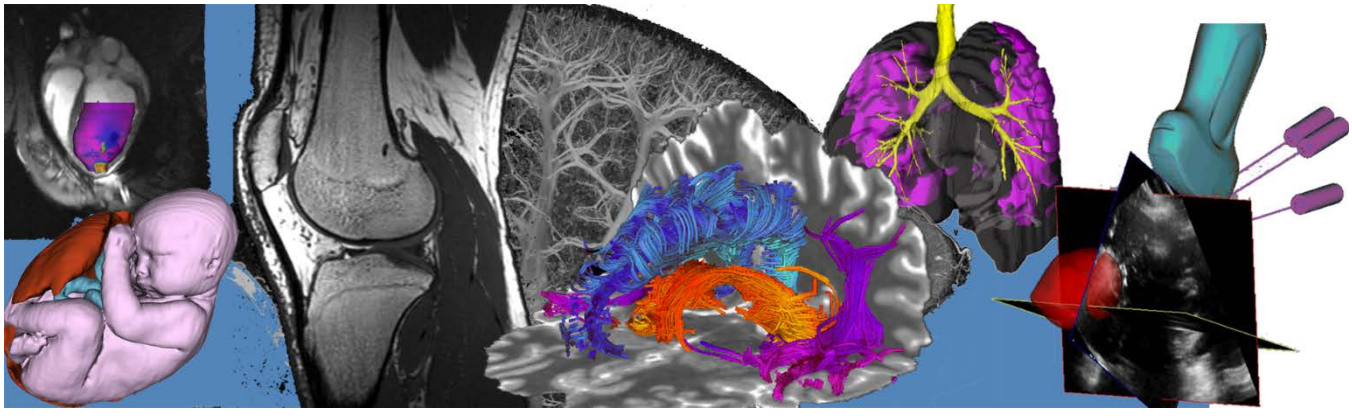
Machine Learning in Medical Imaging Consortium (MaLMIC)